Modeling of fire performance of timber structures assembled with densified wooden dowels

Trong Tuan Tran

▶ **To cite this version:**

Trong Tuan Tran. Modeling of fire performance of timber structures assembled with densified wooden dowels. Thermics [physics.class-ph]. Université de Lorraine, 2021. English. NNT : 2021LORR0298 . tel-03703045

HAL Id: tel-03703045
https://hal.univ-lorraine.fr/tel-03703045

Submitted on 23 Jun 2022

HAL is a multi-disciplinary open access archive for the deposit and dissemination of scientific research documents, whether they are published or not. The documents may come from teaching and research institutions in France or abroad, or from public or private research centers.

L'archive ouverte pluridisciplinaire **HAL**, est destinée au dépôt et à la diffusion de documents scientifiques de niveau recherche, publiés ou non, émanant des établissements d'enseignement et de recherche français ou étrangers, des laboratoires publics ou privés.

AVERTISSEMENT

Ce document est le fruit d'un long travail approuvé par le jury de soutenance et mis à disposition de l'ensemble de la communauté universitaire élargie.

Il est soumis à la propriété intellectuelle de l'auteur. Ceci implique une obligation de citation et de référencement lors de l'utilisation de ce document.

D'autre part, toute contrefaçon, plagiat, reproduction illicite encourt une poursuite pénale.

Contact : ddoc-theses-contact@univ-lorraine.fr

LIENS

Code de la Propriété Intellectuelle. articles L 122. 4
Code de la Propriété Intellectuelle. articles L 335.2- L 335.10
http://www.cfcopies.com/V2/leg/leg_droi.php
http://www.culture.gouv.fr/culture/infos-pratiques/droits/protection.htm

Thèse

Présentée et soutenue publiquement pour l'obtention du titre de

DOCTEUR DE l'UNIVERSITE DE LORRAINE

Mention : Sciences du Bois et des Fibres

par **Trong Tuan TRAN**

Sous la direction de Yann ROGAUME & Mourad KHELIFA

Comportement au feu des structures bois assemblées par des tourillons en bois densifié

Soutenue Publiquement le 17 décembre 2021

Membres of the jury :

Président de jury	**M. Thomas ROGAUME**	**Professeur, Université de Poitiers, Niort**
Directeur(s) de thèse :	**M. Yann ROGAUME**	**Professeur, Université de Lorraine, Epinal**
	M. Mourad KHELIFA	**Maître de Conférences HDR, Université de Lorraine, Epinal**
Rapporteurs :	**Mme Nathalie ROY**	**Professeur, Université de Sherbrooke, Canada**
	M. Thomas ROGAUME	**Professeur, Université de Poitiers, Niort**
Examinateurs :	**Mme Thi Binh CHU**	**Maître de Conférences, Hanoi Architectural University, Vietnam**
	M. Marc OUDJENE	**Maître de Conférences HDR, Université de Lorraine, Epinal**

Acknowledgments

This dissertation is the outcome of my research work carried out in the Wood Material Study and Research Laboratory (LERMAB) at the University of Lorraine. It is only natural to express acknowledgments to those who played a vital role in the successful completion of this work.

First of all, I would like to express my heartfelt gratitude to Mr. ROGAUME Yann (Thesis Director) and Mr. KHELIFA Mourad (Co-Thesis Director), my research supervisors, for their patient guidance and continuous support during the whole span of my study. It is my great honor to carry out my research under their supervision.

I am also grateful to my committee members, Mrs. ROY Nathalie, Mr. ROGAUME Thomas, Mr. OUDJENE Marc, and Mrs. CHU Thi Binh for the insightful comments that have improved the quality of my thesis and have been helpful in the development of my future career.

I would like to thank LERMAB Laboratory for organizing professional working environments and facilitating good researching tools during my Ph.D period. I also address my thanks to my colleagues and all the staff at LERMAB, especially Mr. GIRODS Pierre and Mr. DEBAL Matthieu for their follow-up, their advice, and their constructive remarks.

My thesis was supported by the scholarship from Vietnamese Ministry of Education and Training and funding of European Regional Development Fund (ERDF) via Interreg NWE grant 348 “Towards Adhesive Free Timber Buildings”. These financial supports are gratefully acknowledged.

I do not forget to thank Mr. THI Van Diem and the LEMOINE family for consoling and motivating me in difficult times.

To my family, especially my dear parents, who follow every step I walk with their wholehearted support, I simply cannot thank them enough. Their encouragement has given me more motivation to complete this journey.

Last but not least, I would like to give my special thanks to my wife NGUYEN Thuy Linh for listening to me and being always there when I needed it.

Table of content

List of figures ..... **v**
List of tables ..... **ix**
List of publications ..... **xi**
Nomenclature ..... **xiii**
Introduction générale en français **1**
Chapter 1 State of the art **7**
1.1 Introduction **8**
1.2 General information on wood and densified wood **9**
1.2.1 Wood material 9
1.2.2 Densified wood material 12
1.2.2.1 General information 12
1.2.2.2 The densification process 15
1.2.3 Wood moisture content 18
1.3 Physic-mechanical properties of the wood material and densified wood material **19**
1.3.1 Wood density 19
1.3.2 Thermal conductivity of wood 20
1.3.3 Specific heat capacity of wood 22
1.3.4 Mechanical properties of wood 22
1.3.5 Mechanical properties of densified wood 25
1.4 Thermal degradation of wood material **30**
1.4.1 Drying phase 30
1.4.2 Pyrolysis phase 30
1.4.3 Combustion phase 32
1.5 Conclusion **35**
Bibliography of chapter 1 ..... **36**
Chapter 2 Thermo-mechanical modeling of timber material at high temperature **41**
2.1 Introduction **42**
2.2 Theoretical aspects **44**
2.2.1 Thermal behavior of timber material at high temperature 44
2.2.1.1 Simplified model in Eurocode 5 44
2.2.1.2 Pyrolysis model 44
2.2.1.3 Development of thermal models 53

2.2.2 Mechanical behavior of timber material 56
2.2.2.1 Orthotropic elastic behavior 57
2.2.2.2 Plastic behavior 58
2.2.3 Thermo-mechanical coupling of wood material 61
2.3 Numerical aspects 63
2.3.1 Thermal analysis 63
2.3.1.1 Initial conditions and boundary conditions 63
2.3.1.2 Integral formulation of a thermal problem 64
2.3.1.3 Numerical aspects 65
2.3.2 Mechanical analysis 68
2.3.2.1 Numerical integration methods 68
2.3.2.2 Numerical aspects 69
2.3.3 Thermo-mechanical coupling 71
2.4 Conclusion 74
Bibliography of chapter 2 75
Chapter 3 Experimental characterization and kinetic analysis of wood pyrolysis 77
3.1. Introduction 78
3.2 Experimental characterization of the thermophysical properties of the densified Spruce wood 79
3.2.1 Thermal conductivity λ at room temperature 79
3.2.2 Specific heat 82
3.3 Experimental characterization of the kinetic parameters of the densified Spruce wood ... 84
3.3.1 Thermogravimetric tests 84
3.3.1.1 Test pieces and materials 84
3.3.1.2 Apparatus description 85
3.3.1.3 Different heating conditions 86
3.3.1.4 Experimental results 87
3.3.2 Thermogravimetric analysis 90
3.3.2.1 Optimization method 91
3.3.2.2 Characterization of the kinetic parameters 92
3.3.2.3 Validation model 96
3.4 Cone calorimeter test 98
3.4.1 Samples and cone calorimeter tests 98
3.4.2 Experimental set-up 99
3.4.3 Results 100
3.4.3.1 Study of the smoldering combustion (no flame) 100

3.4.3.2 Study of ignition and extinguishment 101
3.4.3.3 The temperature at the unexposed surface 103
3.4.3.4 Charring depth 104
3.5 Conclusion 106
Bibliography of chapter 3 107
Chapter 4 Structural fire response predictions 111
4.1 Introduction 112
4.2 Thermo-hydric transfer of cone calorimeter tests 113
4.2.1 Heat transfer modeling 113
4.2.2 Results 114
4.2.2.1 The temperature at the unexposed surface 114
4.2.2.2 Charring depth 115
4.2.2.3 Mass loss 117
4.2.3 Mesh sensitivity study 117
4.3 Thermo-hydric transfer of CLT panels using densified wooden dowels 120
4.3.1 Fire tests 120
4.3.2 Finite element thermal analysis 122
4.4 Thermo-mechanical analysis of L-shaped connections with densified wood dowels 125
4.4.1 Fire tests 125
4.4.2 Finite element thermo-mechanical analysis 132
4.4.2.1 Mechanical properties of wood 132
4.4.2.2 Finite element modeling 133
4.4.3 Results 134
4.4.3.1 Thermal transfer 134
4.4.3.2 Deflection at the free end 140
4.5 Influence of various parameters 144
4.5.1 Carbonization - charring rate 144
4.5.2 Densification ratio 146
4.5.3 Type of material of the dowel 150
4.6 Conclusion 154
Bibliography of chapter 4 156
General conclusion and perspectives 157
General conclusion 157
Perspectives 160
General bibliography 161
Appendices 171

Appendix 1: Thermal properties of Oak wood **171**
Appendix 2: Adhesive free timber building (AFTB) project **174**
Abstract **177**
Résumé **179**

List of figures

FIGURE 1 - Assemblage poteau-poutre réalisé par tourillons en densifié. 2
FIGURE 1. 1 - Multiscale structure of wood material [1]..... 9
FIGURE 1. 2 - Microscopic structure (a) a Softwood and (b) a Hardwood [5]. 10
FIGURE 1. 3 - Cross-section of a tree trunk. 11
FIGURE 1. 4 - Optical microscopy images of (a) Undensified and (b) Densified Douglas Fir (Pseudotsuga menziesii), using a Nikon Epiphot TME inverted microscope [9]..... 12
FIGURE 1. 5 - Image of: (a) Undensified and (b) Densified Douglas Fir [9]. 13
FIGURE 1. 6 - The glass transition temperature of wood polymers as a function of the moisture content (Salmén, 1990) [21]. 14
FIGURE 1. 7 - Hydraulic press with heated plates (maximum capacity 1500 kN). 15
FIGURE 1. 8 - Spruce wooden block before and after densification. 16
FIGURE 1. 9 - Temperature and pressure variation during densification as a function of time. 16
FIGURE 1. 10 - Variation of the final density as a function of the initial density of the samples 68% densified spruce. 17
FIGURE 1. 11 - Dowels produced from densified spruce. 17
FIGURE 1. 12 - Loss of mass and carbon content of Fagus sylvatica after heat treatment progressing at a speed of 5 °C/min [31]. 19
FIGURE 1. 13 - Relative density for wood material in Eurocode 5 [32]. 20
FIGURE 1. 14 - Thermal conductivity for wood material in Eurocode 5 [32]. 21
FIGURE 1. 15 - Specific heat for wood material in Eurocode 5 [32]. 22
FIGURE 1. 16 - Main directions of wood. 23
FIGURE 1. 17 - Pyrolysis process in wood. 32
FIGURE 2. 1 - Pyrolysis model for wet wood [12]. 45
FIGURE 2. 2 - Thermal degradation reaction model for the vaporization of water content (kw) and the pyrolysis of wood (ks) [3]. 48
FIGURE 2. 3 - The proposed model of N. Grioui (2006) [13]..... 50
FIGURE 2.4 - The proposed model of D. Blasi (2012) [14]..... 52
FIGURE 2. 5 – The time derivative evolution of wood particle in: (a) Kinetic model of N. Grioui and (b) Kinetic model of D. Blasi. 54
FIGURE 2. 6 - The multi-reactions of pyrolysis of N. Grioui (Modified). 55
FIGURE 2. 7 - The multi-reactions of pyrolysis of D. Blasi (Modified). 56
FIGURE 2. 8 - Main directions of wood material. 58

FIGURE 2. 9 - Reduction factor for the modulus of elasticity [6]. 61
FIGURE 2. 10 - Reduction factor for the mechanical resistance[6]. 62
FIGURE 2. 11 - Boundary conditions of a thermal problem. 63
FIGURE 2. 12 - Global resolution algorithm in the ABAQUS code [23]. 67
FIGURE 3.1 - Photograph and schematic of the hot plate method. 79
FIGURE 3.2 - Steady-state conditions through the sample. 80
FIGURE 3.3 - Test specimens for thermogravimetric test. 85
FIGURE 3.4 - Experimental apparatus for thermogravimetric test. 86
FIGURE 3.5 - Different heating conditions. 87
FIGURE 3.6 - Comparison in the mass and the time derivative evolution of virgin and densified wood powder in condition 6. 87
FIGURE 3.7 - Comparison of DTG curves between virgin and densified wood powder at various heating rates. 88
FIGURE 3.8 - Comparison in the mass and the time derivative evolution of virgin and densified cubic wood in condition 6. 88
FIGURE 3.9 - Comparison of DTG curves between virgin and densified cubic wood at various heating rates. 89
FIGURE 3.10 - (a) The mass and (b) the time derivative evolution of the densified wood powder. 89
FIGURE 3.11 - Testing diagram for thermogravimetric analysis. 91
FIGURE 3.12 - (a) The mass and (b) the time derivative evolution of densified wood powder in condition 5. 94
FIGURE 3.13 - Comparison of the measured and calculated MLR for three different conditions. 95
FIGURE 3.14 - Sample exposed to the cone: (a) Virgin Spruce and (b) Densified Spruce. 98
FIGURE 3.15 - The cone calorimeter. 99
FIGURE 3.16 - Experimental set-up for cone calorimeter test. 100
FIGURE 3.17 - Mass loss (ML) and surface temperature for tests without ignition. 101
FIGURE 3.18 - MLR and surface temperature for tests with ignition. 102
FIGURE 3.19 - Comparison between ignition time and extinguishment time for virgin and densified samples. 102
FIGURE 3.20 - Evolution of temperature at unexposed surface. 103
FIGURE 3.21 - The charring depth for virgin and densified spruce after cone calorimeter tests. 104
FIGURE 4. 1 - Boundary conditions in cone calorimeter modeling. 113
FIGURE 4. 2 - The temperature at the unexposed surface. 114
FIGURE 4. 3 - Formation of char at different fire-exposure times in virgin spruce (T in [K]). 115
FIGURE 4. 4 - Formation of char at different fire-exposure times in densified spruce (T in [K]). 116

FIGURE 4. 5 - Mass loss for samples of virgin and densified Spruce. 117
FIGURE 4. 6 - The cases of meshing. 117
FIGURE 4. 7 - Formation of the charred layer after 25 min exposure (T[K]). 118
FIGURE 4. 8 - Effect of mesh in temperature field at the different positions. 119
FIGURE 4. 9 - Adhesive-free CLT panels. 120
FIGURE 4. 10 - Testing diagram of fire test of CLT panels. 121
FIGURE 4. 11 - Laser scanner and residual cross-section of CLT panels….laser scanning. 121
FIGURE 4. 12 - Temperature distribution and residual cross-section in CLT panels after 15 min exposure on one side. 123
FIGURE 4. 13 - Detailed structure of L-shaped connection. 125
FIGURE 4. 14 - Testing diagram of fire test of connection. 126
FIGURE 4. 15 - Evolution of temperature in L-joint using densified wooden dowels under a heat flux of 49 kW.m^{-2} 127
FIGURE 4. 16 - Evolution of temperature in L-joint using steel….a heat flux of 49 kW.m^{-2}. 128
FIGURE 4. 17 - Evolution of temperature in L-Joint using densified wooden dowels under a heat flux of 60 kW.m^{-2} 129
FIGURE 4. 18 - Evolution of temperature in L-joint using steel….a heat flux of 60 kW.m^{-2}. 129
FIGURE 4. 19 - Residual cross-section of L-shaped connection obtained by laser scanning. 130
FIGURE 4. 20 - Displacement in case of heat flux of 49 kW.m^{-2} 131
FIGURE 4. 21 - Displacement in case of heat flux of 60 kW.m^{-2} 132
FIGURE 4. 22 - Load and deformation curves of connection 133
FIGURE 4. 23 - Mesh of the ahesive-free connection. 134
FIGURE 4. 24 - Simulated and measured temperatures for the thermal transfer in a connection exposed to heat flux of 49 kW.m^{-2}. 135
FIGURE 4. 25 - Simulated and measured temperatures for the thermal transfer in a connection exposed to heat flux of 60 kW.m^{-2}. 136
FIGURE 4. 26 - Temperature distribution and residual cross-section in connection using densified wooden dowels after exposure on two side. 137
FIGURE 4. 27 - Simulated and measured temperatures for the thermal transfer in a connection exposed to heat flux of 49 kW.m^{-2}. 138
FIGURE 4. 28 - Simulated and measured temperatures for the thermal transfer in a connection exposed to heat flux of 60 kW.m^{-2}. 139
FIGURE 4. 29 - Temperature distribution and residual cross-section in connection using steel dowels after exposure on two side. 140
FIGURE 4. 30 - Experimental and numerical displacements of the free end of the connection using

densified wooden dowels under a heat flux of 49 kW.m^{-2}. 141
FIGURE 4. 31 - Experimental and numerical displacements of the free end of the connection using densified wooden dowels under a heat flux of 60 kW.m^{-2}. 141
FIGURE 4. 32 - Experimental and numerical displacements of the free end of the connection using steel dowels under a heat flux of 49 kW.m^{-2}. 142
FIGURE 4. 33 - Experimental and numerical displacements of the free end of the connection using steel dowels under a heat flux of 60 kW.m^{-2}. 142
FIGURE 4. 34 - Charring depth in virgin spruce wood in cone calorimeter test : (a) Heat flux of 20 kW.m^{-2} and (b) Heat flux of 75 kW.m^{-2}. 144
FIGURE 4. 35 - Charring depth in virgin and densified spruce wood in kinetic model (D. Blasi) for cone calorimeter tests: (a) Heat flux of 20 kW.m^{-2} and (b) Heat flux of 75 kW.m^{-2}. 145
FIGURE 4. 36 - Charring depth in densified wooden dowel in kinetic model (D. Blasi). 146
FIGURE 4. 37 - Impact of the densification ratio on the thermal conductivity at the position of 6 mm from the exposed surface of densified wooden dowel. 147
FIGURE 4. 38 - Impact of the densification ratio on the thermal diffusion at the position of 6 mm from the exposed surface of densified wooden dowel. 148
FIGURE 4. 39 - Impact of the densification ratio on the heat transfer through the densified wooden dowel under a heat flux of 49 kW.m^{-2}. 148
FIGURE 4. 40 - Impact of the densification ratio on the heat transfer through the densified wooden dowel under a heat flux of 60 kW.m^{-2}. 149
FIGURE 4. 41 - Temperature distribution in L-joint connection under a heat flux of 49 kW.m^{-2}..... 150
FIGURE 4. 42 - Comparison between layer and dowel on the thermal diffusion at the position of 3mm from the exposed surface under a heat flux of 49 kW.m^{-2}. 151
FIGURE 4. 43 - The degradation of the holes and wood layer in L-joint connection using densified wooden dowels under a heat flux of 49 kW.m^{-2}. 152
FIGURE 4. 44 - The degradation of the holes and wood layer in L-joint connection using steel dowels under a heat flux of 49 kW.m^{-2}..... 153
FIGURE A1. 1 - (a) The mass and (b) the time derivative evolution of the Oak wood powder. 171
FIGURE A1. 2 - Comparison of the measured and calculated MLR. 172
FIGURE A2. 1 - Geographical distribution of AFTB project partners. 174
FIGURE A2. 2 - Example of glue-free products assembled by densified wood dowels (University of Lorraine, University of Liverpool): (a) beams, (b) CLT panels. 175
FIGURE A2. 3 - Example of beam-column and beam-beam connections developed at Galway University. 176

List of tables

Table 1.1. Limit values for the density of wood ρ_o [kg/m^3]. 19
Table 1.2. Some elastic properties of wood material [43]. 24
Table 1.3. Average Poisson's ratio for a wood [42]. 25
Table 1.4. Mechanical properties of uncompressed and compressed wood [46]. 26
Table 1.5. Mechanical properties of uncompressed and compressed wood [47]. 26
Table 1.6. Mechanical properties of uncompressed and compressed wood [51]. 27
Table 1.7. Mechanical properties of uncompressed and compressed wood [52]. 28
Table 1.8. Mechanical properties of uncompressed and compressed wood [55]. 29
Table 1.9. Longitudinal tensile strengths of uncompressed and compressed wood species by Song et al. (2018) [55]. 29
Table 2.1. Parameters of the pyrolysis model of D. K. Shen. 47
Table 2.2. Parameters of the pyrolysis model of G. Cueff. 49
Table 2.3. Kinetic parameters for a model of N. Grioui (2006). 52
Table 2.4. Kinetic parameters for a model with a three-step mechanism. 53
Table 2.5. Kinetic parameters for a model with a five-step mechanism. 53
Table 3.1. Thermal conductivity for virgin Spruce. 82
Table 3.2. Thermal conductivity for 68% compressed Spruce. 82
Table 3.3. Specific heat mean values (J/(kg.K)). 83
Table 3.4. Errors on m and dm/dt (N. Grioui - 2006). 92
Table 3.5. Errors on m and dm/dt (D. Blasi - 2012). 93
Table 3.6. Estimated kinematic constants (after optimization) (N. Grioui - 2006). 95
Table 3.7. Estimated kinematic constants (after optimization) (D. Blasi - 2012). 96
Table 3.8. Activation energies for pyrolysis reactions (Grioui et al. 2006). 96
Table 3.9. Activation energies for pyrolysis reactions (Blasi et al. 2012). 97
Table 3.10. Charring depth for virgin Spruce. 105
Table 3.11. Charring depth for densified Spruce. 105
Table 4.1. Comparison of measured and calculated charring depths at the middle of the panel. 116
Table 4.2. Charring depth in CLT panels after the test. 122
Table 4.3. Comparison of measured and calculated charring depths in CLT panels. 123
Table 4.4. Charring depth in L-shaped connection after the test. 131
Table 4.5. Mechanical properties of the Oak wood at 20 °C. 132
Table 4.6. Mechanical properties of the densified Spruce wood at 20 °C. 133

Table 4.7. Comparison of measured and calculated charring depths in L-joint using wood dowels .. 137
Table 4.8. Comparison of measured and calculated charring depths in L-joint using steel dowels.... 140
Table 4.9. Charring depth and average charring rate in virgin Spruce wood. 144
Table 4.10. Charring depth and average charring rate in virgin and densified Spruce wood..... 145
Table 4.11. Charring depth and average charring rate in densified wooden dowel. 146
Table 4.12. Density and thermal conductivity for different densification ratios of wood dowel. 147
Table 4.13. Charring depth and average charring rate in densified wooden dowels at different densification ratios. 149
Table A1. 1. Thermal conductivity for Oak wood. 171
Table A1. 2. Specific heat mean values (J/(kg.K)). 171
Table A1. 3. Kinetic parameters of Blasi et al. [1]. 173

List of publications

Journals

[1] T. T. Tran, V. D. Thi, M. Khelifa, M. Oudjene, Y. Rogaume, A constitutive numerical modeling of hybrid-based timber beams with partial composite action, Construction and Building Materials 178 (2018) 462-472.

[2] T. T. Tran, M. Khelifa, A. Nadjai, M. Oudjene, Y. Rogaume, Modeling of fire performance of cross laminated timber (CLT) panels, Journal of Physics conference series 1107 (2018).

Conferences

[1] T. T. Tran, V. D. Thi, M. Khelifa, M. Oudjene, Y. Rogaume, Finite element modeling of the fire performance of crossed-laminated timber panels assembled by different techniques, 6èmes journées du GDR 3544 « Sciences du bois », Nantes, France, 21-23 November 2017.

[2] T. T. Tran, M. Khelifa, M. Oudjene, Y. Rogaume, Experimental and numerical studies of the relative fire performance of densified spruce wood, 21st International Conference on Composite Structures (ICCS21), Bologna, Italy, 4-7 september 2018.

[3] T. T. Tran., M. Khelifa., A. Nadjai., M. Oudjene., Y. Rogaume, Modeling of fire performance of Cross Laminated Timber (CLT) panels, 3rd European symposium on fire safety sciences (ESFSS), Nancy, France, 12-14 September 2018.

[4] T. T. Tran., P. Girods., M. Khelifa., M. Oudjene., Y. Rogaume, Characterization of kinetics of thermal decomposition of densified wood materials from isothermal thermo-gravimetric experiments, International Conference on Advanced Materials Mechanics & Manufacturing, Hammamet, Tunisia, 13-15 October 2018.

Nomenclature

A_i [1/s]	Pre-exponential factor
b	Isotropic hardening parameter
C_i [J/(kg.K)]	Specific heat of component i
C_p [J/(kg.K)]	Specific heat
E_i [J/mol]	Reaction active energy
E_0, E_{90} [Mpa]	Modules of elasticity
G_{12}, G_{13}, G_{23}	Shear Modules
$f_{t,0}, f_{t,90}$	Tensile strengths in longitudinal and transverse directions
$f_{c,0}, f_{c,90}$	Compressive strengths in longitudinal and transverse directions
f_v	Shear strengths
F [kN]	Force
f_p	Function of the plasticity criterion
F, G, H, L, M, N	Hill's anisotropy constants
h_c [W/(m^2.K)]	Convection coefficient
k_i [1/s]	Kinetics of thermal degradation
K_θ	Mechanical resistance reduction factor
$\underline{\tilde{n}}$	Normal tensor of the load surface
$Q_r^{"}$ [W/m^3]	Heat source
R [J/(mol.K)]	Constant of gases
$R, \tilde{R}$	Isotropic hardening constants
T [K]	Temperature
t [s]	Time
w	Humidity
q [W/m^2]	Heat flux
$\underline{\underline{H}}$	Hill operator (tensor of order 4)
$\underline{\underline{K_T}}$	Continuous tangent operator (tensor of order 4)

U	Thermal energy
Δh_i^0 [J/kg]	Standard reaction energies
α	Absorptivity
β [mm/min]	Carbonization rate
σ	Stefan-Boltzmann constant
$\underline{\sigma}$	Stress tensor
ε	Emissivity
$\underline{\varepsilon}$	Strain tensor
$\underline{\varepsilon^e}$	Elastic strain tensor
$\underline{\varepsilon^p}$	Plastic strain tensor
$\underline{\underline{\Lambda}}$	Elasticity tensor
ν	Poisson coefficient
$\tau_{12}, \tau_{13}, \tau_{23}$	Shear stresses
λ [W/(m.K)]	Thermal conductivity
Δλ [W/(m.K)]	Plastic multiplier
ρ [kg/m^3]	Density

Indices:

x, y, z	Cartesian coordinates	t, 0	traction, longitudinal direction
0	longitudinal direction	w	wood
90	transverse direction	c, 0	compression, longitudinal direction
c	char	t, 90	traction, transverse direction
g	gas	c, 90	compression, longitudinal direction
l	liquid		

Introduction générale en français

Depuis les trois dernières décennies, l'axe 3 de recherche "*Energétique, Mécanique, Construction Bois"* du LERMAB hébergé à l'ENSTIB et localisé à Epinal, en cohérence avec son environnement pédagogique et industriel, développe des recherches en relation avec le bois et les fibres naturelles, allant de l'échelle microscopique à l'échelle macroscopique du matériau et des structures à grande échelle. En plus de la bonne résistance mécanique, le matériau bois offre un excellent rapport épaisseur/performance thermique comparé aux deux autres matériaux conventionnels le béton et l'acier, les plus utilisés dans la construction. Dans ce contexte particulier, le bois se présente comme une solution économique plus avantageuse dans le domaine de la construction des maisons passives.

Le bois est le seul matériau de construction de nature biologique issu de l'arbre. Par sa densité et sa légèreté du poids, il offre de nombreuses possibilités de réalisations architecturales comparé au béton et à l'acier. Il est en phase avec l'évolution des exigences environnementale et d'économie d'énergie, ce qui explique le recours à son utilisation massive dans la construction durable. Son introduction croissante dans le domaine du Génie-Civil, et en particulier dans celui des structures en bois, nécessite un haut niveau de connaissance et de maîtrise de son comportement dans des conditions normales (ambiantes) et extrêmes (cas d'incendie). D'où l'intérêt de caractériser les propriétés intrinsèques mécaniques et physico-thermiques du matériau bois pour garantir la fiabilité et la stabilité de des ouvrages en bois [1-3].

Dans le cadre d'un projet européen AFTB impliquant plusieurs partenaires universitaires et industriels spécialisés dans la construction bois, un nouvel assemblage par tourillons densifiés permettant de jointer des lamelles en bois est en cours de validation au niveau structurel (Figure I). Ce type d'assemblage possède l'avantage de ne pas utiliser de colles et de permettre de fabriquer des structures de grandes dimensions ne comportant que du bois. L'utilisation de ce type d'assemblages nécessite une multitude de vérifications de dimensionnement et de comportement à des sollicitations diverses dont les variations thermomécaniques. Ainsi, dans le cadre de ce travail de thèse, l'objectif sera de caractériser le comportement des assemblages lamelles de bois par tourillons densifiés soumises à des contraintes thermo-hydriques importantes, notamment lors d'incendie. Pour y parvenir à cet

objectif, nous proposons une approche couplée par expérimentations et par modélisation. Les expérimentations serviront dans un premier temps d'acquérir les données de base pour informer et valider le modèle numérique. La modélisation permettra ensuite de mieux comprendre les mécanismes mis en jeu lors de l'incendie de ces types d'assemblages pour en améliorer les performances. Cela permettra en outre de réduire le nombre d'essais très couteux. Le modèle éléments finis sera validé par des mesures des profils de températures à différentes profondeurs dans la section des lamelles, mais aussi au sein des tourillons densifiés. Ces résultats seront alors confrontés à des résultats des tests d'incendie réels pour validation de la méthodologie numérique. L'outil numérique développé pourra alors être utilisé pour estimer le comportement de structures plus complexes soumises à un incendie et fournir des données de base pour le dimensionnement de bâtiments complets à plusieurs étages. Les résultats pourront également servir de base pour amender les textes réglementaires tels que l'Eurocode5 [1]. C'est l'objectif principal de cette thèse qui consiste à développer et à démontrer la viabilité de nouveaux produits constructifs en bois sans colle en vue d'un usage structurel (Figure I). L'idée est d'utiliser des tourillons en bois densifié comme moyen de substitution au collage et à l'utilisation des organes métalliques.

FIGURE 1 - Assemblage poteau-poutre réalisé par tourillons en densifié.

Si le comportement mécanique du matériau bois sous l'effet de hautes températures est assez bien maîtrisé, celui des assemblages avec des tourillons en bois densifié s'avère plus difficile pour évaluer leur tenue au feu. Dans cette thèse, nous proposons d'étudier la résistance au feu de nouveaux assemblages de lamelles réalisés par des tourillons en bois

densifié sans joint de colle. La ruine de ce type de structures est principalement causée par la défaillance de ces connecteurs. Il s'agit donc de répondre à ce besoin industriel qui vise à démontrer leurs performances en situation d'incendie afin de les intégrer dans la construction. Actuellement, l'Eurocode 5 [1] ne préconise pas une modélisation plus réaliste de ce type d'assemblages. Afin de réduire le nombre d'essais d'incendie souvent onéreux et coûteux, le recours à la simulation numérique se veut nécessaire et indispensable. Dans la littérature, il y a très peu de recherches menées sur ce thème. D'où l'intérêt de fournir les outils numériques permettant la prédiction du comportement des assemblages des structures, constituées de lamelles en bois, réalisés par des tourillons en bois densifié dans des conditions d'incendie et de proposer des préconisations techniques pour leur dimensionnement.

Un frein important pour l'utilisation courante du matériau bois dans la construction est lié à sa combustibilité, qui suscite des interrogations quant à la sécurité des structures en bois vis-à-vis du feu, et au manque de données expérimentales [2-3]. En outre, les éléments disponibles sur ce thème de recherche sont pour la plupart empiriques, et les calculs de résistance sont rares. Par manque de méthodes précises d'analyse de la résistance au feu des structures bois, le bois se trouve pénalisé au niveau de la conception et du dimensionnement. Le développement de modèles généralisés demande un travail de recherche basé d'une part sur l'exploitation des résultats des tests réels d'incendie à petite et grande échelle et d'autre part sur l'analyse par simulation numérique qui nécessite une bonne maîtrise des paramètres d'entrée. Notre étude répond donc à cet objectif. Il s'agit de développer une procédure numérique qui permet de prédire le comportement thermomécanique des structures bois assemblées par tourillons exposées à de hautes températures. De plus, notre travail vise à développer des modèles pour des applications multicouches à plusieurs lamelles qui sont très fréquentes et plus difficiles à modéliser.

Bien que le matériau bois soit combustible, les structures en bois résistent d'une manière remarquable au feu comme en témoignent de nombreuses études [1-3]. La couche du charbon qui se forme à la surface exposée au feu joue un rôle d'isolant qui permet de freiner la propagation du feu vers la section centrale de l'élément où le bois reste sain. Ainsi, la formation de la couche de charbon permet aussi bien de réduit le flux de chaleur entrant. Par ailleurs, pour que la combustion du bois puisse se développer il faut qu'elle soit alimentée en oxygène, ce qui explique son développement en surface exposée seulement. La résistance au feu d'une section en bois selon EC5 [1] est estimée en majorant l'épaisseur de la couche

consumée. En l'absence de données expérimentales réalisées sur des bois de différentes essences, cette hypothèse se heurte à la complexité des phénomènes de la pyrolyse et de la combustion, et elle ne reflète pas le comportement réel au feu du matériau bois où la majorité des données des tests utilisés ont été réalisées conformément à la norme ISO 834-1 [4], qui ne reproduit pas forcement les conditions d'un incendie naturel. En outre l'approche EC5 [1] ne tienne pas compte de la cinétique de la dégradation thermique du matériau bois lors de la phase de pyrolyse. Pour la vérification de la résistance au feu d'une structure en bois, l'approche réglementaire EC5 [1] se limite à l'utilisation des courbes d'évolution des propriétés physico-thermiques (conductivité λ, densité ρ et chaleur spécifique c_p) en fonction de la température réalisées dans des conditions expérimentales spécifiques et seulement sur des résineux. Dans ce thème, plusieurs auteurs [5-7] proposent d'autres formes d'expressions de la conductivité thermique, de la densité et de la chaleur spécifique en fonction de la température. L'application de ces modèles à l'analyse des cas réels d'incendie montrent que le comportement global n'est pas suffisamment bien corrélé à cause de la variabilité des différentes valeurs des constantes (λ, ρ et c_p) [1,5-7]. Ces constantes sont tirées à partir des mesures des tests expérimentaux réalisés sur différentes espèces de bois et dans des conditions expérimentales complétement différentes. Ces modèles sont de nature simples et conservateurs. Ils présentent l'avantage d'être faciles à intégrer dans un logiciel de calcul mais ils restent moins prédictifs comparés aux modèles cinétiques décrivant l'étape de pyrolyse. Ces modèles thermiques simplifiés sont développés en détail dans la thèse de Thi [2] soutenue en 2014, qui constitue la première thèse au LERMAB dédiée à la modélisation du comportement au feu des structures en bois. Cette thèse vient pour améliorer les aspects de la modélisation en remplaçant les modèles thermiques de l'ingénieur par des modèles cinétiques, prenant en compte la phase de la pyrolyse.

Ce travail présente une contribution à la compréhension et à la modélisation de la cinétique de la décomposition thermique du matériau bois en cas d'incendie. Dans ce contexte, depuis plusieurs années, l'approche multi-échelle formulée à partir d'une loi de variation de la vitesse de type « *Arrhenius* » décrite sur la phase gazeuse reste la plus utilisée. Elle présente l'avantage d'augmenter la puissance et la fiabilité des outils de la simulation et de diminuer l'incertitude. Les nombreuses réactions physico-chimiques développées au cours des phases de séchage, de la pyrolyse et de la combustion sont décrites par plusieurs paramètres cinétiques qui sont difficiles à identifier. Ainsi une technique de caractérisation et

d'optimisation de ces paramètres cinétiques a été développée et confrontée aux données des tests. Le travail proposé est aussi relatif à la modélisation du comportement mécanique du matériau bois sous hautes températures. La validation de la méthodologie numérique développée s'appuie sur les tests réalisés en interne et sur ceux disponibles dans la littérature.

Le présent document est structuré en quatre principaux chapitres. Le chapitre 1 présente l'état de l'art sur la morphologie d'un bois résineux de structure et sur l'influence de la température sur ses propriétés mécaniques. Le chapitre 2 est consacré à la modélisation du comportement thermomécanique du matériau bois. Les aspects théoriques et numériques des modèles thermique et mécanique sont abordés. Le chapitre 3 porte sur l'identification des paramètres cinétiques des modèles cinétiques à partir des tests de l'analyse thermogravimétrie réalisés sur des particules en bois normal et densifié. Le chapitre 4 est consacré à la validation des modèles cinétiques. Une fois les paramètres cinétiques sont déterminés, ils sont intégrés dans des routines (Umat et Umatht) implémentées dans Abaqus [8] pour simuler des cas réels d'incendie. Ce rapport se termine par une conclusion générale, formulée à partir des connaissances et des enseignements acquis pendant le développement de ce travail.

Bibliography

[1] Eurocode 5 - Design of timber structures, Part 1-2 : General - Structural fire design, CEN 2004 (European Committee for Standardization), EN 1995-1-2, Brussels, Belgium.

[2] Thi V.D., Modélisation du comportement au feu des structures en bois, PhD Thesis, University of Lorraine, France (2017).

[3] Thi V.D., Khelifa M., El Ganaoui M., Rogaume Y., Finite element modeling of the pyrolysis of wet wood subjected to fire, Fire Safety Journal 81 (2016) 85-96.

[4] ISO 834-1:1999 - Fire-resistance tests - Elements of building construction - Part 1: General requirements, International Organization for Standardization, Geneva, Switzerland (1999).

[5] Knudson R.M., Schniewind A.P., Performance of structural wood members exposed to fire, Forest Products Journal 25(2) (1975) 23-32.

[6] Fredlund B., Modelling of heat and mass transfer in wood structures during fire, Fire Safety Journal 20 (1993) 39-69.

[7] Janssens M.L., Modeling of the thermal degradation of structural wood members exposed to fire, Fire Mater 28 (2004) 199-207.

[8] Abaqus, Theory Manual, Version 6.14, Providence, RI : Dassault Systèmes Simulia Corp (2016).

Chapter 1

State of the art

Summary

1.1 Introduction 8

1.2 General information on wood and densified wood 9

1.2.1 Wood material 9

1.2.2 Densified wood material 12

1.2.2.1 General information 12

1.2.2.2 The densification process 15

1.2.3 Wood moisture content 18

1.3 Physic-mechanical properties of the wood material and densified wood material 19

1.3.1 Wood density 19

1.3.2 Thermal conductivity of wood 20

1.3.3 Specific heat capacity of wood 22

1.3.4 Mechanical properties of wood 22

1.3.5 Mechanical properties of densified wood 25

1.4 Thermal degradation of wood material 30

1.4.1 Drying phase 30

1.4.2 Pyrolysis phase 30

1.4.3 Combustion phase 32

1.5 Conclusion 35

Bibliography of chapter 1 36

1.1 Introduction

Wood is a living material from a plant species that are cultivable and renewable. Understanding its characteristics is still relatively incomplete. Its strong anisotropy makes it difficult to grasp its general properties which are highly dependent on its internal structure such as its composition and cell structure. In addition, its combustible nature makes it difficult to study at high temperatures.

This chapter presents a non-exhaustive state but sufficiently provided a state of current bibliographic knowledge on wood and more particularly on its behavior during a thermal attack. Firstly, we present the wood material and densified wood material derived from wood in their generalities. In the second step, the main physic-mechanical properties of the wood and densified wood material will be discussed. Finally, we will present the phenomena of thermal degradation of wood which are very complex.

1.2 General information on wood and densified wood

1.2.1 Wood material

Wood is a complex polymer composite whose general properties are highly dependent on its internal structure. Its highly heterogeneous microscopic composition makes it possible to explain partly its behavior on a macroscopic scale. From a microscopic point of view, wood is composed of a multitude of cells that constitute the unitary basis of the material. The assembly of these cells, parallel to each other, allows the macroscopic structure to be formed.

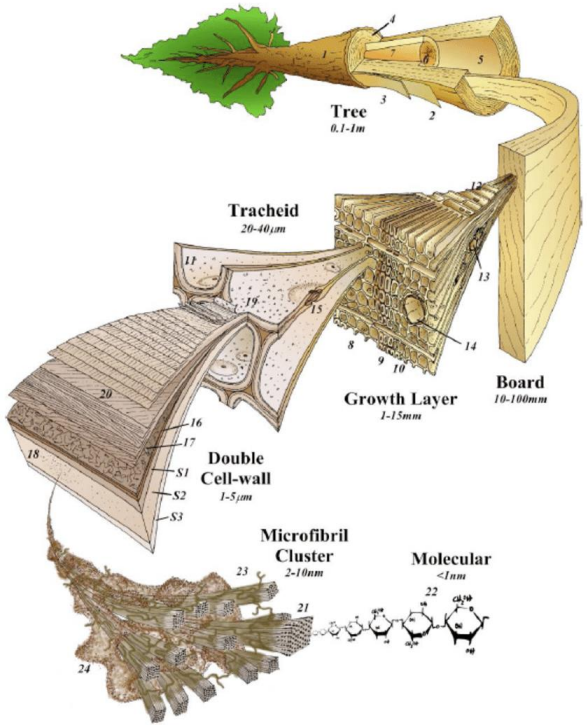

FIGURE 1. 1 - Multiscale structure of wood material [1].

Celluloses are polymers of glucose molecules made up of primary components of cell walls (Figure 1.1). The microscopic structure of a cell consists of a complex assemblage of different components whose proportions vary depending on the species of wood and the growing conditions of the tree. The average composition of the wood components can be as follows [1]:

- Cellulose, at around 43% in terms of mass, is the majority constituent. This cellulose forms the microfibrils which enter into the composition of the cell wall and form the reinforcements of the cellulosic composite. Cellulose contributes to the tensile strength of wood.

- Hemicellulose, at around 30%, helps to regulate the moisture content of the wood by binding to water molecules. This compound partly plays the role of the composite matrix.

- Lignin, at around 27%, regulates the humidity level via hydrophobic properties. The main role of lignin is to bind cells together. This is the main element of the wood composite matrix. It contributes to the rigidity of the wood material through the cohesion of the fibers [2,3].

In reality, the composition of cellulosic material is not reduced to these three components. A weak percentage of components called "extractables" and pectins are also presented in the wood (3% to 7%). These extractables will have different roles such as protecting the wood against fungicidal attacks or supplying nutrients. Pectins, mainly presented in the first thickness of the cellulosic wall, will ensure a certain cohesion of the cells [1].

From a structural point of view, the wood cells divide into layers differentiated by the orientation of their cellulose microfibrils, which are embedded in the lignin and hemicellulose matrix [4].

Woody plants are divided into two distinct wood classes [5], softwood and hardwood, whose structural properties are different (Figure 1.2):

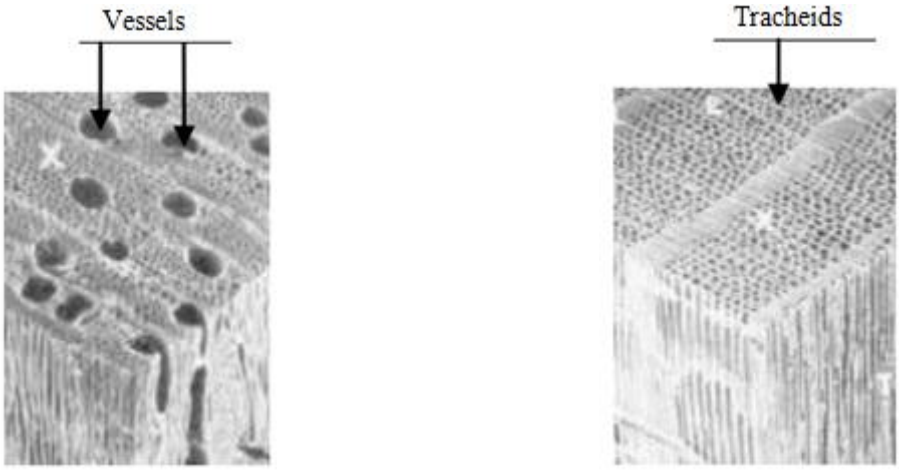

(a) Softwood (b) Hardwood

FIGURE 1. 2 - Microscopic structure (a) a Softwood and (b) a Hardwood [5].

- Softwoods have a simple and uniform organization. They consist of two types of cells: tracheids and parenchyma cells. Raw sap transport and support of the tree are provided by the

tracheids, while the parenchyma cells allow the storage and the distribution of chemicals [6]. Softwoods are 90% made up of tracheids, and they contain woody rays. The most common softwoods are spruce, Douglas, maritime pine.

- Hardwoods are made up of different types of cells (vessels, tracheids, and parenchyma). The vessels are mainly oriented in the direction of the wood fibers. Those oriented radially constitute the woody rays and perform three functions: radial conduction of sap, stem support, and storage of chemicals [6]. Hardwoods can be referred to as oak, beech, chestnut, and poplar.

Wood can be considered as a continuous material at the macroscopic scale. Concerning the macroscopic structure of the wood, or rough structure, we can distinguish five areas that are directly visible to the naked eye as shown in Figure 1.3:

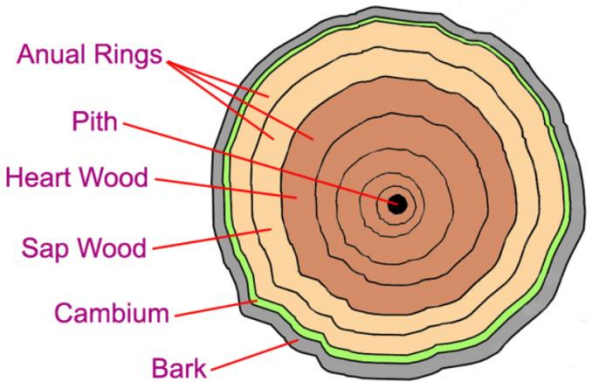

FIGURE 1. 3 - Cross-section of a tree trunk.

- The bark is the external part of the wood. It is used to protect the tree from attacks from its environment such as fungi, climate, or wounds.

- The cambium represents the part of the trunk in which radial growth occurs.

- Sapwood is made up of the living cells of the tree. It is in this area that the manufacture of new cells within the cambium, around the bark, allows the tree growth.

- The heartwood is made up of dead cells. This central part is more compact than the others and its concentration in "extractables" is higher than in sapwood, which gives it a darker color. Its characteristics make it a better quality wood (mechanically and against external attacks).

- The pith represents the center of the tree. It is composed of the tissues formed during the first year of tree growth.

The description of the macroscopic structure of the wood must also take into account the annual growth of the tree. By its biological nature, wood is a porous hygroscopic material formed during the growth in the diameter of the shaft. The cells formed in the cambium (figure 1.3) are different and arrange themselves to ensure the conduction of nutritive materials, the mechanical support of the stem, and the storage of substances.

From a general point of view, the physical and mechanical properties of wood will be directly dependent on this microscopic and macroscopic structure. Therefore, the high variability could be observed according to the different species of wood studied as well as for the same sample depending on the scale and directions of study thereof.

1.2.2 Densified wood material

1.2.2.1 General information

Densified wood (also referred to as compressed wood in the literature) materials is considered as a type of Engineered Wood Products (EWPs). This material is classified in the category of hydro-thermo-mechanical modifications of wood [7]. By reducing the pores and voids (called lumen) between the cell walls of low-density wood through the densification process, as shown in Figure 1.4 and Figure 1.5, the density and other mechanical properties (e.g. strength, Young's modulus, and hardness) will be increased. The densification process also makes the effective thermal conductivities in the tangential and fiber directions of wood increase proportionally [8].

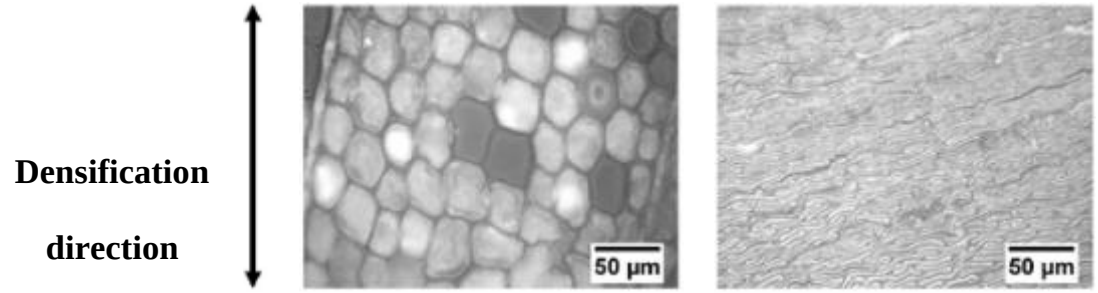

(a) (b)

FIGURE 1. 4 - Optical microscopy images of (a) Undensified and (b) Densified Douglas Fir (Pseudotsuga menziesii), using a Nikon Epiphot TME inverted microscope [9].

Following densification, low-density timber species can be used as an alternative to hardwood species [10]. Densified wood products are used in diverse and advanced

applications (such as jigs and tooling in the construction, aerospace, and automotive industry) due to their higher mechanical properties [11]. For example, Anshari et al. (2012) [12] utilized densified wood as a reinforcement material in glulam beams by its moisture-dependent swelling and improved mechanical properties. In this way, the bending stiffness increased by up to 46% compared to that of unreinforced glulam. To investigate the influence of geometry and arrangement of the densified wood on the pre-camber, bending stiffness, and the maximum load of the reinforced glulam beams, finite element modeling was used [13]. Glass and Zelinka (2010) [14] replaced steel plates and dowels by densified wood plates and dowels in a timber beam-column connection. By utilizing the moisture-dependent swelling effect of densified wood materials a tight-fit was created in these connections. Recyclability, reusability, and relatively lower density are the additional benefits of densified wood when compared with steel [7].

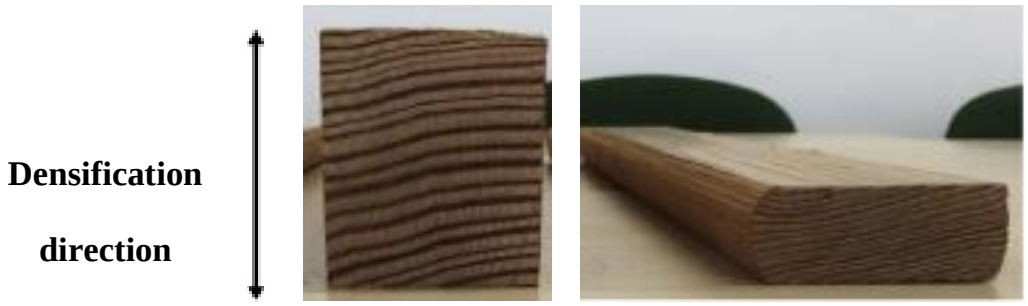

(a) (b)

FIGURE 1. 5 - Image of: (a) Undensified and (b) Densified Douglas Fir [9].

Bulk densification and surface densification can be considered as two categories of wood densification [15]. Bulk densification refers to the compression of wood cells through the total volume of the timber section, whereas surface densification involves the partial compression of the wood cells close to the surface of the timber section [15-17]. The densified wood products have been studied since the 1930s [18-19]. Additionally, timber densification can be also carried by impregnating the voids between the cell walls with different materials such as molten metals/sulfur and polymers [19].

To avoid damage caused by the buckling of the latewood annual rings or the formation of a zigzag pattern on the cross-section faces on the densified wood, densification of wood is typically carried out in the radial direction (rather than tangential direction) [16,20]. At low moisture contents and low temperatures, wood has a glass behavior (stiff and brittle) whereas,

at high moisture contents and high temperatures, it exhibits rubbery behavior [10,21]. The glass transition temperature is defined as the temperature for the happen of transition from glassy to rubbery behavior. The glass transition temperature of wood polymers as a function of their moisture content is depicted in Figure 1.6 [21]. The figure shows that the moisture content affects the glass transition temperature of wood. When the temperature of the wood is greater than the glass transition temperature, densification can occur without damaging wood cells. A temperature between 120 –160 °C is required for the densification of wood [16]. The species, pre/post-treatment conditions, pressing time, pressing temperature, the pressure applied, pressing speed, and compression ratio are the factors that affect the quality and mechanical properties of densified wood [22-23].

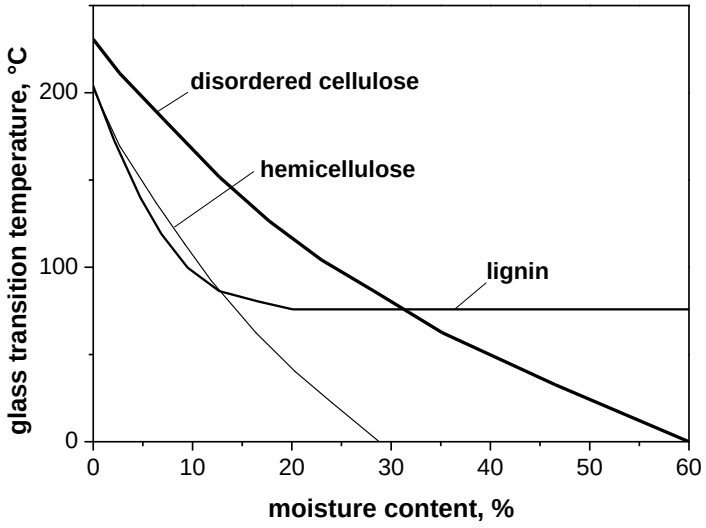

FIGURE 1. 6 - The glass transition temperature of wood polymers as a function of the moisture content (Salmén, 1990) [21].

The compression ratio (or densification ratio) CR is defined as the difference between the initial and final thickness of the wood as a percentage of the initial thickness [9].

$$CR = \frac{E_p(i) - E_p(f)}{E_p(i)} \times 100\% \tag{1.1}$$

where $E_p(i)$ and $E_p(f)$ are the thicknesses (in the compression direction) before and after compression, respectively.

The effect of compression ratios on the mechanical properties of densified wood has been investigated in different studies. The degree of densification is dependent on anatomical

features and the initial density of the wood, so the compression ratios can be limited by the type and species of wood. For example, black locust (Robinia pseudoacacia L.) with an initial density of 750–900 kg/m^3 was compressed to a maximum compression ratio of 50%. Using a higher compression ratio would lead to damage of the cells [7]. Therefore, to avoid macroscopic damage, the compression ratio would need to be less for wood with relatively higher densities (commonly hardwood species). In the same study, beech with 60% radially compression ratio reached the highest density values in the range of 1103–1246 kg/m^3, and exceeding such compression ratio would have fractured the cells [7]. Thus, there are compression limits for different wood species to avoid damage.

1.2.2.2 The densification process

The choice of the densification process is based on the state-of-the-art already presented. Densification thermomechanics with a pre-treatment of the wood was used. A hydraulic press (Figure 1.7) with a capacity of 150 tonnes with heated trays enabled densification in an open system where temperature, pressure, and pressing time were controlled.

FIGURE 1. 7 - Hydraulic press with heated plates (maximum capacity 1500 kN).

Before the densification process, dry wood with a moisture content of 8% was soaked in water heated to 80 °C for only one hour to increase its water content and temperature. This process softens the constituents of the wood which pass from the state glassy in a softened state to facilitate densification. Compression is performed in the radial direction, the pressing temperature was fixed at 130 °C, the choice of this temperature is taken to avoid any degradation of the constituents of wood under high temperature.

Densification is carried out on blocks of spruce (Picea abies), with dimensions in plan 500x120 mm, and 64 mm thick. After plasticization of the spruce, the pressure was applied in stages up to a maximum pressure equal to 18 MPa, under a maximum temperature of 130 °C. This pressure was sufficient to compress the wood to an equal compression ratio (CR) at 68%.

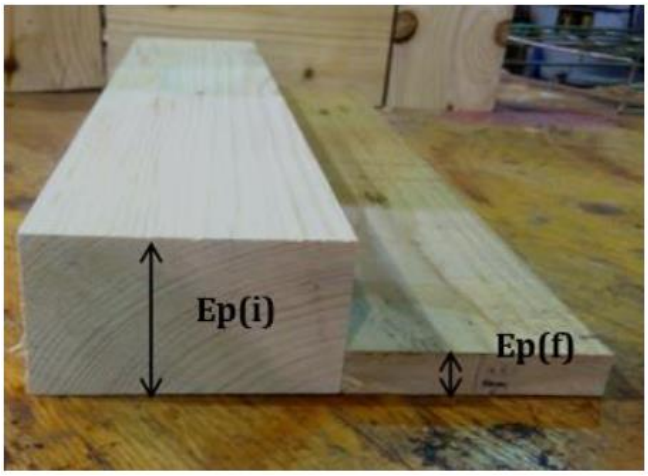

FIGURE 1. 8 - Spruce wooden block before and after densification.

The original 64 mm thick wooden blocks are densified to a final thickness of 20 mm. The total densification of spruce takes 18 min with a maximum pressure of 18 MPa and it remains kept constant for 5 hours until the plates have cooled to a temperature below 65 °C. Cooling is necessary to avoid instant swelling during discharge. Figure 1.8 shows the change in thickness before and after densification.

Figure 1.9 shows the densification process with the variations of the applied loading and temperature as a function of time.

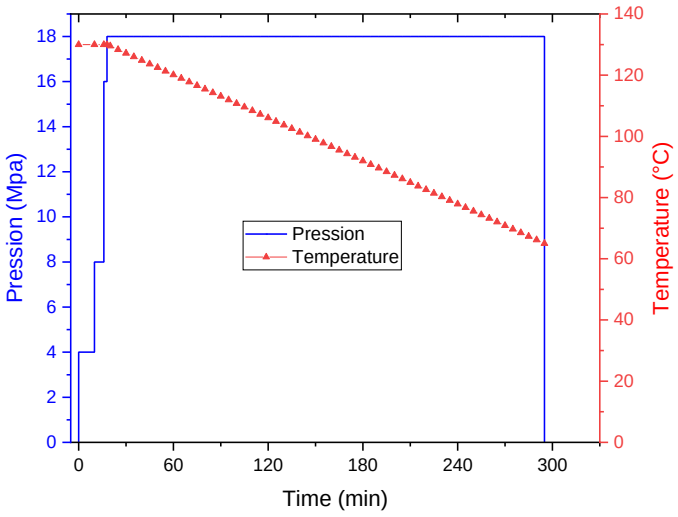

FIGURE 1. 9 - Temperature and pressure variation during densification as a function of time.

After densification, the moisture content of densified wood continues to decrease until stabilizes after three weeks at 10%. Thus, they are weighed to calculate the final density after the densification. The final density is dependent on the initial density of the wood. Figure 1.10 below shows the variation of the final density as a function of the initial density of the spruce blocks. We can see that with the densification we were able to have a type of wood with a high density equal to 1250 kg/m^3. In order to quantify the effect of densification on the mechanical properties of wood, different tests have been carried out.

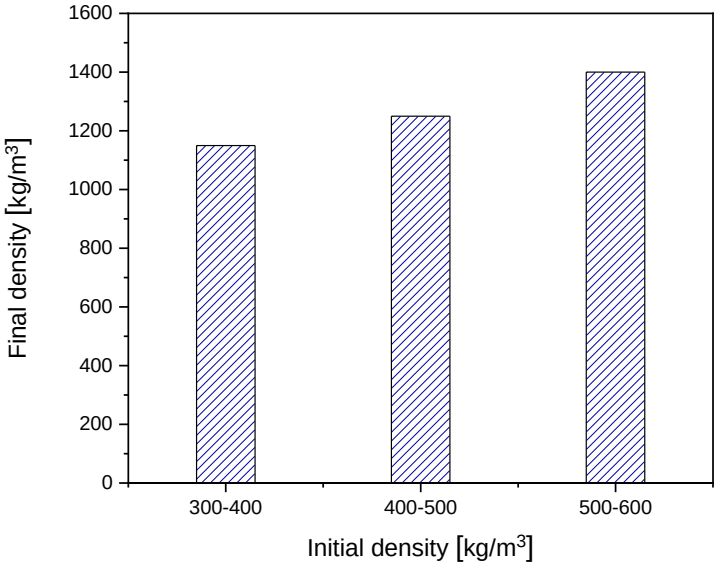

FIGURE 1. 10 - Variation of the final density as a function of the initial density of the samples 68% densified spruce.

After densification, dowels are cut to use to join beams and panels. Figure 1.11 shows densified Spruce dowels used for assemblies panels and beams.

FIGURE 1. 11 - Dowels produced from densified spruce.

1.2.3 Wood moisture content

Wood is a hygroscopic material, which means it absorbs part of the moisture from its environment. Thus, the water content of the wood not only depends on its internal structure but also on its surrounding environment. There are two types of humidity: Moisture on dry and wet wood. Moisture content on dry wood w_S corresponds to the ratio of the mass of water to the mass of anhydrous wood [24]:

$$w_s = \frac{m_w - m_0}{m_0} \tag{1.2}$$

where m_w is the mass of wet wood and m_0 is the mass of dry wood.

Moisture content on wet wood w_B is the quantity of humidity compared to its total mass (mass of wet wood):

$$w_B = \frac{m_w - m_0}{m_w} \tag{1.3}$$

The water circulating in the cell voids is called free water and its evacuation does not cause withdrawal. The water in the cell walls is bound water. It is only evacuated when the free water is evaporated: corresponding to a saturation point of the fibers at a humidity rate of approximately 30%. Removal of bound water can cause shrinkage or swelling. The third form of water, which is an integral part of the chemical structure, is found in the constituent molecules of the wood which can only be released by chemical reaction, pyrolysis, or combustion.

1.3 Physic-mechanical properties of the wood material and densified wood material

1.3.1 Wood density

The density denotes the quotient of the mass m_0 [kg] of the dry wood material related to the initial volume v_0 [m^3]. It is independent of humidity, and its reference value ρ_0 [kg/m^3] is taken equal to:

$$\rho_0 = \frac{m_0}{v_0} \tag{1.4}$$

Knigge and Schulz [25] studied two species of wood, fir, and beech, and the values in terms of density ρ_0 [kg/m^3] are summarized in Table 1.1.

Table 1.1. Limit values for the density of wood ρ_o [kg/m^3].

Essences	$\rho_{0,min}$	ρ_0	$\rho_{0,max}$
Beech (Fagus sylvatica)	540	660	840
Fir (Picea abies)	280	420	610

The mass of the wood changes under the influence of high temperature due to its decomposition. At temperatures between 200 °C and 400 °C, the chemical reactions, which are produced in wood, promote the formation of charcoal [26-28]. Between 400 °C and 600 °C, the production of tars is preferred [29-30]. Volatile matter (gas) begins to form when thermal degradation begins and up to temperatures above 600 °C.

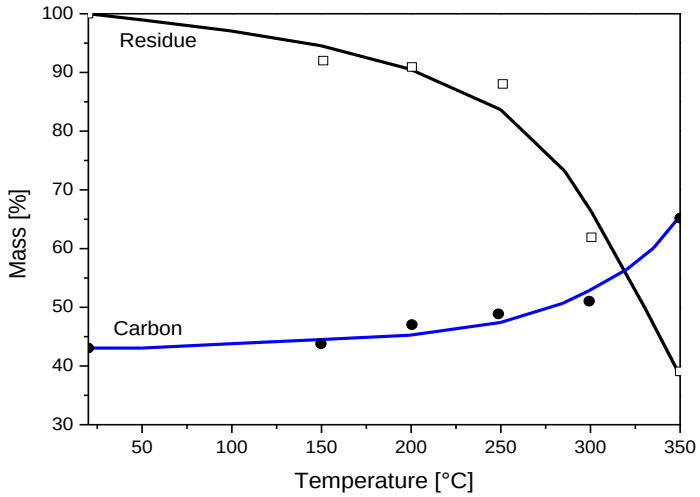

FIGURE 1. 12 - Loss of mass and carbon content of Fagus sylvatica after heat treatment progressing at a speed of 5 °C/min [31].

Figure 1.12 shows the evolution of the loss of mass of a Fagus sylvatica as a function of temperature. At a temperature of 200 °C, the mass loss is 10% and the carbon content begins to gradually increase.

The decrease in density of the wood depending on the temperature is done in three phases:

- For temperatures below 200 °C, the modification of the density of the wood is very weak.

- Between 200 °C and 350 °C, the wood pyrolyzes, and consequently, the degradation of chemical constituents causes a decrease of about 75% in density.

- Beyond 350 °C, there is a charcoal formation and the density varies very little.

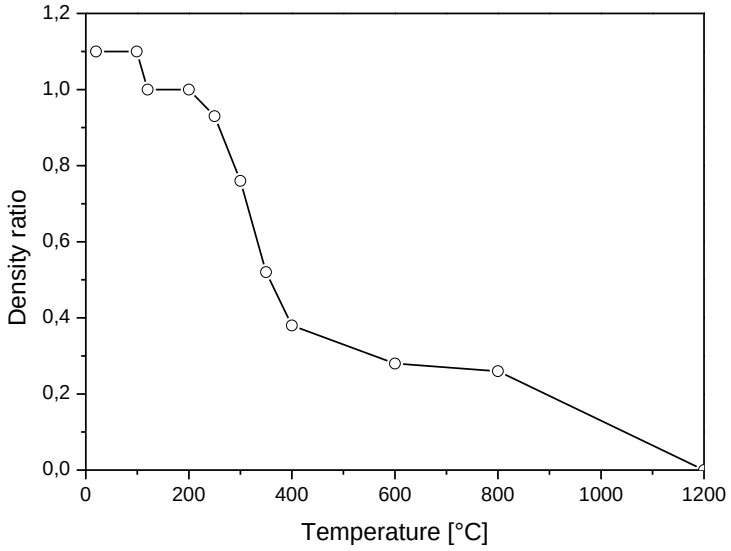

FIGURE 1. 13 - Relative density for wood material in Eurocode 5 [32].

Figure 1.13 shows the evolution of the relative density ρ/ρ_0 as a function of temperature. With temperatures below 100 °C, ρ/ρ_0 is around 1 + w (w is the humidity). At T = 100 °C, this ratio is reduced to 1 (w tends to 0) which corresponds to the evaporation of water. This ratio stabilizes up to T = 220 °C. Its value begins to drop rapidly between T = 220 °C and T = 380 °C. At this temperature level, the wood has lost 75% of its initial mass.

1.3.2 Thermal conductivity of wood

The thermal conductivity of wood λ (W/(m.K)) depends on several parameters such as the volume mass, the water and extractable content of the wood, the internal structure of the cellulosic material, and the temperature [33]. Generally, the thermal conductivity of wood

increases when the density, the water content, or the extractable content increases.

Due to the strong anisotropy of wood, the thermal conductivity strongly depends on the orientation of the sample during measurement. The thermal conductivity in the tangential direction (T) is very close to the value in the radial direction (R). Therefore conductivity in the perpendicular direction with the fibers of wood is generally considered to be the average of these two values. However, the longitudinal conductivity (L) of the wood fibers is significantly higher, by 1.5 to 2.8 times greater than that observed in the transverse plane of the tree trunk [34-37]. We can nevertheless say that wood is a particularly insulating material with a conductivity thermal at 20 °C between 0.12 W/(m.K) to 0.25 W/(m.K). So they are very far from conductor materials such as aluminum (237 W/(m.K)) or certain insulators such as concrete (1 W/(m.K)).

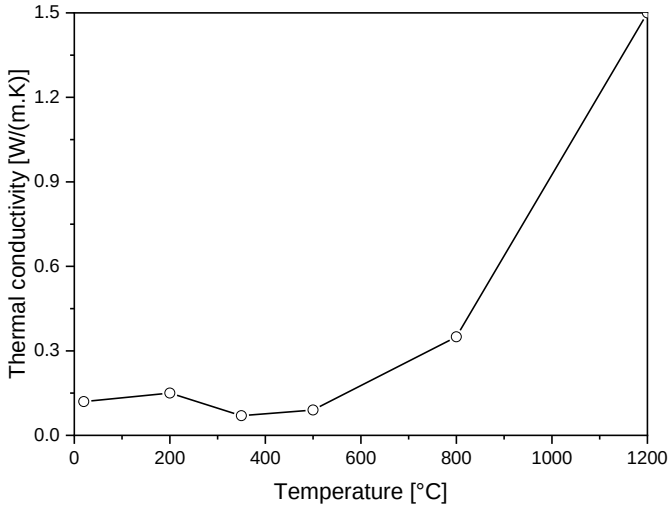

FIGURE 1. 14 - Thermal conductivity for wood material in Eurocode 5 [32].

Figure 1.14 shows the evolution of thermal conductivity λ as a function of temperature. According to the regulatory approach in EC5 [32], beyond a temperature level T = 500 °C, the conductivity λ starts to increase. It goes from λ = 0.09 W/(m.K) (T = 500 °C) to a value of λ = 1.5 W/(m.K) (T = 1200 °C), which is not in accordance with experimental observations. In general, the charcoal layer is formed at T = 300 °C and its conductivity is about six times lower than that of healthy wood. This results in a decrease in the value of λ. This behavior is unlike the values suggested by the EC5 approach [32]. The hypothesis, adopted by EC5 [32], is made to account for (1) the combustion of gases and (2) the increase in heat transfer due to cracks on surfaces directly exposed to fire.

1.3.3 Specific heat capacity of wood

The specific heat Cp [J/(kg.K)] corresponds to the quantity of heat that must be supplied to the unit mass to raise its temperature by 1 K. Like thermal conductivity λ, specific heat Cp is less well known, and its value is measured by experience.

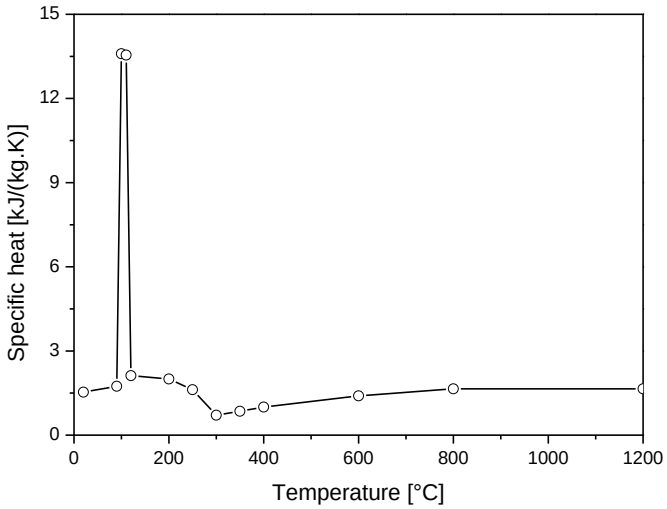

FIGURE 1. 15 - Specific heat for wood material in Eurocode 5 [32].

Figure 1.15 shows the evolution of specific heat Cp as a function of temperature. At a temperature of around 100 °C, and according to the regulatory approach EC5 [32], the specific heat presents a jump from Cp = 1770 J/(kg.K) (T = 99 °C) to Cp = 13500 J/(kg.K) (T = 120 °C). This jump is introduced to take into account the energy required for the water to evaporate during the drying phase.

1.3.4 Mechanical properties of wood

On a macroscopic scale, the mechanical properties of wood depend on the species and the direction of the considered loading [38-41]:

- The biological origin of wood affects its mechanical properties significantly during tree growth. This living material is therefore naturally orthotropic. The cells that compose it have different natures and shapes and it has an irregular density in the trunk. Singularities and growth defects, characterized by the presence of nodes, cause a large variation in mechanical properties in the longitudinal direction of a wooden structure [38-41] (Figure 1.17).

- Due to its fibrous constitution, its mechanical properties vary depending on the direction of the loading concerning the direction of the fibers [41]. The fibers are mainly oriented in the longitudinal direction of the trunk as shown in Figure 1.17. Three main directions are defined:

longitudinal (L), radial (R), and tangential (T) directions (Figure 1.17). These three directions constitute the axes of orthotropic wood. The various mechanical properties of this material are different in these three directions.

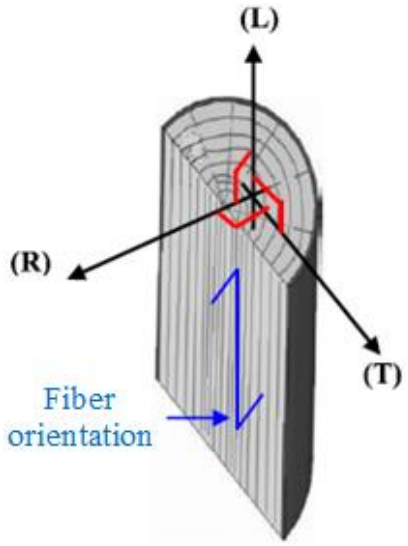

FIGURE 1. 16 - Main directions of wood.

The mechanical properties of wood characterize the ability of the material to deform without damaging its internal structure, under the action of mechanical or thermal stress.

Wood is considered to be an orthotropic material with cylindrical symmetry [42]. In this frame, we find twelve different elastic constants, namely three moduli of elasticity E_L, $E_{R,}$ and E_T, three shear modules G_{LR}, G_{LT}, G_{TR}, and six Poisson's coefficients ν_{LR}, ν_{LT}, ν_{RT}, ν_{TR}, ν_{RL} and ν_{TL}.

The mechanical properties of wood at room temperature are widely studied in the literature. Different authors such as Guitard [38] and Navi [42] present data for solid wood. It is noted that the bibliographic data reveal significant variability in the properties measured between different species as well as for the same wood species. This reflects the heterogeneity of the wood material and the sensitivity of the result to the test protocol used.

Guitard [38] presents a completed state of the art of elastic properties of different wood species as well as general models for hardwoods and softwoods. Elastic properties obtained via these models are based on standard values, corrected according to the density of the wood. The author has extended these research results to all conifers and hardwoods. Modules of elasticity (E_L, E_R, and E_T) measured respectively in the three longitudinal (L), radial (R) and

tangential (T) directions are:

$$E_L = 13100 + 4170(\rho - 0.45) \quad (1.5)$$

$$E_R = 1000 + 2370(\rho - 0.45) \quad (1.6)$$

$$E_T = 636 + 1910(\rho - 0.45) \quad (1.7)$$

where ρ [g/cm^3] is the density of the wood.

According to Guitard (1987), the elastic constants of a standard wood have anisotropy ratios as follow [38]:

$$E_L \gg E_R > E_T;\ E_{LR} \gg E_{LT} > E_{RT}$$

Table 1.2 summarizes some results of studies on the elastic properties of the wood material in the three main directions (L), (R), and (T).

Table 1.2. Some elastic properties of wood material [43].

	Douglas			Spruce		Pine	Chêne	
ρ_m [kg/m^3]	470	440	480	360	390	490	560	590
w [%]	12	12	12	12.8	12	12	12	12
E_L [MPa]	16872	16858	16000	10775	11800	16015	15248	14881
E_R [MPa]	949	848	1010	650	920	1182	1182	1505
E_T [MPa]	934	842	800	349	510	616	616	830
G_{LR} [MPa]	749	713	900	534	760	828	828	970
G_{LT} [MPa]	802	856	900	440	730	688	688	697
G_{RT} [MPa]	114	109	90	41	40	320	320	399

Poisson's ratio for a hardwood with density ρ = 650 kg/m^3 and a softwood of density ρ = 450 kg/m^3, at a humidity rate around 12% are given in Table 1.3 [42].

Table 1.3. Average Poisson's ratio for a wood [42].

Essence	ν_{LR}	ν_{LT}	ν_{RT}	ν_{TR}	ν_{RL}	ν_{TL}
Hardwood	0.39	0.46	0.67	0.38	0.048	0.033
Softwood	0.39	0.43	0.51	0.31	0.030	0.020

The mechanical properties of wood products can vary greatly depending on the product studied. The wood panels must meet mechanical resistance criteria including the requirements presented in standard NF-EN-312 [43]. Characterization tests for this type of product are generally bending (NF-EN-310 [44]) and tearing tests perpendicular to the faces of the panel (NF-EN-319 [45]). Standard NF-EN-312 [43] classifies the panels according to different resistance criteria according to the end use of the product (dry, humid environment, interior fittings, etc.). The flexural modulus required varies from 1050 MPa to 3350 MPa with resistance to flexion ranging from 5.5 MPa to 22 MPa.

1.3.5 Mechanical properties of densified wood

The compressive and shear tests on uncompressed and compressed Japanese cedar were carried out to evaluate their mechanical properties at different compression ratios (33, 50, 67, and 70%) [46]. To avoid cell damage, the compression ratio was limited to 70%. The timber samples were pre-heated for 1 h at 130 °C, before pressing for 30 min, and cooled for about 1.5 h. Table 1.4 presented the mechanical properties of compressed wood, compared with those of uncompressed Japanese cedar (Materials with a CR of 0% refer to uncompressed wood).

Table 1.4 also shows that an increase in the compression ratio typically led to an increase in the density and longitudinal Young's modulus. The highest mechanical properties occur in The samples with a 70% compression ratio, for example, about over 300% increase in the longitudinal modulus compared to that of the uncompressed wood. There are only the elastic properties of compressed wood investigated in this research whereas their strengths were not be reported. Therefore it is important to further study the strengths of compressed wood, as they are an essential set of properties used in the design of load-bearing structures.

Table 1.4. Mechanical properties of uncompressed and compressed wood [46].

CR [%]	Density [kg/m^3]	Young's modulus			Shear modulus		
		E_L [MPa]	E_R [MPa]	E_T [MPa]	G_{LR} [MPa]	G_{LT} [MPa]	G_{RT} [MPa]
0	322	8017	753	275	972	784	31
33	403	19864	338	1592	300	669	122
50	564	27028	354	2267	178	787	170
67	886	28415	523	2347	208	1208	256
70	1162	32858	3111	5061	1590	5717	878

70% of compressed Japanese cedar was fabricated by Jung et al. (2008) [47] (Cryptomeria japonica D Don.). The samples were processed by pressing at 130 °C for 30 min. The flexural tests as well as the strength properties on the timber samples were also reported in this research. Table 1.5 shows the significant increases in the density, flexural modulus, and flexural strength of compressed wood. The value of the longitudinal flexural modulus with an increase from 11 GPa to 30 GPa is slightly smaller than that of the 70% compressed Japanese cedar (~33 GPa) by Anshari et al. (2011) [46]. Furthermore, there was a 185% increase in the bending strength (86 Mpa to 245 MPa).

Table 1.5. Mechanical properties of uncompressed and compressed wood [47].

CR [%]	Density [kg/m^3]	Flexural modulus [GPa]	Flexural strength [GPa]
0	330	11	86
70	1000	30	245

70% compressed Japanese cedar dowels (square and circular) were used as an alternative to maple hardwood dowels in the study of Jung et al. (2008) [47]. The flexural modulus and strength of the maple dowels were 16 GPa and 152 MPa, respectively (see Table 1.5). In the double-shear tests, the compressed wood dowels exhibited a greater ductility than maple dowels and were reasonably close to that of a steel pin. This indicated the prospect of utilizing compressed wood dowels in connections. The study also highlighted that a greater ductile response of the insertion of the compressed wood dowels with the annual ring of the dowel perpendicular to the loading direction (during a push-out double shear test) compared to

insertion parallel to the loading direction.

Compressed wood dowels and plates were also utilized as fasteners in column-sill and column-beam joints by their improved mechanical properties [48-50]. The potential of compressed wood in connections was demonstrated by the results obtained from satisfactory pull-out and moment-rotation properties. In a separate study, Jung et al. (2010a,b) [49-50] used 67% compressed Japanese cedar dowels with a pull-out strength of up to 1.6 times greater than maple hardwood dowels on glued-in-rod joints.

Balsam fir (Abies balsamea) was densified at a temperature of 230 °C for 20 min and was cooled until the temperature was below 60 °C [51]. In this case, wood is at risk of being damaged due to the processing temperature of 230 °C is higher than those reported in the literature [53]. Table 1.6 shows the mechanical properties of uncompressed and compressed balsam fir with a compression ratio of 60%. The Young's modulus of the compressed wood in the radial direction, ER was 66% lower than that of uncompressed balsam fir (284 Mpa compared to 830 MPa). However, Young's modulus (ET) of the compressed balsam fir, was 2551 MPa, which was higher than that of uncompressed balsam fir (234 MPa). Minor fractures of the cell walls during densification may be the cause of the reduction of the ER of compressed wood. However, Young's modulus and the strength properties of compressed balsam fir with the compression ratio of 60% in the longitudinal direction were not be reported by Li et al. [51].

Table 1.6. Mechanical properties of uncompressed and compressed wood [51].

CR [%]	Young's modulus		Shear modulus
	E_R [MPa]	E_T [MPa]	G_{RT} [MPa]
0	830	234	38
60	284	2551	21

Table 1.7 presented the flexural and shear properties of uncompressed and compressed Sitka spruce (Picea sitchensis), which are determined by Yoshihara and Tsunematsu (2007) [52]. The wood was pre-soaked in water (20 °C) for two days, before compressing at a temperature of 180 °C for 10 min. To limit the moisture-dependent swelling of the compressed wood, steam was added at a temperature of 180 °C for about 1 h before cooling in

the next processing. When the wood was compressed by 67%, the density had a 75% increase from 458 kg/m^3 to about 800 kg/m^3. The flexural moduli were 14 GPa and 31 GPa for the uncompressed and 67% compressed wood, respectively. On the other hand, there was not a correlation between an increase in the compression ratio and the flexural strengths. The maximum flexural strength (120 MPa) was obtained from the samples with a 33% CR. Similarly, the compression ratio did not correlate with the shear properties, as shown in Table 1.7. The lower shear properties of the compressed wood may be caused by the soaking and steam treatments. Also, research by Navi and Heger (2004) [53] showed that the macroscopic cracks and a reduction in mechanical properties may be due to the processing of timber at a temperature of 180 °C or higher. Furthermore, Inoue et al. (1993a) [54] showed that post-treatment of wood with steam reducing the moisture-dependent swelling also led to a reduction in the mechanical properties of compressed wood.

Table 1.7. Mechanical properties of uncompressed and compressed wood [52].

CR [%]	Density [kg/m^3]	Flexural modulus [GPa]	Flexural strength [MPa]	Shear modulus		Shear strength	
				G_{LT} [MPa]	G_{LR} [MPa]	S_{LT} [MPa]	S_{LR} [MPa]
0	458	14	90	1	1.1	23	18
33	606	25	120	1.7	0.7	23	16
50	700	26	108	2.6	0.4	15	16
60	817	30	96	1.2	0.6	25	18
77	800	31	115	1.4	0.6	24	17

More recently, a processing method was carried out by Song et al. (2018) [55] to fabricate compressed wood through the combination of high-temperature compression and chemical treatment. Before being compressed at a temperature of 100 °C, lignin and hemicellulose in samples were partially remove by the use and mixture of sodium hydroxide and sodium sulfite. Table 1.8 gives the average mechanical properties. The density of the 80% compressed wood had an approximate 200% increase from 430 kg/m^3 to 1300 kg/m^3. Furthermore, the increase of compression strengths was about 450%, 5100%, and 3300% in the longitudinal, radial, and tangential directions, respectively. The compression ratio was relatively greater (i.e. 80%) and processing temperature was lower (i.e. 100 °C) when

compared to those commonly used in the literature (120–160 °C) [16]. These were perhaps attributed to the partial removal of lignin.

Table 1.8. Mechanical properties of uncompressed and compressed wood [55].

CR [%]	Density [kg/m^3]	Compressive strength		
		σ_L [MPa]	σ_R [MPa]	σ_T [MPa]
0	460	29.6	3.9	2.6
80	1300	163.6	203.8	87.6

The ultimate longitudinal tensile strengths for different species (oak, poplar, cedar, pine, and basswood) were also reproduced in Table 1.9.

Table 1.9. Longitudinal tensile strengths of uncompressed and compressed wood species by Song et al. (2018) [55].

Species	Longitudinal tensile strength [MPa]	
	Uncompressed	Compressed
Oak (Quercus)	115.3	584.3
Poplar (Populus)	55.6	431.5
Western red cedar (Thuja plicata)	46.5	550.1
Eastern white pine (Pinus strobus)	70.2	536.9
Basswood (Tilia)	52	587.0

These results show that the ultimate tensile strengths for both softwood and hardwood species were increased from 47–115 MPa to 432–587 MPa when the processing conditions proposed by Song et al. (2018) were applied. These notably improved mechanic properties are greater than other studies reported in the literature. These are attributed to the chemical treatment of the wood. However, it is not known that the chemical processing stages are costly, energy-intensive, or not. Therefore, we can focus on further research on the sustainability of the processing conditions. The environmental benefits of densified wood might also be decreased due to the addition of chemical solutions.

1.4 Thermal degradation of wood material

The thermal degradation of wood material is described by several authors in the literature [56-59]. It is carried out in two phases in addition to a preliminary drying phase (figure 1.12), namely:

1. Drying
2. Pyrolysis
3. The combustion of pyrolysis gases

These three stages correspond to different phenomena that do not appear in the same temperature ranges and therefore do not have the same effects on the degradation of the cellulosic material.

1.4.1 Drying phase

Wood is a type of hygroscopic material in nature. The increase in the ambient temperature causes the wood to dry out due to the process of water evaporation. The wood drying mechanism takes place in two stages: the loss of free water and then that of bound water. Free water, present in the interstices of the fibers, is lost first. When it has fully withdrawn and if the hygroscopic balance of the wood is still not achieved then the bound water begins to evaporate. The withdrawal of the bound water takes place until a water balance is reached or the wood is at an anhydrous state.

The drying of wood during thermal attack takes place over a fairly restricted temperature range of around 80 °C to 110 °C. When wood reaches these temperatures, internal water migrates towards the outside of the material by capillary action and evaporation mainly at the edges and cracks in the material. The mass of water is transferred preferentially from the wettest zone towards the driest zone and from the hottest zone towards the coldest zone of the wood [60].

During the drying process, there is a considerable change in the internal temperature of the wood. The drying process of wood corresponds to an endothermic reaction where heat is absorbed by the transformation of liquid water into vapor. When the locally anhydrous state is reached, the temperature in wood material gradually increases.

1.4.2 Pyrolysis phase

Pyrolysis is defined as the degradation of a component under thermal action. In the case of cellulosic material, this mechanism consists of the chemical decomposition of the material,

the release of pyrolysis gas followed by the formation of charcoal [27, 61-65].

When the free water and bound water are completely removed, the temperature on the surface of wood material increases rapidly. At temperatures around 180 °C, the pyrolysis mechanism starts and causes a change in wood components. The temperature level for the beginning of the pyrolysis process of wood is different according to the authors [23, 25, 66].

In order to better describe the pyrolysis of wood, various authors have sought to determine the pyrolysis temperatures of wood constituents. The literature shows that it is possible to consider the thermal degradation of each of these constituents over different temperature ranges [57, 67-69].

- From 225 °C to 325 °C: slightly exothermic reactions begin. The degradation of hemicellulosic begins.

- From 325 °C to 375 °C, other exothermic reactions appear and are due to the degradation of cellulose. P. Rousset [57] proposes a degradation of cellulose from 250 °C with a rupture polymerization chain from 150 °C. These reactions of 150 °C to 300 °C are then endothermic.

- From 250 °C to 500 °C: the transformation becomes strongly exothermic and the wood evolves towards charcoal with the release of CO2 and pyroligneous (raw condensate mainly composed of acid water). Lignin degradation takes place. According to [57], this degradation of lignin does not begin until 400 °C.

During the pyrolysis of wood, gases are formed. For temperatures below 200 °C, these gases are composed of approximately 70% of non-combustible carbon dioxide (CO2) and combustible and toxic monoxide carbon (CO). The remaining 30% of gas is composed of hydrogen (H2), methane (CH4), ethylene (C2H4), acetylene (C2H2), and dinitrogen (N2) [70]. From 200 °C, the combustible gas is released more and more and the proportion of CO2 decreases. After the ignition of gases, the temperature on the surface increases rapidly. Wood transforms into charcoal at temperatures around 300 °C. Between 250 °C and 350 °C, the wood loses approximately 60% of its initial mass. The mass of formed charcoal is on average 20% to 25% of the initial mass of wood. During this phase, a large amount of the gases emitted by the degradation of the wood is flammable.

The thermal conductivity of charcoal is about six times lower than that of solid wood.

The charcoal, therefore, acts as an insulator, which creates a protective layer and slows down the heat transfer.

1.4.3 Combustion phase

The reaction of wood combustion consists of the ignition of the gases emitted during the pyrolysis step. This step requires pressure, oxygen, and temperature conditions that are favorable for its performance. The temperature at the surface of the wood increases sharply from this stage.

During the pyrolysis step, it is suitable to estimate that about 20% of the gases emitted by the degradation of wood are flammable gases.

Above 500 °C, the quantity of gas produced is very small, and that of charcoal increases. However, within the wood, there is always a very active pyrolysis phase (temperature from 250 °C to 300 °C) which produces gases. To escape, these gases pass through the charcoal layer and prevent it from being in contact with the oxygen in the air. Then gaps have appeared in the charcoal. In these gaps, the gases from the pyrolysis are evacuated while the other surfaces of charcoal can be in contact with oxygen and burn slowly. Above 1000 ° C, the gases emitted are mainly carbon monoxide (CO) and hydrogen (H2) and are therefore highly flammable.

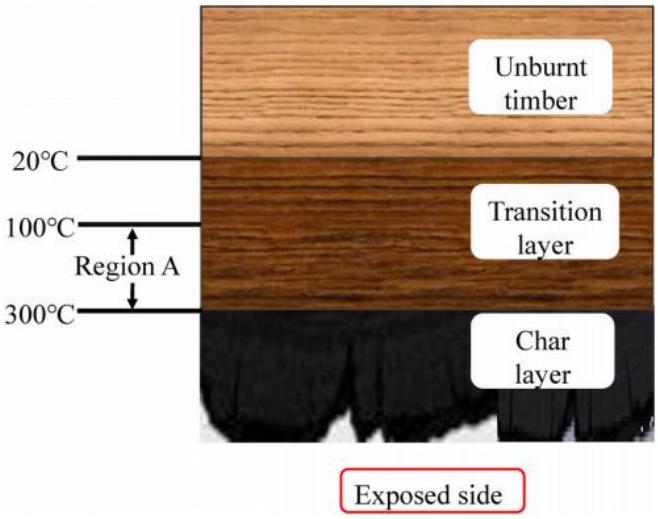

FIGURE 1. 17 - Pyrolysis process in wood.

Thus, during a fire, all the phases take place at the same time but in different areas of the wood. Figure 1.18 shows the section of wood exposed to one-side fire. This section is made up of three layers:

- The char layer corresponds to the part of the wood exposed to fire.

- The transition layer is the part where the wood is dried (20 °C to 100 °C) and chemically altered without being completely decomposed (region A with temperature from 100 °C to 300 °C).

- The unburnt timber.

In recent years, the thermal analysis of wood including three phases of drying, pyrolysis, and combustion have been studied [28-30, 71-73]. These studies are based on a realistic representation of the experimental test.

A wet wood slab, subjected to a radiant heat flux on one side is carried out. As the surface is heated (the other side is assumed to be adiabatic), the wood is first dried and then pyrolyzed by radiant and conductive heat transfer. Pyrolysis of wood to water vapor, gas, and char form a one-step, multi-global reaction scheme for pyrolysis of wet wood. A small portion of the pyrolysis gases and water vapor move inward, while the greater portion passes through the char layer and leaves from the upper surface of the solid [28]. Di Blasi [29] assumed that wood is decomposed into three major products: tar, char, and gas, by three primary reactions. And then, a portion of tar decomposes to gas and char by successive secondary reactions [29].

Park [30] proposed a new wood pyrolysis mechanism based on the experimental and theoretical results. This mechanism accounts for the observed endo/exothermic thermal behavior and the solid mass loss measured in the experiments. There is competition between gas, tar, and intermediate solid yield during wood pyrolysis which depends on the heating conditions at the first decomposition of wood. After that, both char and gas are produced from the tar and intermediate solid is converted only to char at the secondary reactions [30]. A two-stage semi-global kinetic mechanism consisting of four sequential steps was proposed by Grioui [71]. The wood is classified into three pseudo-components. For the first two, similar thermal degradation mechanisms take place in a single reaction step by giving gas products and a non-degradable solid residue “charcoal”. For the third, the thermal degradation takes place in two consecutive steps. The first stage leads to an intermediate product comparable to a solid (large hydrocarbon molecule) and gases. In the second stage, the intermediate product is transformed into a non-degradable solid “charcoal” and gas products.

A four-step series mechanism of the devolatilization/combustion process is proposed by Branca [72]. The first two reactions can be associated mainly with hemicellulose and

cellulose degradation, respectively. The third reaction is representative of the final part of the devolatilization process (lignin decomposition) and the beginning of char combustion. The fourth reaction describes char combustion. Brostrom [73] proposed a five-reaction mechanism, consisting of three devolatilization reactions for the pseudo-components hemicellulose, cellulose, and lignin and, in air, of two additional reactions for char devolatilization and combustion.

1.5 Conclusion

In this chapter, the state of the art for both wood and densified wood are introduced. Firstly, we have presented the general information on wood and densified wood. In the second part, the mechanical properties of wood and densified wood (Modules of elasticity in the different directions and resistance) were discussed. The main thermo-physical properties of the wood material (thermal conductivity, specific heat, and density) are also presented as well as the variation of these properties as a function of temperature according to the regulatory approach EC5 [32]. Lastly, we also sought to identify the various phenomena of thermal degradation of cellulosic materials which must be taken into account during the numerical simulation to transcribe the thermomechanical behavior of cellulosic materials.

The literature presents a large amount of data on the behavior of wood at high temperatures. However, densified wood materials are the subject of very little study. Little information is available on their thermal and mechanical behavior at high temperatures.

.

Bibliography of chapter 1

[1] Vuorine T., Structure and chemistry of wood, lecture 6: wood extractives (2009).

[2] Winandy J.E., Rowell R.M., The Chemistry of Wood Strength, The Chemistry of solid Wood (1983) 211-255.

[3] Harrington J.J., MicroFibril Angle in Wood (1998).

[4] Hughes M., Introduction wood properties and wood product: Wood - Water relationship (2009).

[5] Howord E.T., Manwiller F.G., Anatomical characteristics of southern pine steamwood, Wood Science 2 (1969) 77-86.

[6] Barbe C., Keller R., Les rayons ligneux et le matériau bois, Revue Forestière Française 1 (1996) 63-68.

[7] Riggio M., Sandak J., Sandak A., Densified wooden nails for new timber assemblies and restoration works: a pilot research, Construction and Building Materials 102 (2016) 1084-1092.

[8] Asako Y., Kamikoga H., Nishimura H., Yamaguchi Y., Effective thermal conductivity of compressed woods, International Journal of Heat and Mass Transfer 45 (2002) 2243-2253.

[9] Sotayo A., Bradley D., Bather M., Oudjene M., Review of state of the art of dowel laminated timber members and densified wood materials as sustainable engineered wood products for construction and building applications, Developments in the Built Environment 1(2020).

[10] Kutnar A., Sernek M., Densification of wood, Zbornik gozdarstva in lesarstva (82) 53-62.

[11] Permali D., Densified wood laminate, Accessed: 14th January 2019, Available at: http://www.permalideho.co.uk/hydulignum.asp.

[12] Anshari B., Guan Z., Kitamori A., Jung K., Komatsu K., Structural behaviour of glued laminated timber beams pre-stressed by compressed wood, Construction and Building Materials 29 (2012) 24-32.

[13] Anshari B., Guan Z., Wang Q., Modelling of Glulam beams pre-stressed by compressed wood, Composite Structures165 (2017) 160-170.

[14] Glass S.V., Zelinka S.L., Moisture relations and physical properties of wood, Wood Handbook - Wood as an Engineering Material, U.S. Department of Agriculture Forest Service, Forest Products Laboratory, Madison, WI (2010).

[15] Sandberg D., Kutnar A., Mantanis G., Wood modification technologies - a review, iForest - Biogeosciences and Forestry 10 (2017) 895.

[16] Kutnar A., Sandberg D., Haller P., Compressed and moulded wood from processing to products, Holzforschung 69 (2015) 885-897.

[17] Rautkari L., Properzi M., Pichelin F., Hughes M., An innovative thermo densification method for wooden surfaces, Proceedings of the 10th World Conference on Timber Engineering (2008) 177-184.

[18] Kollmann F.F.P., Technologie des Holzes, Springer-Verlag, Berlin (1936).

[19] Kollmann F., Kuenzi E., Stamm A., Principles of Wood Science and Technology, Springer-Verlag Berlin Heidelberg, Wood Based Materials 12 (1975) 703.

[20] Sandberg D., Haller P., Navi P., Thermo-Hydro and Thermo-Hydro-Mechanical Wood, Processing: an Opportunity for Future Environmentally Friendly Wood Products, Taylor&Francis Group (2013).

[21] Salmen L., On the Interaction between Moisture and Wood Fibre Materials, MRS Online Proceedings Library Archive (1990) 197.

[22] Santos C.M.T., Del Menezzi C.H., De Souza M.R., Properties of thermo-mechanically treated wood from Pinus caribaea var. hondurensis, BioResources 7 (2012) 1850-1865.

[23] Islam M.A., Razzak M.A., Ghosh B., Optimization of thermally-compressed wood of Trewia nudiflora species using statistical Box–Behnken design and desirability function, Journal of the Indian Academy of Wood Science 11 (2014) 5-14.

[24] Thi V.D., Modélisation du comportement au feu des structures en bois, PhD Thesis, University of Lorraine, France (2017).

[25] Knigge W., Schulz H., Grundriss der Forstbenutzung, Verlag Paul Parey, Berlin (1966).

[26] Khelifa M., Khennane A., El Ganaoui M., Rogaume Y., Analysis of the behaviour of multiple dowel timber connections in fire, Fire Safety Journal 68 (2014) 119-128.

[27] Thi V.D., Khelifa M., El Ganaoui M., Rogaume Y., Finite element modeling of the pyrolysis of wet wood subjected to fire, Fire Safety Journal 81 (2016) 85-96.

[28] Shen D.K., Fang M.X., Luo Z.Y., Cen K.F., Modeling pyrolysis of wet wood under external heat Flux, Fire Safety Journal 42 (2007) 210-217.

[29] Di Blasi C., Analysis of convection and secondary reaction effects within porous solid fuels under-going pyrolysis, Combustion Science and Technology 90 (1993) 315-340.

[30] Park W.C., Atreya A., Howard R., Experimental and theoretical investigation of heat and mass transfer processes during wood pyrolysis, Combustion and Flame 157 (2010) 481-494.

[31] Kosik M., Dandarova M., Domansky R., Pyrolyse des Buchenholzes bei niedrigen Temperaturen IX: Chemische Veränderungen im Buchenholz während der Pyrolyse, Holzforschung Holzver wendung 21 (1969) 40-43.

[32] Eurocode 5 - Design of timber structures, Part 1-2: General - Structural fire design, CEN 2004 (European Committee for Standardization), EN 1995-1-2, Brussels, Belgium.

[33] Forest Product Laboratory, Wood Handbook: wood as an engineering material, Centennial Edition (2010).

[34] Menis A., Fire resistance of Laminated Veneer Lumber (LVL) and Cross-Laminated Timber (XLAM) elements, PhD Thesis, Università degli studi di Cagliari, Italy (2012).

[35] Schnabl S., I. Planinc I., G. Turk G., Srpcic S., Fire analysis of timber composite beams with interlayer slip, Fire Safety Journal 44 (2009) 770-778.

[36] Yu Z.T., Xu X., Fan L.W., Hu Y.C., Cen K.F., Experimental measurements of thermal conductivity of wood species in China: Effects of density, temperature, and moisture, Forest Products Journal 61(2011) 130-135.

[37] Oliver V., Karin D.B., Christian H., Alfred T., Ulrich M., Thermal conductivity of wood at angles to the principal anatomical directions, Wood Science and Technology 49 (2015) 577-589.

[38] Guitard D., Mécanique du matériau bois et composites, Nabla, Cepadues éd (1987).

[39] Oudjene M., Khelifa M., Finite element modelling of wooden structures at large deformations and brittle failure prediction, Materials & Design 30 (2009) 4081-4087.

[40] Oudjene M., Khelifa M., Elasto-plastic constitutive law for wood behaviour under compressive Loadings, Construction and Building Materials 23(2009) 3359-3366.

[41] Reiterer A., Stanzl-Tschegg S.E., Compressive behaviour of softwood under uniaxial loading at different orientations to the grain, Mechanics of Materials 33(2001) 705-715.

[42] Navi P. et Heger F., Comportement thermo-hydromécanique du bois: Applications technologiques et dans les structures, P U Polytec ROM, PPUR (2005).

[43] NF-EN-312, Panneaux de particules: exigences (2004).

[44] NF-EN-310, Panneaux à base de bois: détermination du module d'élasticité en flexion et de la résistance à la flexion (1993).

[45] NF-EN-319, Panneaux de particules et panneaux de fibres: détermination de la résistance à la traction perpendiculaire aux faces du panneau (1993).

[46] Anshari B., Guan Z., Kitamori A., Jung K., Hassel I., Komatsu K., Mechanical and moisture-dependent swelling properties of compressed Japanese cedar, Construction and Building Materials 25 (2011) 1718-1725.

[47] Jung K., Kitamori A., Komatsu K., Evaluation on structural performance of compressed wood as shear dowel, Holzforschung 62 (2008) 461-467.

[48] Jung K., Kitamori A., Komatsu K., Development of a joint system using a compressed wooden fastener I: evaluation of pull-out and rotation performance for a column-sill joint, Journal of Wood Science 55 (2009) 273-282.

[49] Jung K., Kitamori A., Komatsu K., Development of a joint system using a compressed wooden fastener II: evaluation of rotation performance for a column-beam joint, Journal of Wood Science 56 (2010a.) 118-126.

[50] Jung K., Murakami S., Kitamori A., Chang W.S., Komatsu K., Improvement of glued-in-rod joint system using compressed wooden dowel, Holzforschung 64 (2010b) 799-804.

[51] Li L., Gong M., Chui Y., Schneider M., Li D., Measurement of the elastic parameters of densified balsamfir wood in the radial-tangential plane using a digital image correlation (DIC) method, Journal of Materials Science 48 (2013) 7728-7735.

[52] Yoshihara H., Tsunematsu S., Bending and shear properties of compressed Sitka spruce, Wood Science and Technology 41 (2007) 117-131.

[53] Navi P., Heger F., Combined densification and thermo-hydro-mechanical processing of wood, MRS Bull 29 (2004) 332-336.

[54] Inoue M., Norimoto M., Tanahashi M., Rowell R.M., Steam or heat fixation of compressed wood, Wood and Fiber Science 25 (1993a) 224-235.

[55] Song J., Chen C., Zhu S., Zhu M., Dai J., Ray U., Li Y., Kuang Y., Li Y., Quispe N., Processing bulk natural wood into a high-performance structural material, Nature 554 (2018) 224.

[56] Drean V., Projet VIRGILE: proposition d'un modèle de combustion des matériaux composites pour simulation sur FDS-5, Rapport Interne EFECTIS France E-R&D-11/010 (2011).

[57] Rousset P., Choix et validation expérimentale d'un modèle de pyrolyse pour le bois traité par haute température: de la micro-particule au bois massif, Thèse doctorat, Université Henri-Poincaré Nancy 1, Nancy (2004).

[58] Schaffer E.L., Elevated temperature effect on the longitudinal mechanical properties of wood, Thèse doctorat, University of Wisconsin (1971).

[59] Audebert M., Approche expérimentale et modélisation du comportement au feu d'assem-blages bois sous différents types de sollicitations, Thèse doctorat, Université Blaise Pascal - Clermont II (2010).

[60] Derome D., About heat and mass transfer in wood (2014).

[61] Kansa E.J., Perlee H.E., Chaiken R.F., Mathematical model of wood pyrolysis including internalforced convection, Combustion and Flame 29 (1997) 311-324.

[62] Bellais M., Davidssonb K.O., Liliedahla T., Sjostroma K., Pettersson J.B.C., Pyrolysis of large wood particles: a study of shrinkage importance in simulation, Fuel 82 (2003) 1541-1548.

[63] Bryden K.M., Hagge M.J., Modeling the combined impact of moisture and char shrinkage on the pyrolysis of a biomass particle, Fuel 82 (2003) 1633-1644.

[64] Thurner F., Mann U., Kinetic investigation of wood pyrolysis, Industrial & Engineering Chemistry Process Design and Development 20 (1981) 482-488.

[65] Chan W.R., Kelbon M., Krieger B.B., Modeling and experimental verification of physical and chemical processes during pyrolysis of a large biomass particle, Fuel 64 (1985) 1505-1513.

[66] Bilbao R., Mastral J.F., Ceamanous J., Aldea M.E., Modeling of the pyrolysis of wet wood, Journal of Analytical and Applied Pyrolysis 36 (1996) 81-97.

[67] Brandt B., Zollfrank C., Franke O., Fromm J., Goken M., Durst K., Micromechanics and ultrastructure of pyrolysed softwood cell walls, Elsevier (2010).

[68] Coppalle A., Feux de compartiment (2010).

[69] Di Blasi C., Modeling chemical and physical processes of wood and biomass pyrolysis, Journal of Energy and Combustion Science 34 (2008) 47-90.

[70] Couhert C., Pyrolyse flash à haute température de la biomasse ligno-cellulosique et de ses composés-production de gaz de synthèse, Thèse doctorat, École des Mines de Paris (2007).

[71] Grioui N., Halouani K., Zoulalian A., HalouaniF., Thermogravimetric analysis and kinetics modeling of isothermal carbonization of olive wood in inert atmosphere, Thermochimica Acta 440 (2006) 23-30.

[72] Branca C., Di Blasi C., Global interinsic kinetics of wood oxidation, Fuel 83 (2004) 81–87.

[73] Broström M., Nordina A., Pommer L., Branca C., Di Blasi C., Influence of torrefaction on the devolatilization and oxidation kinetics of wood, Journal of Analytical and Applied Pyrolysis 96 (2012) 100-109.

Chapter 2

Thermo-mechanical modeling of timber material at high temperature

Summary

2.1 Introduction 42
2.2 Theoretical aspects 44
2.2.1 Thermal behavior of timber material at high temperature 44
2.2.2 Mechanical behavior of timber material 56
2.2.3 Thermo-mechanical coupling of wood material 61
2.3 Numerical aspects 63
2.3.1 Thermal analysis 63
2.3.2 Mechanical analysis 68
2.3.3 Thermo-mechanical coupling 71
2.4 Conclusion 74
Bibliography of chapter 2 75

2.1 Introduction

In most cases, the ruin of a structure exposed to fire is often linked to the number of combustible materials used in the building [1-5]. Therefore, the combustibility of wood poses a serious problem for the fire safety of timber structures, thus hampering its wider introduction as a construction material compared to conventional materials such as concrete and steel [4-5]. However, timber is sustainable, has a low carbon footprint, and has potential recycling benefits at the end of its life cycle. It is not surprising, therefore, that there is an increased interest in the fire resistance of timber structures. It is therefore important to reassess the fire behavior of wood as a material using the most advanced numerical approaches.

Up to now, the construction sector is governed by several rules and standards [1-3]. The standards are largely based on experimental observations. In these cases, the empirical evidence often results in simple calculations. As such, it can be argued that current fire safety regulations are conservative, less precise, and underdeveloped. The regulatory standards, reported in EC5 [6] and in use in most European countries, are designed so that a structure remains stable during a given time of exposure to fire. These normative recommendations make it possible, on one hand, to facilitate the intervention of the fire brigade in order to minimize losses to human life and property damage that can be caused by the rapid spread of a fire, and, on the other hand, to evacuate the building safely. Although wood is a combustible material, timber structures are remarkably fire resistant as shown in numerous studies [6-10]. The charred layer that forms on the surface exposed to fire acts as an insulator that helps stop the spread of fire to the interior of the element, where the wood remains undamaged. Furthermore, for wood combustion to develop, it needs to be supplied with oxygen, which explains why it only develops on the exposed surfaces.

According to EC5 [6], the fire resistance of a timber section is estimated by increasing the thickness of the charred layer. However, in the absence of experimental data on different wood species, this becomes a very simplifying approach as it does not account for the complexities of the pyrolysis and combustion phenomena and does not reflect the actual fire behavior of timber. Furthermore, most of the test data used were performed in accordance with ISO 834-1 [11], which does not necessarily reproduce the conditions of a natural fire. In addition, the EC5 [6] approach does not take into account the kinetics of thermal degradation

of the wood during the pyrolysis phase. For the verification of the fire resistance of a timber structure, the EC5 [6] approach is limited to the use of the evolution curves of the physical-thermal properties (conductivity, density, and specific heat) as functions of temperature obtained on softwood under specific experimental conditions.

Several authors [7-9] have proposed other forms of expressing the physical-thermal properties as functions of temperature. The application of these models to the analysis of real fire scenarios showed that the overall behavior is not sufficiently well correlated due to the variability of the different values of the thermal properties [6-9]. These constants are derived from measurements from experimental tests carried out on different wood species and under completely different experimental conditions. These models are simple and conservative in nature. They have the advantage of being easy to integrate into a computer code, but they remain less reliable compared to kinetic models describing the pyrolysis step.

This chapter presents a contribution to the understanding and modeling of the kinetics of the thermal decomposition of timber in the event of a fire. The numerous physical-chemical reactions developing during the drying, pyrolysis, and combustion phases are described by several kinetic parameters, which are difficult to identify. The proposed work also relates to the modeling of the mechanical behavior of timber under high temperatures. The development of kinetic models of biomass pyrolysis are numerous in the literature, but they are not applied to the study of the behavior of timber structures under fire.

2.2 Theoretical aspects

2.2.1 Thermal behavior of timber material at high temperature

In this section, we present two different types of heat transfer models. The first type of model (simplified thermal models) is based on the regulatory approach used in Eurocode 5 [6] which consists of solving the heat equation by simplifying the drying, pyrolysis, and combustion phenomena through the adaptation of the thermo-physical properties (ρ, λ, Cp). The second type of model (pyrolysis thermal models) takes into account the drying and pyrolysis phenomena to solve the heat transfer equation. This second type of model better describes the real phenomena and therefore must be more predictive [3,12-14].

2.2.1.1 Simplified model in Eurocode 5

The regulatory approach used in EC5 [6] is described by the standard heat transfer equation:

$$\rho . C_p . \frac{\partial T}{\partial t} = \frac{\partial}{\partial x}\left[\lambda_x . \frac{\partial T}{\partial x}\right] + \frac{\partial}{\partial y}\left[\lambda_y . \frac{\partial T}{\partial y}\right] + \frac{\partial}{\partial z}\left[\lambda_z . \frac{\partial T}{\partial z}\right] + Q_r^{"} \quad (2.1)$$

where T [K] is the temperature; λ_x, λ_y, and λ_z [W/(m.K)] are the thermal conductivities in the x, y and z directions; ρ [kg/m^3] is the density; C_p [J/(kg.K)] is the specific heat; t [s] represents time; $Q_r^{"}$ [W/m^3] is the heat source due to the complex reactions produced during the thermal degradation of wood.

To solve the diffusion equation of the heat, the term $Q_r^{"}$ [W/m^3] of equation (2.1) is not taken into account explicitly in the calculations. In other words, this term linked to the thermal degradation of the wood material is deleted in the heat equation and it is implicitly integrated by an adaptation of the thermo-physical properties (λ,C_p and ρ) [6]. The evolution of parameters (ρ, λ, C_p) as a function of temperature is described in detail in section 1.2 (chapter 1).

2.2.1.2 Pyrolysis model

The simulation of the thermal behavior of a cellulosic material requires taking into account thermal degradation induced by complex reactions such as vaporization of water (bound and free water), pyrolysis of wood, combustion of pyrolysis gases, and slow combustion of coal. The reactions linked to the thermal degradation of wood produce heat sources that modify the heat transfer. The heat sources depend on the progress of the mass

loss.

Kinetic parameters k_i [1/s] are modeled by Arrhenius' laws:

$$k_i = A_i . \exp\left(\frac{-E_i}{RT}\right) \tag{2.2}$$

where A_i [1/s] and E_i [J/mol] are pre-exponential factor and reaction active energy, respectively. R = 8.314 J/(mol.K) is the constant of gases and T [K] is the temperature. In kinetic thermal models, the following assumptions are adopted:

- Transfers of heat, the mass of gases, and vapors inside the wood are ignored.

- The pyrolysis gas and the water vapor evaporated from the surface of the solid as soon as they are formed. The mass-loss rate of the solid is therefore considered to be a mass flow of materials volatile.

- The change in volume of the solid is not taken into account during the time of exposure to fire.

1. Pyrolysis model of D.K. Shen (2006)

A 1D pyrolysis model for some wet wood species (Spruce, Douglas, Maritime pine, Oak, Beech, Chestnut, and Poplar) that takes into account the individual degradation in three parts: coal, gas, and steam is proposed by Shen et al in [12]. The pyrolysis mechanism of this model is shown schematically in Figure 2.1: thermal degradation of moist wood is produced by three parallel reactions. Wet wood turns to vapor in the drying process and char and gas in the pyrolysis process.

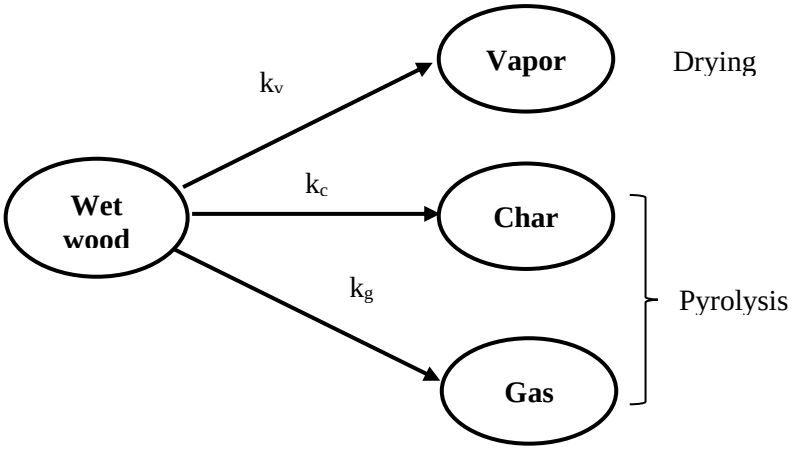

FIGURE 2. 1 - Pyrolysis model for wet wood [12].

In this work, a 2D and 3D model was formulated and developed to generalize the 1D model proposed by Shen et al [12]. To analyze the heat transfer in the thickness of a wooden structure exposed to a fire, conduction is the main mode of heat transfer. In a fire test, the exchange of heat between the outer surfaces of the sample and the environment is by convection and radiation, while the heat transfer that occurs inside the sample is carried out by conduction.

The evolution of the temperature gradient in a wooden sample can be described by the differential equation [12]:

$$\frac{\partial(\rho_w C_w + \rho_c C_c + \rho_l C_l).T}{\partial t} = \frac{\partial}{\partial x}\left[\lambda_{sx}.\frac{\partial T}{\partial x}\right] + \frac{\partial}{\partial y}\left[\lambda_{sy}.\frac{\partial T}{\partial y}\right] + \frac{\partial}{\partial z}\left[\lambda_{sz}.\frac{\partial T}{\partial z}\right] + Q_r^{"} \tag{2.3}$$

The mass conservation equations are [12]:

$$\frac{d\rho_w}{dt} = -(k_c + k_g).\rho_w \tag{2.4}$$

$$\frac{d\rho_c}{dt} = k_c.\rho_w \tag{2.5}$$

$$\frac{d\rho_g}{dt} = k_g.\rho_w \tag{2.6}$$

$$\frac{d\rho_l}{dt} = -k_v.\rho_l \tag{2.7}$$

$$\frac{d\rho_v}{dt} = k_v.\rho_l \tag{2.8}$$

where T [K] is the temperature; t [s] denotes time; ρ_i [kg/m^3] and C_i [J/(kg.K)] are respectively the density and specific heat of component i; λ_{sx}, λ_{sy}, and λ_{sz} [W/(m.K)] are the thermal conductivities of the solid s in the x, y and z directions; $Q_r^{"}$ [W/m^3] is the source of heat due to the complex reactions produced during the thermal degradation of wood. The equivalent thermal conductivity of the solid s in the direction j is calculated by the following relations [12]:

$$\lambda_{sj} = \eta.\lambda_{cj} + (1-\eta).\lambda_{wj} \tag{2.9}$$

$$\eta = \frac{\rho_c}{\rho_c + \rho_w} \tag{2.10}$$

$$\lambda_c = 0{,}105;\ \lambda_w = 0{,}166 + 0{,}369.w \tag{2.11}$$

with w is the humidity.

$Q_r^{"}$ [W/m^3] represents the sum of the heat sources induced by three reactions of pyrolysis at a temperature T [12]:

$$\begin{aligned} Q_r^{"} &= k_c.\rho_w.[\Delta h_c^0 + (C_c - C_w).(T - T_0)] \\ &+ k_g.\rho_w.\left[\Delta h_g^0 + \left(C_g - C_w\right).(T - T_0)\right] \\ &+ k_v.\rho_l.[\Delta h_v^0 + (C_v - C_l).(T - T_0)] \end{aligned} \tag{2.12}$$

Δh_i^0 [J/kg] are the standard reaction energies and they are given in Table 2.1.

Table 2.1. Parameters of the pyrolysis model of D. K. Shen.

	Pyrolysis reactions		drying
	$k_c : wood \rightarrow char$	$k_g : wood \rightarrow gas$	$k_g : liquid \rightarrow vapor$
Ai [1/s]	7,38 .10^5	1,44 .10^4	5,13 .10^{10}
Ei [J/mol]	106.5	88.6	88
Δh_i^0 [J/kg]	-420	-420	-2440
Thermo-physical properties of wood material [12]			
λ [W/(m.K)]	Cp [J/(kg.K)]	ρ_i [kg/m^3]	T_0 [K]
Eq.(1.19-1.21)	C_w =1950	Eq.(2.4-2.8)	298
	C_c = 1390		
	C_g = 2400		
	C_l = 4180		
	C_v = 1580		

2. Pyrolysis model of G. Cueff (2018)

This model is applied for wood-based products and it takes place according to the mechanism shown in Figure 2.2.

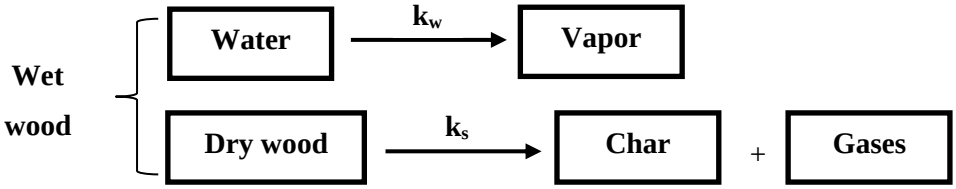

FIGURE 2. 2 - Thermal degradation reaction model for the vaporization of water content (kw) and the pyrolysis of wood (ks) [3].

The heat transfer equation [3]:

$$\frac{\partial[\rho_{tot}.Cp_{tot}.T]}{\partial t} = \frac{\partial}{\partial x}\left[\lambda_x.\frac{\partial T}{\partial x}\right] + \frac{\partial}{\partial y}\left[\lambda_y.\frac{\partial T}{\partial y}\right] + \frac{\partial}{\partial z}\left[\lambda_z.\frac{\partial T}{\partial z}\right] + Q_W + Q_S \qquad (2.13)$$

where T [K] is the temperature; λ_x, λ_y, and λ_z [W/(m.K)] are the thermal conductivities in the x, y and z directions; ρ_{tot} [kg/m^3] and Cp_{tot} [J/(kg.K)] are the density and specific heat of solid.

$$\lambda_{tot} = (1 - X_s).\lambda_s + \frac{\rho_s}{\rho_{char}}.\gamma.X_s.\lambda_{char} + \frac{\rho_s}{\rho_w}.\beta.(1 - X_w).\lambda_w \qquad (2.14)$$

$$\rho_{tot} = \rho_s.[1 + X_s.(\gamma - 1) + \beta.(1 - X_w)] \qquad (2.15)$$

$$Cp_{tot} = \frac{(1 - X_s).Cp_s + \gamma.X_s.Cp_{char} + \beta.(1 - X_w).Cp_w}{[1 + X_s.(\gamma - 1) + \beta.(1 - X_w)]} \qquad (2.16)$$

The influence of temperature on the variation of thermal properties is non-negligible for thermal simulations. From the theory presented in [15], a mixture law controlled by the thermal reactions in the linen was developed to take into account the impact of temperature on the thermal properties of linen material. According to Eqs. (2.14-2.15), thermal conductivity and density of solid are calculated based on the mass fraction of the dry solid (linen, wood, and resin), water, and char. Similarly, specific heat capacity also depends on the volume fraction of these three components, according to Eq. (2.16). The degrees of reaction X_w and X_s that respectively correspond to the vaporization of water and the pyrolysis of cellulosic material, are taken into account in Eqs. (2.13-2.16). For each process, the degree of

reaction X_w and X_s is linked to the kinetics of reactions $\frac{dX_w}{dt}$ and $\frac{dX_s}{dt}$ respectively, described in Eq. (2.17-2.18).

$$\frac{dX_w}{dt} = k_w.(1 - X_w) \tag{2.17}$$

$$\frac{dX_s}{dt} = k_s.(1 - X_s) \tag{2.18}$$

where k_w and k_s are the rate constants, which are calculated according to the first-order Arrhenius law (Eq. 2.2), representative of the thermal reactions schematized in Figure 2.2.

The char formation is depicted by the rate of production γ (expressed as a mass fraction of the dry product). The initial moisture content of the material is represented by the coefficient β.

The thermal conductivity of wood depends at room temperature on the moisture content. Substituting $X_w = 0$ and $X_s = 0$, equation (2.14) becomes:

$$\lambda_t = \lambda_s + \frac{\rho_s}{\rho_w}.\beta.\lambda_w \tag{2.19}$$

where λ_t, λ_s, and λ_w [W/(m.K)] are the thermal conductivities of wet wood, dry wood, and water at room temperature, respectively.

Table 2.2. Parameters of the pyrolysis model of G. Cueff.

	ρ [kg/m^3]	C_p [J/(kg.K)]	λ [W/(m.K)]
Wood (+linen + resin)	373	1636	0.123
Char	78	1150	0.11
Water	1000	4286	0.658
Kinetic parameters of wood material [3]			
	Water vaporisation		Pyrolysis
Ei [J/mol]	160		330
Ai [1/s]	1,00.10^{19}		5,1.10^{31}
Hr (J/kg)	-3,0.10^6		2,0.10^6

In this model, the heat source due to the reactions of thermal degradation breaks down into two terms: the first term Q_w represents the vaporization, and the second term Q_s designates pyrolysis, according to Eq. (2.20-2.21).

$$Q_w = \frac{dX_w}{dt}.\rho_w.Hr_w \tag{2.20}$$

$$Q_s = \frac{dX_s}{dt}.\rho_s.Hr_s \tag{2.21}$$

where $\rho_{s,w}$ is the compound density. Hr_w and Hr_s are the heat of reactions associated with vaporization and pyrolysis respectively. These three parameters have not been directly measured. The compound density used in the simulations is common values (see Table 2.2). Heats of reactions have been initially estimated from a literature review. In this review, a lot of dispersion has been noticed. So the heat of reaction associated with water vaporization and wood pyrolysis have been used as ‘‘fitting parameters” for the simulations. Especially the energy associated with water vaporization has been adjusted depending on the type of test (test on small scale panels or test on the furnace) [13].

3. Pyrolysis model of N. Grioui (2006)

The kinetic model presented by Grioui and al. (2006) to describe the thermal degradation of olive wood particles is adopted. This model as mentioned previously is divided into three pseudo-fractions A_1, A_2, and A_3. A kinetic mechanism is illustrated in Figure 2.3 which includes decomposition, described by three parallel reactions (k_1, k_2, and k_3) for the pseudo-components A_1, A_2, and A_3, and the kinetic decomposition of intermediate solid B is performed by reaction k_4.

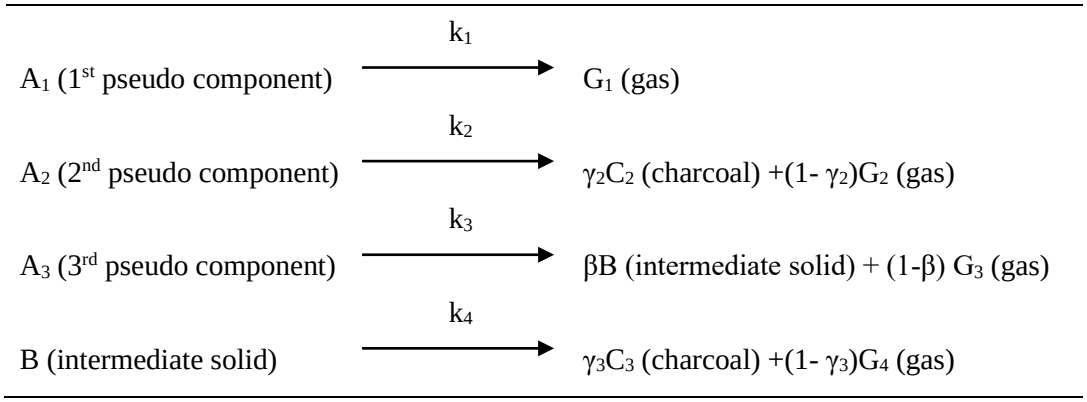

FIGURE 2. 3 - The proposed model of N. Grioui (2006) [13].

The products of the two first single stage reactions (k_1 and k_2) are gas products (G_1) and (G_2), respectively, and a non-degradable solid residue "charcoal" (C_2). The third pseudo-component A_3 degrades in two consecutive reaction stages. In the first stage, the pseudo-component A_3 is transformed into an intermediate product (B) comparable to a solid (large hydrocarbon molecule) and gas products (G_3). The second stage leads to a non-degradable solid "charcoal" (C_3) and gases (G_4) from the thermal degradation of the intermediate product (B). However, the degradation rate of the constituent B is relatively lower than the ones of the pseudo-components A_1, A_2, and A_3. The mass fractions (β) of the intermediate product (B) and the coefficients of the non-degradable solid "charcoal" ($\gamma_2$and γ_3) are as a function of temperature.

The chemical reactions for pyrolysis of wood are described by the first-order Arrhenius law (Eq. 2.2). The equations of mass conservation for each component in solid are expressed as follows:

$$\frac{dm_{A1}}{dt} = -k_1.m_{A1} \tag{2.22}$$

$$\frac{dm_{A2}}{dt} = -k_2.m_{A2} \tag{2.23}$$

$$\frac{dm_{A3}}{dt} = -k_3.m_{A3} \tag{2.24}$$

$$\frac{dm_{C2}}{dt} = \gamma_2.k_2.m_{A2} \tag{2.25}$$

$$\frac{dm_B}{dt} = \beta.k_3.m_{A3} - k_3.m_B \tag{2.26}$$

$$\frac{dm_{C3}}{dt} = \gamma_3.k_4.m_B \tag{2.27}$$

The kinetic parameters in thermal degradation of olive wood with a four-step mechanism are depicted in Table 2.3. This work is conducted by N. Grioui et al [13].

Table 2.3. Kinetic parameters for a model of N. Grioui (2006).

Reaction	1	2	3	4
$A_i(s^{-1})$	$3,5 .10^7$	$3,72.10^6$	$7,23.10^{11}$	$3,4.10^{-1}$
E_i(kJ/mol)	105,89	106,78	169,56	51,04
v_i	0,16	0,24	0,6	

4. Pyrolysis model of D. Blasi (2012)

A kinetic model for spruce wood chips torrefied is shown in Figure 2.4 which includes decomposition, described by three parallel reactions (k_1, k_2, and k_3), and oxidation, illustrated by two parallel reactions (k_4 and k_5).

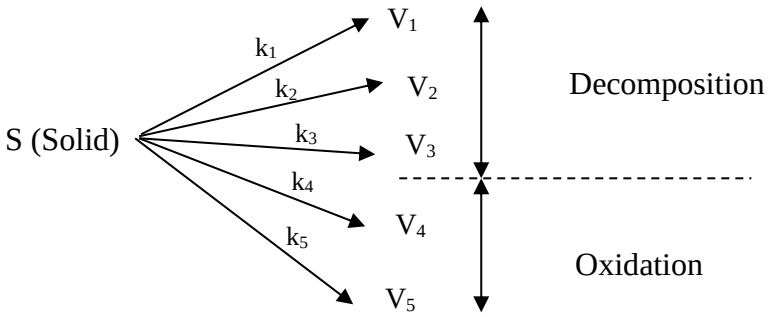

FIGURE 2.4 - The proposed model of D. Blasi (2012) [14].

where S is the wood sample and products V_i (i = 1,…,5) are the lumped volatile created by the thermal degradation of wood. To avoid the overlap between different components in the measurement of weight loss, the term "pseudo-component" is used in the kinetic model.

From the physical point of view, sample decomposition and char oxidation are sequential processes. This feature can be easily guaranteed by using an appropriate set of parameter values in the parallel reaction mechanism. These parameter values can also describe well the possible overlap between the various reactions at the same time. Moreover, there is approximately the same in the estimation of kinetic constants with the two approaches.

The equations of mass conservation for each component in solid are expressed as follows:

$$\frac{dY_i}{dt} = -k_i . Y_i^n \tag{2.28}$$

where Y_i is the mass fractions of 5 ordinary differential reactions of the solid fuel. $n_1 -$

n_4 = 1 correspond to the decomposition and char devolatilization. To take into account the evolution of the pore surface area during the char oxidation, a power law with exponent n_5 (n_5 # 1) is used. This parameter depends on the mass fractions of lumped volatile species released.

The rate of pyrolysis reactions of wood is also determined by the first-order Arrhenius law according to Eq. 2.2. Tables 2.4 and 2.5 show the kinetic parameters in thermal degradation of wood with three-step and five-step mechanisms respectively. These two mechanisms correspond to two models of heat transfer of wood: pyrolysis and combustion. This study is carried out by D. Blasi et al [14].

Table 2.4. Kinetic parameters for a model with a three-step mechanism.

Reaction	1	2	3
$A_i(s^{-1})$	$3,6 .10^6$	$4,17.10^{15}$	$1,0.10^0$
E_i(kJ/mol)	100,6	213,1	38,6
v_i	0,37	0,33	0,17
n_i	1	1	1

Table 2.5. Kinetic parameters for a model with a five-step mechanism.

Reaction	1	2	3	4	5
$A_i(s^{-1})$	$2,0 .10^7$	$8,8.10^{16}$	$5,69.10^7$	$5,6.10^5$	$4,32.10^{11}$
E_i(kJ/mol)	100,6	213,1	121,2	106,2	197,9
v_i	0,18	0,46	0,08	0,11	0,17
n_i	1	1	1	1	0,64

2.2.1.3 Development of thermal models

The thermal models developed in this part aim to simulate the thermal behavior of a cellulosic material during a fire resistance test in order to provide an analysis tool of fire performance in the construction sector. So the object of this numerical model is to provide an answer to a defined studied case. Therefore it is necessary to develop thermal models allowing to take into account the main phenomena of thermal degradation of cellulosic material and possibly applicable in the study. So the simplified model in Eurocode 5 does not meet this goal.

The choice of the pyrolysis models must be adapted to what we want to simulate and the information that we have. This requires the choice of a suitable simulation scale. Model of D. K. Shen and G. Cueff describe the pyrolysis mechanism at a simple level. In pyrolysis models of N. Grioui and D. Blasi, wood is divided into 3 pseudo-components corresponding to 3 peaks in the mass loss rate curve (Figure 2.5). The decomposition of three parts in the model of D. Blasi corresponds to the decomposition of three main components of wood (hemicellulose, cellulose, and lignin). However, this is not necessary for the model of N. Grioui.

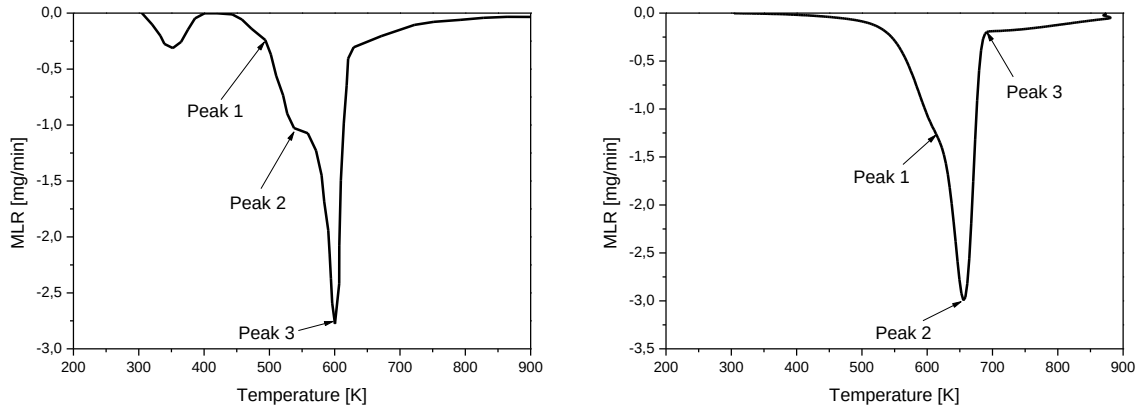

(a) Kinetic model of N. Grioui (b) Kinetic model of D. Blasi

FIGURE 2. 5 – The time derivative evolution of wood particle in: (a) Kinetic model of N. Grioui and (b) Kinetic model of D. Blasi.

Therefore, we decided on the basis of these observations, to develop kinetic thermal models allowing us to simulate the thermal behavior of cellulosic materials. So two kinetic models of N. Grioui and D. Blasi are selected and developed for simulation of the thermal behavior of wood material. These thermal models are based on the use of Arrhenius law to simulate the vaporization reaction of water and pyrolysis reactions of wood. The thermal properties of cellulosic materials are strongly impacted by temperature, it was decided to couple them with the advancement of vaporization and thermal degradation reactions. The vaporization reaction of water was also added to these two models. These thermal models are shown in Figures 2.6-2.7.

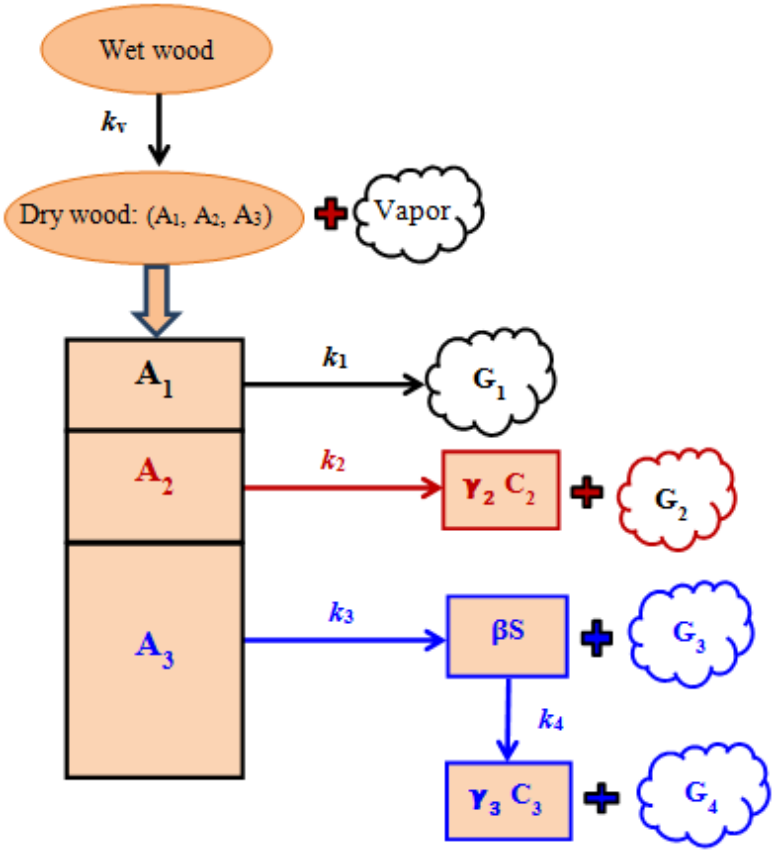

FIGURE 2. 6 - The multi-reactions of pyrolysis of N. Grioui (Modified).

The heat transfer in the pyrolysis model of the wood is described by the energy conservation equation as follow:

- Modified pyrolysis model of N. Grioui:

$$\frac{\partial[(\rho_{A1}+\rho_{A2}+\rho_{A3})Cp_w+\rho_{is}Cp_{is}+(\rho_{c2}+\rho_{c3})Cp_c+\rho_l Cp_l].T}{\partial t} = \frac{\partial}{\partial x}\left[\lambda_x.\frac{\partial T}{\partial x}\right]+\frac{\partial}{\partial y}\left[\lambda_y.\frac{\partial T}{\partial y}\right]+\frac{\partial}{\partial z}\left[\lambda_z.\frac{\partial T}{\partial z}\right]+Q_r^{"} \quad (2.29)$$

where $Q_r^{"}$ is the sum of reaction heat of the four pyrolysis reactions at the temperature T:

$$\begin{aligned} Q_r^{"} &= k_v.\rho_l.[\Delta h_v^0+(C_v-C_l).(T-T_0)]+k_1.\rho_{A1}.[\Delta h_1^0+(C_G-C_{A1}).(T-T_0)] \\ &+k_2.\rho_{A2}.\gamma_2[\Delta h_2^0+(C_C-C_{A2}).(T-T_0)]+k_2.\rho_{A2}.(1-\gamma_2)[\Delta h_2^0+(C_G-C_{A2}).(T-T_0)] \\ &+k_3.\rho_{A3}.\beta[\Delta h_3^0+(C_B-C_{A3}).(T-T_0)]+k_3.\rho_{A3}.(1-\beta)[\Delta h_3^0+(C_G-C_{A3}).(T-T_0)] \\ &+k_4.\rho_B.\gamma_3[\Delta h_4^0+(C_C-C_B).(T-T_0)]+k_4.\rho_B.(1-\gamma_3)[\Delta h_4^0+(C_G-C_B).(T-T_0)] \end{aligned} \quad (2.30)$$

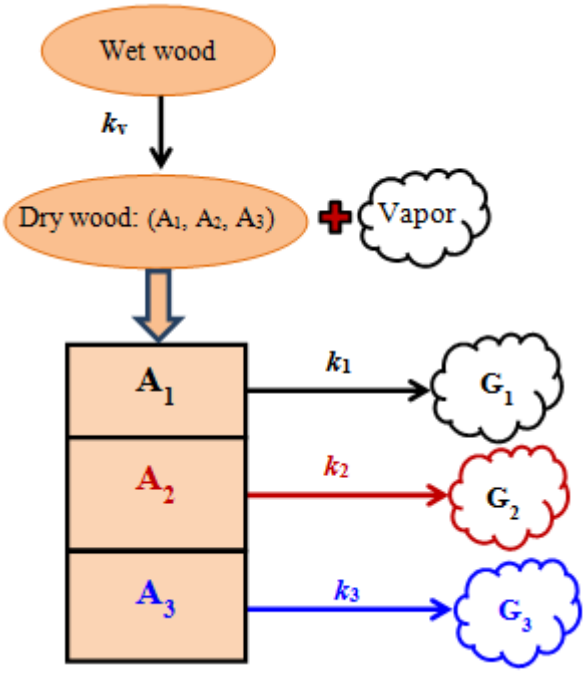

FIGURE 2. 7 - The multi-reactions of pyrolysis of D. Blasi (Modified).

- Modified pyrolysis model of D. Blasi:

$$\frac{\partial[(\rho_1+\rho_2+\rho_3)Cp_w+\rho_c Cp_c+\rho_l Cp_l].T}{\partial t} = \frac{\partial}{\partial x}\left[\lambda_x.\frac{\partial T}{\partial x}\right]+\frac{\partial}{\partial y}\left[\lambda_y.\frac{\partial T}{\partial y}\right]+\frac{\partial}{\partial z}\left[\lambda_z.\frac{\partial T}{\partial z}\right]+Q_r^{"} \quad (2.31)$$

where $Q_r^{"}$ is the sum of reaction heat of the four pyrolysis reactions at the temperature T:

$$Q_r^{"} = k_v.\rho_l.[\Delta h_v^0+(C_v-C_l).(T-T_0)]+k_1.\rho_1.[\Delta h_1^0+(C_G-C_W).(T-T_0)] +k_2.\rho_2.[\Delta h_2^0+(C_C-C_W).(T-T_0)]+k_3.\rho_3.[\Delta h_3^0+(C_G-C_W).(T-T_0)] \quad (2.32)$$

2.2.2 Mechanical behavior of timber material

Theoretical modeling of the mechanical behavior of the wood material makes it possible to avoid the use of systematic experimental testing campaigns, often very expensive, intended for characterization mechanics of wood material. In view of the massive use of wood material in different structures, it is necessary to have more precise modeling which is essential for its development. The evolution of numerical methods has allowed the emergence of calculation codes capable of simulating the behavior of a wooden structure subjected to mechanical loading. In this area, the finite element method is able to estimate with some precision the

local response in terms of stresses-strains of the wood material. Most of the finite element codes, available in the literature, use laws that are relatively easy to implement, but they cannot restore an elastoplastic response only for simple load cases.

We present here the important points of the theory of plasticity as well as the phenomenological laws most frequently used by finite element codes, under the assumptions of small perturbations (HPP) and large finite transformations (TF). Coupling between the two domains (orthotropic elasticity, and anisotropic plasticity) is the key necessary to understand the plastic behavior of wood material.

2.2.2.1 Orthotropic elastic behavior

The elastic strain $\underline{\varepsilon}^e$ is reversible and can be related to the Cauchy stress $\underline{\sigma}$ by a law elastic by introducing the tensor of order 4 of the elastic constants $\underline{\underline{\Lambda}}$:

$$\underline{\sigma} = \underline{\underline{\Lambda}} : \underline{\varepsilon}^e \tag{2.33}$$

For an orthotropic material, the tensor $\underline{\underline{\Lambda}}$ is calculated by:

$$\underline{\underline{\Lambda}} = \begin{bmatrix} C_{11} & C_{12} & C_{13} & 0 & 0 & 0 \\ C_{12} & C_{22} & C_{23} & 0 & 0 & 0 \\ C_{13} & C_{23} & C_{33} & 0 & 0 & 0 \\ 0 & 0 & 0 & C_{44} & 0 & 0 \\ 0 & 0 & 0 & 0 & C_{55} & 0 \\ 0 & 0 & 0 & 0 & 0 & C_{66} \end{bmatrix} \tag{2.34}$$

with:

$$\mathrm{C}_{11} = \frac{1 - \nu_{23}\nu_{32}}{\Delta E_2 E_3}; \mathrm{C}_{22} = \frac{1 - \nu_{13}\nu_{31}}{\Delta E_1 E_3}; \ \mathrm{C}_{33} = \frac{1 - \nu_{12}\nu_{21}}{\Delta E_1 E_2} \tag{2.35}$$

$$\mathrm{C}_{12} = \frac{\nu_{21} + \nu_{31}\nu_{23}}{\Delta E_2 E_3}; \mathrm{C}_{13} = \frac{\nu_{31} + \nu_{21}\nu_{32}}{\Delta E_2 E_3}; \ \mathrm{C}_{23} = \frac{\nu_{32} + \nu_{12}\nu_{31}}{\Delta E_1 E_3} \tag{2.36}$$

$$\mathrm{C}_{44} = 2\mathrm{G}_{12}; \mathrm{C}_{55} = 2\mathrm{G}_{13}; \ \mathrm{C}_{66} = 2\mathrm{G}_{23} \tag{2.37}$$

$$\Delta = \frac{1 - \nu_{12}\nu_{21} - \nu_{23}\nu_{32} - \nu_{13}\nu_{31} - 2\nu_{21}\nu_{32}\nu_{13}}{E_1 E_2 E_3} \tag{2.38}$$

E_i is Young's modulus in direction (i), ν_{ij} and $\mathrm{G_{ij}}$ are respectively the Poisson's ratio and

the Coulomb modulus in the plane (i-j). The directions of orthotropy are shown in Figure 2.8.

Figure 2.8 shows that, for timber, the direction (x) is assumed to coincide with the longitudinal direction fibers (L), the axis (y) is carried by the radial direction (R) and the axis (z) is normal to the plane (L-R) and which represents the transverse direction to the rings (T).

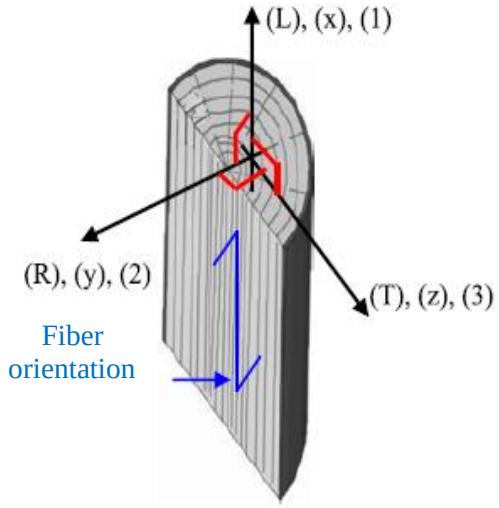

FIGURE 2. 8 - Main directions of wood material.

2.2.2.2 Plastic behavior

In phenomenological plasticity, the small disturbance hypothesis (HPP) allows us to decompose the total $\underline{\varepsilon}$ deformation of order 2 in the elastic part $\underline{\varepsilon}^e$ and plastic part $\underline{\varepsilon}^p$:

$$\underline{\varepsilon} = \underline{\varepsilon}^e + \underline{\varepsilon}^p \tag{2.39}$$

Plastic deformation is irreversible and cannot be directly related to stress. It depends on the history of the loading imposed on the material. In this case, the strain field is connected to that of the stresses by an incremental law, which depends on the type of hardening considered during plastic flow. The plastic behavior is initiated when the stress reaches a threshold value called elastic limit σ_e is and is reflected by the evolution of a load surface in space called plasticity criterion f_p.

The plasticity criterion f_p can be written in a general form [16, 17]:

$$f_p = \|\underline{\sigma}\| - (R + \sigma_e); R = \frac{Q}{b}(1 - e^{-b\Delta\lambda}) \tag{2.40}$$

$\|\underline{\sigma}\|$ represents the norm of the stress tensor $\underline{\sigma}$; R represents the isotropic strain hardening

stress; $\Delta\lambda$ is the cumulated plastic strain; Q and b are the isotropic hardening parameters.

Research studies which mainly focus on the analysis of the plastic behavior of wood material under different directions [18-20] show that Hill's plasticity criteria (1948) and Hoffman (1967), presented respectively in [21, 22], allow us to obtain an approximation correlated well with test data. Therefore, we limit ourselves to the presentation of Hill's plasticity criteria (1948) in this section.

Hill's (1948) quadratic criterion, presented in [21], applies to a particular anisotropy that preserves the three planes of symmetry of the material. The intersections of these planes of symmetry are the main axes of orthotropy which are taken as a benchmark for the writing of the criterion.

$$F(\sigma_y - \sigma_z)^2 + G(\sigma_z - \sigma_x)^2 + H(\sigma_x - \sigma_y)^2 + 2L\tau_{yz}^2 + 2M\tau_{zx}^2 + 2N\tau_{xy}^2 = 1 \tag{2.41}$$

$$\Leftrightarrow \sqrt{\underline{\sigma} : \underline{\underline{H}} : \underline{\sigma}} = 1 \tag{2.42}$$

with:

$$\underline{\underline{H}} = \begin{bmatrix} G+H & -H & -G & 0 & 0 & 0 \\ -H & H+F & -F & 0 & 0 & 0 \\ -G & -F & F+G & 0 & 0 & 0 \\ 0 & 0 & 0 & 2N & 0 & 0 \\ 0 & 0 & 0 & 0 & 2M & 0 \\ 0 & 0 & 0 & 0 & 0 & 2L \end{bmatrix} \tag{2.43}$$

where F, G, H, L, M and N are the six parameters that characterize the anisotropic behavior of the material according to Hill. The parameters are to be determined experimentally and are expressed as a function of the thresholds of plasticity in compression and shear, respectively along with the main directions of orthotropy.

Six Hill's Anisotropy Constants (F, G, H, L, M, and N) can be calculated by the following relations:

- Before plastic flow, the isotropic strain hardening variable R = 0 ($\Delta\lambda \rightarrow 0$), hence the equation (2.40) reduces to:

$$\mathrm{f_p} = \left\|\underline{\sigma}\right\| - \sigma_e = 0 \Leftrightarrow \sqrt{\underline{\sigma} : \underline{\underline{H}} : \underline{\sigma}} = \sigma_e \tag{2.44}$$

$$\Leftrightarrow \sqrt{F(\sigma_y - \sigma_z)^2 + G(\sigma_z - \sigma_x)^2 + H(\sigma_x - \sigma_y)^2 + 2L\tau_{yz}^2 + 2M\tau_{zx}^2 + 2N\tau_{xy}^2} = \sigma_e \tag{2.45}$$

- Let the uniaxial threshold stresses be σ_L, $\sigma_R$and σ_T (determined from the compression tests), three Hill's constants (F, G, and H) can be identified by the following expressions:

$$\sigma_L\sqrt{\mathrm{G} + \mathrm{H}} = \sigma_e \Rightarrow \sigma_L = \frac{\sigma_e}{\sqrt{\mathrm{G} + \mathrm{H}}} \tag{2.46a}$$

$$\sigma_R = \frac{\sigma_e}{\sqrt{\mathrm{F} + \mathrm{H}}} \tag{2.46b}$$

$$\sigma_T = \frac{\sigma_e}{\sqrt{\mathrm{F} + \mathrm{G}}} \tag{2.46c}$$

Equation (2.46a) shows that the constants G and H affect the direction (L). The same remark can be done for the other two directions (R) and (T).

- If τ_{RT}, τ_{LT}, and τ_{LR} are shear stresses, the Hill anisotropy coefficients (L, M, and N) are obtained by the following relations:

$$2L = \frac{\sigma_e^2}{\tau_{\mathrm{RT}}^2};\ 2M = \frac{\sigma_e^2}{\tau_{\mathrm{LT}}^2};\ 2N = \frac{\sigma_e^2}{\tau_{\mathrm{LR}}^2} \tag{2.47}$$

The anisotropy coefficients L, M, and N are strictly greater than zero.

The disadvantage of this criterion is that it does not distinguish between the differences between the zone of traction and compression, which is not the case in reality. The breakage for wood often begins in the zone of tension and then propagates towards the zone of compression.

$$\underline{\dot{\varepsilon}}^p = \dot{\lambda}\frac{\partial f}{\partial \underline{\sigma}} = \dot{\lambda}\frac{\underline{\underline{H}} : \underline{\sigma}}{\left\|\underline{\sigma}\right\|} = \dot{\lambda}\underline{n} \tag{2.48}$$

$$\dot{r} = -\dot{\lambda}\frac{\partial f}{\partial R} = \dot{\lambda}[1 - br] \tag{2.49}$$

where $\dot{\lambda}$ is the plastic multiplier which is obtained from the consistency condition ($f = \dot{f} = 0$), $\underline{n}$ is the outward normal to the yield surface, and $\dot{r}$ is the isotropic hardening strain rate.

2.2.3 Thermo-mechanical coupling of wood material

The mechanical properties of the wood material at room temperature are relatively well known and under control, which does not happen in fire conditions where temperatures are very high.

Knowledge of the evolution of mechanical properties of wood as a function of temperature is, therefore, necessary to assess its mechanical resistance under extreme fire conditions. An update of this information, which relates to the definition of a thermo-mechanical law appropriating to wood, must help engineers predict the fire behavior of wooden structures before carrying out large-scale fire tests in specialized laboratories, which are often very expensive.

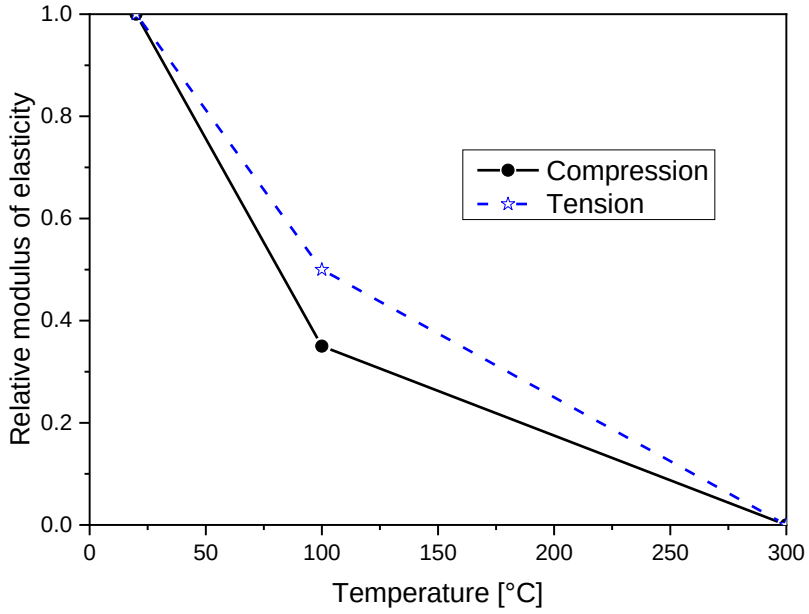

FIGURE 2. 9 - Reduction factor for the modulus of elasticity [6].

Standard EN-1995-1-2 [6] presents the variation of the modulus of elasticity of wood, stressed in tension or in compression, depending on the temperature. The variation of E takes place in two linear phases. In the tension, Young's modulus decreases linearly and it decreases to 50% of its initial value at a temperature T = 100 °C. Another linear phase of reduction is observed between 100 °C and 300 °C. Beyond 300 °C, Young's modulus vanishes. In

compression, the modulus of elasticity drops by 65% at T = 100 °C compared to wood in tension. Between 100 °C and 300 °C, the wood in compression is worn like wood in voltage. The modulus of elasticity is considered as zero at a temperature of about 300 °C which corresponds to the start of coal formation.

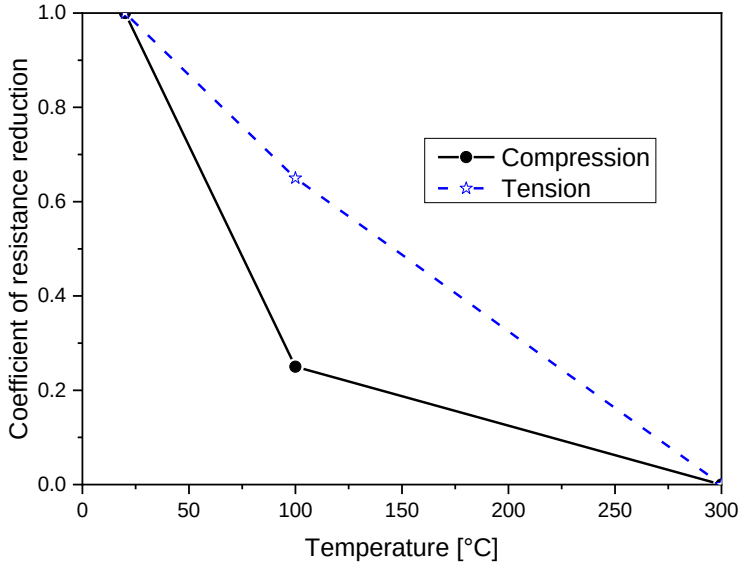

FIGURE 2. 10 - Reduction factor for the mechanical resistance[6].

The reduction of the mechanical resistance in compression is composed of two linear parts. It varies linearly up to 100 °C, which corresponds to the evaporation of water wood (wood drying step), followed by another linear part up to 300 °C with a slope slightly higher (start of the carbonization step). At T = 100 °C, the compressive strength is about 22% of its original value. It cancels out at 300 °C where the wood turns completely into charcoal.

Similar to the thermo-physical properties, there is also temperature dependence in the mechanical properties of wood. Verification of the fire behavior of wooden structures according to standard EN-1995-1-2 [6] suggests that:

1. The local values in terms of modulus of elasticity and mechanical resistance for softwoods in tension and compression are multiplied by reduction factors depending on the temperature according to Figure 2.9.

2. The same reduction in resistance, illustrated in Figure 2.10 for compression parallel to the fibers, can be applied for compression perpendicular to the fibers.

3. For the case of shear in which the two stress components are perpendicular to the axis, the same resistance reduction factor can be applied.

2.3 Numerical aspects

2.3.1 Thermal analysis

For a thermal diffusion problem, the heat equation is written:

$$\rho C_p \dot{T} = -\nabla q + Q \tag{2.50}$$

with:

$$q = -\lambda \nabla T \text{ on } \partial\Omega_q: \vec{q} = q\underline{n} \tag{2.51}$$

T denotes the temperature at the current time; Q represents the heat source; q is the flux of thermal vector; $\underline{n}$ is the normal vector outgoing at $\partial\Omega_q$; λ is the coefficient of thermal conductivity; ρ is the density; C_p is the specific heat.

2.3.1.1 Initial conditions and boundary conditions

The solid with a body Ω, density ρ, specific heat C_p, thermal conductivity λ, and the border ∂Ω is subjected to (Figure 2.11):

- A heat source $Q_r^{"}$

- A flow on the border $\partial\Omega_q$

- An imposed temperature T* on the border $\partial\Omega_T$ with $\partial\Omega = \partial\Omega_q \cup \partial\Omega_T$ and $\partial\Omega_q \cup \partial\Omega_T = \emptyset$

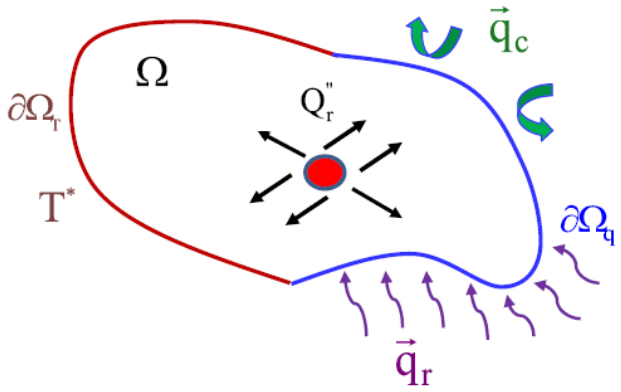

FIGURE 2. 11 - Boundary conditions of a thermal problem.

Solving the differential equation of a heat diffusion problem requires the definition of the initial temperature and boundary conditions of the problem. Initial temperature distribution in

a wooden sample at time t = 0 is described by:

$$T(x,y,z,t)_{t=0} = T_0(x,y,z) \tag{2.52}$$

The imposed temperature T on the surface $\partial\Omega_T$ is defined by the boundary conditions of Dirichlet:

$$T(x,y,z,t) = T^*(x,y,z,t) \text{ over } \partial\Omega_T \tag{2.53}$$

The boundary conditions of Neumann given by the heat flow are:

$$\vec{q} = -\lambda \frac{\partial T}{\partial \vec{n}} \quad \text{on } \partial\Omega_q \tag{2.54}$$

The heat exchange of the surrounding medium with the external surfaces of the sample exposed to fire is done either by convection, or by radiation, or by the combination of the two mechanisms, and which may be expressed subject to the following boundary conditions:

$$\vec{q} = \vec{q}_r = \sigma\varepsilon(T^4 - T_\infty^4)\vec{n} \text{ (influence)} \tag{2.55}$$

$$\vec{q} = \vec{q}_c = h_c(T - T_\infty)\vec{n} \text{ (convection)} \tag{2.56}$$

$$\vec{q} = \vec{q}_r + \vec{q}_c = \sigma\varepsilon(T^4 - T_\infty^4)\vec{n} + h_c(T - T_\infty)\vec{n} \text{ (combination)} \tag{2.57}$$

$\vec{n}$ represents the normal to the surface of the sample tested and it is directed outwards; $\vec{q}_r$ [W/m^2] and $\vec{q}_c$ [W /m^2] are the heat fluxes caused by radiation and convection, respectively; h_c [W/(m^2.K)] is the coefficient of heat transfer by convection; T_∞ [K] represents the ambient temperature; σ = 5,67x10^8 W/(m^2.K^4) is the Stefan-Boltzmann constant; ε is emissivity.

2.3.1.2 Integral formulation of a thermal problem

Let δT be a continuous virtual temperature field such that δT = 0 on $\partial\Omega_T$. The weak formulation of the problem is obtained by integrating the product of equation (2.46) with a virtual temperature field δT on a volume Ω:

$$\int_\Omega \delta T.\dot{U}.\,d\Omega = -\int_\Omega \delta T.\nabla q.\,d\Omega + \int_\Omega \delta T.\,Q.\,d\Omega \tag{2.58}$$

with:

$$\rho C_p \dot{T} = \dot{U} \tag{2.59}$$

U is the thermal energy in the volume Ω.

By integration by part, we can write:

$$\int_\Omega \delta T.\nabla q.\,d\Omega = \int_\Omega \nabla(\delta T.\,q).\,d\Omega - \int_\Omega q.\nabla(\delta T).\,d\Omega \tag{2.60}$$

By the divergence theorem, we have:

$$\int_\Omega \nabla(\delta T.\,q).\,d\Omega = \int_{d\Omega_q} \delta T.\,q.\,\underline{n}.\,dS - \int_{d\Omega_q} \delta T.\,\vec{q}.\,dS \tag{2.61}$$

By replacing equations (2.60) and (2.61) in (2.58), we obtain:

$$\int_\Omega \delta T.\,\rho.\,C_p.\,\dot{T}.\,d\Omega - \int_\Omega \lambda.\,(\nabla\delta T).\,(\nabla T).\,d\Omega = \int_{d\Omega_q} \delta T.\,\vec{q}.\,dS + \int_\Omega \delta T.\,Q.\,d\Omega \tag{2.62}$$

2.3.1.3 Numerical aspects

The finite element method is used to solve the thermal diffusion problem. the equilibrium equation can be written as follows:

$$\{f_{n+1}^{ext}\} = [K].\{T_{n+1}\} \tag{2.63}$$

In an implicit static analysis, the previous equation reduces to:

$$\{R_{n+1}\} = \{f_{n+1}^{int}\} - \{f_{n+1}^{ext}\};\ \{f_{n+1}^{int}\} = [K].\{T_{n+1}\} \tag{2.64}$$

where [K] is the rigid matrix, $\{T_{n+1}\}$ is the temperature vector nodes (the unknown of the problem), $\{f_{n+1}^{ext}\}$ is the vector of external forces, $\{f_{n+1}^{int}\}$ is the vector of internal forces and $\{R_{n+1}\}$ is the residual vector of static equilibrium at time t_{n+1}. The iterative method of Newton-Raphson [5] is used within the framework of the code ABAQUS / Standard [23] for the calculation of the residue $\{R_{n+1}\}$. It is then linearized thanks to the Taylor expansion of order 1:

$$\{R_{n+1}\}^{(i+1)} = \{R_{n+1}\}^{(i)} + \left[\frac{\partial\{R_n\}}{\partial\{T_n\}}\right]^{(i)} \delta\{T_n\} = 0 \tag{2.65}$$

with $\delta\{T_n\} = \{T_n\}^{(i+1)} - \{T_n\}^{(i)}$ is the temperature increment between successive iterations (i + 1) and (i). To ensure the convergence of the iterative system, this iterative process continues until the residue is very small [23].

A UMATHT calculation procedure is used to define the thermal behavior of the material wood. It is called at each point of integration, and at each iteration, in order to participate in the resolution of the diffusion problem thanks to a Newton-Raphson algorithm [5].

The variables required to be defined as inputs for the UMATHT procedure are:

- Internal thermal energy U;

- The variation of U with respect to the temperature $\frac{\partial U}{\partial T}$;

- The variation of U with respect to the temperature gradients $\frac{\partial U}{\partial(\partial T/\partial x_i)}$ (i = 1, 2, 3);

- The flux vector defined by $\vec{q} = q\underline{n}$;

- The variation of q compared to the temperature $\frac{\partial q}{\partial T}$;

- The variation of q with respect to the temperature gradients $\frac{\partial q}{\partial(\partial T/\partial x_i)}$ (i = 1, 2, 3);

These quantities make it possible to define the Jacobian matrix of the Newton-Raphson algorithm [5, 23]. Figure 2.12 shows the resolution algorithm by the step method necessarily in the physical sense variables.

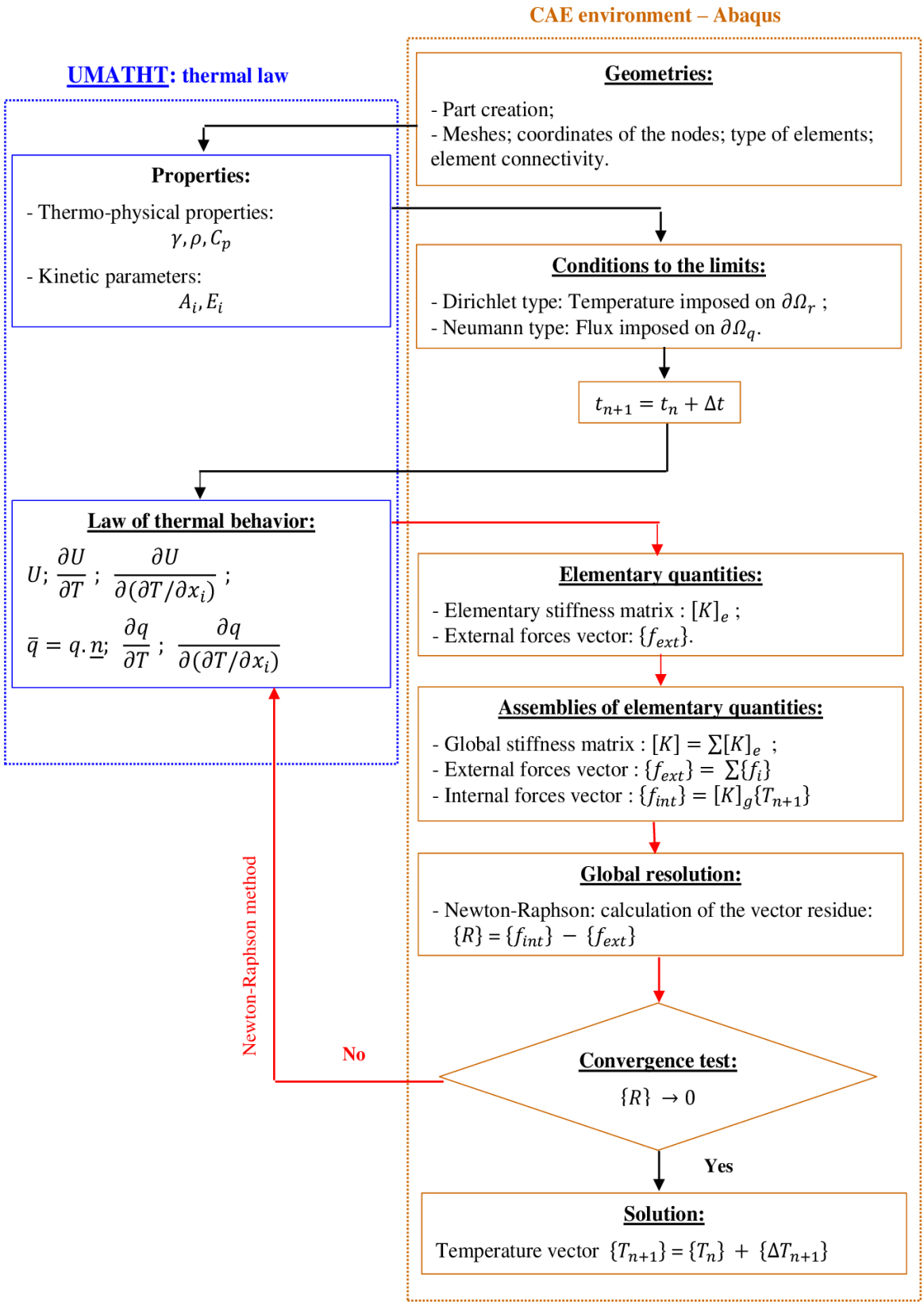

FIGURE 2. 12 - Global resolution algorithm in the ABAQUS code [23].

2.3.2 Mechanical analysis

In this section, we are interested in the study of the numerical aspects of the elasto-plastic model presented in Chapter 2. The numerical integration of the model (elasticity-plasticity) by an iterative implicit scheme combining the technique of radial return with reducing the number of equations is discussed. The Static Implicit (SI) resolution of a static equilibrium problem is discussed.

2.3.2.1 Numerical integration methods

The behavioral equations described in chapter 2 represent the temporal evolution of the plastic deformation and strain hardening variable. These differential equations ordinary (ODE) nonlinear of order 1 can be formally noted in the form:

$$\dot{\mathrm{Y}} = \mathrm{F}(\mathrm{t}, \mathrm{Y}) \tag{2.66}$$

The associated initial conditions are:

$$\mathrm{Y}(\mathrm{t} = 0) = Y_0 \tag{2.67}$$

For the temporal integration of EDOs, it is necessary to use methods based on a temporal discretization by finite differences (several details on these techniques are given in [24, 25].

The digital integration of EDOs is done either by linked-step methods (Adams-Bashforth method, Adams-Moulton method,. . .) or by methods with independent steps (explicit method of 1st or 2nd order Euler, explicit method of Runge Kutta; Hughes-Taylor implicit method: ∅-method,. . .). In this analysis, we use the independent step methods where the value of Y(t) is calculated at the instant t_{n+1} from the quantities obtained at the instant t_{n+1}, independently of the values obtained at the preceding instants t_n.

In general, the choice of a numerical integration method depends on the desired precision; of convergence and the digital stability it presents. In this study, the integration of the constitutive equations is made on the basis of the implicit method of the θ-method type and asymptotic method.

1. θ-method

The θ-method initially developed by Hughes and Taylor [26], is an implicit method of order 0 (Δt^2) based on the introduction of a parameter θ in the Euler equation. Its expression

in the form generalized is:

$$Y_{n+\theta} = (1-\theta)Y_n + \theta Y_{n+1} \tag{2.68}$$

$$Y_{n+1} = Y_n + \Delta t.\, \mathrm{F}(t_{n+\theta}, Y_{n+\theta}) \tag{2.69}$$

The form of the generalized trapezius method is:

$$Y_{n+1} = Y_n + \left[(1-\theta)\dot{\mathrm{F}}(t_n, Y_n) + \theta.\, \dot{\mathrm{F}}(t_{n+1}, Y_{n+1})\right]\Delta t \tag{2.70}$$

where θ is between 0 and 1. When θ = 0 we find the explicit scheme; for θ = $\frac{1}{2}$, we find the semi-implicit scheme, and if θ = 1 the scheme is implicit.

2. Asymptotic method

The asymptotic integration method was initially proposed by Freed and Walker [27].

The differential equations are expressed in the following form:

$$\dot{Y} = \varphi(Y)[A(Y) - Y] \tag{2.71}$$

Several discretizations of the previous equation are considered including that of the midpoint:

$$Y_\theta = e^{-\theta\varphi(Y_\theta)\Delta t} Y_t + \left[1 - e^{-\theta\varphi(Y_\theta)\Delta t}\right] A(Y_\theta) \tag{2.72}$$

$$Y_{t+\Delta t} = e^{-\theta\varphi(Y_{t+\Delta t})\Delta t} Y_t + \left[1 - e^{-\theta\varphi(Y_{t+\Delta t})\Delta t}\right] A(Y_\theta) \tag{2.73}$$

2.3.2.2 Numerical aspects

The finite element method is used to solve numerically the global equilibrium equations with the coupled constitutive equations presented in section 2.2. Based on the implicit approach, the nonlinear equilibrium equation can be written as follows:

$$[K].\{\ddot{u}\}_{n+1} + \{R\}_{n+1} = 0 \tag{2.74}$$

with:

$$\{R\}_{n+1} = \{f_{int}\}_{n+1} - \{f_{ext}\}_{n+1} \tag{2.75}$$

where [K] is the rigid matrix, $\{f_{int}\}_{n+1}$ and $\{f_{ext}\}_{n+1}$ are the vectors of internal and external forces, respectively. $\{R\}_{n+1}$ is the residue vector. The solution of the problem is obtained when the vector residue tends towards zero.

The use of the implicit approach, which is standard in the simulation of non-linear problems, needs both spatial discretization of the body and time discretization using an appropriate finite difference method. In an implicit static analysis, equation (2.70) reduces to:

$$\{R\}_{n+1} = \{f_{int}\}_{n+1} - \{f_{ext}\}_{n+1} \tag{2.76}$$

The iterative Newton-Raphson method is used within the framework of the ABAQUS/Standard code [23]. The residue is then linearized thanks to the Taylor expansion of order 1:

$$\{\mathrm{R}\}_{\mathrm{n+1}}^{\mathrm{s+1}} = \{\mathrm{R}\}_{\mathrm{n+1}}^{\mathrm{s}} + \left(\frac{\partial\{\mathrm{R}\}_{\mathrm{n}}}{\partial\{\mathrm{U}\}_{\mathrm{n}}}\right)^{(\mathrm{s})} \{\delta\mathrm{U}_{\mathrm{n}}\} + \ldots = 0 \tag{2.77}$$

with $\{\delta\mathrm{U}_{\mathrm{n}}\} = \{\mathrm{U}_{\mathrm{n}}\}^{(s+1)} - \{\mathrm{U}_{\mathrm{n}}\}^{(s)}$ is the displacement increment between successive iterations (s + 1) and (s). This iterative process continues until the residue is sufficiently weak (convergence of the iterative system).

The tangent matrix of this system at the iteration (s) is written:

$$\left[\mathrm{K}_{\mathrm{T}}^{(\mathrm{s})}(\{\mathrm{U}_{\mathrm{n}}\})\right] = -\left(\frac{\partial\{\mathrm{R}\}_{\mathrm{n}}}{\partial\{\mathrm{U}\}_{\mathrm{n}}}\right)^{(\mathrm{s})} \tag{2.78}$$

$\left[\mathrm{K}_{\mathrm{T}}^{(\mathrm{s})}(\{\mathrm{U}_{\mathrm{n}}\})\right]$ plays a central role in the speed of convergence of this implicit iterative scheme. The determination of this operator necessarily involves the calculation of the residue {R}.

The integration of equations Eq. (2.48) and Eq. (2.49) is performed using the θ-method [26] for the plastic deformation and the asymptotic method [27] for the isotropic hardening variable. Then, the incremental equations are given as:

$$\varepsilon_{n+1}^{p} = \varepsilon_{n}^{p} + \Delta\lambda.\underline{n}_{n+1} \tag{2.79}$$

$$r_{n+1} = r_n e^{-b\Delta\lambda} + \frac{(1 - e^{-b\Delta\lambda})}{b} \tag{2.80}$$

To determine the solutions σ_{n+1} and R_{n+1}, the above coupled constitutive equations should be integrated numerically over each time step, using the elastic prediction and plastic correction procedure resulting in the following system [27]:

$$\begin{cases} f_{n+1}(\Delta\lambda, \underline{n}_{n+1}) = \|\sigma_{n+1}\| - R_{n+1} - \sigma_e = 0 \\ h_{n+1}(\Delta\lambda, \underline{n}_{n+1}) = \underline{\underline{H}} : \sigma_{n+1} - \|\sigma_{n+1}\|. \underline{n}_{n+1} = 0 \end{cases} \tag{2.81}$$

where:

$$\|\sigma_{n+1}\| = \sqrt{\underline{\sigma} : \underline{\underline{H}} : \underline{\sigma}} \tag{2.82}$$

$$\sigma_{n+1} = \sigma_n + \underline{\underline{\Lambda}} : [\Delta\underline{\varepsilon} - \Delta\lambda\, \underline{n}_{n+1}] \tag{2.83}$$

$$R_{n+1} = Q\left(r_n e^{-b\Delta\lambda} + \frac{(1 - e^{-b\Delta\lambda})}{b}\right) \tag{2.84}$$

The equations system Eq. (2.81) is solved iteratively according to the classical Newton–Raphson iterative scheme to obtain the unknowns $\Delta\lambda$ and $\underline{n}_{n+1}$ which allow the computation of the other internal variables including the stress tensor at the end of the time increment [28,29].

2.3.3 Thermo-mechanical coupling

EC5 [6] suggests using three linear approximations different of the reducing coefficient K_θ according to the type of stresses (traction, compression, or shear). These approximations give K_θ = 1 at an ambient temperature (T = 20 °C) where the behavior is totally mechanical. At a temperature T = 100 °C, K_θ which applies for the reduction of Young's modulus varies between 0.35 to 0.5. For the same temperature, it varies from 0.25 to 0.65 for the case of reduction of mechanical strength. This variability makes the choice of the value of K_θ more difficult. In the continuation of this work, all the simulations were carried out by adopting K_θ defined for the voltage according to the approach regulation EC5 [6], the most used for the sizing of wooden structures. This choice is motivated by the fact that surfaces exposed to fire

are more often in tension overall examples treated within the framework of this thesis.

To understand the effect of this reduction coefficient K_θ on the thermomechanical behavior, it is advised to make a parametric study. This point is not addressed in this study. The implementation of the thermomechanical behavior of softwood in the ABAQUS code [23] is done in the following two steps:

1. The thermal analysis is carried out first at each instant t_{n+1}. Knowing the temperature T_{n+1}, the reduction coefficient K_θ is calculated.

2. When the values of K_θ are determined, the mechanical analysis is carried out.

The integration of mechanical and thermal laws in ABAQUS [23] requires the identification of elastic properties (Young's moduli, Poisson's coefficients, and shear moduli), and physical parameters (conductivity, specific heat, and density).

The approximation proposed for the calculation of the modulus of elasticity Ei and of the mechanical resistance fi is written:

$$\begin{cases} E_i = E_{0i} \times K_\theta^E(T) \\ f_i = f_{0i} \times K_\theta^f(T) \end{cases} \tag{2.85}$$

with:

$$\begin{cases} T < 20\,°C & : K_\theta^E(T) = 1 \\ 20\,°C \le T < 100\,°C & : K_\theta^E(T) = -6{,}25 \times 10^{-3}T + 1{,}125 \\ 100\,°C \le T \le 300\,°C & : K_\theta^E(T) = -2{,}5 \times 10^{-3}T + 0{,}75 \\ 300\,°C < T & : K_\theta^E(T) = 0 \end{cases} \tag{2.86}$$

And:

$$\begin{cases} T < 20\,°C & : K_\theta^f(T) = 1 \\ 20\,°C \le T < 100\,°C & : K_\theta^f(T) = -4{,}375 \times 10^{-3}T + 1{,}0875 \\ 100\,°C \le T \le 300\,°C & : K_\theta^f(T) = -1{,}75 \times 10^{-3}T + 0{,}825 \\ 300\,°C < T & : K_\theta^f(T) = 0 \end{cases} \tag{2.87}$$

E_{0i} and f_{0i} are the initial moduli of elasticity and mechanical strength, respectively,

depending on the direction (i), determined at an ambient temperature T = 20 °C; $K_{\theta}^{E}(T)$ and $K_{\theta}^{f}(T)$ are the reduction functions modulus of elasticity and mechanical strength, respectively.

The coupled thermo-elastic law is expressed by:

$$\begin{cases} E_1 = E_{01} \times K_{\theta}^{E};\ E_2 = E_{02} \times K_{\theta}^{E};\ E_3 = E_{03} \times K_{\theta}^{E} \\ G_{ij} = G_{0ij} \times K_{\theta}^{G} \qquad with \quad K_{\theta}^{G} = K_{\theta}^{E}\ (Shear) \end{cases} \tag{2.88}$$

The coupling is carried out by introducing the variation of the mechanical characteristics of wood according to the defined approaches by equation (2.88).

It is worth noting that the reduction of strength and modulus of elasticity to zero at 300°C were assumed in the EC5 [6] for standard fire exposure. To define these as equal to zero is not possible in the ABAQUS [23]; therefore, values two orders of magnitude smaller than the values at ambient temperature were adopted.

2.4 Conclusion

In this chapter, we have presented the thermo-mechanical modeling of timber material at high temperatures in two aspects: theoretical aspects and numerical aspects.

Firstly, the theoretical aspects of the model were discussed. The thermal law is described by the standard heat equation which requires knowledge of the variation of thermal conductivity, specific heat, and mass volume as a function of temperature as well as thermal degradation of wood during the drying, pyrolysis, and combustion phases. In particular, we were interested in the study of two different types of thermal models (simplified and kinetic models). The mechanical law is modeled within the framework of the thermodynamics of irreversible processes. It takes into account the coupling between the behavior orthotropic elastic, the anisotropic plastic flow with isotropic nonlinear strain hardening. Plastic flow is described by plasticity criteria (Hill (1948). Then, the thermomechanical coupling is carried out, according to the regulatory approach EC5 [6] relating to the fire resistance of structures in wood, by applying the reduction factor K_θ to the mechanical resistance of a softwood.

The second part will present all the numerical aspects related to the thermomechanical model developed as well as the procedure for its implementation in the platform by ABAQUS [23]. The classical spatial discretization of the principle of virtual powers by the finite element method is recalled. The thermal law is described by the standard heat equation. The thermal model chosen integrates the three modes of heat transfer namely conduction, radiation, and convection during exposure to fire. The thermal diffusion problem is discretized by the finite element method. The strategy for implementing this thermal law is also presented. The method of solving the system of nonlinear equations to be solved by the Newton-Raphson method is developed in detail. The digital integration of constitutive equations of the model of anisotropic plasticity is performed by the implicit method.

Bibliography of chapter 2

[1] Laplanche K., Etude du comportement au feu des assemblages de structures bois: Approche expérimentale et modélisation, PhD Thesis, University of Blaise Pascal (Clermont-Ferrand), France (2006).

[2] Cueff G., Développement d'un modèle thermomécanique du comportement sous agressions thermiques de matériaux cellulosiques. Application à l'étude de résistance au feu de panneaux de bloc-porte en aggloméré de bois, PhD Thesis, University of Bordeaux, France (2004).

[3] Cueff G., Mindeguia J.C., Dréan V., Breysse D., Auguin G, Experimental and numerical study of the thermomechanical behaviour of wood-based panels exposed to fire, Construction and Building Materials 160 (2018) 668-678.

[4] Thi V.D., Modélisation du comportement au feu des structures en bois, PhD Thesis, University of Lorraine, France (2017).

[5] Thi V.D., Khelifa M., Oudjene M., El Ganaoui M., Rogaume Y., Finite element analysis of heat transfer through timber elements exposed to fire, Engineering Structures 143 (2017) 11-21.

[6] Eurocode 5 - Design of timber structures. Part 1-2: General - Structural fire design, CEN 2004 (European Committee for Standardization), EN 1995-1-2, Brussels, Belgium.

[7] Knudson R.M., Schniewind A.P, Performance of structural wood members exposed to fire, Forest Products Journal 25(2) (1975) 23-32.

[8] Fredlund B., Modelling of heat and mass transfer in wood structures during fire, Fire Safety Journal 20 (1993) 39-69.

[9] Janssens M.L., Modeling of the thermal degradation of structural wood members exposed to fire, Fire Mater 28 (2004) 199-207.

[10] Thi V.D., Khelifa M., El Ganaoui M., Rogaume Y., Finite element modeling of the pyrolysis of wet wood subjected to fire, Fire Safety Journal 81 (2016) 85-96.

[11] ISO 834-1 - Fire-resistance tests - Elements of building construction, Part 1: General requirements, International Organization for Standardization, Geneva, Switzerland (1999).

[12] Shen D.K., Fang M.X., Luo Z.Y., Cen K.F., Modeling pyrolysis of wet wood under external heat Flux, Fire Safety Journal 42 (2007) 210-217.

[13] Grioui N., Halouani K., Zoulalian A., HalouaniF., Thermogravimetric analysis and kinetics modeling of isothermal carbonization of olive wood in inert atmosphere, Thermochimica Acta 440 (2006) 23-30.

[14] Broström M., Nordina A., Pommer L., Branca C., Di Blasi C., Influence of torrefaction on the devolatilization and oxidation kinetics of wood, Journal of Analytical and Applied

Pyrolysis 96 (2012) 100-109.

[15] Flynn D.R., Response of High Performance Concrete to Fire Conditions: Review of Thermal Property Data and Measurement Techniques, Report NIST GCR (1999) 99-767.

[16] Oudjene M., Khelifa M., Finite element modelling of wooden structures at large deformations and brittle failure prediction, Materials & Design 30(10) (2009) 4081-4087.

[17] Oudjene M., Khelifa M., Elasto-plastic constitutive law for wood behaviour under compressive loadings, Construction and Building Materials 23(11) (2009) 3359-3366.

[18] Reiterer A., Stanzl-Tschegg S.E., Compressive behaviour of softwood under uniaxial loading at different orientations to the grain, Mechanics of Materials 33(12) (2001) 705-715.

[19] Xu B.H., Bouchaïr A., Taazount M., Vega E.J., Numerical and experimental analyses of multiple-dowel steel-to-timber joints in tension perpendicular to grain, Engineering Structures 31 (2009) 2357-2367.

[20] Racher P., Laplanche K., Dhima D., Bouchaïr A., Thermo-mechanical analysis of the fire performance of dowelled timber connection, Engineering Structures 32 (2010) 1148-1157.

[21] Hill R., A theory of yielding and plastic flow of anisotropic metals, Proceedings of the Royal Society of London (1948) 281.

[22] Hoffman O., The brittle strength of orthotropic materials, Journal of Composite Materials 1 (1967) 200-206.

[23] Abaqus, Theory Manual, Version 6.14, Providence, RI : Dassault Systèmes Simulia Corp (2016).

[24] Dahlquist G., Bjork A., Numerical Methods, Prentice-Hall, Englewoods (1974).

[25] Gear C. W., Numerical Initial Value Problems in Ordinary Differential Equations, Prentice-Hall, Englewoods (1993).

[26] Hugues T. J. R., Taylor R. L., Unconditionally stable algorithms for quasistatic elastoviscoplasticity finite element analysis, Computers and Structures 4 (1978) 169-173.

[27] Freed A. D., Walker K. P., Exponential Integration algorithms Applied to Viscoplasticity, 3rd International Conference on Computational Plasticity, Barcelona (1992) 1757-1768.

[28] Khelifa M., Oudjene M., Khennane A., Fracture in sheet metal forming: effect of ductile damage evolution, Computers & Structures 85 (2007) 205-212.

[29] Khelifa M., Oudjene M., Numerical damage prediction in deep-drawing of sheet metals, Journal of Materials Processing Technology 200 (2008) 71-76.

Chapter 3

Experimental characterization and kinetic analysis of wood pyrolysis

3.1. Introduction 78
3.2 Experimental characterization of the thermophysical properties of the densified Spruce wood 79
3.2.1 Thermal conductivity λ at room temperature 79
3.2.2 Specific heat 82
3.3 Experimental characterization of the kinetic parameters of the densified Spruce wood ... 84
3.3.1 Thermogravimetric tests 84
3.3.2 Thermogravimetric analysis 90
3.4 Cone calorimeter test 98
3.4.1 Samples and cone calorimeter tests 98
3.4.2 Experimental set-up 99
3.4.3 Results 100
3.5 Conclusion 106
Bibliography of chapter 3 107

3.1. Introduction

Several experimental campaigns have been carried out in this project. The general objective is to better understand densified wood and, on the other hand, is to measure the necessary properties of the compressed wood for modeling its thermomechanical behavior.

Two types of experimental campaigns have been implemented: characterization tests of thermal properties and tests allowing to validate digital models of heat transfer.

The material characterized in this study is densified Spruce wood used in the manufacture of fire-resistant wooden dowels. This material was supplied by a plan of Europe and was tested in the three types of samples: the powder sample, the cubic sample of 5x5x5 mm^3, and the panel sample of 102x102x19 mm^3.

The measurement campaign is to determine the thermophysical properties and kinetic parameters required to simulate the heat transfer of densified wood. The thermophysical properties measured are thermal conductivity, the specific heat, and the density of densified wood. The kinetic parameters determined include pre-exponential factor Ai [s^{-1}] and reaction active energy Ei [J/mol].

The validation test for the heat transfer of densified wood carried out during this project consists of a cone calorimeter test. It will feed a base of data for the validation of the numerical models developed in chapter 2.

3.2 Experimental characterization of the thermophysical properties of the densified Spruce wood

The thermal behavior of the compressed wood depends on the constituents, the morphology, and the microstructure in the material. Unlike other wood materials, the material studied here contains a small proportion of air voids, thus reducing the thermal insulation properties of the densified wood when compared to virgin wood. However, it still exhibits excellent insulation properties due to the thermal conductivity of this material is less than 0.2 W/(m.K). The presence of moisture in the material influences the value of thermal conductivity. Hence, the thermal behavior of the densified wood will be described in this section using experimental data obtained on the variations of the density, thermal conductivity, and specific heat at elevated temperatures.

3.2.1 Thermal conductivity λ at room temperature

Thermal conductivity is one of the properties to assess the insulation capacity of building materials. The intrinsic characteristics of the material's composition, morphology, and microstructure determine its thermal conductivity.

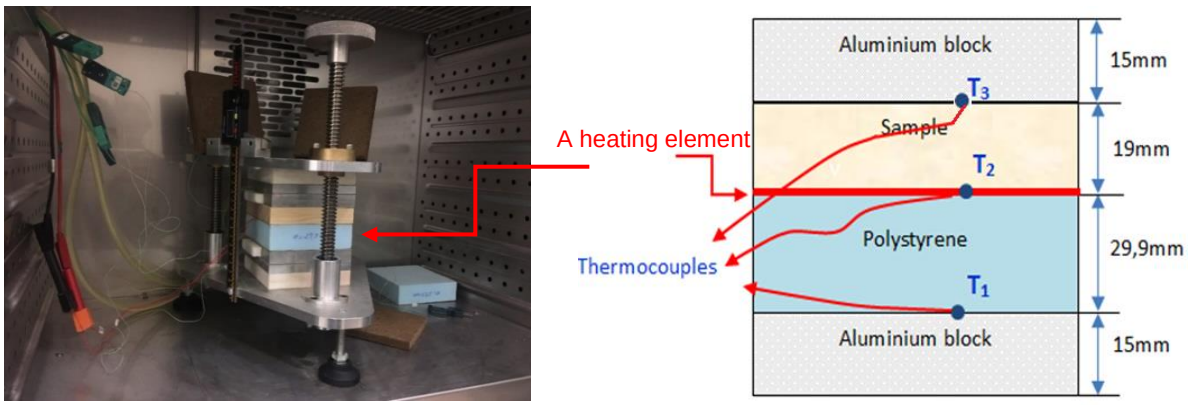

FIGURE 3.1 - Photograph and schematic of the hot plate method.

The hot plate method [1] was used to measure the thermal conductivity of the material. Figure 3.1 shows the experimental setup for the determination of the thermal conductivity in an environmental chamber. The temperature in the chamber is about 23 °C. The samples with the dimension of 102x102x19 mm^3 (Figure 3.1) made from the linen panel and densification panel of Spruce were inserted between two aluminum blocks. At the interface between the sample and the polystyrene insulation, there is a heating element with the electrical resistance R. The insulation layer is used to ensure that all heat flux is transmitted through the sample.

The temperature values T_1, T_2, and T_3, are recorded by three thermocouples, which are placed at different positions. In this case, the conduction is the only heat transfer in the test.

The heat flux between the two faces of the sample is created through the imposition of the thermal gradient by the heating element. After the system stabilizes and establishes steady-state conditions (about 20 min), temperature measurement is conducted. Figure 3.2 shows the process of heat transfer according to the one-dimensional type flows with the temperature T varying linearly in the x-direction. These flow lines are perpendicular to the surface of the sample.

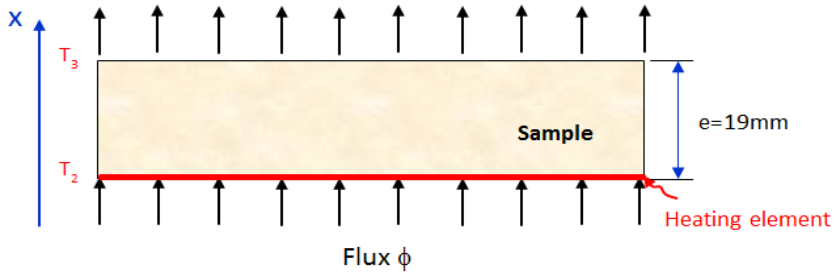

FIGURE 3.2 - Steady-state conditions through the sample.

The rate of the heat flux ϕ is written by using Fourier's law of heat conduction as follow:

$$d\emptyset = -\lambda \frac{dT}{dx} A \tag{3.1}$$

where A is the sample area exposed to the flux and $\frac{dT}{dx}$ is the gradient of temperature.

If the losses across the lateral sidewalls are assumed to be negligible, the entire heat flux will be transmitted from the lower face to the upper face. Integrating equation (2.1) and taking into account the boundary conditions yields:

$$\emptyset = \frac{\lambda A}{e}(T_3 - T_2) \tag{3.2}$$

where T_2 and T_3 are the surface temperatures of the sample, and e = 19 mm is the thickness of the sample.

The heat flux passing through the sample and the one absorbed by the polystyrene insulation layer is combined as [2-3]:

$$\emptyset = \frac{\lambda A}{e}(T_3 - T_2) + \frac{\lambda_0 A}{e_0}(T_2 - T_1) \quad (3.3)$$

where T_1, T_2, and T_3 are the measured temperatures by the thermocouples as depicted in Figure 2.1. λ_0 = 0.0302 W/(m.K) and e_0 = 29,9 mm are the thermal conductivity and the thickness of the polystyrene layer respectively.

The uniform heat flux is created by acting as a source of heat of the heating element. This heat flux is applied to the surface of the sample tested through the imposition by modifying the electrical voltage U [V]. The value of the voltage U [V] and the electrical resistance R [Ω] are measured by a console and an electronic ohmmeter respectively. Thus, evaluating the amount of heat (Joule effect) in the system is possible. The heat flux passing through the sample and insulation is assumed equivalent to the electrical heat flux, $\frac{U^2}{R}$; that is [2]:

$$\emptyset = \frac{U^2}{R} = -\frac{\lambda A}{e}(T_3 - T_2) + \frac{\lambda_0 A}{e_0}(T_2 - T_1) \quad (3.4)$$

The previous equation is rearranged to yield the conductivity of the sample, λ:

$$\lambda = \frac{e}{(T_2 - T_3)}\left[\frac{U^2}{R.A} - \frac{\lambda_0}{e_0}(T_2 - T_1)\right] \quad (3.5)$$

Substituting $U = R \times I$, equation (2.5) becomes:

$$\lambda = \frac{e}{(T_2 - T_3)}\left[\frac{R.I^2}{A} - \frac{\lambda_0}{e_0}(T_2 - T_1)\right] \quad (3.6)$$

with the electrical resistance and the intensity of the current in Amperes are known and respectively equal to $R = 39.8\,\Omega$ and $I = 0.16\,A$.

Table 3.1. Thermal conductivity for virgin Spruce.

Samples	Humidity (%)	Density (kg/m^3)	Conductivity (W/(m.K))
1	7,5	442,5	0,097
2		472,5	0,0979
3		435,4	0,0956
4		445,5	0,0948
Mean		448,9	0,0963
C.o.V		3,13%	0,01%

Table 3.2. Thermal conductivity for 68% compressed Spruce.

Samples	Humidity (%)	Density (kg/m^3)	Conductivity (W/(m.K))
1	8,5	1201	0,184
2		1194	0,171
3		1211	0,172
4		1232	0,176
Mean		1210	0,175
C.o.V		1,37%	0,03%

The results for each type of wood (mean values of 4 tests) are shown in Tables 3.1-3.2. The average conductivity value λ = 0.096 W/(m.K) for virgin Spruce and λ = 0.175 W/(m.K) for densified Spruce.

The variations in the results of thermal conductivity coefficients are very small. This demonstrates that the results of the experiment for the determination of the thermal conductivity coefficients are very reliable. It can be seen that the density of densified Spruce is nearly three times greater than virgin Spruce while the thermal conductivity of densified Spruce is nearly twice greater than virgin Spruce. The variability of densities is due to the porosity of the wood.

3.2.2 Specific heat

The specific heat capacity is presented in Table 3.3. The measurements were carried out

for both virgin and densified Spruce wood at different temperatures from 20 °C to 60 °C. The results show that there is a small difference between virgin and densified Spruce wood in the value of specific heat.

Table 3.3. Specific heat mean values (J/(kg.K)).

	20 °C	30 °C	40 °C	50 °C	60 °C
Virgin Spruce	1215	1257	1298	1340	1382
68% compressed Spruce	1227	1268	1311	1364	1405

3.3 Experimental characterization of the kinetic parameters of the densified Spruce wood

When wood is heated at elevated temperatures, the thermal-chemical decomposition takes place (conversion of liquid on vapor, wood to char, and gas…). Decomposition kinetics are described by Arrhenius's first-order law. These thermal reactions absorb or release energies, which need to be taken into account in the heat transfer equation.

Therefore, the kinetics parameters are needed to identify to model more accurately the behavior of timber structures under fire.

Note that in this study, we focus only on the pyrolysis reactions. Considering the combustion of combustible gases released in the pyrolysis phase needs to determine the calorific value of wood. Such tests will be carried out in the next step.

3.3.1 Thermogravimetric tests

Thermogravimetric tests (ATG) carry out measuring the variation over time of the mass of a small sample subjected to a rise of temperature. This method allows to quantify the mass loss and determine the temperature for the thermal degradation of a compound.

An ATG test allows studying the rate of mass loss during a thermal transfer, to obtain the necessary kinetic constants of Arrhenius' law for chemical reactions of the thermal degradation mechanisms of wood components by reverse analysis. These constant kinetic parameters can then be used in the models of simulation of wood pyrolysis.

3.3.1.1 Test pieces and materials

To assess the impact of the densification process in the thermogravimetric test, virgin and densified wood chips are subjected to different temperature values. The samples of the thermogravimetric test are generally very small in order to minimize the thermal gradients within the material during the test. The mass of these samples varies from milligrams to a few grams according to the authors [4]. The shape of the samples also varied from powder to small wooden cubes. In our case, two types of samples including powder and cubic samples are used to study the effect of sample shape on the mass loss of wood when exposed to high temperatures. A presentation of the test pieces used for the mass loss tests is presented in Figure 3.3.

(a) Powder sample

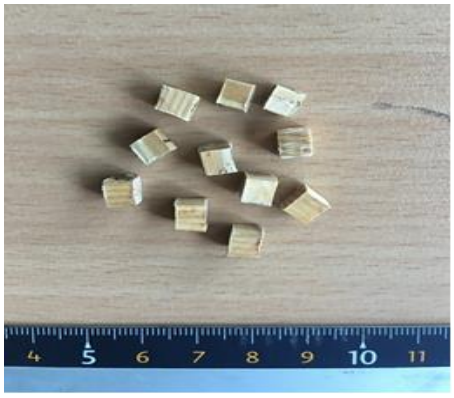

(b) Cubic sample

FIGURE 3.3 - Test specimens for thermogravimetric test.

Local spruce wood is used as feedstock. The densified wood chips are compressed 48 hours before cutting to particles. The dimensions of the cubic samples are 5x5x5 mm^3, which is equivalent to a mass ranging from 50 mg to 150 mg. Small pieces of virgin and densified wood were crushed by a robot and the obtained powder was sieved through two sieves. The maximum thickness of the sieved powder was about 4 mm. The dimension of the wood powder must be small so that the temperature is uniformly distributed over the entire surface of the sample. All testing samples are dried at 105 °C to obtain a moisture content of less than 4%.

3.3.1.2 Apparatus description

A thermobalance apparatus (Figure 3.4) is used for the thermogravimetric analysis. This apparatus records the different data concerning the evolution of the temperature and the mass loss. The thermobalance consists of three main parts:

- A controller that allows the transfer of the experimental data (mass, temperature) to a computer that records and treats them by Setsys software (e.g. DTG).

- An oven composed of electrical resistance in graphite and a double envelope cooled by circulation of water to control the heat flow and then the temperature. A PDI regulator allows to vary the rate of temperature change between 1 and 50 $K.min^{-1}$.

- A micro-balance, based on a compensation permitting to measure the mass of the sample placed in a basket, continuously balanced and thus maintained at a fixed position

during the experiment. This allows avoiding eventual intra-particle temperature gradients in isothermal conditions in the oven. The oven temperature is adjustable with a precision of 0.1 K and can reach a maximum of 1473 K. In order to establish an inert atmosphere during all experiments, a controlled argon flow fixed to 7.2l h^{-1} at 273 K and 1 atm, sweeps the measurement cell that is purged for 20 min before starting the heating program.

FIGURE 3.4 - Experimental apparatus for thermogravimetric test.

3.3.1.3 Different heating conditions

Several authors have assumed that the kinetic parameters Ai [1/s] and Ei [J/mol] depend only on the material and the mechanism of thermal degradation [5-9]. Theoretically, these parameters remain constant although the boundary conditions of the thermo-balance tests are different. Inspired by this idea, we perform a set of thermo-balance tests with different conditions. The estimated values of the kinetic parameters must therefore allow the chosen model presented in the previous section to successfully produce the evolution of the mass as a function of time under the different conditions.

The different heating conditions are grouped in Figure 3.5. These conditions are in dynamic mode. In order to reproduce the conditions close to a real fire by thermo-gravimetric analysis, the conditions are therefore designed in a temperature range between 600-800 °C at three different high heating rates 30, 40, 50 $K.min^{-1}$ and a real fire curve. A real fire curve is a

temperature curve similar to the Iso fire curve at the lower level of temperature increase. To facilitate communication later, these conditions are numbered as follows:

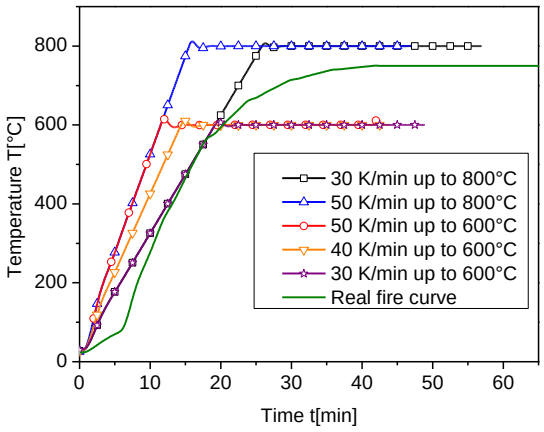

FIGURE 3.5 - Different heating conditions.

- Condition 1: 30 K/min up to 800 °C, then the temperature remains stable for 30 minutes.
- Condition 2: 50 K/min up to 800 °C, then the temperature remains stable for 30 minutes.
- Condition 3: 50 K/min up to 600 °C, then the temperature remains stable for 30 minutes.
- Condition 4: 40 K/min up to 600 °C, then the temperature remains stable for 30 minutes.
- Condition 5: 30 K/min up to 600 °C, then the temperature remains stable for 30 minutes.
- Condition 6: A real fire curve.

3.3.1.4 Experimental results

Figure 3.6 compares the evolution of the m/m_0 ratio and dm/dt of virgin and densified wood powders in condition 6.

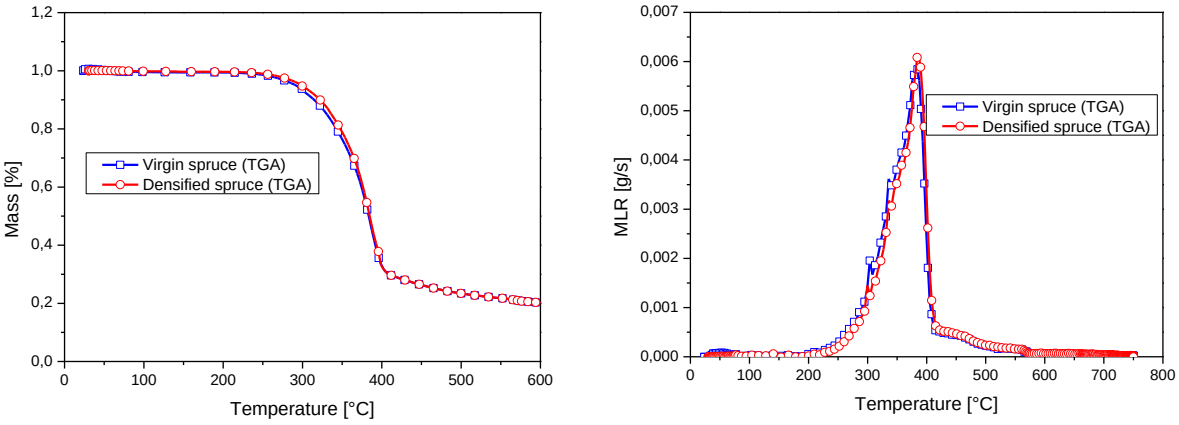

(a) m/m_0 (b) dm/dt

FIGURE 3.6 - Comparison in the mass and the time derivative evolution of virgin and densified wood powder in condition 6.

It can be seen that the results obtained for densified and normal wood powder are practically the same. Similar observations were found for the remaining conditions. This is due to the TGA tests performed on small particles where the effect of conduction is not considerable. A comparison between the virgin and densified Spruce wood powder in mass-loss rate for the various heating rates is shown in Figure 3.7.

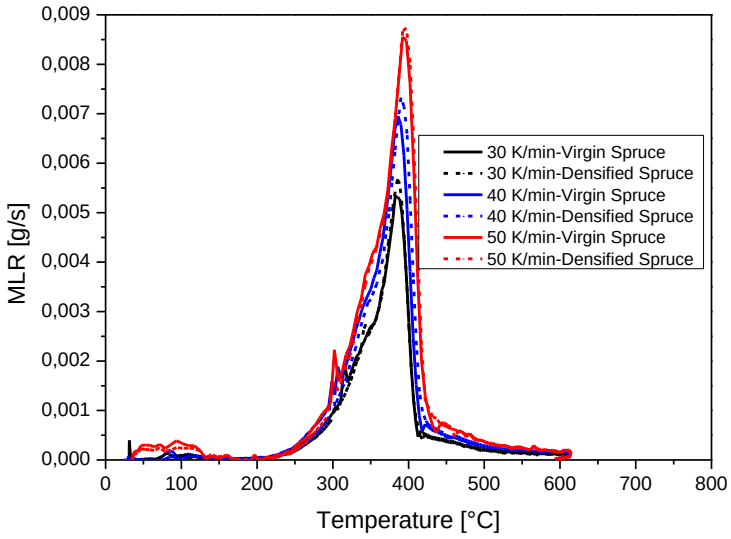

FIGURE 3.7 - Comparison of DTG curves between virgin and densified wood powder at various heating rates.

Figure 3.8 shows the comparison in the evolution of mass and mass loss rate between virgin and densified cubic wood in condition 6.

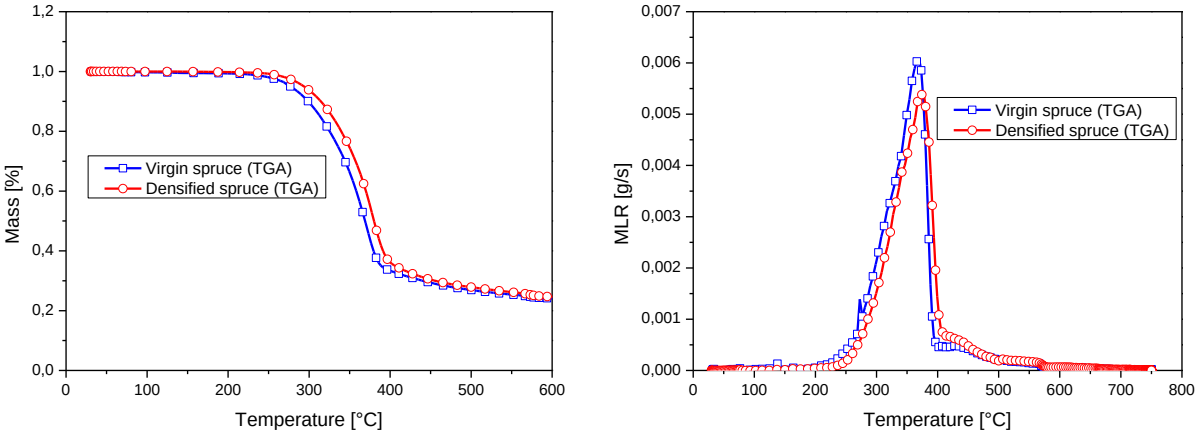

(a) m/m_0 (b) dm/dt

FIGURE 3.8 - Comparison in the mass and the time derivative evolution of virgin and densified cubic wood in condition 6.

Unlike the results of wood powder, densified cubic wood exhibits slower mass loss than virgin cubic wood. This difference is probably due to the shape of the cubic sample which makes it not possible to ignore the transfer of heat in the cubic wood. A comparison between the virgin and densified cubic wood in mass-loss rate for the various heating rates is shown in Figure 3.9.

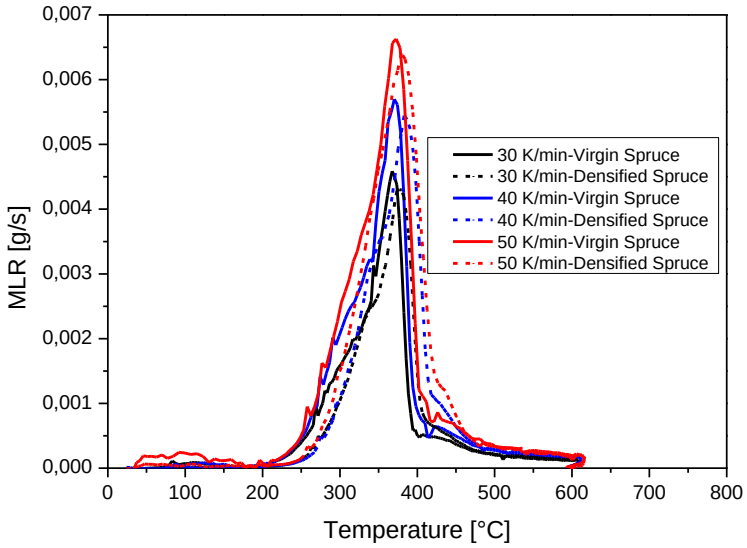

FIGURE 3.9 - Comparison of DTG curves between virgin and densified cubic wood at various heating rates.

The mass evolutions of densified wood powder, under an inert atmosphere, as a function of the temperature are illustrated in Figure 3.10, for the six conditions studied.

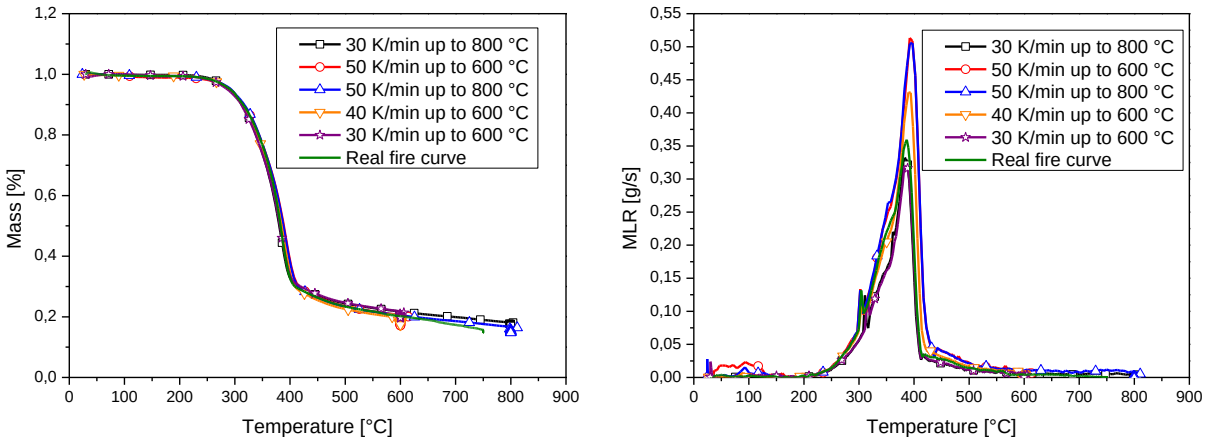

(a) m/m_0 (b) dm/dt

FIGURE 3.10 - (a) The mass and (b) the time derivative evolution of the densified wood powder.

The curves of mass evolution as a function of temperature for densified wood powder, given in Figure 3.10a, show the following changes, whatever the heating rate considered:

- From the ambient temperature of 20 °C to 260 °C, around 7% of the initial mass is lost, corresponding to the wood particles dehydration.

- Between 260 °C and 340 °C, a mass loss of around 41% is recorded.

- Between 340 °C and 400 °C, a mass loss is about 70% is observed.

- A quite slow mass loss (of about 15%) is observed between 400 °C and the end of the test, with a final quantity of residue at the end of the tests corresponding to about 15% of the initial sample mass.

- Qualitatively, the evolution of mass loss curves is similar for all samples (virgin and densified woods), and the three heating rates.

Figure 3.10b shows the evolution of the mass-loss rate (MLR) curves as a function of temperature for different heating rates under an inert atmosphere. From the MLR curves, we can note the following remarks:

- The MLR increases with an increase in the heating rate.

- The thermal degradation starts at the temperature T = 200 °C.

- The maximum intensity of the MLR is obtained at T = 400 °C. Beyond this limit, the MLR decreases strongly until 500 °C as a function of the heating rate.

- The same remarks are observed by many authors (Fateh et al. 2013 [10] and Broström et al. 2012 [11]).

3.3.2 Thermogravimetric analysis

The kinetic analysis of the resulting curves is performed to characterize multi-step reaction mechanisms and to calculate the kinetic parameters of the pyrolysis models presented by N. Grioui (2006) [5] and D. Blasi (2012) [11].

The main assumptions considered in this study for the pyrolysis models of dry wood particles are listed as follows (Shen et al. 2007 [6] and Thi et al. 2016 [9]):

- The heat transfer of wood particles is considered to be one-dimensional.

- Heat and mass transfer of the gases inside the wood particle is neglected.

- All chemical reactions for pyrolysis of dry wood are described by the first-order Arrhenius Law.

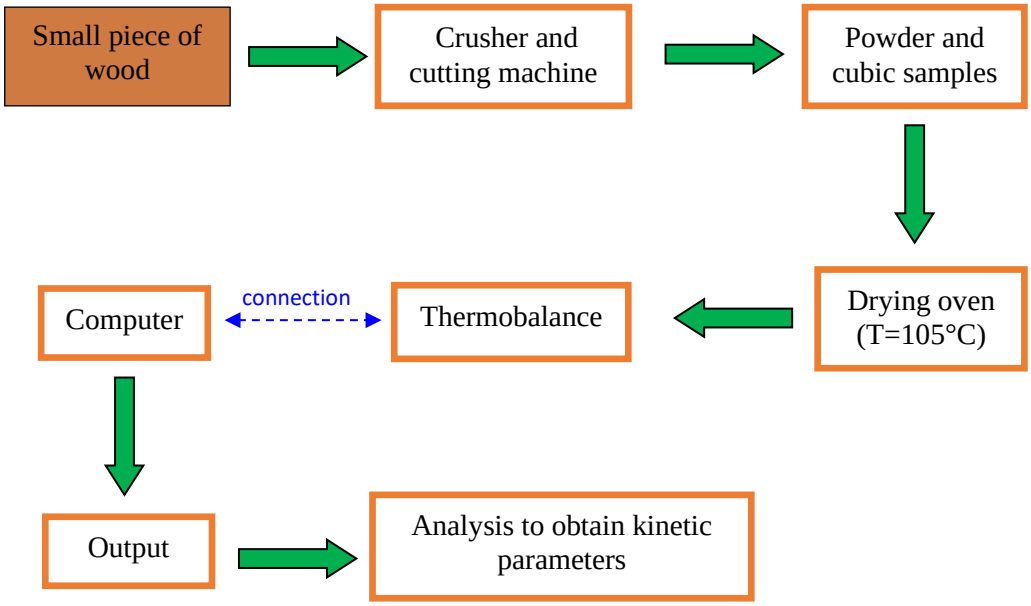

FIGURE 3.11 - Testing diagram for thermogravimetric analysis.

A general diagram for the determination process of kinetic parameters of wood is shown in Figure 3.11.

3.3.2.1 Optimization method

The first step of the modeling process consists of simply looking at data graphically and trying to recognize trends. In this study, we will limit the most standard method of curve fitting and parameter estimation, least squares regression.

The idea to use the least-squares method is to sum these vertical distances and minimize the total error. In practice, we square the errors to keep them positive and to avoid possible difficulty with differentiation (due to the absolute values), which will be required for minimization.

The total least squares error function for mass loss and mass loss (MLR) rate are respectively:

$$\delta_i^m = \frac{\Delta t}{t_{final} - t_0} \sqrt{\sum_{t_0}^{t_{final}} \left(m_{num}(t) - m_{exp}(t)\right)^2} \tag{3.7}$$

$$\delta_i^{dm} = \frac{\Delta t}{t_{final} - t_0} \sqrt{\sum_{t_0}^{t_{final}} \left(\frac{dm_{num}(t)}{dt} - \frac{dm_{exp}(t)}{dt} \right)^2} \quad (3.8)$$

3.3.2.2 Characterization of the kinetic parameters

The idea to use the least-squares method is to sum these vertical distances and minimize the total error. In practice, we square the errors to keep them positive and to avoid possible difficulty with differentiation (due to the absolute values), which will be required for minimization.

- Firstly, we give estimated values of the pre-exponential factors Ai, the activation energies Ei, and the stoichiometric coefficients v_i which are determined by N. Grioui (2006) and D. Blasi (2012). The reaction orders n_i are taken as 1.

- These estimated parameters will then be used to determine the mass and its time derivative at time t using: 1st order Arrhenius law; finite difference method to solve differential equations of mass conservation.

- From the mass and its derivative by the numerical analysis, we will estimate the error by comparing the numerical solutions and the experimental observations. The optimization of these errors by using the "solver" of the Excel software, will obtain the kinetic parameters which allow describing at best experimental results.

The errors of the optimization are depicted in Tables 3.4 - 3.5.

Table 3.4. Errors on m and dm/dt (N. Grioui - 2006).

Conditions	δ_i^m	δ_i^{dm}
Condition 1	$4{,}99\times10^{-4}$	$4{,}99\times10^{-6}$
Condition 2	$7{,}12\times10^{-4}$	$6{,}68\times10^{-6}$
Condition 3	$4{,}08\times10^{-4}$	$8{,}5\times10^{-6}$
Condition 4	$6{,}75\times10^{-4}$	$7{,}96\times10^{-6}$
Condition 5	$5{,}29\times10^{-4}$	$5{,}54\times10^{-6}$
Condition 6	$2{,}87\times10^{-4}$	$5{,}63\times10^{-6}$
Total	$3{,}11\times10^{-3}$	$3{,}93\times10^{-5}$

Table 3.5. Errors on m and dm/dt (D. Blasi - 2012).

Conditions	δ_i^m	δ_i^{dm}
Condition 1	$4{,}1\times10^{-4}$	$4{,}83\times10^{-6}$
Condition 2	$3{,}51\times10^{-4}$	$1{,}1\times10^{-5}$
Condition 3	$3{,}93\times10^{-4}$	$1{,}36\times10^{-5}$
Condition 4	$1{,}76\times10^{-4}$	$6{,}01\times10^{-6}$
Condition 5	$1{,}87\times10^{-4}$	$5{,}7\times10^{-6}$
Condition 6	$3{,}3\times10^{-4}$	$3{,}8\times10^{-6}$
Total	$1{,}847\times10^{-3}$	$4{,}494\times10^{-5}$

The total error δ_{total} is the sum of the errors of each condition δ_i:

The total error on the mass:

$$\delta_{total}^{m} = \sum_{i=1}^{N} \delta_i^m \tag{3.9}$$

The total error on the time derivative of the mass:

$$\delta_{total}^{m} = \sum_{i=1}^{N} \delta_i^m \tag{3.10}$$

With the errors of each condition, δ_i are determined according to equations 2.7 - 2.8 (least-squares method).

N = 6 is the total number of conditions. t_0 and t_{final} (s) are the initial and final times of the thermogravimetric test. $\Delta t = 0{,}1$ (min) is the increment of time in numerical calculations.

Using the finite difference method requires small increments of time to ensure the accuracy of the solution. A time step $\Delta t = 0{,}1$ min was chosen for this study. A disadvantage will be encountered when using this method. This is because the optimization of the error value in using the solver tool in Excel is dependent on the initial values of the kinetic parameters. In other words, they must not be too far from the solution to ensure digital convergence. On the other hand, the values after optimization do not always represent the physics of the thermo-physical reactions but they are estimated so that the error between the

numerical results and those of the experiment is the smallest. To remedy this, we must start from initial values close to reality, which is not always obvious and it requires experience.

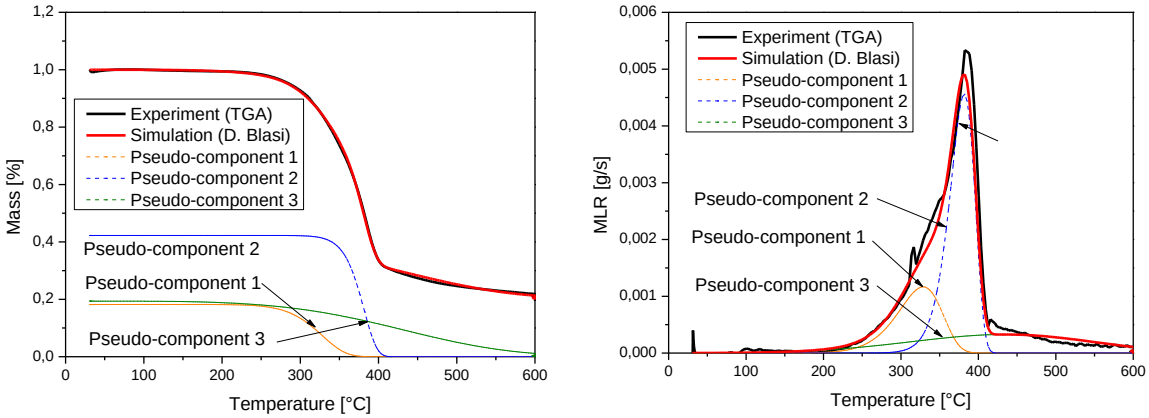

(a) m/m_0 (b) dm/dt

FIGURE 3.12 - (a) The mass and (b) the time derivative evolution of densified wood powder in condition 5.

The results of a study ATG and simulation (D. Blasi) on a densified wood for condition 5 are presented in Figure 3.12. We observe three successive peaks of the mass loss rate corresponding to three pseudo-components of wood. Here we propose a comparison of the obtained values of temperature for each peak with those available in the literature. Overall the comparisons with literature results can be considered good. Indeed, the typical temperature is of the order of 210–320 °C for hemicellulose decomposition [12], against a value of about 320 °C of peak 1. Temperature for cellulose decomposition [12] is reported to vary between 300 and 375 °C against a value of about 375 °C of peak 2. For the third peak, the temperature is of the order of 420 °C which is located in the ranges of the values available in the literature between 350 and 450 °C corresponding to lignin decomposition [13].

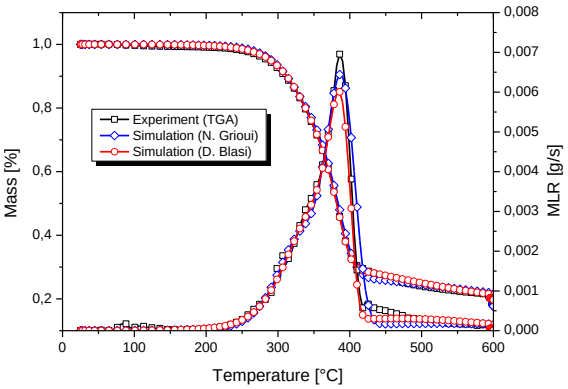

(a) Heating rate 40 K/min

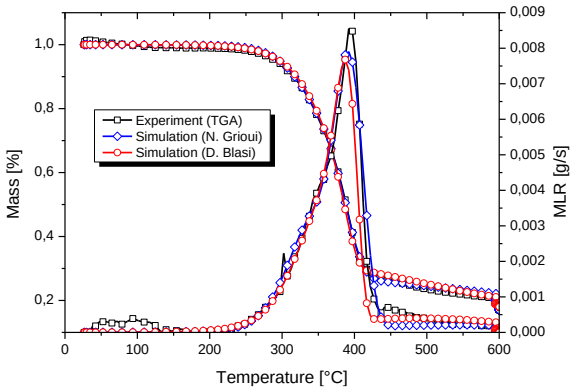

(b) Heating rate 50 K/min

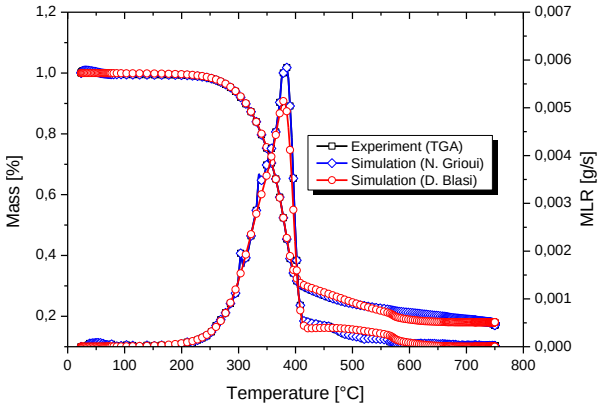

(c) Real fire curve

FIGURE 3.13 - Comparison of the measured and calculated MLR for three different conditions.

Figure 3.13 shows the comparison between the measured values given by the TGA and the predicted values of the mass-loss rate (MLR) for three different conditions (40, 50 K/min, and real fire curve). Qualitatively, the results of the simulations are in good agreement with those of the tests. The kinetic model can display well the peak, the beginning, and the end of the MLR curves. We can then conclude that the pyrolysis models are validated, and the kinetic parameters are correctly identified.

Table 3.6. Estimated kinematic constants (after optimization) (N. Grioui - 2006).

Reactions	E_i [kJ/mol]	A_i [1/s]	v_i
(1)	113,74	$2{,}4\times10^{8}$	0,174
(2)	24,23	$1{,}15\times10^{-1}$	0,216
(3)	172,46	$1{,}47\times10^{12}$	0,61
(4)	108	$3{,}28\times10^{3}$	-

Table 3.7. Estimated kinematic constants (after optimization) (D. Blasi - 2012).

Reactions	E_i [kJ/mol]	A_i [1/s]	v_i
(1)	102	$1{,}15\times10^{7}$	0,25
(2)	220,9	$1{,}16\times10^{16}$	0,37
(3)	30	$5{,}85\times10^{-1}$	0,2

The optimized kinetic parameters, used in the simulations, are summarized in Tables 3.6-3.7.

3.3.2.3 Validation model

Table 3.8 compares the estimated values of activation energies for pyrolysis reactions, used in simulations, with those of the values published in the literature. For more information, readers can see the work presented by Grioui et al. (2006). Two estimated values of *E*i of reactions 1 and 4 are located in the ranges of the values available in Table 3.8. For the third reaction, the activation energy is of the order of 170 kJ/mol which is relatively high compared to those available in the literature [14–17]. The higher value estimated here can be due to the difficulty, for isothermal conditions, to separate the decomposition of the pseudo component A_3 from that of other components (A_2, particularly). The activation energy of 24,23 kJ/mol is obtained for the second reaction, corresponding to the decomposition of the second pseudo-component A_2. The lower value estimated here compared to those in the literature (80–108 kJ/mol) [17, 18] can be explained by the wider range of heating rates considered here or the different geographical origin, age, and specific part of the tree [19].

Table 3.8. Activation energies for pyrolysis reactions (Grioui et al. 2006).

Reactions	Limit of E_i [kJ/mol]	E_i [kJ/mol] (N. Grioui)	Estimated value E_i [kJ/mol]
(1)	80 to 140	105,89	113,74
(2)	73 to 121	106,78	24,23
(3)	112 to 133	169,56	172,46
(4)	80 to 108	51,04	108

A comparison is made in Table 3.9 between the results obtained from the three-step mechanism of the model of D. Blasi (2012) and the current state of the art on biomass

devolatilization in an inert atmosphere, which uses differential data and, in some cases, multiple curves for parameter estimation [20].

Table 3.9. Activation energies for pyrolysis reactions (Blasi et al. 2012).

Reactions	Limit of E_i [kJ/mol]	E_i [kJ/mol] (M. Broström)	Estimated value E_i [kJ/mol]
(1)	100 to 122	100,6	102
(2)	195 to 240	213,1	220,9
(3)	35 to 65	38,6	30

It is found that the three-step mechanism of the model of D. Blasi (2012) produces good predictions of the devolatilization process with parameters (Table 3.9) that are very close to those previously estimated. The activation energies of the first two reactions, 102 and 221 kJ/mol, are in the range of those reported [20] for the decomposition of hemicellulose (100–122 kJ/mol) and cellulose (195–240 kJ/mol) components in biomass. The activation energy estimated for the third reaction step, 30 kJ/mol, is slightly lower than the range of values usually estimated for the decomposition of lignin components (35–65 kJ/mol, see Ref. [20]). This difference can be plausibly attributed to the wider range of heating rates considered here and probably to the different geographical origin, age, and specific part of the tree [19]. Therefore it is possible to say that the kinetic parameters are correctly estimated in this present work.

3.4 Cone calorimeter test

The cone calorimeter test is one of the normative tests for the characterization of the thermodynamic properties of materials used in building construction, especially with wood-based materials. This work's aim is to obtain a wider knowledge of the degradation of densified wood and comparisons against virgin wood in terms of temperature evolution, mass loss rate, charring rate, and fire performance through the ignition time and extinguishment time. In collaboration with the LEMTA laboratory in Nancy, we make experiments on their device. To suddenly remove the external heat flux for studying extinguishment and ignition of samples, the sliding cone is used. Samples were submitted to two heat fluxes, 20 and 75 kW/m^2, corresponds to the absence and presence of the flame in the test [21].

3.4.1 Samples and cone calorimeter tests

(a) Virgin Spruce (b) Densified Spruce

FIGURE 3.14 - Sample exposed to the cone: (a) Virgin Spruce and (b) Densified Spruce.

The samples made from the linen panel and densification panel of Spruce were selected for the tests. The dimension of the samples was 102×102×19 mm^3. The moisture content for normal and compressed wooden plates was 6,7% and 6,0%, corresponding to an average density of 417,6 and 1114,7 kg/m^3 respectively. The top side of the sample was free for submitting to the radiative flux while the other sides were wrapped with two layers of aluminum foil according to the standard ISO 5660-1[22]. The distance between the sliding cone and the sample was 25 mm. The samples were exposed vertically to external constant heat fluxes of 20 and 75 kW/m^2. The radiative heat flux emitted by the cone was controlled before each test thanks to a Schmidt-Boelter fluxmeter (by Medtherm). The cone emission could be assumed to be close to those of a blackbody [23].

FIGURE 3.15 - The cone calorimeter.

3.4.2 Experimental set-up

Surface or ignition temperatures are usually measured using thermocouples. However, these measurements are punctual and could be false due to the heat sink along the thermocouple wire, the cone radiation, or the bad contact between the thermocouple and the sample. This contact seems all the more difficult for the wood that is degrading, producing char and cracks [24]. In this work, exposed surface temperatures were measured thanks to a multispectral infrared camera (Orion SC7000 by FLIR). This non-intrusive measurement allows studying the temperature field evolution on a large surface. The contact problem is also eliminated. In fire safety, this measurement is increasingly used [25, 26], especially owing to its accuracy. During infrared measurements, the flame between the infrared camera and the sample surface may lead to a mismeasurement of the temperature. Some studies have shown that the emission by flames is observed to be predominant in specific wavelengths where major combustion gases (CO, CO2, and H2O) can emit [27]. Outside these bands, only soot can emit, and since the optical thickness of flames involved in the cone calorimeter experiments is very small, the flame can be considered almost transparent in these specific wavelengths. For the present study, the selected wavelength filter for the IR camera is 3.9 μm (2564 cm^{-1}), which is outside the emission bands of combustion gases and corresponds to a wavelength where wood emissivity remains almost constant around 0.9 during the degradation [22]. This type of measurement was already successfully performed by LEMTA's team on other materials. More details are presented in [28].

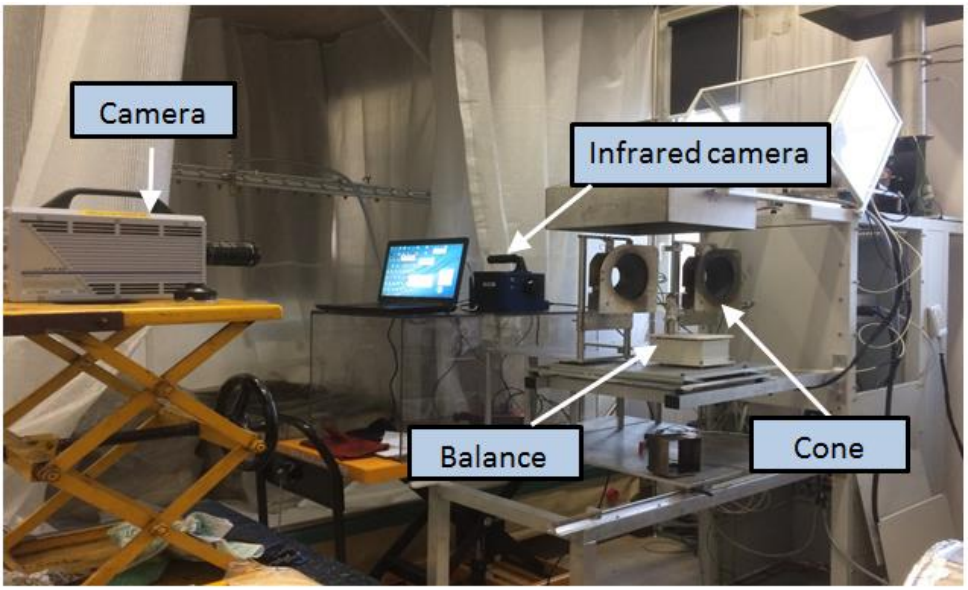

FIGURE 3.16 - Experimental set-up for cone calorimeter test.

A precision scale was used to record the mass loss during the test. A thermocouple is placed at the unexposed side of the sample to measure the temperature at the end of the sample. Temperatures are recorded every second via a USB TC-08 PICO type acquisition center. The charring rates of panels were also investigated after finishing the cone calorimeter test.

3.4.3 Results

Samples were submitted to two external heat fluxes (20 and 75 $kW.m^{-2}$). Flame ignition was observed only for a test at 75 $kW.m^{-2}$. For the test at 20 $kW.m^{-2}$, only smoldering combustion was observed. In the following, we will present the first results regarding smoldering combustion only. Then we will focus on the ignition/extinguishment studies as well as the evolution of temperatures at the unexposed surface and the charring depth of the sample after the tests.

3.4.3.1 Study of the smoldering combustion (no flame)

After the 1200 s of exposure time, the cone was slid for tests with an external heat flux of 20 kW/m^2. The ML and evolution of surface temperature measures by the balance and the IR camera were shown in Figure 3.17. In this test, about 400 °C there is an increase of the temperature corresponding to the smoldering combustion phenomenon (no flame appeared). An additional amount of released energy was created due to the beginning of the smoldering combustion of the char. The lower the density is (virgin spruce compared to densified spruce),

the more the transition between the pyrolysis without char combustion and pyrolysis accompanied by smoldering combustion is pronounced. At 600 °C there is a plateau of the surface temperature. This step is reached at 800 and 1000 s for virgin and densified spruce respectively.

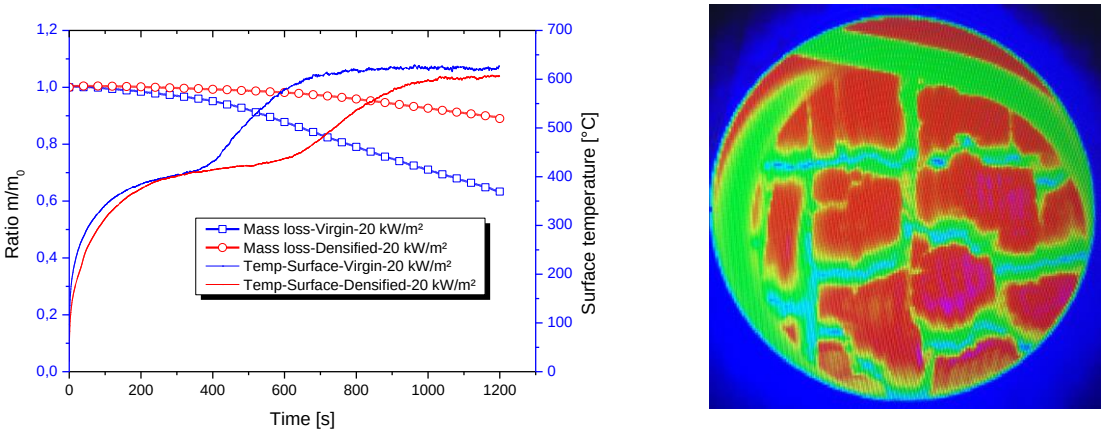

FIGURE 3.17 - Mass loss (ML) and surface temperature for tests without ignition.

Differences between mass loss curves obtained for virgin and densified Spruce are very large. A quite slow mass loss of densified Spruce is observed with a final quantity of residue at the end of the tests corresponding to about 15% of the initial sample mass. On the contrary, mass loss of virgin Spruce is shown at a faster speed, around 41% of the initial mass is lost, corresponding to the plateau of the surface temperature.

3.4.3.2 Study of ignition and extinguishment

To assess the fire performance of both virgin and densified spruce wood when the flame appears, a higher radiative heat flux of 75 kW/m^2 was also carried out. The ML and evolutions of the surface temperature of samples in these tests were depicted in Figure 3.18. In these tests, similar overall trends are observed when compared to the tests using an external heat flux of 20 kW/m^2 (without ignition). The drastic increase in the ML and the surface temperature when the ignition occurs is the main difference. The ignition occurs around 14,5 s and 18,5 s for virgin spruce and densified spruce respectively.

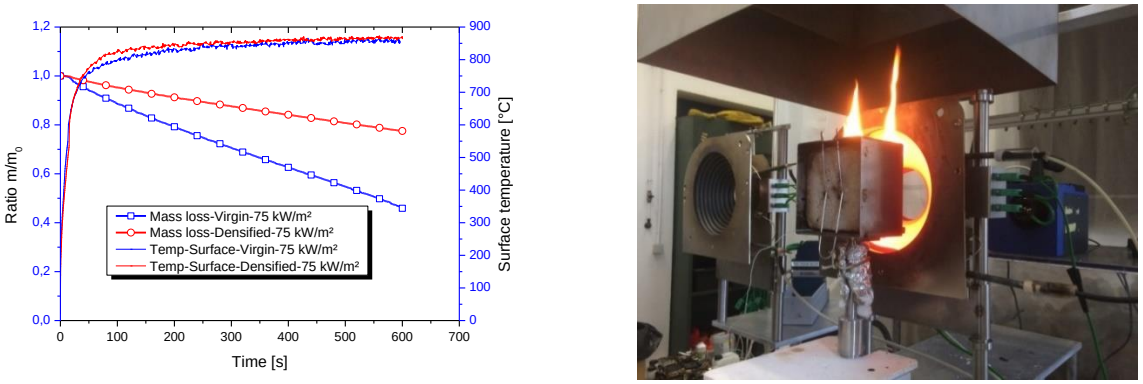

FIGURE 3.18 - MLR and surface temperature for tests with ignition.

The corresponding surface temperatures were estimated to be 850 °C for 75 kW.m^{-2}. For the same heat flux, the surface temperature is about 5% lower when the density increases. The maximum ML is more important for this flux. Generally, density has a significant impact on the ML. At about 600 s, mass losses observed are about 55% and 17% for virgin spruce and densified spruce respectively.

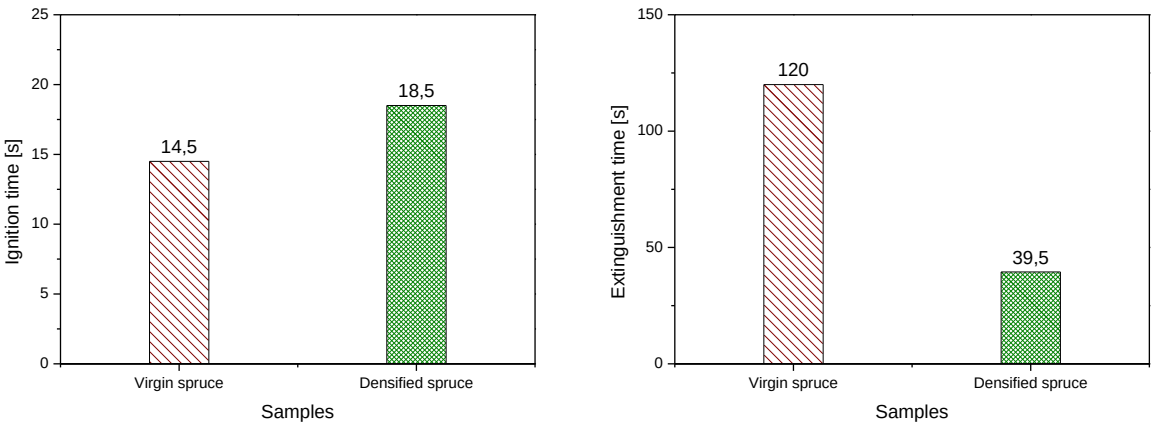

FIGURE 3.19 - Comparison between ignition time and extinguishment time for virgin and densified samples.

The total time in these tests was 600 s. After this time, the cone was slid. The extinguishment of the sample was considered completed when there is no existence of flames on the exposed surface. For the heat flux of 75 kW/m^2 where the ignition occurred, samples auto-extinguished of 120 and 39,5 s for virgin spruce and densified spruce respectively. This can be attributed to the fact that densified wood involves much less O_2 leading to delay of the flame and in turn accelerate its extinguishment.

3.4.3.3 The temperature at the unexposed surface

The temperature at the unexposed surface for both virgin and densified spruce is depicted in Figure 3.20. Due to the influence of high temperature, the connection between the sample and thermocouples K is no longer tight. This leads to inaccuracy in the measurement of thermocouples K (expressed by the recoil of the temperature curve). So the result of temperature at the unexposed surface is only shown in a short time (about 10 and 20 minutes for the heat flux of 75 kW/m^2 and 20 kW/m^2, respectively).

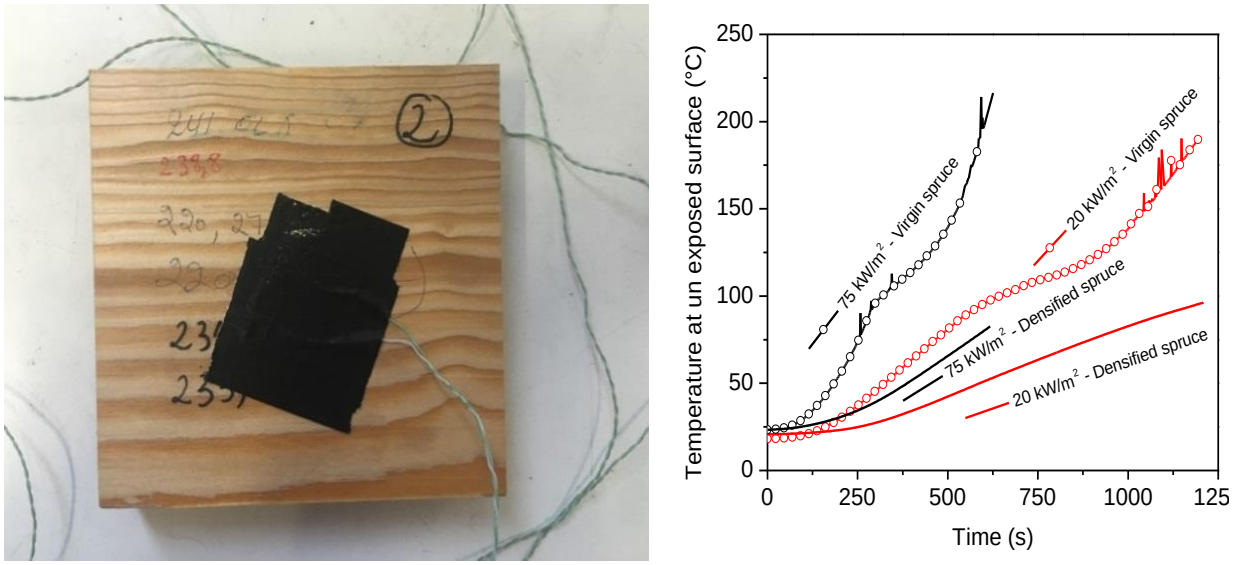

FIGURE 3.20 - Evolution of temperature at unexposed surface.

From Figure 3.20 it can be seen that experimental temperatures in densified Spruce samples gradually increased without any significant perturbation for both heat fluxes of 20 kW/m^2 and 75 kW/m^2. Only a slight slowdown was observed between 600 s and 1000 s of heating of heat flux of 20 kW/m^2, which corresponds to the stabilization of the imposed temperature.

Virgin Spruce samples exhibit different thermal behavior (Figure 3.20). The main difference is that experimental temperatures are clearly slowed down after the first phase of heating similar to the measurements on densified Spruce samples. The time at which the slowing down of temperature starts depends on the heat flux: around 250 s at a heat flux of 75 kW/m^2 and around 600 s at a heat flux of 20 kW/m^2. This slowdown is such that a ‘‘plateau” of temperature stabilization is observed. The plateau is longer for heat flux smaller. This temperature plateau is attributed to the water vaporization in the material. Indeed, at around

100 °C (at normal atmospheric pressure), the energy supplied by the heating is entirely consumed for the transformation of the water phase, i.e. its vaporization. Consequently, the local temperature of the solid does not increase as long as the water is still not entirely vaporized. The transport of water through the material can involve an increase in the effect of temperature gradients. That can explain the reason why the temperature plateau is longer for smaller heat fluxes.

3.4.3.4 Charring depth

The charring depths of panels made of two different wood, virgin Spruce, and densified Spruce were also investigated (Figure 3.21). These charring depths would depend on the variation in the density of wood and exposed heat fluxes.

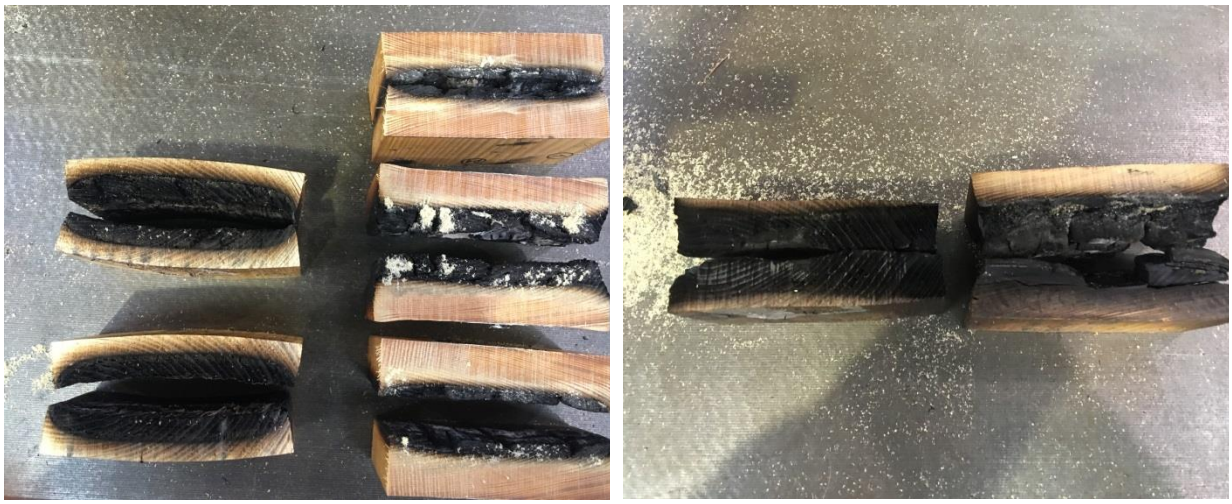

FIGURE 3.21 - The charring depth for virgin and densified spruce after cone calorimeter tests.

The comparison of the maximum of the charring depth at the middle of panels made of different wood species (virgin and densified spruce) under 2 types of heat fluxes (20 kW/m^2 and 75 kW/m^2) were depicted in Tables 3.10-3.11. The results showed that the panel made of densified spruce had a lower charring rate than the panel made of virgin spruce. Timber with low density, such as virgin spruce tended to burn and char at lower temperature or heat flux because of its low decomposition energy and thermal conductivity.

Table 3.10. Charring depth for virgin Spruce.

Heat flux (kW/m^2)	Time (min)	Charring depth (mm)
20	20	12
75	20	15

Table 3.11. Charring depth for densified Spruce.

Heat flux (kW/m^2)	Time (min)	Charring depth (mm)
20	10	3
75	10	7

3.5 Conclusion

In this chapter, experimental studies were carried out to provide a better understanding of the fire behavior of densified wood. Firstly, the thermal-physical properties (density, thermal conductivity, and specific heat) were measured. We were able to measure thermal conductivity and specific heat for both virgin and densified Spruce wood by the hot place method. By using a balance and a drying oven, the mass of wet wood and dry wood can be determined. From that, we were also able to measure density and humidity for both virgin and densified Spruce wood.

The second part will present the thermogravimetric study for the characterization of the kinetic parameters of densified wood. The thermogravimetric tests were conducted to measure the mass and the time derivative evolution for both virgin and densified Spruce wood. The Arrhenius law and the least-squares method for optimization were used to determine the chemical reactions in terms of activation energy and pre-exponential factor. The confrontation of the predicted values to the measured values given by TGA shows a good agreement. Moreover, the confrontation of the activation energy values with than reported in the literature has been well approached and justified, which validates the proposed model.

Lastly, the cone calorimeter test was presented with the aim to study the thermal behavior of both virgin and densified wood for different conditions. The results of the cone calorimeter tests will form the basis for the validation of the thermal model developed. The thermal characterization results presented in this chapter will be used as input data for the thermal and thermomechanical model presented in the next chapter.

Bibliography of chapter 3

[1] Jannot Y., Degiovani A., Grigorova-Moutiers V., Godefroy J., A passive guard for low thermal conductivity measurement of small samples by the hot plate method, Journal of Measurement Science and Technology 28 (2017).

[2] Bal H., Jannot Y., Gaye S., Demeurie F., Measurement and modelisation of the thermal conductivity of a wet composite porous medium: Laterite based bricks with millet waste additive, Construction and Building Materials 41 (2013) 586-593.

[3] Jannot Y., Remy B., Degiovanni A., Measurement of thermal conductivity and thermal resistance with a tiny hot plate, High Temperatures - High Pressures 39(2010) 11-31.

[4] Di Blasi C., Modeling chemical and physical processes of wood and biomass pyrolysis, Journal of Energy and Combustion Science 34 (2008) 47-90.

[5] Grioui N., Halouani K., Zoulalian A., HalouaniF., Thermogravimetric analysis and kinetics modeling of isothermal carbonization of olive wood in inert atmosphere, Thermochimica Acta 440 (2006) 23-30.

[6] Shen D.K., Fang M.X., Luo Z.Y., Cen K.F., Modelling pyrolysis of wet wood under external heat flux, Fire Safety Journal 42 (2007) 210-217.

[7] Di Blasi C., Analysis of convection and secondary reaction effects within porous solid fuels undergoing pyrolysis, Combustion Science and Technology 90 (1993) 315-340.

[8] Park W.C., Antrya A., Baum H.R., Experimental and theoretical investigation of heat and mass transfer processes during wood pyrolysis, Combustion and Flame Journal 157 (2010) 481-494.

[9] Thi V.D., Khelifa M., Khennane A., El Ganaoui M., Rogaume Y., Finite element modeling of the pyrolysis of wet wood subjected to fire, Fire Safety Journal 81 (2016) 85-96.

[10] Fateh T., Rogaume T., Luche J., Richard F., Jabouille F., Modeling of the thermal decomposition of a treated plywood from thermo-gravimetry and Fourier-transformed infrared spectroscopy experimental analysis, Journal of Analytical and Applied Pyrolysis 101 (2013) 35-44.

[11] Broström M., Nordina A., Pommer L., Branca C., Di Blasi C., Influence of torrefaction on the devolatilization and oxidation kinetics of wood, Journal of Analytical and Applied Pyrolysis 96 (2012) 100-109.

[12] Zhao C., Zhang X., Liu L., Yu Y., Zheng W., Song P., Probing Chemical Changes in Holocellulose and Lignin of Timbers in Ancient Buildings, Journal List, Polymers, Basel (2019).

[13] Nassar M., Mackay M., Mechanism of thermal decomposition of lignin, Wood and Fiber Science 16 (1984) 441-453.

[14] Thurner F., Mann U., Kinetic investigation of wood pyrolysis, Industrial & Engineering Chemistry Product Research and Development 20 (1981) 482-488.

[15] Chan W., Kelbon M., Krieger B., Modeling and experimental verification of physical and chemical processes during pyrolysis of a large biomass particle, Fuel 64 (1985) 1505-1513.

[16] Front R., Marcilla A., Verdu E., Devessa J., Kinetics of the pyrolysis of almond shells and almond shells impregnated with cobalt dichloride in a fluidized bed reactor and in a pyroprobe 100, Industrial & Engineering Chemistry Research 29 (1990) 1846-1855.

[17] Grönli M., Melaaen M., Mathematical Model for Wood Pyrolysis Comparison of Experimental Measurements with Model Predictions, Energy Fuels 14 (2000) 791-800.

[18] Liden A., Berruti F., Sott D., A kinetic model for the production of liquids from the flash pyrolysis of biomass, Chemical Engineering Communications 65 (1988) 207-221.

[19] Várhegyi G., Gronli M.G., Di Blasi C., Effects of sample origin, extraction and hot water washing on the devolatilization kinetics of chestnut wood, Journal of Industrial & Engineering Chemistry Research 43 (2004) 2356–2367.

[20] Várhegyi G., Antal M.J., Jakab E., Szabo P., Kinetic modeling of biomass pyrolysis, Journal of Analytical and Applied Pyrolysis 42 (1997) 73-87.

[21] Terrei L., Acem Z., Lardet P., Georges V., Boulet P., Parent G., Experimental tools applied to the ignition study of spruce wood under cone calorimeter, Journal of Physics: Conference series volume 1107.

[22] ISO 5660-1 - Reaction-to-fire tests - Heat release, smoke production and mass loss rate - Part 1: heat release rate (cone calorimeter method) (2002).

[23] Boulet P., Parent G., Acem Z., Rogaume T., Fateh T., Zaida J., Richard F., Characterization of the radiative exchanges when using a cone calorimeter for the study of the plywood pyrolysis. Fire safety journal 51 (2012) 53-60.

[24] Urbas J., Parker W. J., Luebbers G. E., Surface temperature measurements on burning materials using an infrared pyrometer: accounting for emissivity and reflection of external radiation, Fire and materials 28(1) (2004) 33-53.

[25] Chaos M., Spectral aspects of bench-scale flammability testing: application to hardwood pyrolysis, Fire Safety Science 11 (2014) 165-178.

[26] De Vries J., Ren N., Chaos M., Temperature measurements on solid surfaces in rack-storage fires using IR thermography, In Thermosense: Thermal Infrared Applications XXXVII, International Society for Optics and Photonics (2015).

[27] Parent G., Acem Z., Lechêne S., Boulet P., Measurement of infrared radiation emitte by the flame of a vegetation fire, International Journal of Thermal Sciences 49(3) (2010) 555-562.

[28] Terrei L., Acem Z., Georges V., Lardet P., Boulet P., Parent G., Experimental tools applied to the ignition study of spruce wood under cone calorimeter, 3rd European Symposium on Fire Safety Science, 12-14 Sep 2018, Nancy, proceeding to be published in Journal of Physics: Conference Series.

Chapter 4

Structural fire response predictions

Summary

4.1 Introduction 112
4.2 Thermo-hydric transfer of cone calorimeter tests 113
4.2.1 Heat transfer modeling 113
4.2.2 Results 114
4.2.3 Mesh sensitivity study 117
4.3 Thermo-hydric transfer of CLT panels using densified wooden dowels 120
4.3.1 Fire tests 120
4.3.2 Finite element thermal analysis 122
4.4 Thermo-mechanical analysis of L-shaped connections with densified wood dowels 125
4.4.1 Fire tests 125
4.4.2 Finite element thermo-mechanical analysis 132
4.4.3 Results 134
4.5 Influence of various parameters 144
4.5.1 Carbonization - charring rate 144
4.5.2 Densification ratio 146
4.5.3 Type of material of the dowel 150
4.6 Conclusion 154
Bibliography of chapter 4 156

4.1 Introduction

In this chapter, the simulations of the thermal and thermomechanical behavior of wood material exposed to severe imposed thermal loading are presented. The developed model allows transcribing a heat transfer within the densified wooden material taken into account the vaporization of water and thermal degradation reactions, i.e. wood pyrolysis as well as the modification of the physical properties induced by these degradation reactions. In this model, the energy aspects and the modification of the thermal properties of the material as well as the mass transfers are taken into account.

Numerical modelings are carried out with ABAQUS software [1]. Firstly, the simulation is applied for the experiments that we conducted in this project (cone calorimeter tests, adhesive-free CLT, and adhesive-free connections). The thermal properties (thermophysical properties and kinetic parameters) used in this modeling are determined through the experiments presented in chapter 3 (hot plate method and thermogravimetric test). In the second step, the influence of various parameters of densified wood (carbonization, densification ratio…) is studied with the model developed.

4.2 Thermo-hydric transfer of cone calorimeter tests

4.2.1 Heat transfer modeling

The simulations are carried out on samples of 102x102x19 mm^3 in normal wood and densified wood in cone calorimeter test. One surface of these panels is exposed to the constant fluxes off f = 20 kW/m^2 and f = 75 kW/m^2. The other surfaces are in contact with the environment with the temperature T = 22 °C. The temperature on the exposed face and with the room temperature on the unexposed face was taken into account with convective heat transfer coefficients h respectively equal to 12,5 and 4 $W/(m^2.K)$ and radiative transfer coefficients ε equal to 0.9.

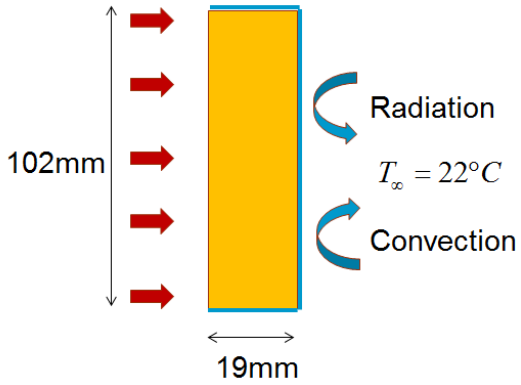

FIGURE 4. 1 - Boundary conditions in cone calorimeter modeling.

Due to symmetry, only one-half of the cross-section of the panel was modeled. A 2D plane analysis using a 4-node plane element is used for the finite element discretization, involving 969 elements type DC2D4 available in the Abaqus software for thermal analysis. The moisture contents of the samples were about 6,7% and 6%, and the corresponding initial density was equal to q_o = 417,6 kg/m^3 and q_o = 1114,7 kg/m^3 for virgin and densified spruce, respectively.

The thermal conductivity of the wood compound depends on the mass fraction of the three following components: dry wood, water, and char. After the drying process, the thermal conductivity value was combined from those corresponding to wood and char. These values are determined according to the equations [2]:

- Normal Spruce:

$$\lambda_w = \lambda_{dry} + 0{,}275 \times \beta = 0{,}12 + 0{,}275 \times \beta \quad (4.1)$$

- Densified Spruce:

$$\lambda_w = \lambda_{dry} + 0{,}733 \times \beta = 0{,}175 + 0{,}733 \times \beta \quad (4.2)$$

where β is the moisture content of the wood. A variation for the solid thermal conductivity with solid conversion η was assumed as:

$$\lambda_s = \eta.\lambda_c + (1-\eta).\lambda_w \quad (4.3)$$

$$\eta = \frac{\rho_c}{\rho_s} = \frac{\rho_c}{\rho_c + \rho_w} \quad (4.4)$$

The subscript s, c, and w are the solid, char, and wood components respectively.

4.2.2 Results

4.2.2.1 The temperature at the unexposed surface

Simulated temperatures were compared to the measurement in Figure 4.2. The thermal transfer across the sample was relatively well simulated in the pyrolysis model (N. Grioui [3] and D. Blasi [4]). In particular, the temperature on the unexposed surface was correctly reproduced, which is the main criterion to be reproduced for the assessment of fire resistance of virgin and densified wood.

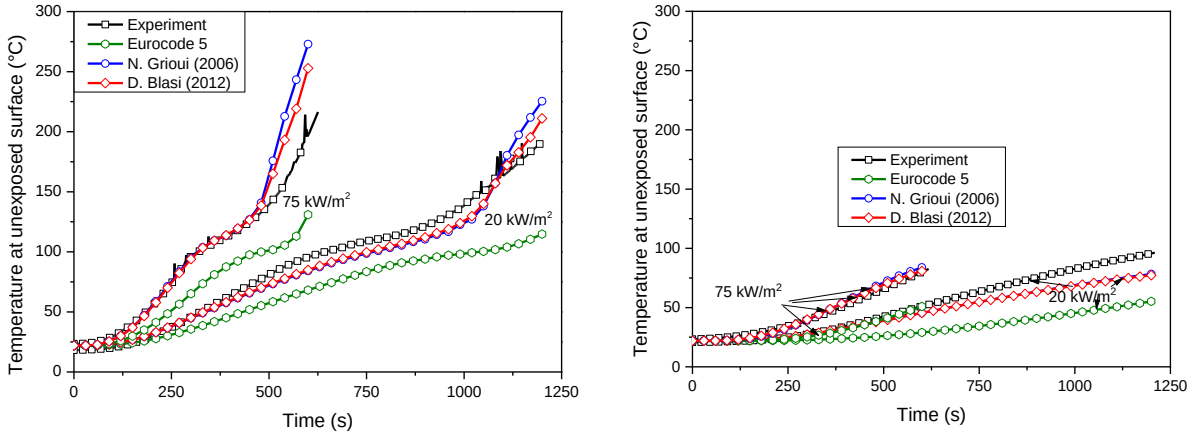

a) Virgin Spruce b) Densified Spruce

FIGURE 4. 2 - The temperature at the unexposed surface.

From a numerical point of view, the simulation of such a temperature plateau is complex if the transport of mass (water) is not considered in the model. In our model, the latent energy

of water vaporization was taken into account through a source of energy associated with a thermally-activated reaction. Taking into account the sink of energy associated with water vaporization it becomes possible to obtain a temperature slowdown around 100 °C, particularly the model managed to simulate pronounced temperature plateaus like in experiments.

4.2.2.2 Charring depth

The temperature profiles and the residual cross-section evolution obtained numerically at different fire exposure times for virgin and densified Spruce wood are reported in Figures 4.3-4.4. The grey and red colors represent the charred material and the 300 °C isotherms, respectively. The blue contour corresponds to a temperature close to the ambient temperature.

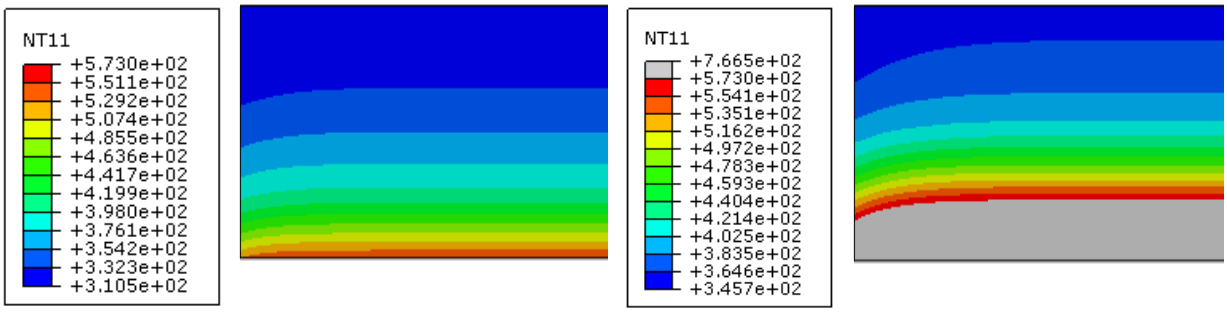

(a) t = 5 min (b) t = 10 min

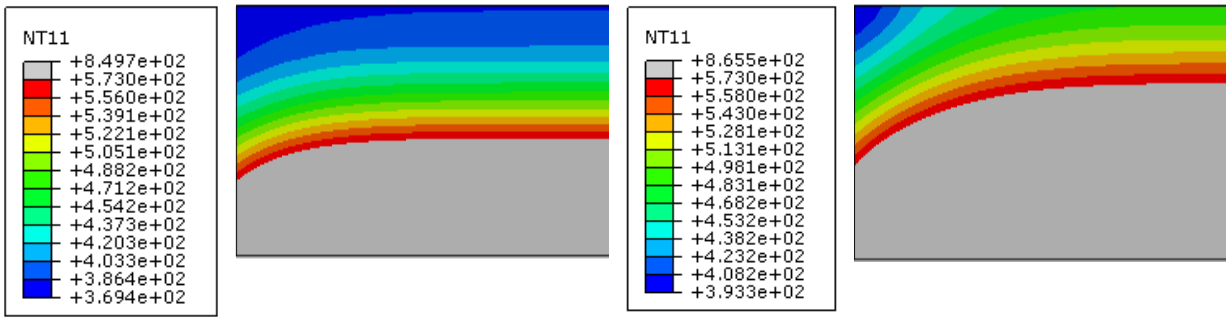

(c) t = 15 min (d) t = 20 min

FIGURE 4. 3 - Formation of char at different fire-exposure times in virgin spruce (T in [K]).

The part of ambient temperature in the cross-section of the densified wood is much smaller when compares to virgin wood. This can be explained by the much higher thermal diffusion of virgin wood than densified wood.

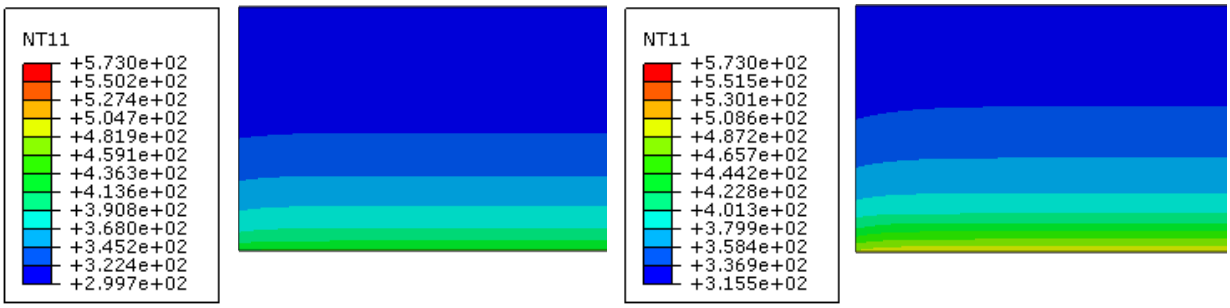

(a) t = 5 min (b) t = 10 min

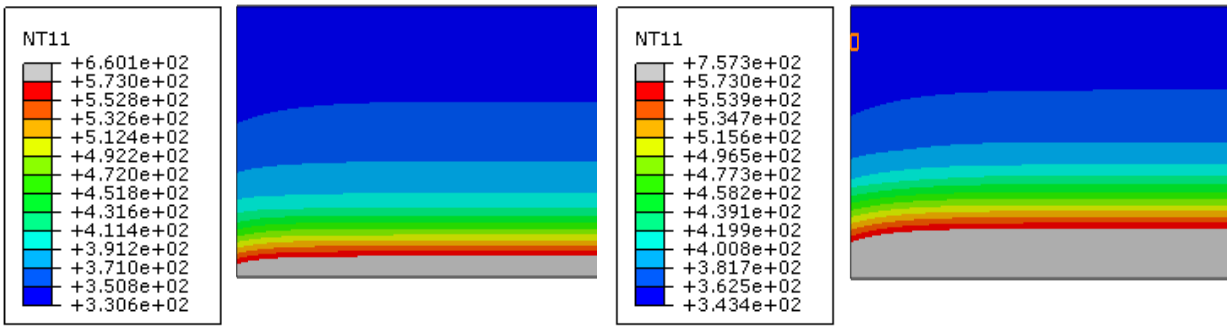

(c) t = 15 min (d) t = 20 min

FIGURE 4. 4 - Formation of char at different fire-exposure times in densified spruce (T in [K]).

The values of charring depth at the middle of the sample are compared with the experimental ones from Table 4.1. It can be seen a fairly good agreement between the finite element model prediction and the experimental observation. The approximation of the finite element model is instead good for the predictions of the residual cross-section.

Table 4.1. Comparison of measured and calculated charring depths at the middle of the panel.

	Heat flux (kW/m^2)	Time (min)	Charring depth (Experiment)	Charring depth (N. Grioui [3])	Charring depth (D. Blasi [4])	Charring depth (EC5[5])
Virgin spruce	20	20	12	13,5	13	8
	75	10	15	17	16	13
Densified spruce	20	20	3	4	3,5	3,5
	75	10	7	8	7	8

4.2.2.3 Mass loss

The comparison of the mass loss for samples of virgin and densified Spruce under two different heat fluxes are reported in Figure 4.5. Good agreement is obtained between measurements and predictions for the solid mass fractions as functions of time, as also indicated by the fit between measured and calculated curves.

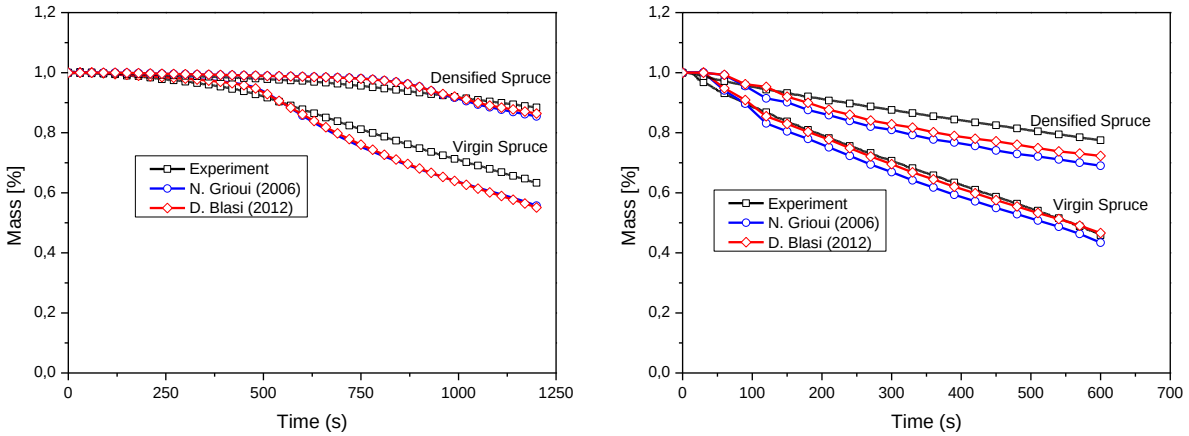

a) Heat flux 20 kW/m^2 b) Heat flux 75 kW/m^2

FIGURE 4. 5 - Mass loss for samples of virgin and densified Spruce.

4.2.3 Mesh sensitivity study

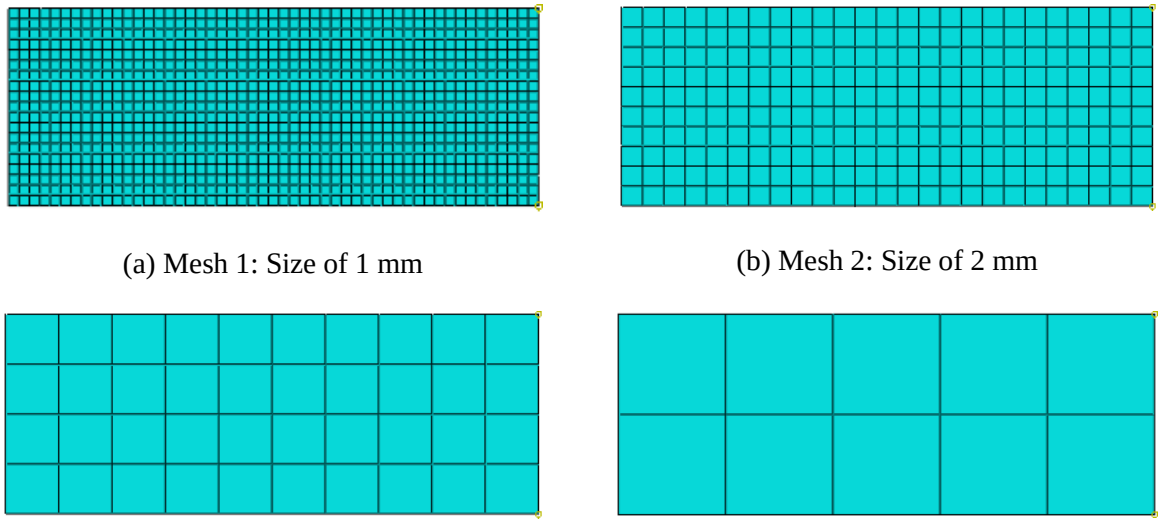

(a) Mesh 1: Size of 1 mm (b) Mesh 2: Size of 2 mm

(c) Mesh 3: Size of 5 mm (d) Mesh 4: Size of 10 mm

FIGURE 4. 6 - The cases of meshing.

To evaluate the dependency of temperature profile as well as the formation of charcoal

upon the mesh, some different meshes were carried out in numerical analyses. There are four meshes tested with different sizes: 1, 2, 5, and 10 mm for the thermal modeling of cone calorimeter tests on virgin spruce specimens exposed to a heat flux of 20 $kW.m^{-2}$ on one side. The timber cross-section was 102x19 mm^2.

The influence of temperature on thermal properties is replaced by the pyrolysis model of D. Blasi (2012). In subroutine UMATHT, the material is defined through its thermo-physical and kinetic parameters. Due to symmetry, only one-half of the cross-section of the specimen was modeled. A 2D plane analysis using a 4-node plane element is used for the finite element discretization in the Abaqus software for thermal analysis. The moisture contents of the samples were about 6,7%, and the initial density was equal to q_o = 417,6 kg/m^3. Temperatures were recorded at the center and the unexposed surface of the sample.

The temperature profiles for four different sizes of the mesh after 25 min exposure are depicted in Figure 4.7. The charred layer forms above T = 300 °C and is shown in grey. The undamaged wood is shown in blue. Between the charred layer and the undamaged wood, there are areas of pyrolysis (red, yellow, and green) and drying (turquoise). The shape of the red curve is uniform for two first two cases (Figure 4.7a,b). This is non-uniform for the remaining cases, especially for the last case (Figure 4.7d).

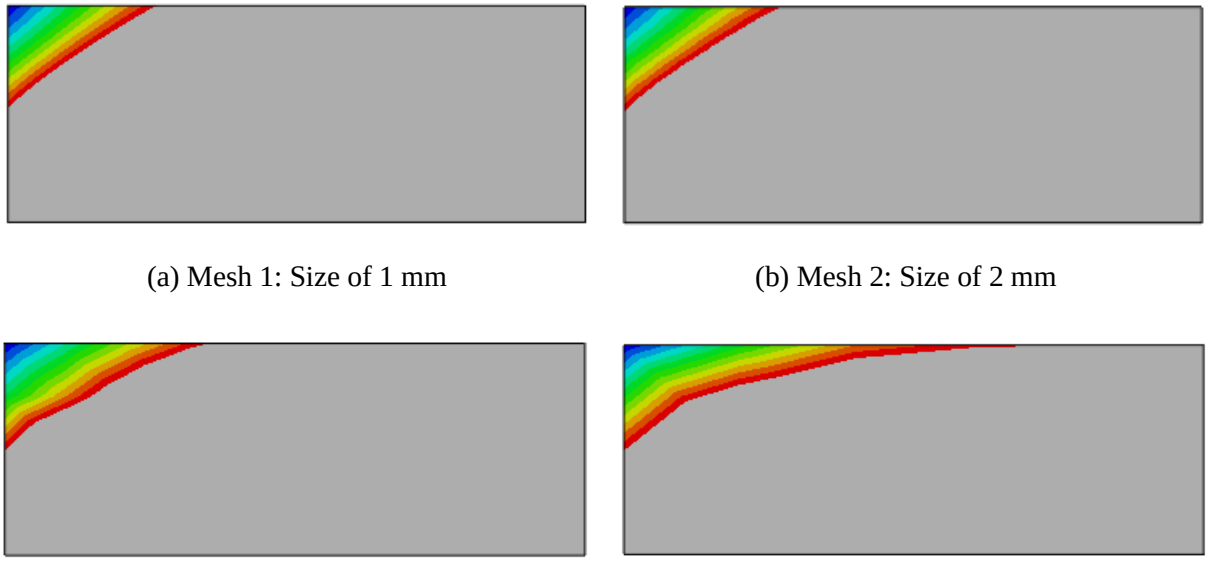

(a) Mesh 1: Size of 1 mm

(b) Mesh 2: Size of 2 mm

(c) Mesh 3: Size of 5 mm

(d) Mesh 4: Size of 10 mm

FIGURE 4. 7 - Formation of the charred layer after 25 min exposure (T[K]).

Figure 4.8 shows the temperature field in different positions for four cases of mesh. It can be seen that the evolution of temperature in models using mesh 1 and mesh 2 are almost the same. Beyond this size of the mesh, there are differences in the evolution of temperature. We note that the difference is more serious when the size of the mesh is large.

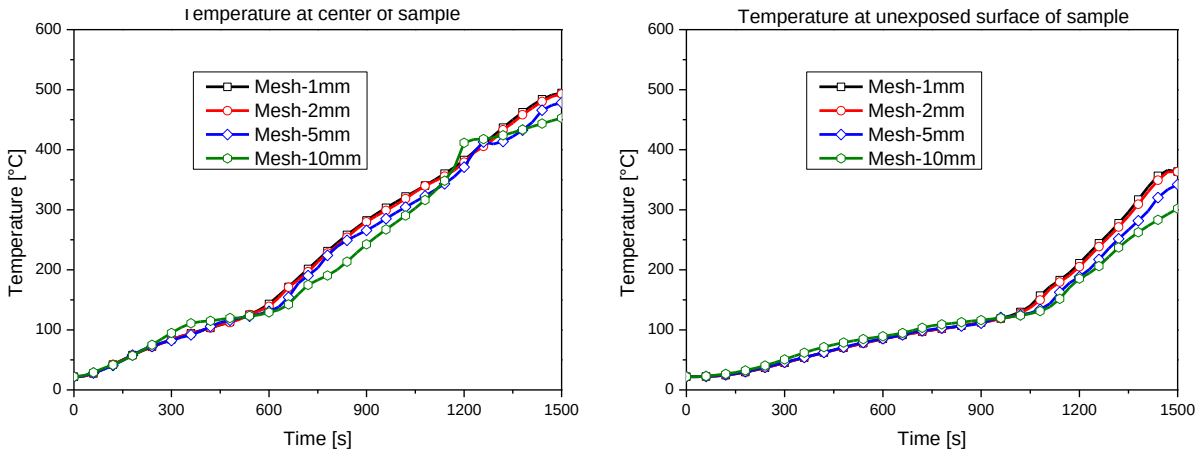

FIGURE 4. 8 - Effect of mesh in temperature field at the different positions.

From the above results, to ensure the best combination between the accuracy of the solution and computational time needed, mesh 2 is the best choice and will apply for heat transfer of wood when using the pyrolysis model.

4.3 Thermo-hydric transfer of CLT panels using densified wooden dowels

4.3.1 Fire tests

The fire tests of adhesive-free CLT panels were carried out for the validation of the thermal model developed. The results obtained are the basis to assess the fire performance of densified wooden dowels used in adhesive CLT panels. The CLT panels are made up of the association of three layers through the densified wooden dowels of 16 mm diameter. Each layer is composed of 3 panels. The thickness of each panel is 25 mm. The dimensions of each panel are also presented in Figure 4.9. The material of layers used in this test is Oak wood with the measured mean values for moisture content of 10%. The dowels were made from densified Spruce with the same moisture content of the layer.

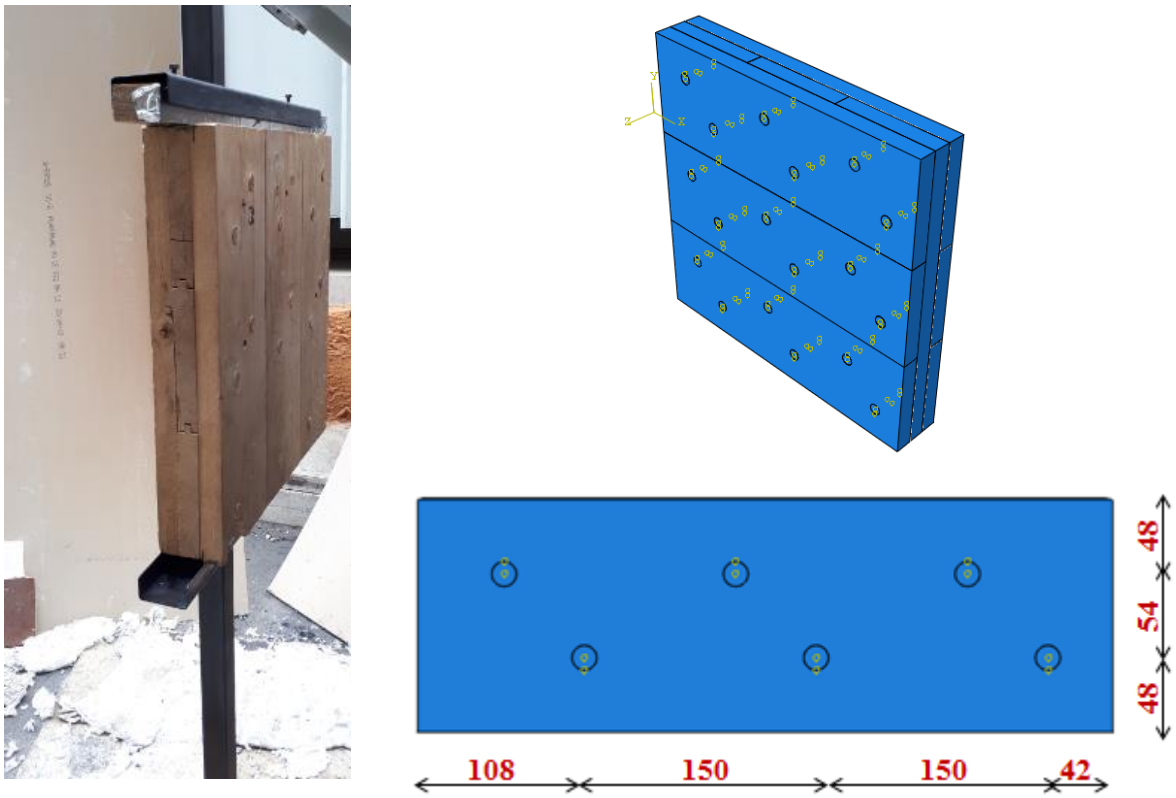

FIGURE 4. 9 - Adhesive-free CLT panels.

The testing rig detail of the fire test of CLT panels is shown in Figure 4.10. A test furnace has been developed specifically for carrying out these measurements. The heat source is also provided by four radiant panels with nominal power equal to 100 kW/m^2 and capable of reaching a maximum surface temperature of the order 2000 °C. Only one surface of CLT panels was exposed horizontally to external constant heat fluxes. The distance between the

connection and the heater was 20 and 30 cm for heat fluxes of 60 and 49 $kW.m^{-2}$, respectively.

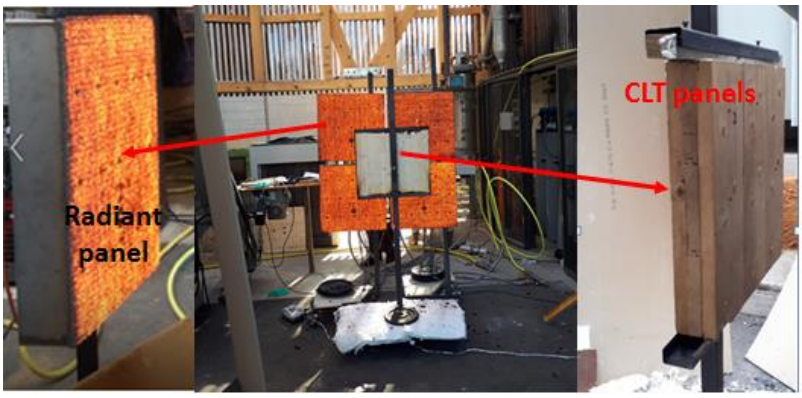

FIGURE 4. 10 - Testing diagram of fire test of CLT panels.

Figure 4.11 showed the measurement of the residual cross-section of the test specimens by laser scanning after removing the charred layer. The laser-scanning technology used for the determination of the residual cross-sections was found to be a quicker and more exact method than the commonly used measurement method.

(a) Laser scanner

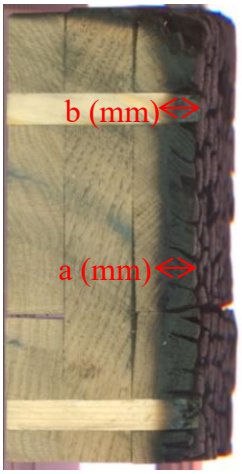

(b) Residual cross-section of CLT panels

FIGURE 4. 11 - Laser scanner and residual cross-section of CLT panels obtained by laser scanning.

The charring depths in the wood layer and densified wooden dowels under 2 types of heat fluxes (49 kW/m^2 and 60 kW/m^2) were depicted in Table 4.2. After the test, normal wood exhibited more charring than compressed wood dowels: this confirmed previous results (cone calorimeter tests). This proved that compressed wood dowels cannot be considered as the weakest elements under fire.

Table 4.2. Charring depth in CLT panels after the test.

	Heat flux (kW/m^2)	Time (min)	Charring depth in wood layer: a (mm)	Charring depth in wood dowel: b (mm)
Panel 1	60	15	15	11
Panel 2	60	15	15	11,5
Panel 3	49	15	13	10,5

4.3.2 Finite element thermal analysis

In addition to the fire tests, an extensive thermal numerical study was performed using the FEM (finite element method). The development of charring depth in the CLT panels was calculated using three-dimensional finite element models implemented in ABAQUS [1]. The 20-node hexahedral solid elements are used for each part of the connection. The heat transfer to the surface of the member was given with the convective heat transfer coefficient h = 12.5 $W/(m^2.K)$ and the emissivity coefficient ε = 0.9. Mass transfer of moisture into or out of the wood was neglected. For the FE thermal analysis, the initial densities were 650 kg/m^3 and 1210 $kg/m^3$for wood layer and densified wooden dowel respectively (average values of test specimens). The measured mean values for moisture content were 10% for both wood layer and densified wooden dowel.

The layers were made up of Oak wood. The thermal properties of Oak wood (thermo-physical properties and kinetic parameters) were also measured by experiment (hot place method and thermogravimetric analysis), detailed in Annex 1. Thermal conductivity of wood compound are determined according to the equations [2]:

- Oak wood:

$$\lambda_w = \lambda_{dry} + 0{,}396 \times \beta = 0{,}135 + 0{,}396 \times \beta \quad (4.5)$$

Figure 4.12 highlights the distribution of temperature and the residual cross-section of adhesive free CLT panels obtained numerically after 15 min of exposure to two heat fluxes of 49 kW/m^2 and 60 kW/m^2. Charcoal formation begins at a temperature of about 300 °C, so the red solid line represents the 300 °C isotherms and, therefore, the residual cross-section at the end of the fire test using the finite element model with the new proposal (kinetic model of D. Blasi) is observed.

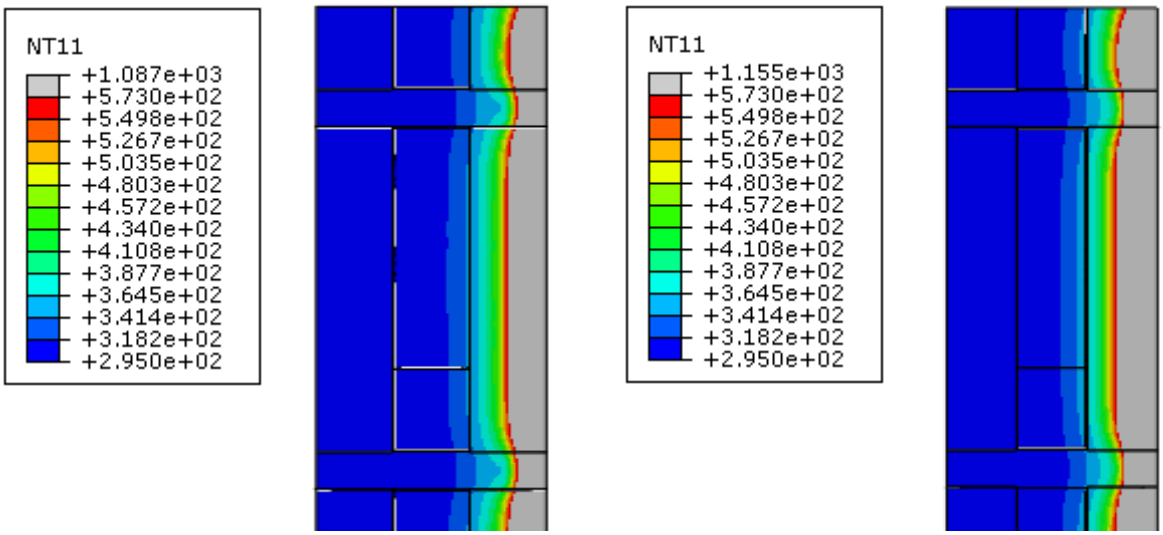

(a) Heat flux of 49 kW/m^2 (b) Heat flux of 60 kW/m^2

FIGURE 4. 12 - Temperature distribution and residual cross-section in CLT panels after 15 min exposure on one side.

The comparison between the experimental and numerical residual cross-section of CLT panels using densified wooden dowels after a fire exposure of 15 minutes is reported in Table 4.3. The charring depth in the numerical models has nearly the same depth as in the wood layer at the end of the test in case of heat flux of 49 kW.m^{-2} (14,5 mm of EC5 approach and 13 mm of D. Blasi approach instead of 13 mm). A similar result is observed with a heat flux of 60 kW.m^{-2} (18 mm of EC5 approach and 14,5 mm of D. Blasi approach instead of 15 mm). This proves that the approximation of the finite element model is instead well for the predictions of the residual cross-section and charring depth in the normal wood.

Table 4.3. Comparison of measured and calculated charring depths in CLT panels.

	Heat flux (kW/m^2)	Time (min)	Charring depth (Test 1)	Charring depth (Test 2)	Charring depth (D. Blasi [4])	Charring depth (EC5[5])
Wood layer	49	15	13	-	13	14,5
	60	15	15	15	14,5	18
Densified wood dowel	49	15	10,5	-	10	12
	60	15	11	11,5	11	14,5

About the residual cross-section in densified wooden dowels, the EC5 approach falls behind the experimental measurement, specifically for the heat flux of 60 $kW.m^{-2}$ (14,5 mm instead of 11,5 mm). On the contrary, the kinetic model of D. Blasi predicts the depth of charcoal in the same place as the experiment (10 mm and 11 mm compared to 10,5 mm and 11,5 mm for two external heat fluxes of 49 and 60 $kW.m^{-2}$, respectively). This result shows more suitability of D. Blasi's kinetic model in predicting the residual section of densified wooden dowels under the external heat fluxes.

4.4 Thermo-mechanical analysis of L-shaped connections with densified wood dowels

In this section, a thermomechanical analysis of the connection is carried out. The combination of the wood layer and densified wooden dowels makes it possible to carry out a coupled heat transfer and stress analysis. It is possible therefore to simulate the deflection at the free end of the connection during fire exposure. The model accounts for the impact of the pyrolysis reactions on the mechanical properties of the connection through the kinetic models of D. Blasi (2012) [4].

4.4.1 Fire tests

The fire tests of connections carried out during this project aim to provide a reliable database for the validation of the thermomechanical model developed. The results obtained are the basis to assess that timber connections using compressed wooden dowels outperform conventional ones made with steel dowels or not. The connections are made up by the association of a column and a beam through 4 dowels of 16 mm diameter. Both beams and columns are three-layer structures with a thickness of 32 mm for each layer. The dimensions of the L-shaped connection are also presented in Figure 4.13.

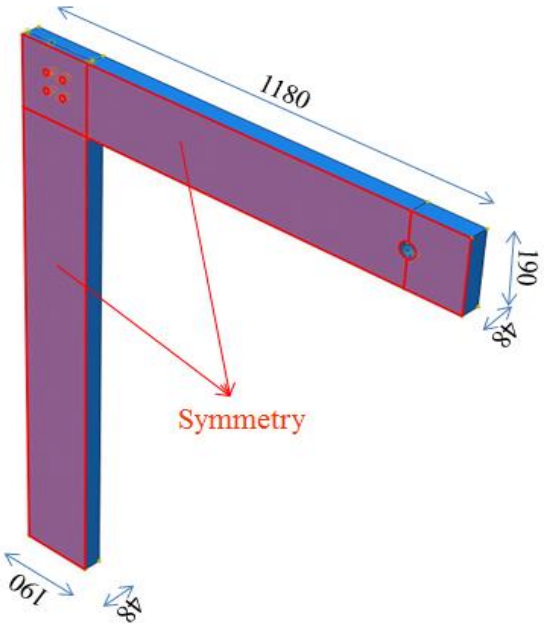

FIGURE 4. 13 - Detailed structure of L-shaped connection.

The material of layers used in both tests is Oak wood with the measured mean values for moisture content of 10%. The fire tests of connections are implemented for 2 cases of material

of dowel: steel dowel and densified Spruce dowels. This allows evaluating the effectiveness of the use of compressed wooden dowels instead of conventional connections by steel dowels.

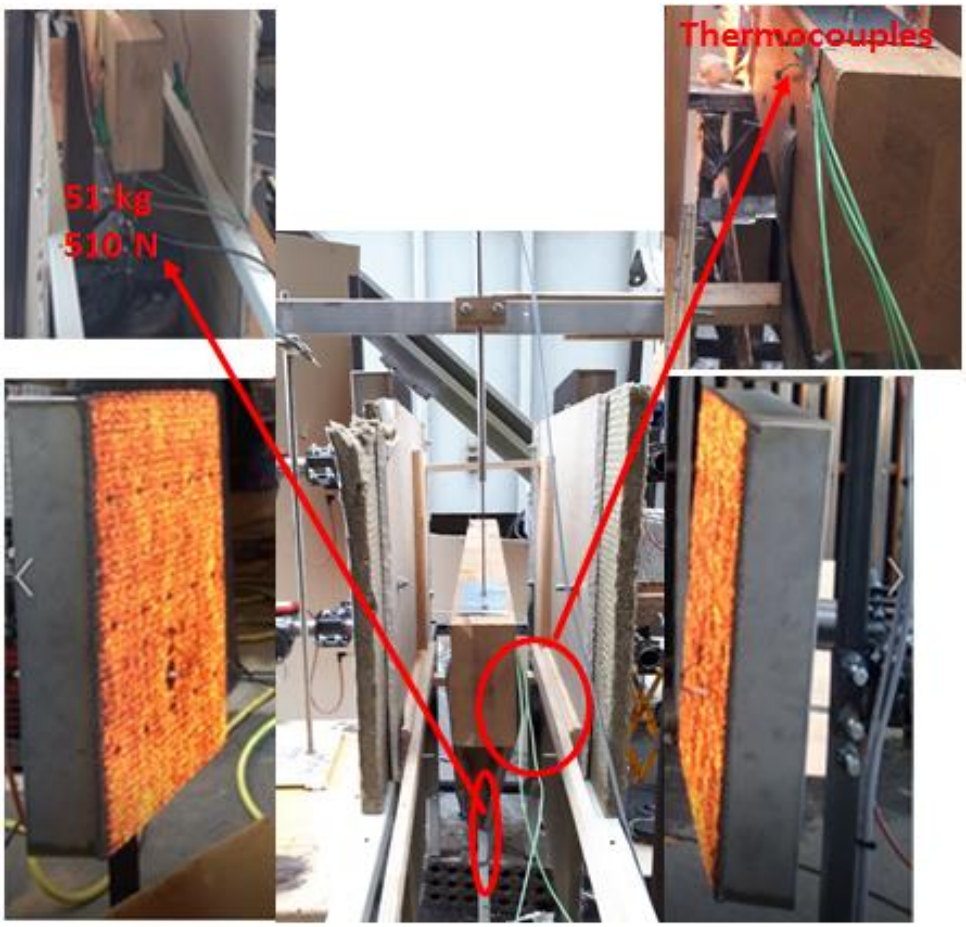

FIGURE 4. 14 - Testing diagram of fire test of connection.

The testing rig detail of fire tests of connection is shown in Figure 4.14. The heat source is also provided by the radiant panels with nominal power equal to 100 kW/m^2 and capable of reaching a maximum surface temperature of the order 2000 °C. To avoid side effects of the heat source surrounding the beams and columns, two gypsum plasterboard was used for the isolation. The connections were exposed horizontally to two external constant heat fluxes of 49 and 60 kW/m^2. The distance between the connection and the heater was 20 and 30 cm for heat fluxes of 60 and 49 kW.m^{-2}, respectively. In this test, a multispectral infrared camera (Orion SC7000 by FLIR) was used for measuring the surface temperatures. This non-intrusive measurement allows studying the temperature field evolution on a large surface. The contact problem is also eliminated. Temperatures within connections are recorded by thermocouples type K, of diameter of 1 mm, at 2 mm, 3 mm, 6 mm, and 11 mm for the timber layers and at 3

mm and 6 mm for densified wooden dowels from the exposed side. With the steel dowels, temperatures are recorded at the interface between the wood layer and steel dowel in the positions of 3 mm and 6 mm from the exposed side. Temperatures are recorded every second via a USB TC-08 PICO type acquisition center. A linear voltage displacement transducers (LVDTs) were positioned on each specimen to record the deflection at the free end.

Samples were submitted to two external heat fluxes (49 and 60 $kW.m^{-2}$). In the following, we will present the first results regarding the evolution of temperatures inside the samples. Then we will focus on the displacement studies as well as the charring depth of the sample after the tests.

1. Evolution of temperature inside samples

For tests with a 49 $kW.m^{-2}$ external heat flux, the total exposure time was 1200 s. After this time, the heat flux was removed. The sample moisture was 10%. Tests were repeated three times, two times for connection using densified wooden dowels and one time for another one. Figures 4.15 and 4.16 presents the temperatures measured on the 0, 2, 3, and 6 mm from the exposed side in layer and dowel for the two types of connection (using densified wooden dowels and steel dowels) under a heat flux of 49 $kW.m^{-2}$. The surface temperature evolution was provided by the IR camera and the inside temperature was measured by the thermocouples.

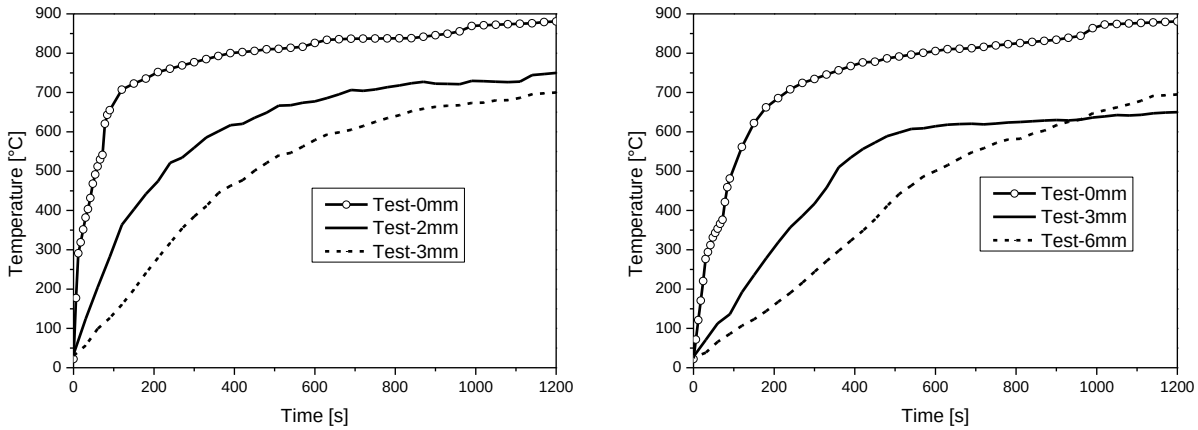

(a) Temperature in wood layer (b) Temperature in densified wooden dowels

FIGURE 4. 15 - Evolution of temperature in L-joint using densified wooden dowels under a heat flux of 49 $kW.m^{-2}$.

For the surface temperatures (0 mm) in connection using densified wooden dowels, an increase of the temperature is observed from 400 °C. This phenomenon may correspond to the beginning of the smoldering combustion of the char that leads to an additional amount of released energy. This confirmed previous results (cone calorimeter). A plateau of the surface temperature occurs at about 750 °C. This plateau is reached at 100 and 200 s for wood layer and densified wood dowel respectively.

Temperatures measured for the wood dowel (densified wood) increase gradually after a small temperature plateau at about 100 °C. This small temperature plateau can be attributed to the water vaporization of the wood. Indeed, around 100 °C (at normal atmospheric pressure), the energy provided by the heating is no longer the engine of an increase in the temperature of the material but is used for the phase change of water into vapor (vaporization). For the wood layer (Oak wood), a slight slowdown in heat transfer is observed between 150 and 250 seconds, which corresponds to the change in slope and stabilization of the loading temperature on the exposed face. This is also observed for wood dowel but a time between 300 and 400 seconds. The different materials have different thermal behavior. Indeed, the temperature rise in the steel dowel and densified wooden dowel is clearly slower than one in the wood layer (Oak wood).

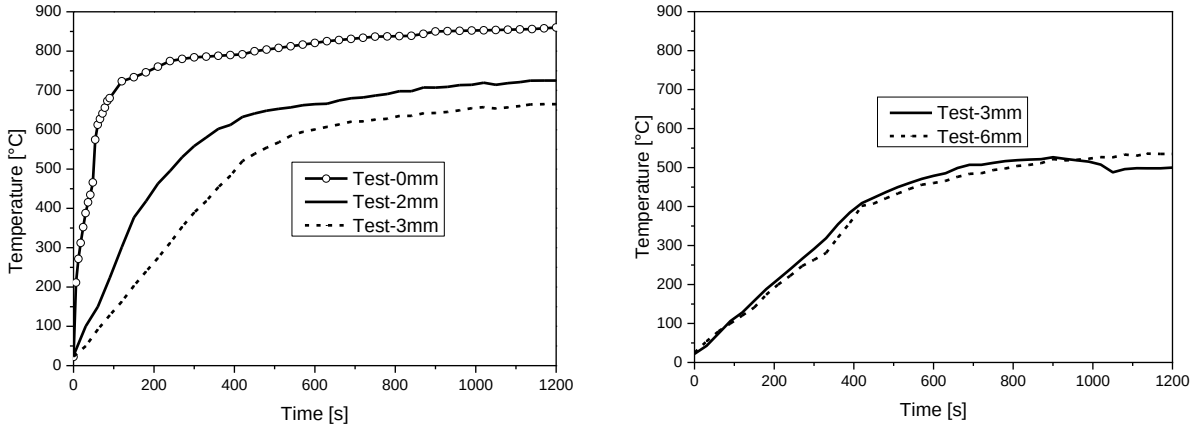

(a) Temperature in wood layer (b) Temperature in steel dowels

FIGURE 4. 16 - Evolution of temperature in L-joint using steel dowels under a heat flux of 49 kW.m^{-2}.

It can be seen that the evolution of temperature at 3mm and 6 mm from the exposed surface in steel dowel are nearly the same. This proved that the heat transfer in steel dowel is very fast due to the very high thermal conductivity of steel material.

Tests were also carried out with higher radiative heat fluxes for which the ignition occurs.

After 900 s of exposure, the radiant panel was removed. The moisture sample was also 10%. The evolution of temperature measured on the 0, 2, 3, and 6 mm from the exposed side in layer and dowel for the two types of connection under a heat flux of 60 kW.m^{-2} is depicted in Figures 4.17 and 4.18.

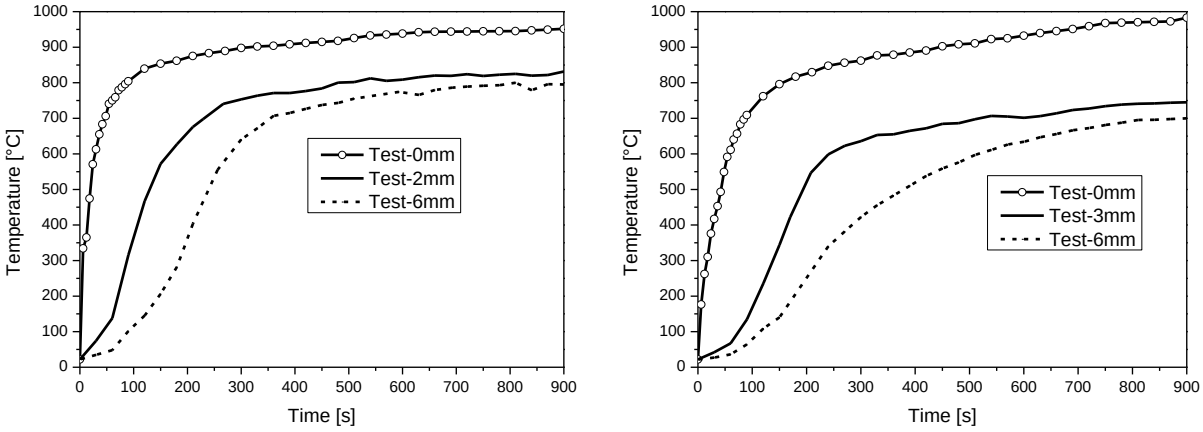

(a) Temperature in wood layer (b) Temperature in densified wooden dowels

FIGURE 4. 17 - Evolution of temperature in L-Joint using densified wooden dowels under a heat flux of 60 kW.m^{-2}.

In these tests, similar overall trends are observed when compared to the tests using an external heat flux of 49 kW.m^{-2}. The drastic increase in the surface temperature when the ignition occurs is the main difference. This also confirmed previous results (cone calorimeter) under external heat flux of 75 kW.m^{-2}. At 850 °C there is a plateau of the surface temperature. This step is reached at 100 and 200 s for wood layer and densified wood dowel respectively.

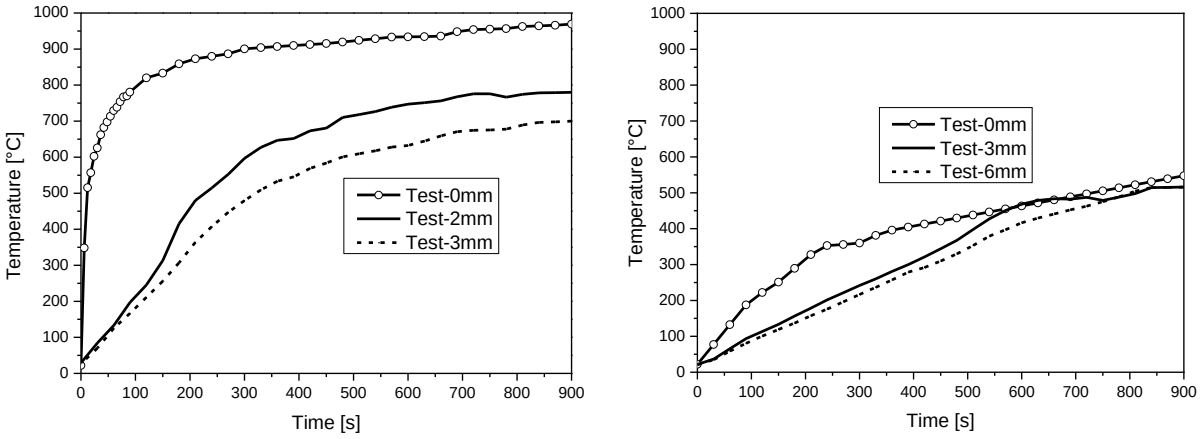

(a) Temperature in wood layer (b) Temperature in steel dowels

FIGURE 4. 18 - Evolution of temperature in L-joint using steel dowels under a heat flux of 60 kW.m^{-2}.

2. Charring depth

The residual cross-section of the test specimens was also measured by laser scanning after removing the charred layer. Figure 4.19 showed the residual cross-section of connection using densified wooden dowels and steel dowels under a heat flux of 49 $kW.m^{-2}$. In L-joint connection using densified wooden dowels, the charred layers were formed in the direction of heat transfer while whole holes and wood surrounding steel dowels in the L-joint connection using steel dowels are completely charred (black area). This led to the reduction of friction between wood layers and steel dowels.

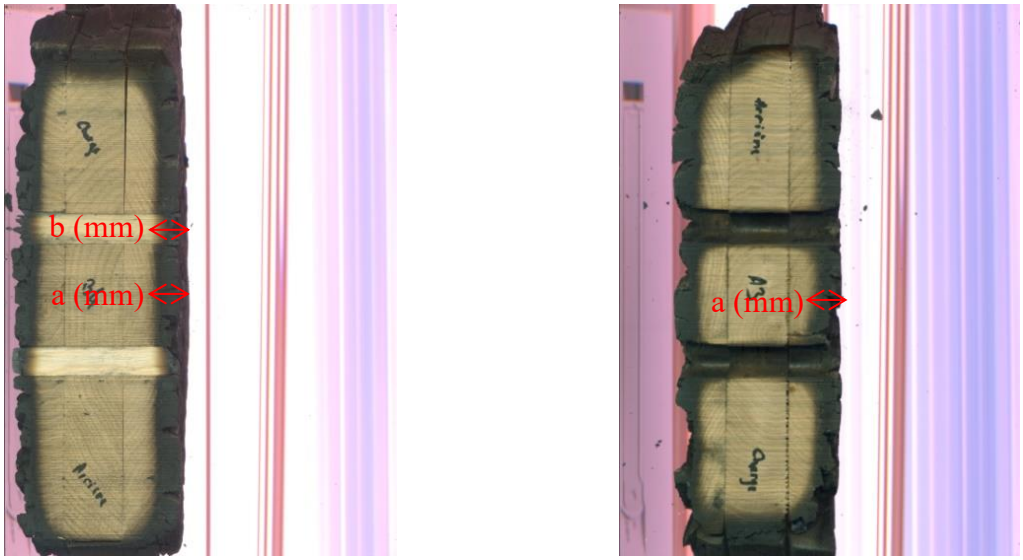

(a) Connection using densified wooden dowels (b) Connection using steel dowels

FIGURE 4. 19 - Residual cross-section of L-shaped connection obtained by laser scanning.

Table 4.4 depicted the charring depths in the wood layer and densified wooden dowels under 2 types of heat fluxes (49 kW/m^2 and 60 kW/m^2) for both connections using densified wooden dowels and steel dowels. In the similarity with the previous experiment (CLT panels using densified wooden dowels), normal wood also exhibited more charring than compressed wood dowels.

Table 4.4. Charring depth in L-shaped connection after the test.

	Tye of dowel (wood and steel)	Heat flux (kW/m^2)	Time (min)	Charring depth in wood layer a (mm)	Charring depth in wood dowel b (mm)
Conection 1	Densified wood	60	15	16	11
Conection 2	Steel	60	15	17	-
Conection 3	Densified wood	60	15	16,5	11
Conection 4	Steel	60	15	17	-
Conection 5	Densified wood	49	20	15	12
Conection 6	Steel	49	20	17	-
Conection 7	Densified wood	49	20	14,5	10

4. Deflection at the free end

As the sample was exposed to external heat flux, the residual cross-section and stiffness of the sample were reduced due to the perimeter of the specimen began charring, leading to an increase in displacement. A potentiometer on the top side of the sample was used to measure the displacement at the free end of the connection. Figures 4.20 and 4.21 show the displacement at the free end in the joint subjected to a constant of 51 kg under two external heat fluxes (49 and 60 $kW.m^{-2}$).

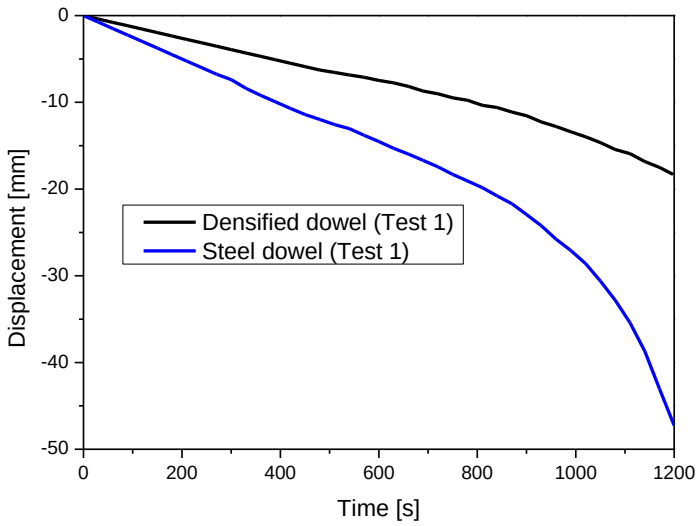

FIGURE 4. 20 - Displacement in case of heat flux of 49 $kW.m^{-2}$.

The displacements show an approximately linear increase except for the case of connection using steel dowel with a plastic increase. As it would be expected, it can be seen that the displacement in the connection with densified wooden dowels is slower than conventional ones made with steel dowels. This result can be explained by the reduction of friction between wood layers and steel dowels due to the formation of the charred layer in the wood around steel dowels (previous section).

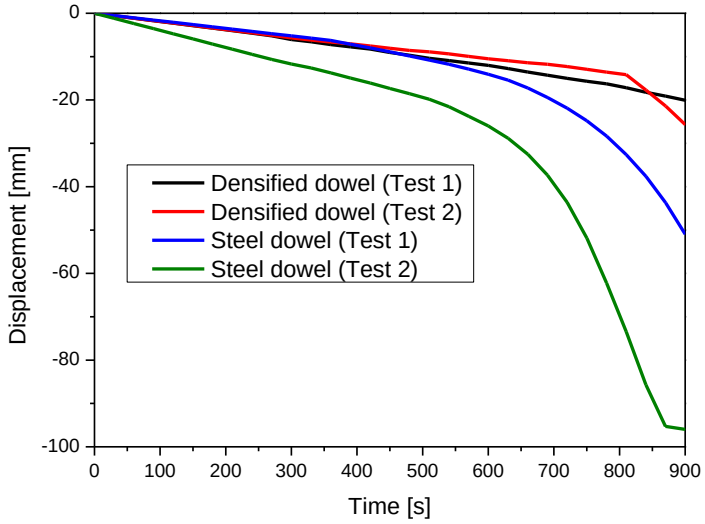

FIGURE 4. 21 - Displacement in case of heat flux of 60 kW.m^{-2}.

The experimental tests demonstrated that timber connections using compressed wood dowels outperform more than conventional ones made with steel dowels about bearing capacity in the event of a fire.

4.4.2 Finite element thermo-mechanical analysis

4.4.2.1 Mechanical properties of wood

The initial mechanical properties of Oak wood and densified Spruce wood used in the simulations are given in Tables 4.5-4.6.

Table 4.5. Mechanical properties of the Oak wood at 20 °C.

Young's modulus [MPa]		Poisson's Coefficients		Shear modulus [MPa]	
E_1	11380	$\nu_{12} = \nu_{13}$	0.41	$G_{12} = G_{13}$	690
$E_2 = E_3$	370	ν_{23}	0.3	G_{23}	50

Table 4.6. Mechanical properties of the densified Spruce wood at 20 °C.

Young's modulus [MPa]		Poisson's Coefficients		Shear modulus [MPa]	
E_1	25500	$\nu_{12} = \nu_{13}$	0.408	$G_{12} = G_{13}$	1890
$E_2 = E_3$	2050	ν_{23}	0.03	G_{23}	137

The mechanical properties of wood were verified by the mechanical modeling of an L-shaped connection under a load of 51 kg. Figure 4.22 shows the comparison between experiments and predictions for the deflection at the free end of the connection. There was a good agreement between the experimental and numerical results. This demonstrated that the mechanical properties of wood and the boundary conditions used in the model were very closed with the experiment.

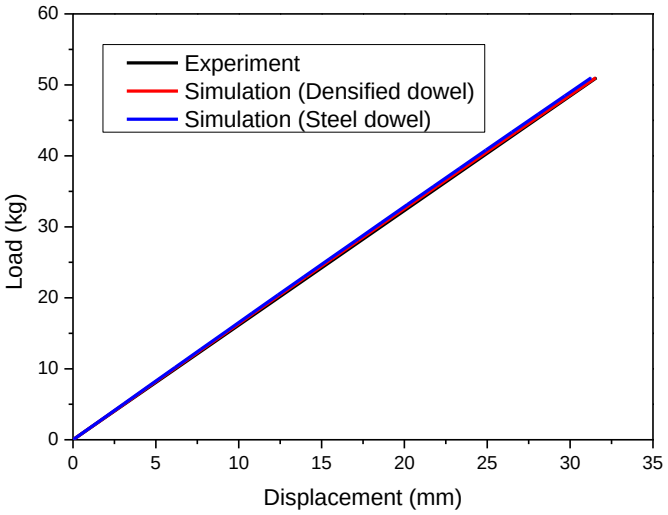

FIGURE 4. 22 - Load and deformation curves of connection.

4.4.2.2 Finite element modeling

The three-dimensional finite element models implemented in ABAQUS [1] for the calculation of the temperature development, charring depth, and deflection at the free end of L-shaped connections. The 20-node hexahedral solid elements are used for each part of the connection. The heat transfer to the surface of the member was given with the convective heat transfer coefficient h = 12.5 W/(m^2.K) and the emissivity coefficient ε = 0.9. The density, thermal conductivity, and specific heat capacity of steel vary as a function of the temperature, which was assumed according to EN 1993-1-2 [6]. For the FE thermo-mechanical analysis, the initial densities were 650 kg/m^3 and 1210 kg/m^3 for wood layer and densified wooden

dowel respectively (average values of test specimens). The measured mean values for moisture content were 10% for both wood layer and densified wooden dowel.

The thermo-mechanical modeling was verified with a series of fire tests on adhesive-free connections exposed to two external heat fluxes (49 and 60 $kW.m^{-2}$) on two sides under a load of 51 kg. The other surfaces are in contact with the environment with the temperature T = 22 °C. Due to symmetrical conditions, only half of the joint is discretized by the finite element method (figure 4.23) in order to reduce the calculating time. The global mesh, however, is continuous. The mesh consists of 243670 C3D8T elements (134578 for the column, 96804 for the beam, 12288 for the dowel.

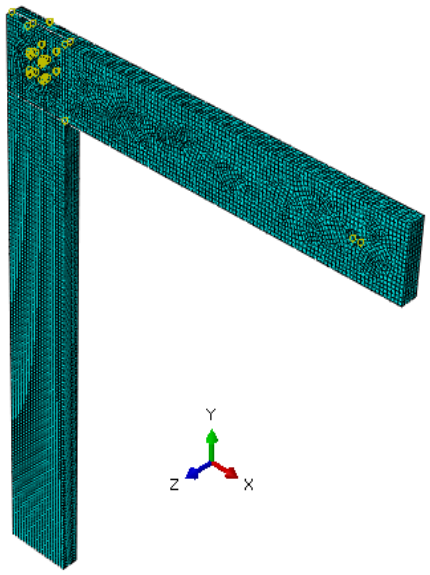

FIGURE 4. 23 - Mesh of the ahesive-free connection.

4.4.3 Results

4.4.3.1 Thermal transfer

1. L-shaped connection using densified wooden dowels

Comparison between simulated and measured temperatures in the wood layer (at 0 mm and 2 mm from the exposed surface), and densified wooden dowel (at 0 mm and 3 mm from the exposed surface) of the connection under two external heat fluxes (49 and 60 $kW.m^{-2}$) is presented in Figures 4.24 and 4.25.

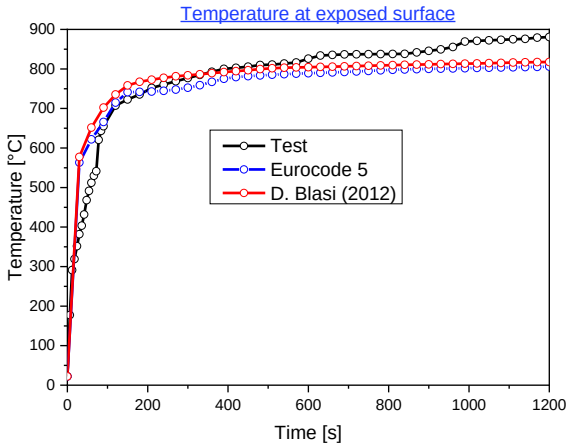

(a) Temperature in wood layer (0 mm)

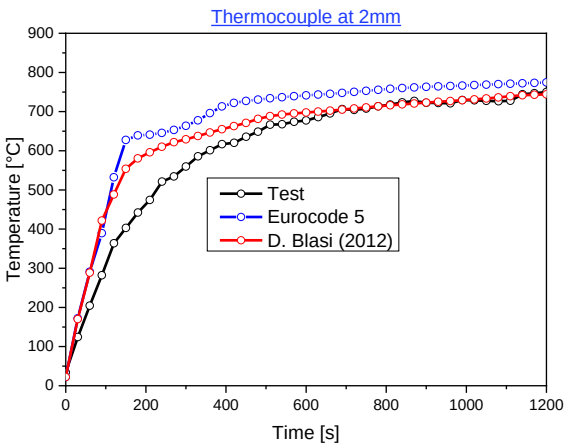

(b) Temperature in wood layer (2 mm)

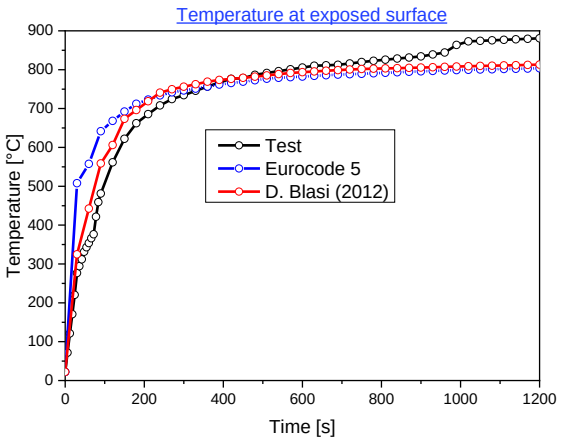

(c) Temperature in wood dowel (0 mm)

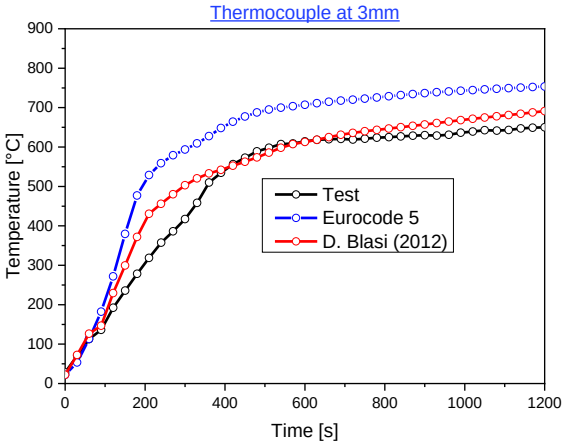

(d) Temperature in wood dowel (3 mm)

FIGURE 4. 24 - Simulated and measured temperatures for the thermal transfer in a connection exposed to heat flux of 49 kW.m^{-2}.

Experimental temperatures are values obtained from measurements in two connections using densified wooden dowels for each heat flux (the studied connection that was differently fixed on the masonry frame of the furnace). As for the cone calorimeter tests (Section 3.3), temperature plateaus were observed around 100 °C, and these are associated with water vaporization. It is also noted that the higher the heat flux, the longer the duration of the plateau. Taking into account the sink of energy associated with water vaporization allows a temperature slowdown of around 100 °C to be obtained in the kinetic model of D. Blasi (2012).

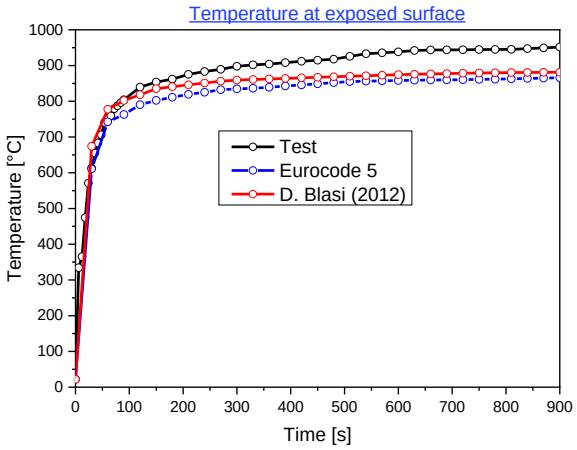

(a) Temperature in wood layer (0 mm)

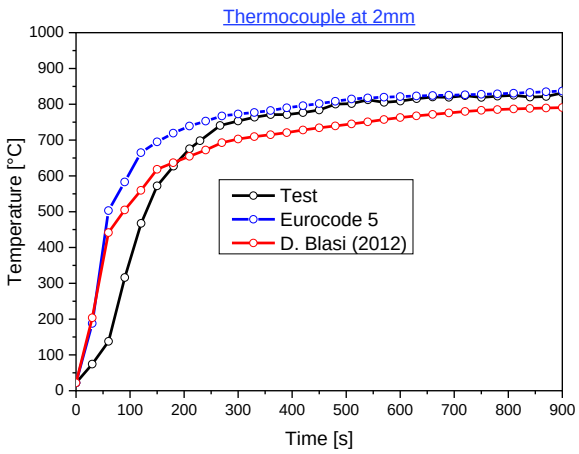

(b) Temperature in wood layer (2 mm)

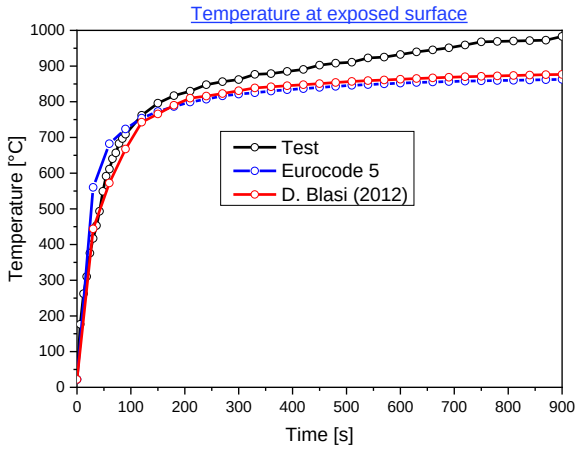

(c) Temperature in wood dowel (0 mm)

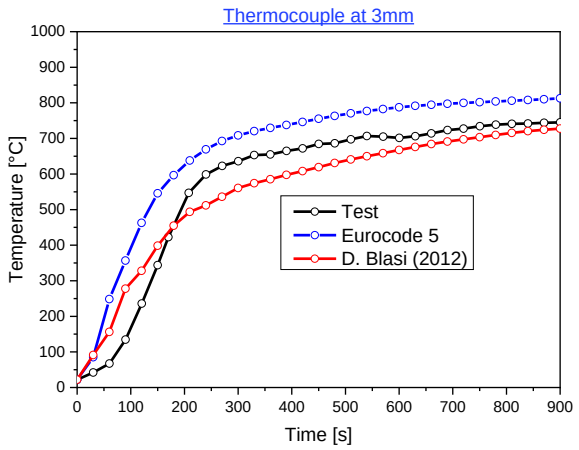

(d) Temperature in wood dowel (3 mm)

FIGURE 4. 25 - Simulated and measured temperatures for the thermal transfer in a connection exposed to heat flux of 60 kW.m^{-2}.

Above 100 °C, the general trend of the thermal transfer was simulated with the simplified model of Eurocode 5 and the kinetic model of D. Blasi (2012). The simulated temperatures at the end of the experiment, and particularly under the heat flux of 49 kW.m^{-2}, are in quite good agreement with the measurements. Calculated temperatures in the case of heat flux of 60 kW.m^{-2} are lower than experimental ones. This implies a slight delay for the simulated temperatures.

Figure 4.26 highlights the distribution of temperature and the residual cross-section of connection using densified wooden dowels obtained numerically after exposure of two heat fluxes of 49 kW/m^2 and 60 kW/m^2. The grey and red colors represent the charred material and

the 300 °C isotherms, respectively. The blue contour corresponds to a temperature close to the ambient temperature.

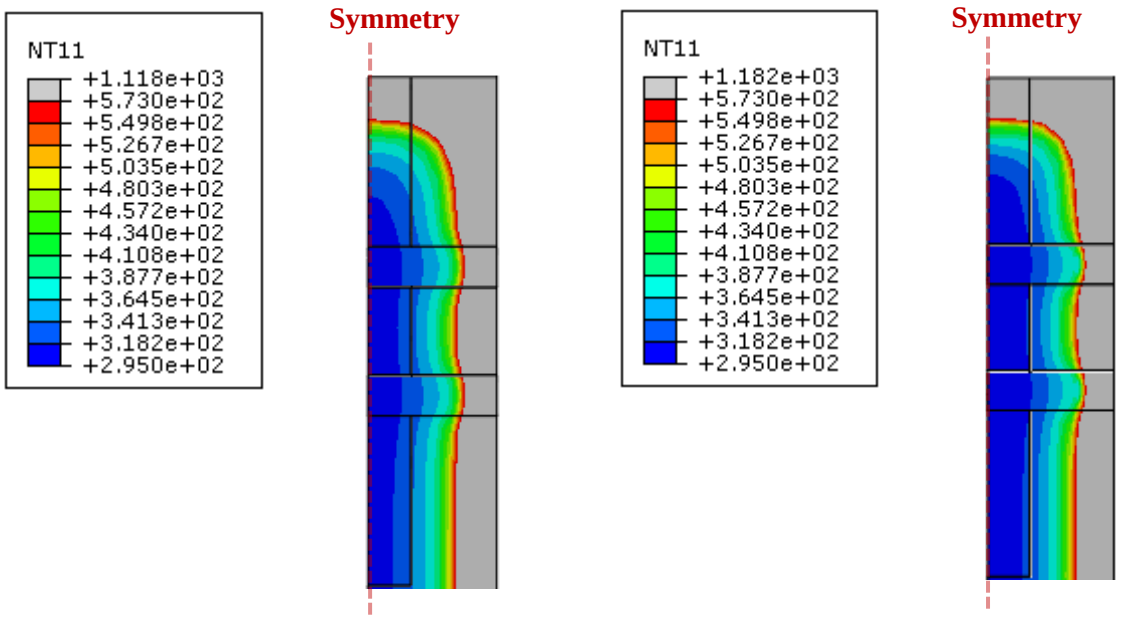

(a) Heat flux of 49 kW/m^2 (b) Heat flux of 60 kW/m^2

FIGURE 4. 26 - Temperature distribution and residual cross-section in connection using densified wooden dowels after exposure on two side.

Table 4.7 presents the comparison between the experimental and numerical residual cross-section of connection using densified wooden dowels after exposure to two heat fluxes (49 kW.m^{-2} and 60 kW.m^{-2}). A similar result to the previous experiment (CLT panels using densified wooden dowels) is observed.

Table 4.7. Comparison of measured and calculated charring depths in L-joint using wood dowels.

	Heat flux (kW/m^2)	Time (min)	Charring depth (Test 1)	Charring depth (Test 2)	Charring depth (D. Blasi [4])	Charring depth (EC5[5])
Wood layer	49	20	15	14,5	15	18
	60	15	16	16,5	14,5	18
Densified wood dowel	49	20	12	10	12	15
	60	15	11	11	11	14,5

2. L-shaped connection using steel dowels

Figures 4.27 and 4.28 show the comparison between simulated and measured temperatures in the wood layer (at 0 mm and 2 mm from the exposed surface), and steel dowel (at 0 mm, 3 mm, and 6 mm from the exposed surface) of the connection under two external heat fluxes (49 and 60 kW.m^{-2}).

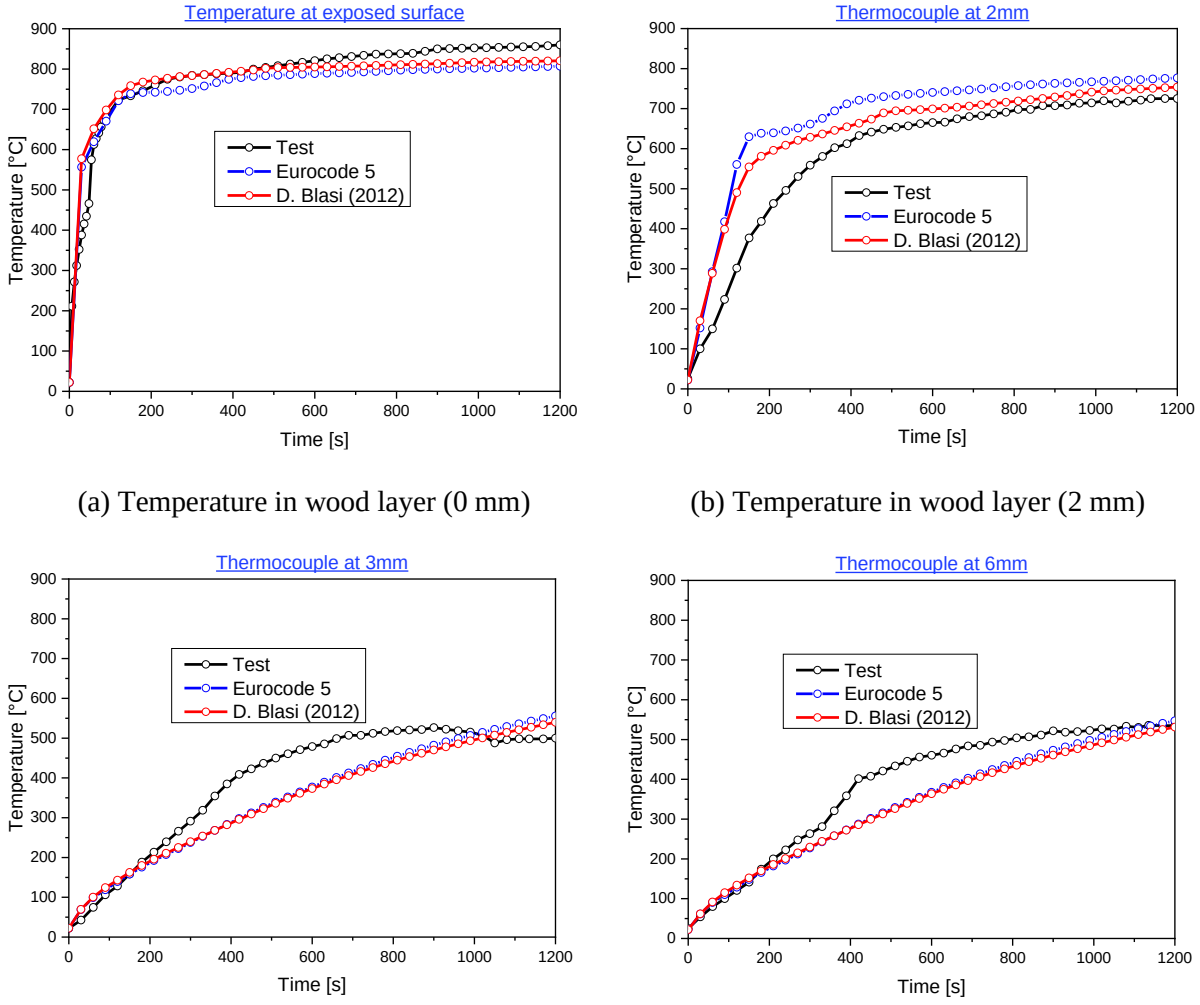

(a) Temperature in wood layer (0 mm)

(b) Temperature in wood layer (2 mm)

(c) Temperature in steel dowel (3 mm)

(d) Temperature in steel dowel (6 mm)

FIGURE 4. 27 - Simulated and measured temperatures for the thermal transfer in a connection exposed to heat flux of 49 kW.m^{-2}.

A similar trend of the thermal transfer in the wood layer when compared with the previous connection was observed according to the simplified model of Eurocode 5 and the kinetic model of D. Blasi (2012). The simulated temperatures in steel dowel, particularly under the heat flux of 60 kW.m^{-2}, are in quite good agreement with the measurements.

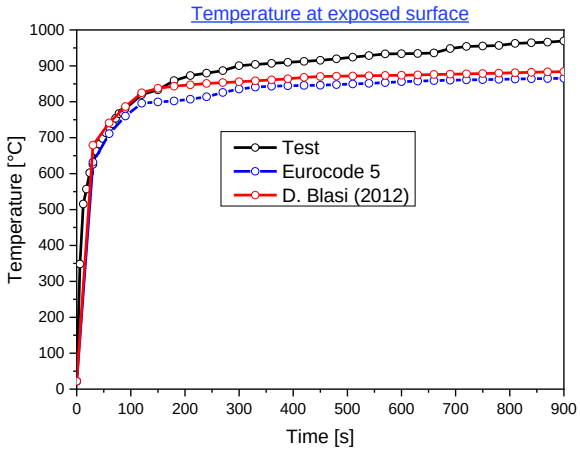

(a) Temperature in wood layer (0 mm)

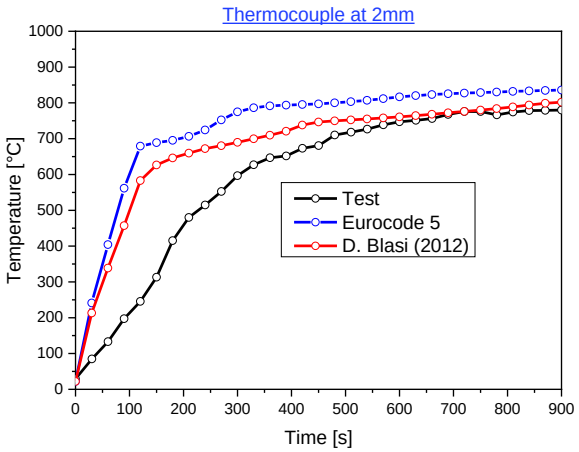

(b) Temperature in wood layer (2 mm)

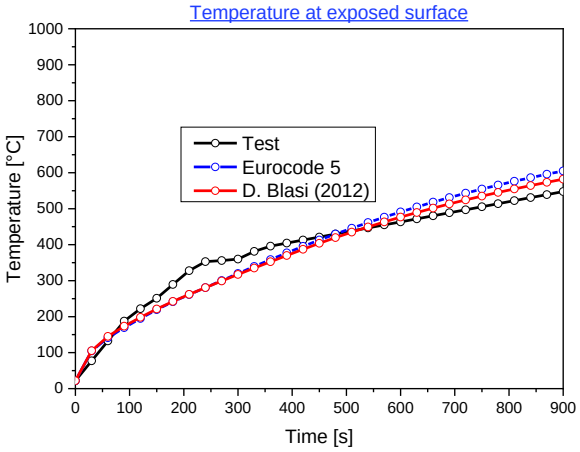

(c) Temperature in steel dowel (0 mm)

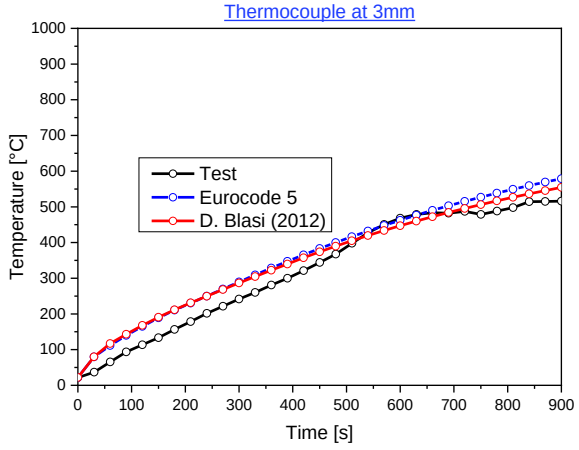

(d) Temperature in steel dowel (3 mm)

FIGURE 4. 28 - Simulated and measured temperatures for the thermal transfer in a connection exposed to heat flux of 60 kW.m^{-2}.

The distribution of temperature and the residual cross-section of connection using steel dowels obtained numerically after exposure of two heat fluxes of 49 kW/m^2 and 60 kW/m^2 were highlighted in Figure 4.29.

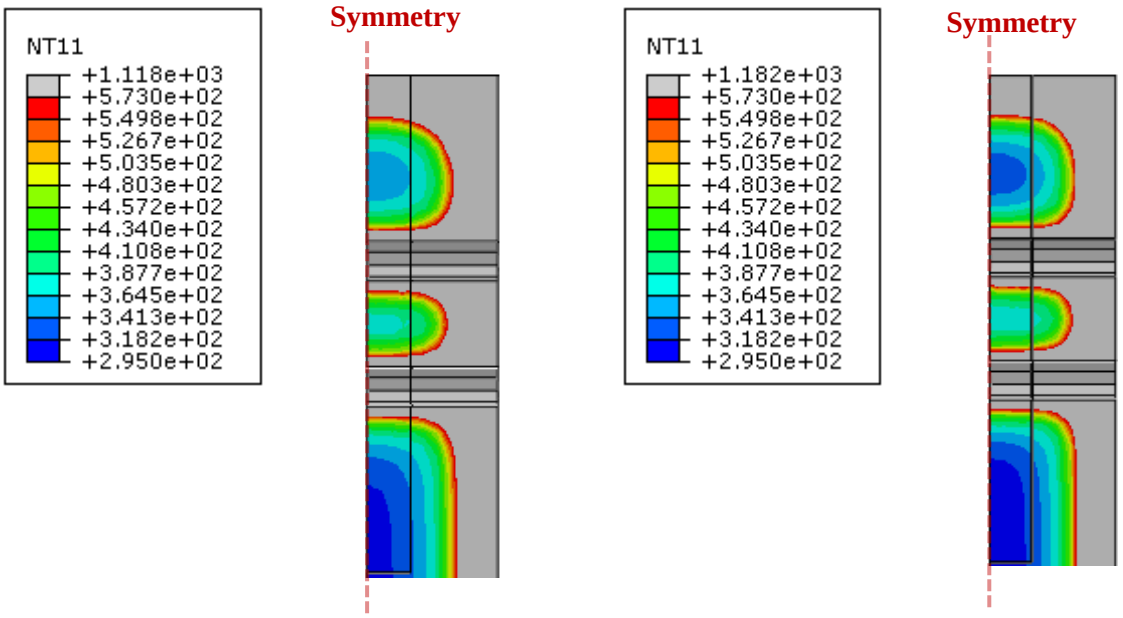

(a) Heat flux of 49 kW/m^2 (b) Heat flux of 60 kW/m^2

FIGURE 4. 29 - Temperature distribution and residual cross-section in connection using steel dowels after exposure on two side.

The comparison between the experimental and numerical residual cross-section of connection using steel dowels after exposure of two heat fluxes (49 kW.m^{-2} and 60 kW.m^{-2}) is depicted in Table 4.8. A good agreement between experiment and prediction is observed.

Table 4.8. Comparison of measured and calculated charring depths in L-joint using steel dowels.

	Heat flux (kW/m^2)	Time (min)	Charring depth (Test 1)	Charring depth (Test 2)	Charring depth (D. Blasi [4])	Charring depth (EC5[5])
Wood layer	49	20	17	-	17	18
	60	15	17	17	16,5	18

4.4.3.2 Deflection at the free end

1. L-shaped connection using densified wooden dowels

The simulation was carried out for the L-shaped joint using densified wooden dowels with the loading of 51 kg under two external heat fluxes (49 and 60 kW.m^{-2}). The result obtained in terms of displacement of the free end of the connection as a function of the time of exposure to fire is illustrated in Figures 4.30 and 4.31 for 2 models: EC5 and kinetic model of D. Blasi.

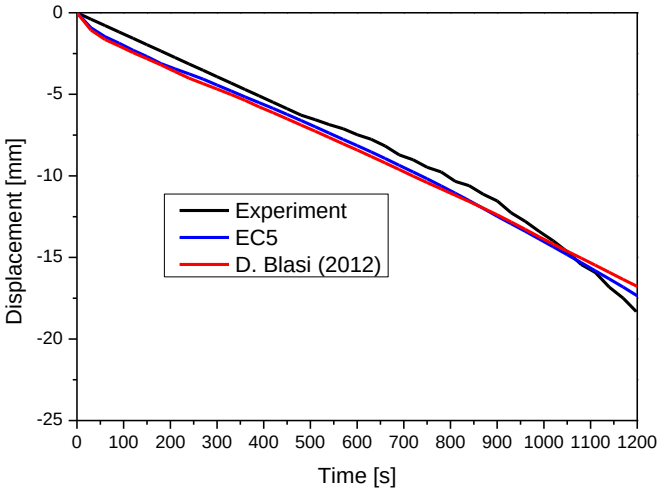

FIGURE 4. 30 - Experimental and numerical displacements of the free end of the connection using densified wooden dowels under a heat flux of 49 kW.m^{-2}.

The tests were stopped after approximately 20 and 15 min for the heat flux of 49 and 60 kW.m^{-2} respectively. Overall, the predicted displacement is very close to the experimental one. The model based on the EC5 regulatory approach [5] gives somehow a less estimate than the pyrolysis model of D. Blasi et al. [4]. The predicted displacements increase gradually but remain almost linear, which is the same with the tests.

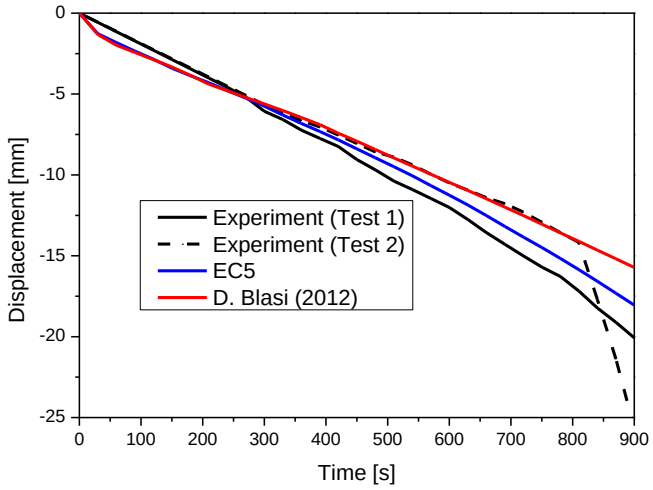

FIGURE 4. 31 - Experimental and numerical displacements of the free end of the connection using densified wooden dowels under a heat flux of 60 kW.m^{-2}.

2. L-shaped connection using steel dowels

Figures 4.32 and 4.33 show the displacement at the free end of the connection using steel dowels as a function of the time of exposure to fire. Overall, the predicted displacements give

somehow less estimate than experiment measurements, especially for the case of heat flux of 49 kW.m^{-2}.

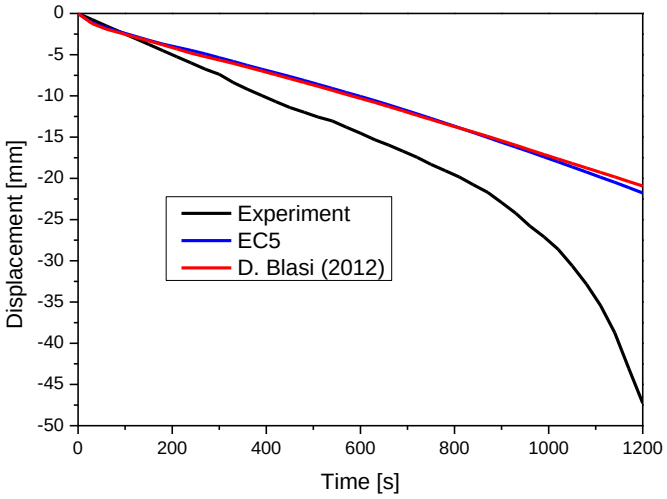

FIGURE 4. 32 - Experimental and numerical displacements of the free end of the connection using steel dowels under a heat flux of 49 kW.m^{-2}.

The large difference between prediction and experiment in the case of heat flux of 49 kW.m^{-2} may come from limiting the validity of comparisons. The comparison is based on only one test. Measurements were not repeated, mainly due to technical and financial reasons. This is confirmed in the case of heat flux of 60 kW.m^{-2} with repeated measurements (2 times). The global displacement is correctly estimated in about 10 minutes of the test, but further modifications will be needed to improve the estimation of the displacements during the whole test. More fire tests are therefore needed to validate the mechanical part of the model.

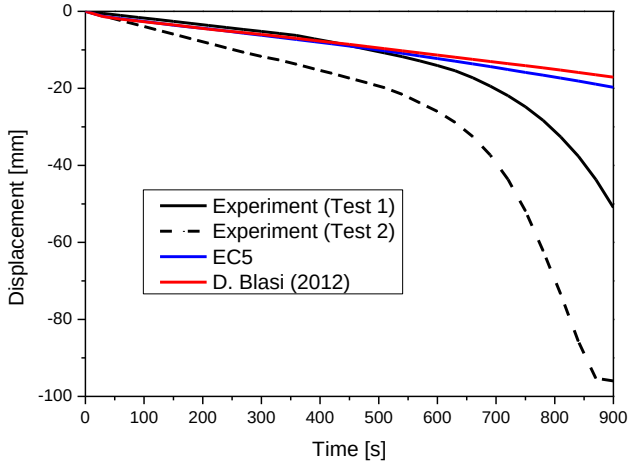

FIGURE 4. 33 - Experimental and numerical displacements of the free end of the connection using steel dowels under a heat flux of 60 kW.m^{-2}.

After 10 minutes of the test, there is an important gap with the experimental and numerical displacement. The possible explanation may come from the difference between experimental and simulated friction between wood layers and steel dowels (see Section 4.4.1). In particular, the friction coefficients vary significantly due to the formation of charcoal surrounding steel dowel while in the model, this value is assumed constant equal to 0,5.

4.5 Influence of various parameters

4.5.1 Carbonization - charring rate

The calculated temperatures of the charred parts are similar to the experimental values, i.e., close to the 300 °C isotherms. Timber carbonization rate is calculated in relation to the 300 °C isotherms by measuring the distance from the outside to the inside of the timber members [7].

Table 4.9. Charring depth and average charring rate in virgin Spruce wood.

	Charring depth [mm]		Charring rate [mm/min]	
	20 kW/m^2	75 kW/m^2	20 kW/m^2	75 kW/m^2
Experiment	12	15	0,6	1,5
Eurocode 5	8	13	0,4	1,3
D. Blasi	13	16	0,65	1,6

The charring depths, as well as the computed charring rates in the panel made in virgin spruce wood (cone calorimeter tests), by assuming linear development, after the fire-exposure time of 20 min and 10 min under two heat fluxes of 20 kW/m^2 and 75 kW/m^2 respectively, are summarized in Table 4.9. Due to the difference in the boundary conditions of the imposed temperature (the heat fluxes and the ISO curve), the charred depths (and charring rates) are different from the value recommended by Eurocode 5 (0.70 mm/min) [5].

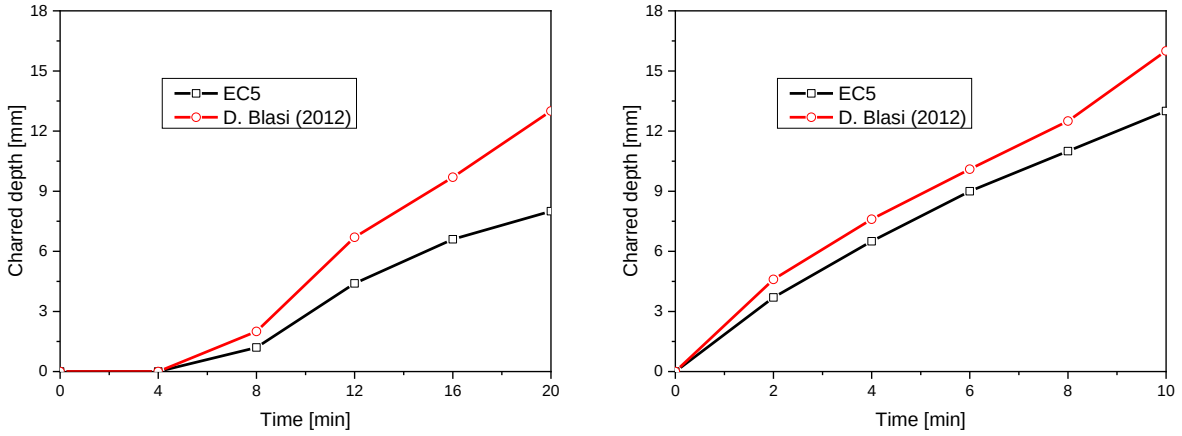

(a) Heat flux of 20 kW/m^2 (b) Heat flux of 75 kW/m^2

FIGURE 4. 34 - Charring depth in virgin spruce wood in cone calorimeter test : (a) Heat flux of 20 kW.m^{-2} and (b) Heat flux of 75 kW.m^{-2}.

Figure 4.34 shows the charring depths in virgin spruce wood in cone calorimeter test are calculated, based on the 300 °C isotherm movement, and plotted versus fire-exposure time. It can be seen that the charring rate is non-linear with exposed time. This result is consistent with the literature [8].

Table 4.10. Charring depth and average charring rate in virgin and densified Spruce wood.

	Charring depth [mm]		Charring rate [mm/min]	
	20 kW/m^2	75 kW/m^2	20 kW/m^2	75 kW/m^2
Virgin wood	13	16	0,65	1,6
Densified wood	3,5	7	0,175	0,7

Table 4.10 shows the numerically predicted maximum charring depths as well as charring rates (Kinetic model of D. Blasi), by assuming linear development, under two heat fluxes of 20 kW/m^2 and 75 kW/m^2 for both virgin and densified Spruce wood. It can be observed from Table 4.10, the charred depth (and charring rate) is higher in virgin Spruce wood as compared to the densified one. This can be explained by the effect of the densification process. Indeed, the densification process reduces the pores and voids (called lumen) between the cell walls of low-density wood, so the density will be increased. Timber with high density, such as densified spruce tended to burn and char at higher temperature or heat flux because of its high decomposition energy and thermal conductivity.

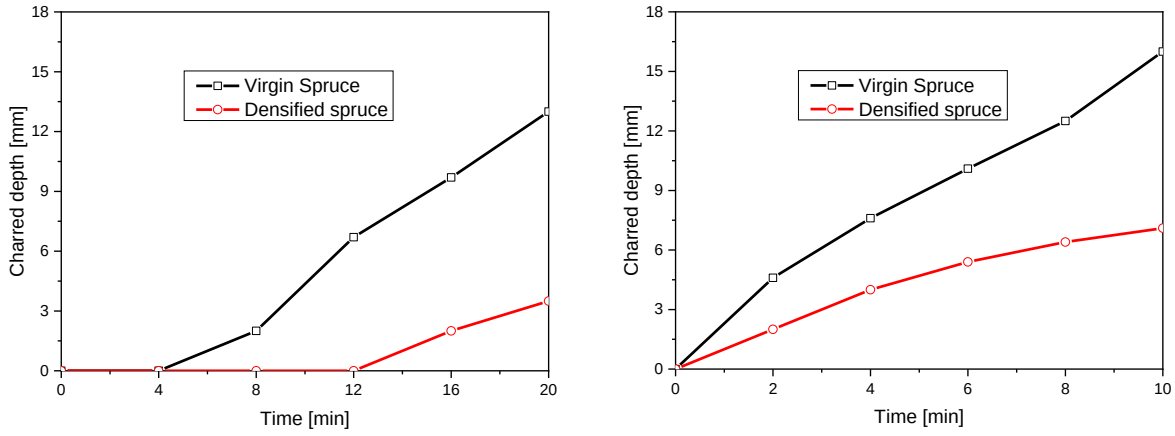

(a) Heat flux of 20 kW/m^2 (b) Heat flux of 75 kW/m^2

FIGURE 4. 35 - Charring depth in virgin and densified spruce wood in kinetic model (D. Blasi) for cone calorimeter tests: (a) Heat flux of 20 kW.m^{-2} and (b) Heat flux of 75 kW.m^{-2}.

In addition, the charring depths in both virgin and densified Spruce wood are calculated, based on the 300 °C isotherm movement, and plotted versus fire-exposure time in Figure 4.35.

The experimentally measured and the numerically predicted (Kinetic model of D. Blasi) maximum charring depths as well as the average charring rates, by assuming linear development, under two heat fluxes of 49 kW/m^2 and 60 kW/m^2 for densified wooden dowels (L-joint connection) are summarized in Table 4.11. It can be seen that the higher of heat flux, the higher the charred depth (and charring rate) in the densified wooden dowel.

Table 4.11. Charring depth and average charring rate in densified wooden dowel.

	Charring depth [mm]		Charring rate [mm/min]	
	49 kW/m^2	60 kW/m^2	49 kW/m^2	60 kW/m^2
Experiment	11	11	0,55	0,73
D. Blasi	12	11	0,6	0,73

Furthermore, the numerically predicted charring depth using the kinetic model (D. Blasi) is calculated based on the 300 °C isotherm movement and displayed in Figure 4.36 as a function of fire-exposure time under two heat fluxes of 49 kW/m^2 and 60 kW/m^2 for densified wooden dowels (L-joint connection).

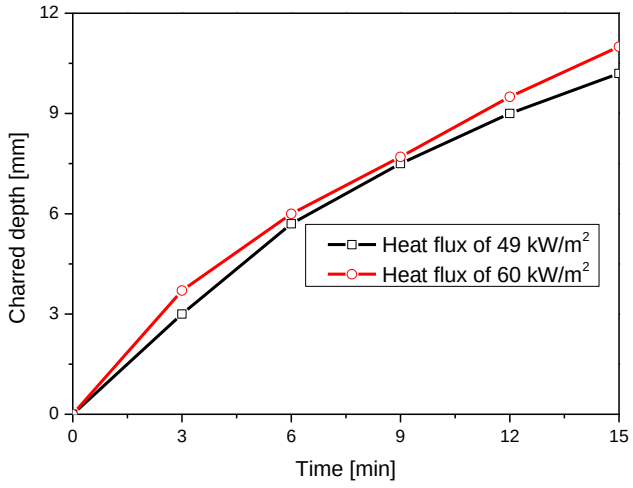

FIGURE 4. 36 - Charring depth in densified wooden dowel in kinetic model (D. Blasi).

4.5.2 Densification ratio

A study on the impact of the densification ratio of the material on the heat transfer results is presented in this section. The thermal model is used on the L-joint connection for different

densification ratios of densified wooden dowel (33%, 68%, and 80%). As a reminder, taking into account the pyrolysis process in wood is done using the kinetic model of D. Blasi. The initial density and thermal conductivity are presented in Table 4.12.

Table 4.12. Density and thermal conductivity for different densification ratios of wood dowel.

Densification ratio [%]	Density [kg/m^3]	Thermal conductivity [W/(m.K)]
33%	822	0,134
68%	1210	0,175
80%	1343	0,189

In Figure 4.37, we notice that the thermal conductivity is well affected by the densification ratio of the material through the law of mixtures used in the thermal model. About the thermal conductivity of the material, the higher the densification ratio, the higher the thermal conductivity. The same is true for the density of the material.

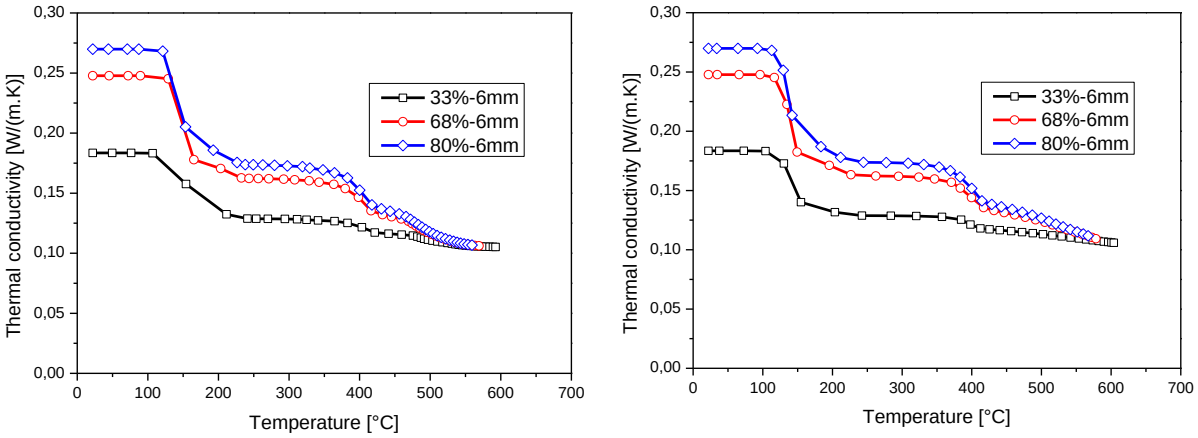

(a) Heat flux of 49 kW/m^2 (b) Heat flux of 60 kW/m^2

FIGURE 4. 37 - Impact of the densification ratio on the thermal conductivity at the position of 6 mm from the exposed surface of densified wooden dowel.

The thermal diffusion calculated in the position of 6 mm from the exposed surface of densified wooden dowel for the different densification ratios is presented in Figure 4.38. We note that the thermal diffusion is higher when the densification ratio is low. This can be explained by the heat transfer which is faster in this case.

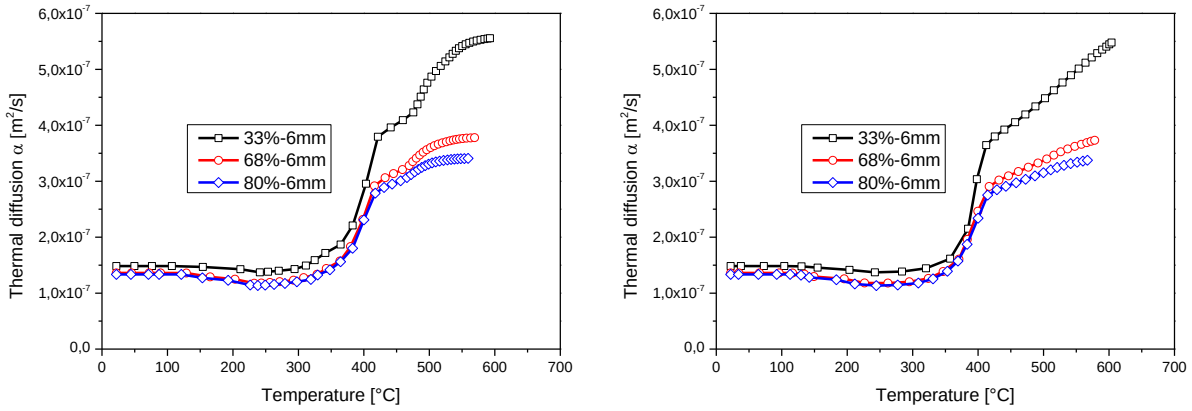

(a) Heat flux of 49 kW/m^2 (b) Heat flux of 60 kW/m^2

FIGURE 4. 38 - Impact of the densification ratio on the thermal diffusion at the position of 6 mm from the exposed surface of densified wooden dowel.

Figures 4.39 and 4.40 presented the temperatures on the exposed side and on the 6mm from the exposed side under two external heat fluxes (49 and 60 kW.m^{-2}). There is a clear impact of the densification ratio of the material on the simulated temperatures with a reduction in the rate of heat transfer when the densification ratio increases. As the amount of density is greater, a greater amount of energy is necessary for its thermal degradation which reduces the kinetics of temperature rise.

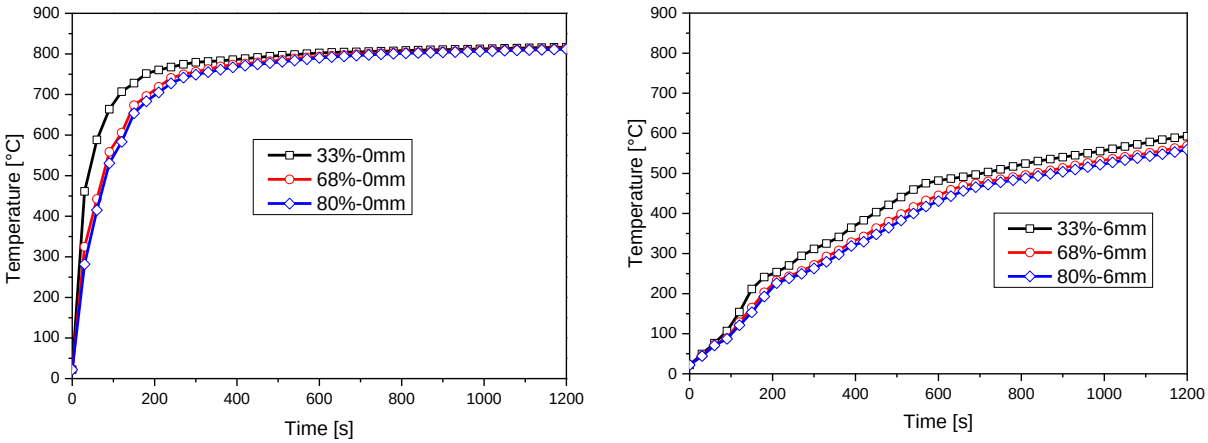

FIGURE 4. 39 - Impact of the densification ratio on the heat transfer through the densified wooden dowel under a heat flux of 49 kW.m^{-2}.

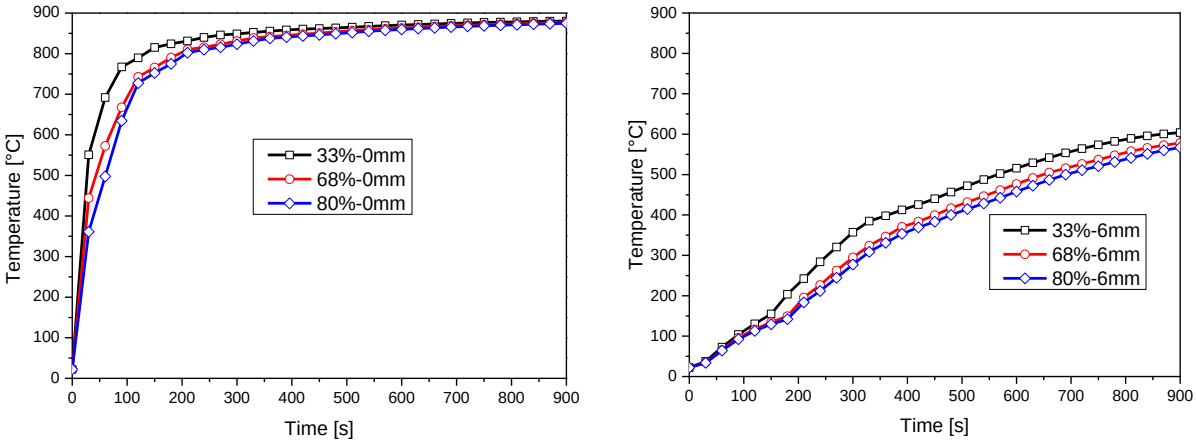

FIGURE 4. 40 - Impact of the densification ratio on the heat transfer through the densified wooden dowel under a heat flux of 60 kW.m^{-2}.

The charring depths, as well as the computed charring rates in the densified wooden dowel at different densification ratios, by assuming linear development, after the fire-exposure time of 20 min and 15 min under two heat fluxes of 49 kW/m^2 and 60 kW/m^2 respectively, are summarized in Table 4.13. A similar effect of densification ratio of material on carbonization - charring rate to the previous study (evolution of temperature profiles) is observed. The higher of densification ratio, the lower the charred depth (and charring rate) in the densified wooden dowel.

Table 4.13. Charring depth and average charring rate in densified wooden dowels at different densification ratios.

	Charring depth [mm]		Charring rate [mm/min]	
	49 kW/m^2	60 kW/m^2	49 kW/m^2	60 kW/m^2
33%	13,5	12,5	0,675	0,833
68%	12	11	0,6	0,733
80%	11,8	10,8	0,59	0,72

From a general point of view, we find that there is a significant impact of the densification ratio of the material on the simulation results of heat transfer. However, an overestimation of the densification ratio will therefore result in an insignificant change of the simulated fire resistance of the cellulosic material (a small difference between densification ratio of 68% and 80%) which would lead to damage of the cells due to the densification

process. In contrast, an underestimated densification ratio, for example of 33%, results in a relatively rapid heat transfer which will result in reducing the effectiveness of densified wood in both bearing and heat-resistant aspects.

4.5.3 Type of material of the dowel

During this study, we have studied the impact of the type of the material of the dowel on the temperature distribution in the wood layer and the degradation of the holes and wood layer. This study was carried out on the L-joint connection under a heat flux of 49 kW/m^2 with two types of material of dowel: densified wooden dowel and steel dowel.

The temperature distribution of the connection with densified wooden dowels is shown in Figure 4.41a after 20 min of exposure to heat flux of 49 kW/m^2. It can be seen that most of the inner parts of the wood layer and densified wooden dowel show ambient temperature and there is almost no effect of the densified wooden elements on the temperature distribution of the wood layer. This can be explained by the slower heat transfer in densified wood due to the smaller thermal diffusion of densified wood when compared to the wood layer. This is also confirmed with previous results (cone calorimeter tests and CLT panels using densified wooden dowels). Figure 4.42 presents the comparison between the wood layer and the densified wood dowel on the thermal diffusion at the position of 3 mm from the exposed surface under a heat flux of 49 kW/m^2.

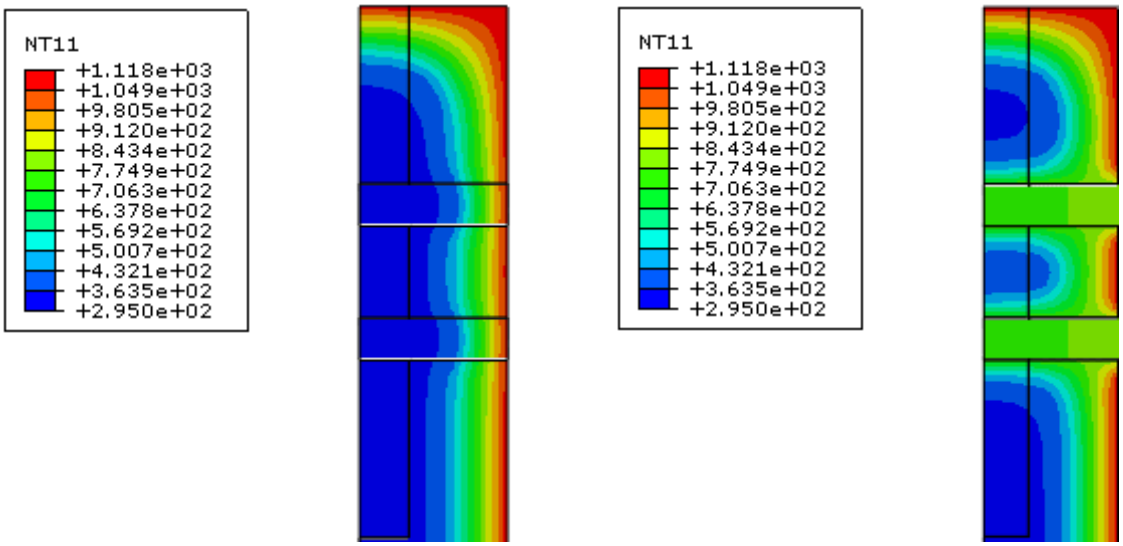

(a) Connection using densified wooden dowel (b) Connection using steel dowel

FIGURE 4. 41 - Temperature distribution in L-joint connection under a heat flux of 49 kW.m^{-2}.

The influence of the steel elements on the temperature distribution of the wood layer can be seen in Figure 4.41b for L-joint connection using steel dowels after 20 min exposed to heat flux of 49 kW/m^2. Due to the high thermal conductivity of steel, the heat flux from the steel elements into the wood layer led to much higher temperatures inside the wood layer, especially for the wood layer which is near steel dowel.

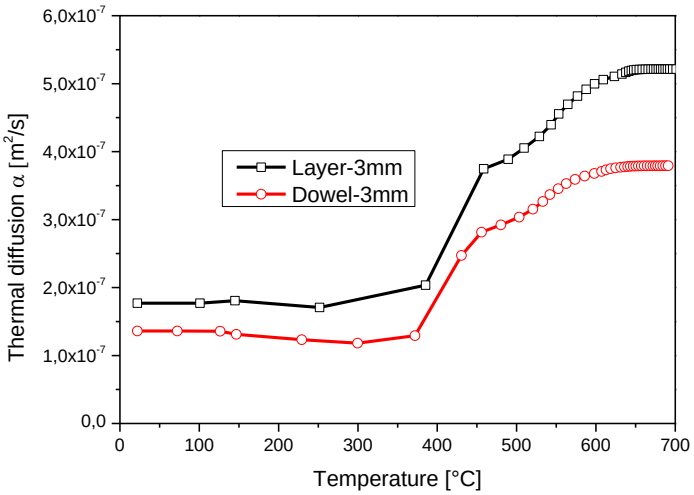

FIGURE 4. 42 - Comparison between layer and dowel on the thermal diffusion at the position of 3mm from the exposed surface under a heat flux of 49 kW.m^{-2}.

To study the impact of the type of the material of the dowel on the degradation of the holes and wood layer, the simulation is carried out in a longer period of time (about 60 minutes). The degradation of the holes and wood layer in the L-joint connection for both two types of dowels (densified wooden dowels and steel dowels) is presented in Figures 4.43 and 4.44. The charred layer forms above T = 300 °C and is shown in grey. The undamaged wood is shown in blue. Between the charred layer and the undamaged wood, there are areas of pyrolysis (red, yellow, and green) and drying (turquoise).

In general, we observe that the degradation of the holes and wood layer in the L-joint connection using steel dowels is much faster than the remaining one. Indeed, it can be seen that, after 5 minutes of exposure, most of the holes in the L-joint connection using densified wooden dowels are undamaged wood (blue area). Meanwhile, the whole holes in the L-joint connection using steel dowels are areas of pyrolysis (red, yellow, and green) and drying (turquoise). This can be explained by the transfer of heat flux from the steel elements into the wood layer due to the high thermal conductivity of steel. This result is consistent with the literature [9].

At about 10 minutes exposed to the heat flux of 49 kW/m^2, the whole holes in the L-joint connection using steel dowels are completely charred (grey area) and the steel dowels are embedded in charred wood. The degradation of the wood layer near the steel dowel (charred layer) grows in both directions: the direction of heat transfer and the direction perpendicular to it. This can be clearly observed at 20 and 40 minutes of exposure.

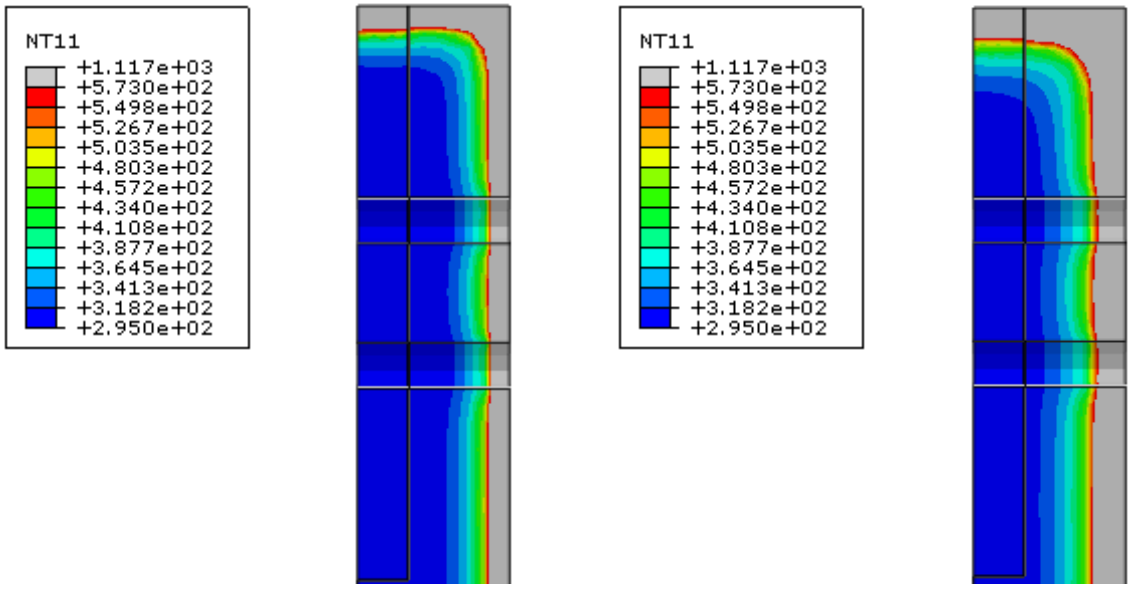

(a) t = 5 min (b) t = 10 min

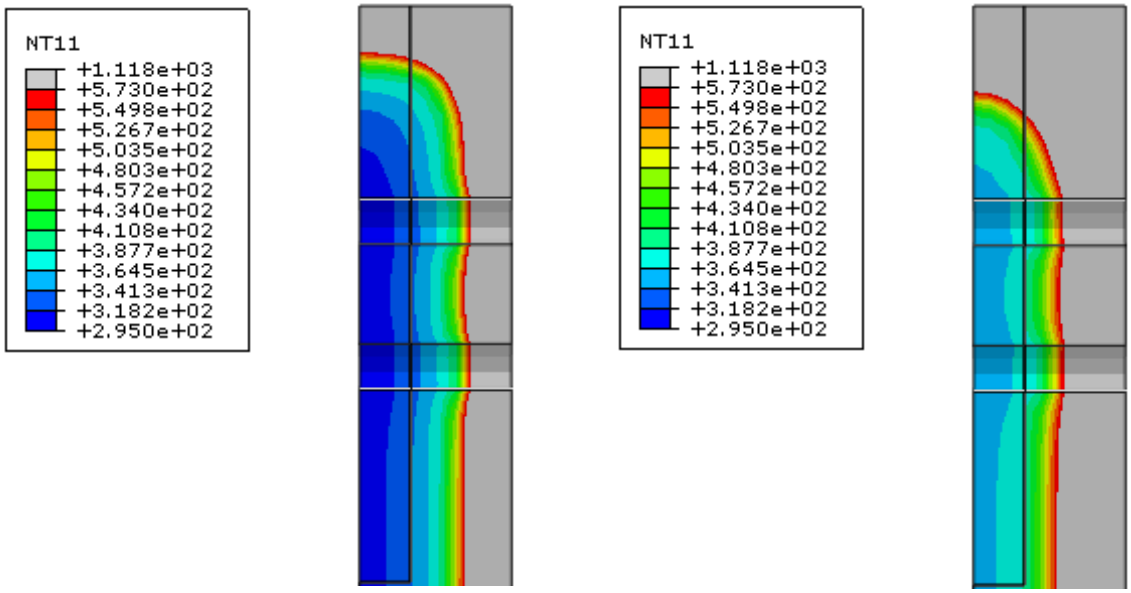

(c) t = 20 min (d) t = 40 min

FIGURE 4. 43 - The degradation of the holes and wood layer in L-joint connection using densified wooden dowels under a heat flux of 49 kW.m^{-2}.

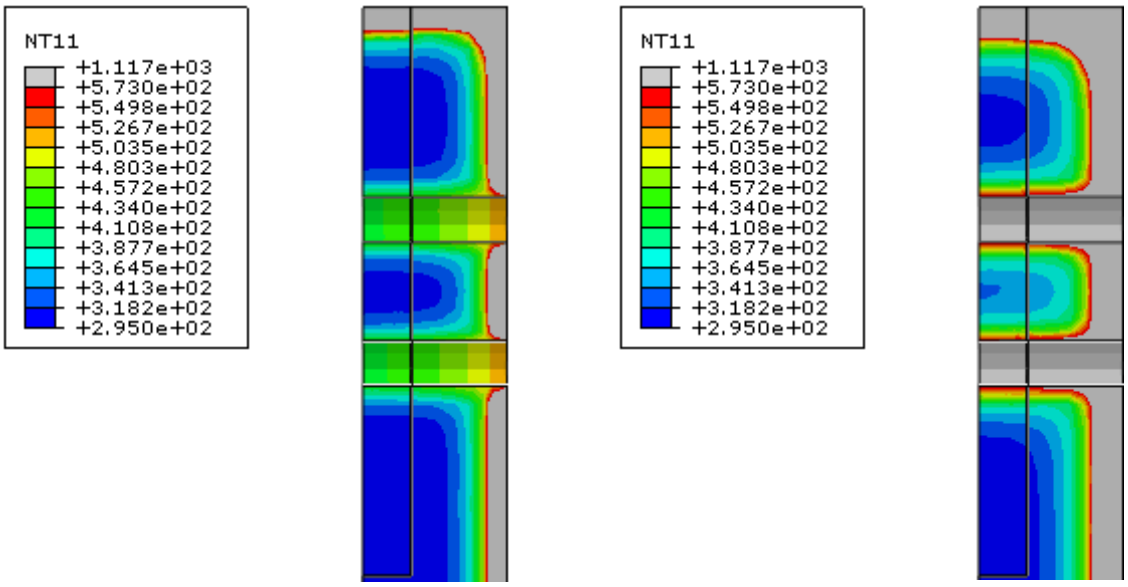

(a) t = 5 min (b) t = 10 min

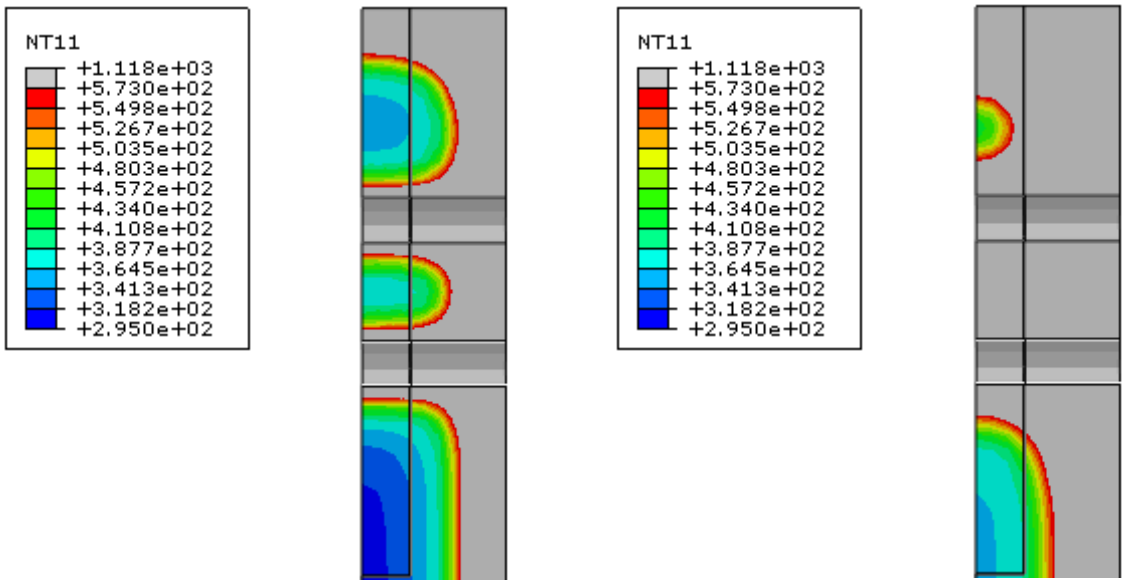

(c) t = 20 min (d) t = 40 min

FIGURE 4. 44 - The degradation of the holes and wood layer in L-joint connection using steel dowels under a heat flux of 49 $kW.m^{-2}$.

After 40 minutes of exposure, all holes and surrounding wood in the L-joint connection using steel dowels are completely charred (grey area). In L-joint connection using densified wooden dowels, about half of the holes and wood layer are charred layers in the direction of heat transfer.

4.6 Conclusion

In this chapter, the thermal characterization results presented in chapter 3 were used as input data for the thermal and thermomechanical model of the fire tests in our project. Firstly, a numerical model to simulate the thermal behavior of the cone calorimeter tests has been presented. This model takes into account heat sources to simulate the reactions vaporization and thermal degradation, i.e. pyrolysis of the material and combustion pyrolysis gases. This is added to the calculation of the local variation of thermal properties depending on the progress of the pyrolysis reactions to take into account the variation in properties of the material during its thermal degradation.

Secondly, we carried out the tests and modeling for CLT panels using densified wooden dowels in the fire condition. The simulation results are relatively consistent and in good agreement with experimental measurements. The results of the adhesive-free CLT panels test and modeling will serve as the basis for the evaluation of the heat transfer process of densified wooden dowels.

In the next step, a methodology for predicting the thermomechanical behavior of the wood material has been proposed and applied to the simulation of L-joint tests. We note that the use of 2 cases of material of dowel (steel dowel and densified Spruce dowels) had aim to evaluate the effectiveness of the use of compressed wooden dowel instead of conventional connection by steel dowels. From a qualitative point of view, the simulation results obtained on all the examples are very close to the test results.

Lastly, the influence of various parameters of densified wood (carbonization, densification ratio…) is carried out with the model developed. Overall, the heat transfer speed of densified wood is lowest when compared to virgin wood and steel material. This indicates the effectiveness of using densified wood in fire-safe conditions.

At the end of this study, we can say that the main objective of the thesis program is largely achieved. An advanced approach has been developed to predict the fire resistance of wooden structures using densified wooden dowels. However, some points of improvement are necessary in order to enrich the methodology incremental and to provide the engineer with a real virtual simulation tool:

- The application of kinetic thermal models on the various tests shows that the kinetic models describe better the fire behavior of the wood material compared to thermal models

simplified (EC5). The simulations reveal a dispersion of predictions compared to experimental measurements at temperatures above 450 °C. Remember that these models do not hold account of the combustion phase. It is therefore desirable to improve this point in order to enrich these models.

- The thermo-mechanical coupling is carried out according to the regulatory approach EC5 [5] relating to the fire resistance of wooden structures, by applying the reduction factor $K_{\emptyset}$ to the mechanical resistance of a softwood tree. The application and integration of this coupling technique in a finite element code are kept simple. The choice of the reduction coefficient $K_{\emptyset}$ is indicated by the detailed bibliographic study in chapter 2, section 2.3.3. We recommend doing a more in-depth study to improve the results that flow from its use, especially for densified wood material.

- From the point of view of the study of the fire performance of the connection, the numerical simulations show that the reduction of tight-fitting of joint is needed to take into account numerically. This type of modification can lead to a substantial reduction in the bearing capacity of connection in the event of a fire. It is also possible to describe the change of the friction coefficient between wood layers and dowels as a function of temperature.

Bibliography of chapter 4

[1] Abaqus, Theory Manual, Version 6.14, Providence, RI : Dassault Systèmes Simulia Corp (2016).

[2] Cueff G., Mindeguia J.-C., Dréan V., Breysse D., Auguin G, Experimental and numerical study of the thermomechanical behaviour of wood-based panels exposed to fire, Construction and Building Materials 160 (2018) 668-678.

[3] Grioui N., Halouani K., Zoulalian A., HalouaniF., Thermogravimetric analysis and kinetics modeling of isothermal carbonization of olive wood in inert atmosphere, Thermochimica Acta 440 (2006) 23-30.

[4] Broström M., Nordina A., Pommer L., Branca C., Di Blasi C., Influence of torrefaction on the devolatilization and oxidation kinetics of wood, Journal of Analytical and Applied Pyrolysis 96 (2012) 100-109.

[5] Eurocode 5 - Design of timber structures. Part 1-2: General - Structural fire design, CEN 2004 (European Committee for Standardization), EN 1995-1-2, Brussels, Belgium.

[6] Eurocode 3: Design of Steel Structures - Part 1-2: General rules - Structural Fire Design, British Standards Institute, London, UK (2004).

[7] Samaké A., Taazount M., Audebert P., Palmili P., Thermo-hydric transfer within timber connections under fire exposure: Experimental and numerical investigations, Applied Thermal Engineering 63 (2014) 254-265.

[8] Schnabl S., Turk G., Planinc I., Buckling of timber columns exposed to fire, Fire Safety Journal 46 (2011) 431-439.

[9] Erchinger C., Frangi A., Fontana M., Fire design of steel-to-timber dowelled connections, Engineering Structures 32 (2010) 580-589.

General conclusion and perspectives

General conclusion

The main objective of this thesis was to develop a digital tool to predict the thermomechanical behavior of wood structures assembled by densified wooden dowels during a fire resistance test. Therefore, a numerical model making it possible to take into account the particularities of the thermal degradation of cellulosic materials has been designed, capable in particular of simulating vaporization reactions water, wood pyrolysis, and pyrolysis gas combustion while taking into account the variation of thermal and mechanical properties of the material as a function of temperature.

On the basis of a bibliographic study (chapter 1), the necessary information to understand the thermal and mechanical behavior of wood and densified wood under the influence of temperature and humidity could be established. The various phenomena of thermal degradation of cellulosic materials which must be taken into account during the numerical simulation to transcribe the thermomechanical behavior of cellulosic materials were also discussed in this part.

The second part presents the theoretical and numerical aspects of the thermomechanical model. The thermal (isotropic) model takes into account to some extent the impact of reactions vaporization and thermal degradation (pyrolysis and combustion of pyrolysis gases) of the material through thermally activated reactions and through the application of heat sources volumic. A three-dimensional thermomechanical model using a reduction factor K_θ on the modulus of elasticity and the mechanical resistance of a softwood suggested in the Eurocode 5 regulation, relating to resistance to fire of wooden structures, has been developed. The numerical aspects of the thermo-mechanical model with a classical variational formulation with two fields (temperature and displacement) have been used. After discretization by the finite element method of the two functionals, a coupled thermomechanical system is obtained.

To provide the necessary parameters for the digital models developed, various experiment programs were carried out (chapter 3). Thermo-physical properties (thermal conductivity, specific heat, and density) were measured via the hot plate method. The kinetic parameters of the pyrolysis reaction were determined by means of an analysis

thermogravimetric (ATG) to obtain activation energy and pre-exponential factor of the pyrolysis reaction for given test conditions (rate of heating, atmosphere, etc.). Once these necessary parameters are determined, they are integrated into a complete numerical model to simulate the behavior under the fire of structures using densified wood on small and large scales. To study the thermal behavior of both virgin and densified wood for different conditions, the cone calorimeter test was presented. The results of the cone calorimeter tests will form the basis for the validation of the thermal model developed. The measures are undertaken to present an innovative character in view of the little documentation available on the properties of densified wood, and in particular on their evolution with the temperature.

In the last part, the numerical procedures were applied and validated on several fire tests. The tests were carried out with a fire defined by radiant panels to create different heat fluxes. Some fire tests were carried out in the laboratory on test specimens with small sizes made up of wood and densified wood (cone calorimeter tests). Other tests were carried out on full-size (CLT panels and connections using densified wooden dowels).

Concerning the results of the simulations, the thermal model allows to correctly transcribe heat transfers within a cellulosic material and to find the loss of mass measured during the test as well as the formation of charcoal after the test. Thus, this model has been validated for different cellulosic materials (normal wood and densified wood). In fact, this model does not take into account the mass transfers from the liquid and gas phases to the within the material, the structural modification of the exposed face (cracking and fall of carbon from wood) as well as the evolution of the thermal properties of charcoal as a function of temperature. Nevertheless, the global trends of heat transfer are well transcribed by the model (chapter 4).

Concerning the thermomechanical model, the simulated displacements are relatively close to those measured at the free end of connections. The use of mechanical properties measured on the normal wood and densified wood makes it possible to obtain better estimates of deflections. However, only one or two validation test is available. The repeatability of the measurement of displacements is therefore not verified.

Finally, we present the influence of various parameters of densified wood (carbonization, densification ratio…) with the model developed. Overall, densified wood shows the best fire

performance when compared to virgin wood and steel material. The effectiveness of using densified wood in fire-safe conditions is confirmed.

Perspectives

Based on the results obtained during this thesis, several points can be improved in order to enrich the digital methodology and to put a real 3D simulation tool available to the engineer. For this, different recommendations are considered.

As a first step, it seems important to take into account the combustion of gases and the oxidation of charcoal in order to improve the thermal transfer simulation results. This can be done by applying the kinetic model of D. Blasi with a five-step mechanism to replace the current thermal model with a three-step mechanism. Nevertheless, the use of this type of model seems difficult because of its complexity and large numbers of parameters to be determined as a function of the temperature.

Secondly, it seems necessary to improve the mesh technique used (3D). Indeed, the meshes developed during the present work are not yet adapted to the simulation for numerical reasons (calculation time too long in an engineering process). Likewise, it is difficult to increase the mesh density if a more detailed simulation of the phenomena is desired. It could be possible to improve this point by decoupling thermal and mechanical calculations. Behavior simulation thermomechanics would then be done in two stages: a study of heat transfer on a simplified geometry but strongly meshed followed by a mechanical study with a projection of temperature fields and thermal degradation parameters on a less dense mesh. This would probably allow a reduction in mechanical computation time while approaching the solution wanted.

Thirdly, it is important to take into account the reduction of tight-fitting of joints to improve the thermo-mechanical simulation results. This can be performed by using the friction coefficient as a function of temperature.

Lastly, it is necessary to carry out several tests to validate the model. In particular, on the basis of the test presented in section 4.4, it will be necessary to improve and enrich the measurement of temperature and displacement of samples for thermal and mechanical boundary conditions known. Indeed, we do not have measurements deemed sufficiently reliable and numerous to validate the model.

General bibliography

[A]

Abaqus, Theory Manual, Version 6.14, Providence, RI : Dassault Systèmes Simulia Corp (2016).

Anshari B., Guan Z., Kitamori A., Jung K., Hassel I., Komatsu K., Mechanical and moisture-dependent swelling properties of compressed Japanese cedar, Construction and Building Materials 25 (2011) 1718-1725.

Anshari B., Guan Z., Kitamori A., Jung K., Komatsu K., Structural behaviour of glued laminated timber beams pre-stressed by compressed wood, Construction and Building Materials 29 (2012) 24–32.

Anshari B., Guan Z., Wang Q., Modelling of Glulam beams pre-stressed by compressed wood, Composite Structures 165 (2017) 160-170.

Asako Y., Kamikoga H., Nishimura H., Yamaguchi Y., Effective thermal conductivity of compressed woods, International Journal of Heat and Mass Transfer 45 (2002) 2243-2253.

Audebert M., Approche expérimentale et modélisation du comportement au feu d'assem-blages bois sous différents types de sollicitations, Thèse doctorat, Université Blaise Pascal - Clermont II (2010).

[B]

Bal H., Jannot Y., Gaye S., Demeurie F., Measurement and modelisation of the thermal conductivity of a wet composite porous medium: Laterite based bricks with millet waste additive, Construction and Building Materials 41 (2013) 586-593.

Barbe C., Keller R., Les rayons ligneux et le matériau bois, Revue Forestière Française 1 (1996) 63-68.

Bellais M., Davidssonb K.O., Liliedahla T., Sjostroma K., Pettersson J.B.C., Pyrolysis of large wood particles: a study of shrinkage importance in simulation, Fuel 82 (2003) 1541-1548.

Bilbao R., Mastral J.F., Ceamanous J., Aldea M.E., Modeling of the pyrolysis of wet wood, Journal of Analytical and Applied Pyrolysis 36 (1996) 81-97.

Boulet P., Parent G., Acem Z., Rogaume T., Fateh T., Zaida J., Richard F., Characterization of the radiative exchanges when using a cone calorimeter for the study of the plywood pyrolysis, Fire safety journal 51 (2012) 53-60.

Branca C., Di Blasi C., Global interinsic kinetics of wood oxidation, Fuel 83 (2004) 81–87.

Brandt B., Zollfrank C., Franke O., Fromm J., Goken M., Durst K., Micromechanics and ultrastructure of pyrolysed softwood cell walls, Elsevier (2010).

Broström M., Nordina A., Pommer L., Branca C., Di Blasi C., Influence of torrefaction on the devolatilization and oxidation kinetics of wood, Journal of Analytical and Applied Pyrolysis 96 (2012) 100-109.

Bryden K.M., Hagge M.J., Modeling the combined impact of moisture and char shrinkage on the pyrolysis of a biomass particle, Fuel 82 (2003) 1633-1644.

[C]

Chan W.R., Kelbon M., Krieger B.B., Modeling and experimental verification of physical and chemical processes during pyrolysis of a large biomass particle, Fuel 64 (1985) 1505-1513.

Chaos M., Spectral aspects of bench-scale flammability testing: application to hardwood pyrolysis, Fire Safety Science 11 (2014) 165-178.

Coppalle A., Feux de compartiment (2010).

Couhert C., Pyrolyse flash à haute température de la biomasse ligno-cellulosique et de ses composés-production de gaz de synthèse, Thèse doctorat, École des Mines de Paris (2007).

Cueff G., Développement d'un modèle thermomécanique du comportement sous agressions thermiques de matériaux cellulosiques. Application à l'étude de résistance au feu de panneaux de bloc-porte en aggloméré de bois, PhD Thesis, University of Bordeaux, France (2004).

Cueff G., Mindeguia J.C., Dréan V., Breysse D., Auguin G, Experimental and numerical study of the thermomechanical behaviour of wood-based panels exposed to fire, Construction and Building Materials 160 (2018) 668-678.

[D]

Dahlquist G., Bjork A., Numerical Methods, Prentice-Hall, Englewoods (1974).

De Vries J., Ren N., Chaos M., Temperature measurements on solid surfaces in rack-storage fires using IR thermography, In Thermosense: Thermal Infrared Applications XXXVII, International Society for Optics and Photonics (2015).

Derome D., About heat and mass transfer in wood (2014).

Di Blasi C., Analysis of convection and secondary reaction effects within porous solid fuels under-going pyrolysis, Combustion Science and Technology 90 (1993) 315-340.

Di Blasi C., Modeling chemical and physical processes of wood and biomass pyrolysis, Journal of

Energy and Combustion Science 34 (2008) 47-90.

Drean V., Projet VIRGILE: proposition d'un modèle de combustion des matériaux composites pour simulation sur FDS-5, Rapport Interne EFECTIS France E-R&D-11/010 (2011).

[E]

Eurocode 3: Design of Steel Structures - Part 1-2: General rules - Structural Fire Design, British Standards Institute, London, UK (2004).

Eurocode 5 - Design of timber structures, Part 1-2 : General - Structural fire design, CEN 2004 (European Committee for Standardization), EN 1995-1-2, Brussels, Belgium.

Erchinger C., Frangi A., Fontana M., Fire design of steel-to-timber dowelled connections, Engineering Structures 32 (2010) 580-589.

[F]

Fateh T., Rogaume T., Luche J., Richard F., Jabouille F., Modeling of the thermal decomposition of a treated plywood from thermo-gravimetry and Fourier-transformed infrared spectroscopy experimental analysis, Journal of Analytical and Applied Pyrolysis 101 (2013) 35-44.

Forest Product Laboratory, Wood Handbook: wood as an engineering material, Centennial Edition (2010).

Flynn D.R., Response of High Performance Concrete to Fire Conditions: Review of Thermal Property Data and Measurement Techniques, Report NIST GCR (1999) 99-767.

Fredlund B., Modelling of heat and mass transfer in wood structures during fire, Fire Safety Journal 20 (1993) 39-69.

Freed A. D., Walker K. P., Exponential Integration algorithms Applied to Viscoplasticity, 3rd International Conference on Computational Plasticity, Barcelona (1992) 1757-1768.

Front R., Marcilla A., Verdu E., Devessa J., Kinetics of the pyrolysis of almond shells and almond shells impregnated with cobalt dichloride in a fluidized bed reactor and in a pyroprobe 100, Industrial & Engineering Chemistry Research 29 (1990) 1846-1855.

[G]

Gear C. W., Numerical Initial Value Problems in Ordinary Differential Equations, Prentice-Hall, Englewoods (1993).

Glass S.V., Zelinka S.L., Moisture relations and physical properties of wood, Wood Handbook - Wood as an Engineering Material, U.S. Department of Agriculture Forest Service, Forest

Products Laboratory, Madison, WI (2010).

Grioui N., Halouani K., Zoulalian A., HalouaniF., Thermogravimetric analysis and kinetics modeling of isothermal carbonization of olive wood in inert atmosphere, Thermochimica Acta 440 (2006) 23-30.

Grönli M., Melaaen M., Mathematical Model for Wood Pyrolysis Comparison of Experimental Measurements with Model Predictions, Energy Fuels 14 (2000) 791-800.

Guitard D., Mécanique du matériau bois et composites, Nabla, Cepadues éd (1987).

[H]

Harrington J.J., MicroFibril Angle in Wood (1998).

Hill R., A theory of yielding and plastic flow of anisotropic metals, Proceedings of the Royal Society of London (1948) 281.

Hoffman O., The brittle strength of orthotropic materials, Journal of Composite Materials 1 (1967) 200-206.

Howord E.T., Manwiller F.G., Anatomical characteristics of southern pine steamwood, Wood Science 2 (1969) 77-86.

Hughes M., Introduction wood properties and wood product: Wood - Water relationship (2009).

Hugues T. J. R., Taylor R. L., Unconditionally stable algorithms for quasistatic elastoviscoplasticity finite element analysis, Computers and Structures 4 (1978) 169-173.

[I]

Inoue M., Norimoto M., Tanahashi M., Rowell R.M., Steam or heat fixation of compressed wood, Wood and Fiber Science 25 (1993a) 224-235.

Islam M.A., Razzak M.A., Ghosh B., Optimization of thermally-compressed wood of Trewia nudiflora species using statistical Box–Behnken design and desirability function, Journal of the Indian Academy of Wood Science 11 (2014) 5-14.

ISO 5660-1 - Reaction-to-fire tests - Heat release, smoke production and mass loss rate - Part 1: heat release rate (cone calorimeter method) (2002).

ISO 834-1:1999 - Fire-resistance tests - Elements of building construction - Part 1: General requirements, International Organization for Standardization, Geneva, Switzerland (1999).

[J]

Jannot Y., Degiovani A., Grigorova-Moutiers V., Godefroy J., A passive guard for low thermal

conductivity measurement of small samples by the hot plate method, Journal of Measurement Science and Technology 28 (2017).

Jannot Y., Remy B., Degiovanni A., Measurement of thermal conductivity and thermal resistance with a tiny hot plate, High Temperatures - High Pressures 39(2010) 11-31.

Janssens M.L., Modeling of the thermal degradation of structural wood members exposed to fire, Fire Mater 28 (2004) 199-207.

Jung K., Kitamori A., Komatsu K., Development of a joint system using a compressed wooden fastener I: evaluation of pull-out and rotation performance for a column-sill joint, Journal of Wood Science 55 (2009) 273-282.

Jung K., Kitamori A., Komatsu K., Development of a joint system using a compressed wooden fastener II: evaluation of rotation performance for a column-beam joint, Journal of Wood Science 56 (2010a.) 118-126.

Jung K., Kitamori A., Komatsu K., Evaluation on structural performance of compressed wood as shear dowel, Holzforschung 62 (2008) 461-467.

Jung K., Murakami S., Kitamori A., Chang W.S., Komatsu K., Improvement of glued-in-rod joint system using compressed wooden dowel, Holzforschung 64 (2010b) 799-804.

[K]

Kansa E.J., Perlee H.E., Chaiken R.F., Mathematical model of wood pyrolysis including internalforced convection, Combustion and Flame 29 (1997) 311-324.

Khelifa M., Khennane A., El Ganaoui M., Rogaume Y., Analysis of the behaviour of multiple dowel timber connections in fire, Fire Safety Journal 68 (2014) 119-128.

Khelifa M., Oudjene M., Khennane A., Fracture in sheet metal forming: effect of ductile damage evolution, Computers & Structures 85 (2007) 205-212.

Khelifa M., Oudjene M., Numerical damage prediction in deep-drawing of sheet metals, Journal of Materials Processing Technology 200 (2008) 71-76.

Knigge W., Schulz H., Grundriss der Forstbenutzung, Verlag Paul Parey, Berlin (1966).

Knudson R.M., Schniewind A.P., Performance of structural wood members exposed to fire, Forest Products Journal 25(2) (1975) 23-32.

Kollmann F.F.P., Technologie des Holzes, Springer-Verlag, Berlin (1936).

Kollmann F., Kuenzi E., Stamm A., Principles of Wood Science and Technology, Springer-Verlag

Berlin Heidelberg, Wood Based Materials 12 (1975) 703.

Kosik M., Dandarova M., Domansky R., Pyrolyse des Buchenholzes bei niedrigen Temperaturen IX: Chemische Veränderungen im Buchenholz während der Pyrolyse, Holzforschung Holzver wendung 21 (1969) 40-43.

Kutnar A., Sandberg D., Haller P., Compressed and moulded wood from processing to products, Holzforschung 69 (2015) 885-897.

Kutnar A., Sernek M., Densification of wood, Zbornik gozdarstva in lesarstva (82) 53-62.

[L]

Laplanche K., Etude du comportement au feu des assemblages de structures bois: Approche expérimentale et modélisation, PhD Thesis, University of Blaise Pascal (Clermont-Ferrand), France (2006).

Liden A., Berruti F., Sott D., A kinetic model for the production of liquids from the flash pyrolysis of biomass, Chemical Engineering Communications 65 (1988) 207-221.

Li L., Gong M., Chui Y., Schneider M., Li D., Measurement of the elastic parameters of densified balsamfir wood in the radial-tangential plane using a digital image correlation (DIC) method, Journal of Materials Science 48 (2013) 7728-7735.

[M]

Menis A., Fire resistance of Laminated Veneer Lumber (LVL) and Cross-Laminated Timber (XLAM) elements, PhD Thesis, Università degli studi di Cagliari, Italy (2012).

[N]

Nassar M., Mackay M., Mechanism of thermal decomposition of lignin, Wood and Fiber Science 16 (1984) 441-453.

Navi P., Heger F., Combined densification and thermo-hydro-mechanical processing of wood, MRS Bull 29 (2004) 332-336.

Navi P., Heger F., Comportement thermo-hydromécanique du bois: Applications technologiques et dans les structures, P U Polytec ROM, PPUR (2005).

NF-EN-310, Panneaux à base de bois: détermination du module d'élasticité en flexion et de la résistance à la flexion (1993).

NF-EN-312, Panneaux de particules: exigences (2004).

NF-EN-319, Panneaux de particules et panneaux de fibres: détermination de la résistance à la traction perpendiculaire aux faces du panneau (1993).

[O]

Oliver V., Karin D.B., Christian H., Alfred T., Ulrich M., Thermal conductivity of wood at angles to the principal anatomical directions, Wood Science and Technology 49 (2015) 577-589.

Oudjene M., Khelifa M., Elasto-plastic constitutive law for wood behaviour under compressive loadings, Construction and Building Materials 23(2009) 3359-3366.

Oudjene M., Khelifa M., Finite element modelling of wooden structures at large deformations and brittle failure prediction, Materials & Design 30 (2009) 4081-4087.

[P]

Parent G., Acem Z., Lechêne S., Boulet P., Measurement of infrared radiation emitte by the flame of a vegetation fire, International Journal of Thermal Sciences 49(3) (2010) 555-562.

Park W.C., Atreya A., Howard R., Experimental and theoretical investigation of heat and masstransfer processes during wood pyrolysis, Combustion and Flame 157 (2010) 481-494.

Permali D., Densified wood laminate, Accessed: 14th January 2019, Available at: http://www.permalideho.co.uk/hydulignum.asp.

[R]

Racher P., Laplanche K., Dhima D., Bouchaïr A., Thermo-mechanical analysis of the fire performance of dowelled timber connection, Engineering Structures 32 (2010) 1148-1157.

Rautkari L., Properzi M., Pichelin F., Hughes M., An innovative thermo densification method for wooden surfaces, Proceedings of the 10th World Conference on Timber Engineering (2008) 177-184.

Reiterer A., Stanzl-Tschegg S.E., Compressive behaviour of softwood under uniaxial loading at different orientations to the grain, Mechanics of Materials 33(2001) 705-715.

Riggio M., Sandak J., Sandak A., Densified wooden nails for new timber assemblies and restoration works: a pilot research, Construction and Building Materials 102 (2016) 1084-1092.

Rousset P., Choix et validation expérimentale d'un modèle de pyrolyse pour le bois traité par haute température: de la micro-particule au bois massif, Thèse doctorat, Université Henri-Poincaré Nancy 1, Nancy (2004).

[S]

Salmen L., On the Interaction between Moisture and Wood Fibre Materials, MRS Online Proceedings Library Archive (1990) 197.

Samaké A., Taazount M., Audebert P., Palmili P., Thermo-hydric transfer within timber connections under fire exposure: Experimental and numerical investigations, Applied Thermal Engineering 63 (2014) 254-265.

Sandberg D., Haller P., Navi P., Thermo-Hydro and Thermo-Hydro-Mechanical Wood, Processing: an Opportunity for Future Environmentally Friendly Wood Products, Taylor&Francis Group (2013).

Sandberg D., Kutnar A., Mantanis G., Wood modification technologies - a review, iForest - Biogeosciences and Forestry 10 (2017) 895.

Santos C.M.T., Del Menezzi C.H., De Souza M.R., Properties of thermo-mechanically treated wood from Pinus caribaea var. hondurensis, BioResources 7 (2012) 1850-1865.

Schaffer E.L., Elevated temperature effect on the longitudinal mechanical properties of wood, Thèse doctorat, University of Wisconsin (1971).

Schnabl S., I. Planinc I., G. Turk G., Srpcic S., Fire analysis of timber composite beams with interlayer slip, Fire Safety Journal 44 (2009) 770-778.

Schnabl S., Turk G., Planinc I., Buckling of timber columns exposed to fire, Fire Safety Journal 46 (2011) 431-439.

Shen D.K., Fang M.X., Luo Z.Y., Cen K.F., Modeling pyrolysis of wet wood under external heat Flux, Fire Safety Journal 42 (2007) 210-217.

Song J., Chen C., Zhu S., Zhu M., Dai J., Ray U., Li Y., Kuang Y., Li Y., Quispe N., Processing bulk natural wood into a high-performance structural material, Nature 554 (2018) 224.

Sotayo A., Bradley D., Bather M., Oudjene M., Review of state of the art of dowel laminated timber members and densified wood materials as sustainable engineered wood products for construction and building applications, Developments in the Built Environment 1 (2020).

[T]

Terrei L., Acem Z., Georges V., Lardet P., Boulet P., Parent G., Experimental tools applied to the ignition study of spruce wood under cone calorimeter, 3rd European Symposium on Fire Safety Science, 12-14 Sep 2018, Nancy, proceeding to be published in Journal of Physics: Conference Series.

Terrei L., Acem Z., Lardet P., Georges V., Boulet P., Parent G., Experimental tools applied to the

ignition study of spruce wood under cone calorimeter, Journal of Physics: Conference series volume 1107.

Thi V.D., Khelifa M., El Ganaoui M., Rogaume Y., Finite element modeling of the pyrolysis of wet wood subjected to fire, Fire Safety Journal 81 (2016) 85-96.

Thi V.D., Khelifa M., Oudjene M., El Ganaoui M., Rogaume Y., Finite element analysis of heat transfer through timber elements exposed to fire, Engineering Structures 143 (2017) 11-21.

Thi V.D., Modélisation du comportement au feu des structures en bois, PhD Thesis, University of Lorraine, France (2017).

Thurner F., Mann U., Kinetic investigation of wood pyrolysis, Industrial & Engineering Chemistry Process Design and Development 20 (1981) 482-488.

[U]

Urbas J., Parker W. J., Luebbers G. E., Surface temperature measurements on burning materials using an infrared pyrometer: accounting for emissivity and reflection of external radiation, Fire and materials 28(1) (2004) 33-53.

[V]

Várhegyi G., Antal M.J., Jakab E., Szabo P., Kinetic modeling of biomass pyrolysis, Journal of Analytical and Applied Pyrolysis 42 (1997) 73-87.

Várhegyi G., Gronli M.G., Di Blasi C., Effects of sample origin, extraction and hot water washing on the devolatilization kinetics of chestnut wood, Journal of Industrial & Engineering Chemistry Research 43 (2004) 2356-2367.

Vuorine T., Structure and chemistry of wood, lecture 6: wood extractives, 2009.

[W]

Winandy J.E., Rowell R.M., The Chemistry of Wood Strength, The Chemistry of solid Wood (1983) 211-255.

[X]

Xu B.H., Bouchaïr A., Taazount M., Vega E.J., Numerical and experimental analyses of multiple-dowel steel-to-timber joints in tension perpendicular to grain, Engineering Structures 31 (2009) 2357-2367.

[Y]

Yoshihara H., Tsunematsu S., Bending and shear properties of compressed Sitka spruce, Wood Science and Technology 41 (2007) 117-131.

Yu Z.T., Xu X., Fan L.W., Hu Y.C., Cen K.F., Experimental measurements of thermal conductivity of wood species in China: Effects of density, temperature, and moisture, Forest Products Journal 61(2011) 130-135.

[Z]

Zhao C., Zhang X., Liu L., Yu Y., Zheng W., Song P., Probing Chemical Changes in Holocellulose and Lignin of Timbers in Ancient Buildings, Journal List, Polymers, Basel (2019).

Appendices

Appendix 1: Thermal properties of Oak wood

Thermo-physical properties

The initial thermo-physical properties of Oak wood used in the simulations are given from the experiment (hot plate method) in Tables A1.1-A1.2.

Table A1. 1. Thermal conductivity for Oak wood.

Samples	Humidity (%)	Density (kg/m^3)	Conductivity (W/(m.K))
1	7,5		0,097
2			0,0979
3			0,0956
4			0,0948
Mean		650	0,0963
C.o.V			0,028%

Table A1. 2. Specific heat mean values (J/(kg.K)).

	20 °C	30 °C	40 °C	50 °C	60 °C
Oak wood	1222	1263	1310	1352	1408

Kinetic parameters

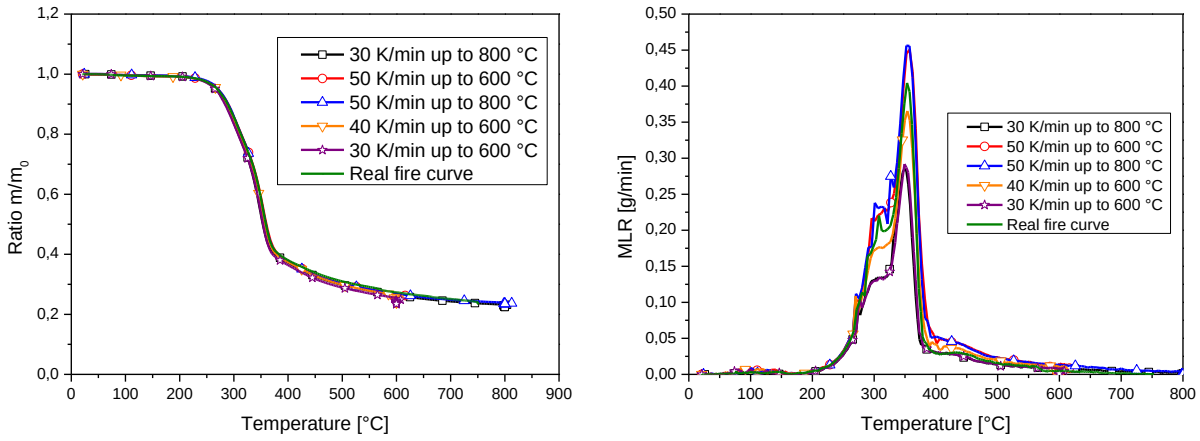

(a) m/m_0 (b) dm/dt

FIGURE A1. 1 - (a) The mass and (b) the time derivative evolution of the Oak wood powder.

The TGA results analyzed here were carried out on powder of Oak wood. The six different heating conditions as in the experiment were tested. Thermal loading of 600 °C and 800 °C increased at the rate of 30, 40, 50 K/min, and a real fire curve was applied. The combustion of the pyrolysis gases was not observed during the tests. The mass evolutions of Oak wood powder, under an inert atmosphere, as a function of the temperature are illustrated in Figure A1.1, for the six conditions studied.

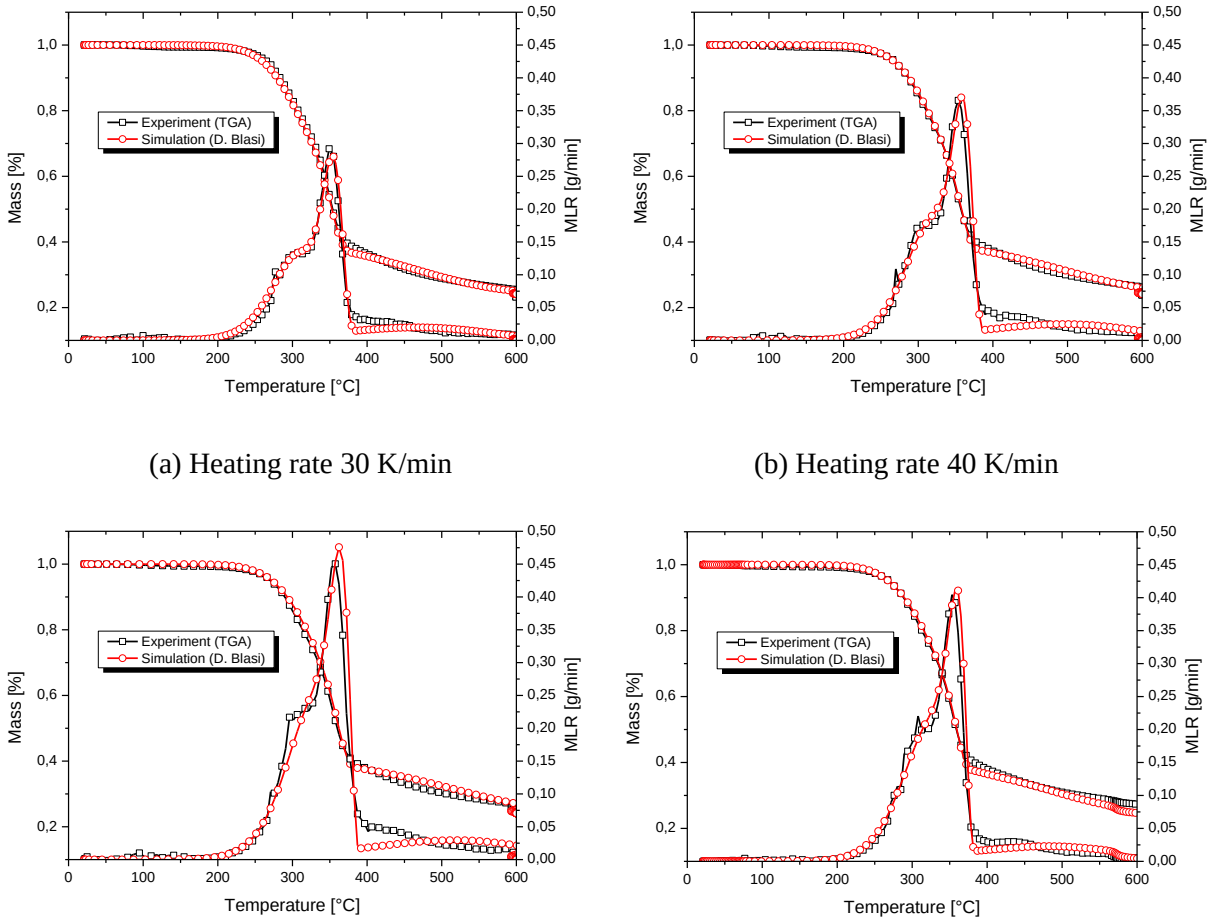

(a) Heating rate 30 K/min

(b) Heating rate 40 K/min

(c) Heating rate 50 K/min

(d) Real fire curve

FIGURE A1. 2 - Comparison of the measured and calculated MLR.

The values of the curves measured by the TGA are simulated with the model of Di Blasi et al. [1]. Figure A1.2 shows the results of the simulations obtained using the pyrolysis model of Blasi et al. [1]. There is a similarity between the results presented in Figure A1.2. The optimized kinetic parameters used in the simulations are summarised in Table A1.3. Qualitatively, the values calculated by the pyrolysis model, Di Blasi et al. [1], are very close to the experimental results. The optimum kinetic parameters summarized in Table A1.3 are

integrated into a finite element model to simulate fire tests.

Table A1. 3. Kinetic parameters of Blasi et al. [1].

Reaction (i)	(1)	(2)	(3)
$A_i[s^{-1}]$	9.89E6	3.58E15	2.62E0
E_i[kJ/mol]	95.14	203.62	39.24
Mass fraction υ_i	0.241	0.353	0.165

The estimated values of activation energies for pyrolysis reactions, used in simulations, are compared to those of the values published in the literature. The activation energies of the second and third reactions, 203.62 and 39.24 kJ/mol, are in the range of those reported [2] for the decomposition of cellulose (195–240 kJ/mol) and lignin (35–65 kJ/mol) components in biomass. The activation energy estimated for the first reaction step, 95.14 kJ/mol, is slightly lower than the range of values usually estimated for the decomposition of hemicellulose components (100–122 kJ/mol, see Ref. [2]). This difference can be plausibly attributed to the wider range of heating rates considered here and probably to the different geographical origin, age, and specific part of the tree [3]. Therefore it is possible to say that the kinetic parameters are correctly estimated in this present work.

Bibliography

[1] Broström M., Nordina A., Pommer L., Branca C., Di Blasi C., Influence of torrefaction on the devolatilization and oxidation kinetics of wood, Journal of Analytical and Applied Pyrolysis 96 (2012) 100-109.

[2] Várhegyi G., Antal M.J., Jakab E., Szabo P., Kinetic modeling of biomass pyrolysis, Journal of Analytical and Applied Pyrolysis 42 (1997) 73-87.

[3] Várhegyi G., Gronli M.G., Di Blasi C., Effects of sample origin, extraction and hot water washing on the devolatilization kinetics of chestnut wood, Journal of Industrial & Engineering Chemistry Research 43 (2004) 2356-2367.

Appendix 2: Adhesive free timber building (AFTB) project

The European Commission conducts a specific policy aimed at developing an economy with low carbon by reducing greenhouse gas emissions by 80% by 2050 [1]. It is in this context, the European AFTB (Adhesive Free Timber Building) project was born (2016-2020). Its main objective is the development of engineered wood products without glue. The idea is to use dowels (trunnions) made of densified wood, therefore very resistant, to the assembly of wood slats as an alternative solution to synthetic glues.

AFTB project partners

Several academic and industrial partners were involved in the AFTB project. The partners are all from North West Europe (Figure A2.1):

- L'Université de Lorraine (France);
- L'université de Liverpool (Royaume-Uni);
- L'Université Nationale de Galway (Irlande);
- L'Université Technique de Dresde (Allemagne);
- L'Institut des Sciences et Technologie du Luxembourg (Luxembourg);
- L'Office Économique Wallon du Bois (Belgique);
- Plusieurs entreprises en France, en Allemagne et au Royaume-Uni.

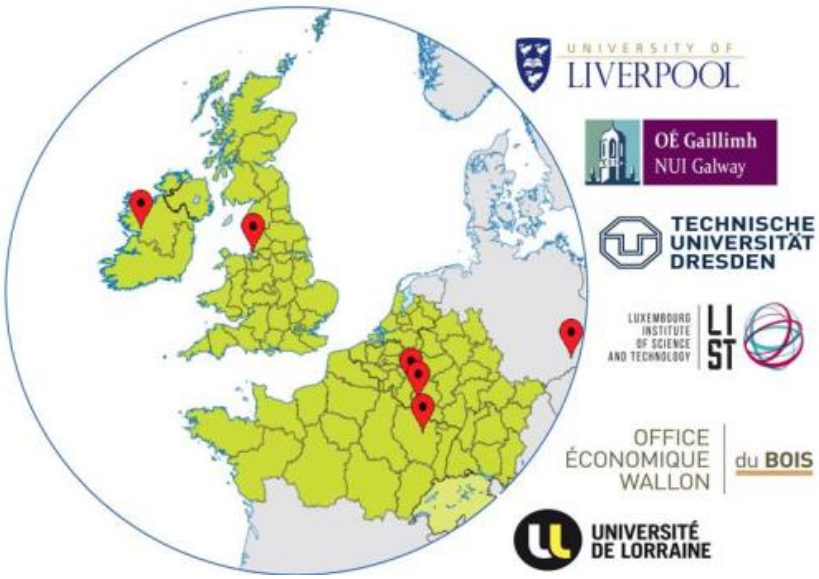

FIGURE A2. 1 - Geographical distribution of AFTB project partners.

AFTB project partners

The work focused on the realization of beams and CLT panels with three lamellae assembled by densified wooden trunnions. Two types of wood were used for the manufacture of beams, namely spruce and oak. As for the CLT panels they were manufactured using oak (Figure A2.2).

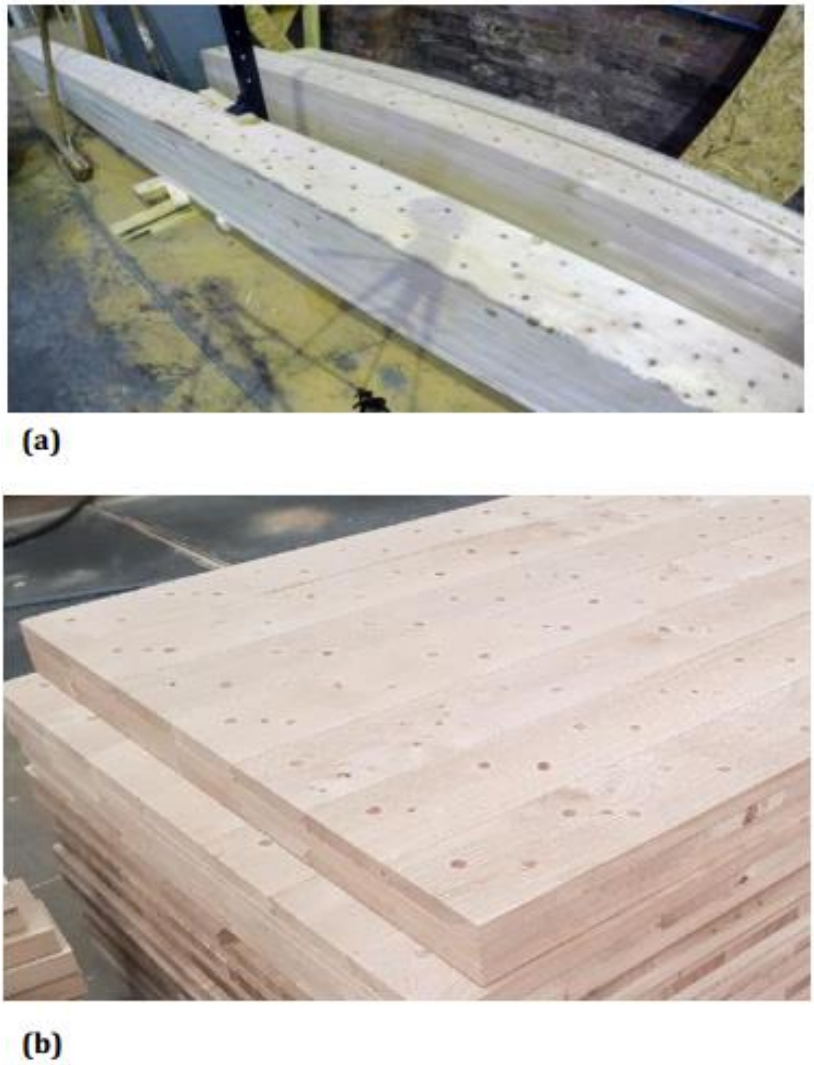

FIGURE A2. 2 - Example of glue-free products assembled by densified wood dowels (University of Lorraine, University of Liverpool): (a) beams, (b) CLT panels.

In order to characterize the assemblies using trunnions in densified wood, double shear connections were also made from two essences: spruce and oak. Other types of assemblies have also been considered in the framework of the work carried out by the Irish partner (Figure A2.3).

FIGURE A2. 3 - Example of beam-column and beam-beam connections developed at Galway University.

Bibliography

[1] European Commission, A Roadmap for moving to a competitive low carbon economy in 2050 (2012) 100-109.

Abstract

As part of a European project, a new assembly using densified dowels to hold wooden slats is currently being validated at the structural level. This type of assembly has the advantage of not using glues and of making it possible to manufacture large-sized structures consisting only of wood. The principle consists of positioning the wooden planks as desired, then drilling and inserting densified dowels: under the effect of moisture absorption, the densified dowels swell and block the assembly, making the structure rigid.

The use of this type of assembly requires a multitude of sizing and behavior checks under various stresses, including thermomechanical variations. Thus, within the framework of this thesis work, the objective will be to characterize the behavior of wood lamellar assemblies by densified dowels subjected to significant thermo-hydric stresses, in particular during the fire. To do this, we propose an approach coupled with experiments and numerical modeling. The experiments will first allow the acquisition of the basic data to develop the model. Numerical modeling will then make it possible to better understand the mechanisms involved in the fire of these types of structures in order to improve their performance. This will also reduce the number of expensive trials. The model will be validated by temperature measurements at different depths in the section of the lamellae, but also within the densified dowels. These results will then be compared to experimental tests for validation on a few fire tests under mechanical stress.

This model can then be used to estimate the behavior of more complex structures subjected to fire and to provide basic data for the sizing of complete buildings. The results can also serve as a basis for amending regulatory texts such as Eurocode 5.

Keywords: Fire performance, numerical simulations, wood structures, wood dowels, wood densification, multilayer structures, assembly by densified dowels, wood pyrolysis.

Résumé

Dans le cadre d'un projet européen, un nouvel assemblage par tourillons densifiés permettant de maintenir des lamelles en bois est en cours de validation au niveau structurel. Ce type d'assemblage possède l'avantage de ne pas utiliser de colles et de permettre de fabriquer des structures de grandes dimensions ne comportant que du bois. Le principe consiste à mettre en place les planches de bois comme souhaité, puis à percer et introduire des tourillons densifiés : sous l'effet de la reprise d'humidité, les tourillons densifiés gonflent et bloquent l'assemblage, rendant la structure rigide.

L'utilisation de ce type d'assemblages nécessite une multitude de vérifications de dimensionnement et de comportement à des sollicitations diverses dont les variations thermomécaniques. Ainsi, dans le cadre de ce travail de thèse, l'objectif sera de caractériser le comportement des assemblages lamelles de bois par tourillons densifiées soumises à des contraintes thermo-hydriques importantes, notamment lors d'incendie. Pour ce faire, nous proposons une approche couplée par expérimentations et par modélisation numérique. Les expérimentations permettront dans un premier temps d'acquérir les données de base pour développer le modèle. La modélisation numérique permettra ensuite de mieux comprendre les mécanismes mis en jeu lors de l'incendie de ces types de structures pour en améliorer les performances. Cela permettra en outre de réduire le nombre d'essais couteux. Le modèle sera validé par des mesures de températures à différentes profondeurs dans la section des lamelles, mais aussi au sein des tourillons densifiés. Ces résultats seront alors confrontés à des essais expérimentaux pour validation sur quelques essais au feu en sollicitations mécaniques.

Ce modèle pourra alors être utilisé pour estimer le comportement de structures plus complexes soumises à un incendie et fournir des données de base pour le dimensionnement de bâtiments complets. Les résultats pourront également servir de base pour amender les textes réglementaires tels que l'Eurocode 5.

Mots-clés: Comportement au feu, simulations numériques, structures en bois, chevilles bois, densification du bois, structures muliticouches, assemblage par chevilles densifiées, pyrolyse du bois.